



**HAL**  
open science

# Polarization-resolved Second Harmonic Microscopy in collagenous tissues: theoretical and experimental developments, and application to microstructural imaging during biomechanical assays in tendon.

Ivan Gusachenko

► **To cite this version:**

Ivan Gusachenko. Polarization-resolved Second Harmonic Microscopy in collagenous tissues: theoretical and experimental developments, and application to microstructural imaging during biomechanical assays in tendon.. Optics [physics.optics]. Ecole Polytechnique X, 2012. English. NNT: . pastel-00910146

**HAL Id: pastel-00910146**

**<https://pastel.hal.science/pastel-00910146>**

Submitted on 27 Nov 2013

**HAL** is a multi-disciplinary open access archive for the deposit and dissemination of scientific research documents, whether they are published or not. The documents may come from teaching and research institutions in France or abroad, or from public or private research centers.

L'archive ouverte pluridisciplinaire **HAL**, est destinée au dépôt et à la diffusion de documents scientifiques de niveau recherche, publiés ou non, émanant des établissements d'enseignement et de recherche français ou étrangers, des laboratoires publics ou privés.



Dissertation submitted for the degree of

Doctor of Ecole Polytechnique

Speciality: *Physics*

IVAN GUSACHENKO

**POLARIZATION-RESOLVED SECOND HARMONIC MICROSCOPY IN  
COLLAGENOUS TISSUES: THEORETICAL AND EXPERIMENTAL  
DEVELOPMENTS, AND APPLICATION TO MICROSTRUCTURAL  
IMAGING DURING BIOMECHANICAL ASSAYS IN TENDON**

performed at Laboratory for Optics and Biosciences  
and defended on October 29, 2012 at Ecole Polytechnique

Defence committee:

Mme Céline FIORINI	CEA-Saclay	referee
M. François TREUSSART	ENS-Cachan	referee
Mme Sophie BRASSELET	Institut Fresnel, Université Aix-Marseille	examiner
M. Pierre-François BREVET	LASIM, Université Claude Bernard Lyon	examiner
M. Jean-Marc ALLAIN	LMS, Ecole Polytechnique	examiner
Mme Marie-Claire SCHANNE-KLEIN	LOB, Ecole Polytechnique	Ph.D. supervisor



# Contents

<b>1</b>	<b>Collagen</b>	<b>13</b>
1.1	Structure and synthesis . . . . .	13
1.1.1	Collagen types . . . . .	13
1.1.2	Collagen type I structure and synthesis . . . . .	14
1.1.3	Hierarchical organization of collagen assemblies . . . . .	16
1.2	Tendon biomechanics . . . . .	17
1.3	Collagen visualization techniques and challenges . . . . .	20
1.3.1	Conventional visualization techniques . . . . .	21
1.3.1.1	Electron microscopy . . . . .	21
1.3.1.2	Atomic force microscopy . . . . .	21
1.3.1.3	Polarized light microscopy . . . . .	22
1.3.1.4	Optical coherence tomography . . . . .	22
1.3.1.5	Histological and immunohistochemistry staining . . . . .	22
1.3.2	Challenges in collagen visualization . . . . .	23
1.4	Conclusion . . . . .	24
<b>2</b>	<b>Theoretical background of polarization-resolved SHG microscopy</b>	<b>25</b>
2.1	Principles and contrast mechanisms of multiphoton microscopy . . . . .	25
2.1.1	Making intense fields . . . . .	26
2.1.2	Optical sectioning . . . . .	26
2.1.3	Two-photon excited fluorescence (2PEF) . . . . .	28
2.1.4	Second and third harmonic generation . . . . .	29
2.1.5	Coherent anti-Stokes Raman Scattering . . . . .	31
2.2	Second Harmonic Generation microscopy . . . . .	31
2.2.1	Mechanisms and principles . . . . .	31
2.2.1.1	Physical origins . . . . .	31
2.2.1.2	The role of coherence in SHG . . . . .	32
2.2.1.3	Resolution: comparison between SHG microscopy and other techniques . . . . .	34

2.2.2	Origin of SHG in collagen . . . . .	37
2.3	Collagen tensorial response . . . . .	39
2.3.1	Tensorial formalism of medium polarization . . . . .	40
2.3.2	Symmetries of collagen assemblies and nonlinear response tensors . . . . .	42
2.3.3	Second harmonic response of collagen at molecular and fibrillar scale . . . . .	43
2.3.4	P-SHG signal for $C_{\infty v}$ symmetry . . . . .	45
2.3.5	Tensorial response variation versus disorder in collagen fascicle . . . . .	47
2.4	Conclusion . . . . .	49
<b>3</b>	<b>Linear optical effects in polarization-resolved SHG microscopy</b>	<b>51</b>
3.1	Experimental setup for simultaneous SHG/2PEF imaging . . . . .	52
3.2	Experimental artefacts in thick anisotropic tissue . . . . .	54
3.2.1	Polarization-resolved Second Harmonic microscopy in anisotropic thick tissues . . . . .	55
3.3	Numerical simulations . . . . .	70
3.3.1	Overview of SHG simulation in tendon . . . . .	70
3.3.2	Focal field calculation in birefringent media . . . . .	71
3.3.2.1	Field propagation in a uniform medium. Angular spectrum representation. . . . .	71
3.3.2.2	Field in a birefringent medium . . . . .	73
3.3.2.3	Boundary conditions between isotropic and birefringent media . . . . .	75
3.3.2.4	Results and discussion . . . . .	76
3.3.3	SH radiation in tendon . . . . .	81
3.3.3.1	Radiation of a punctual dipole in a birefringent medium . . . . .	81
3.3.3.2	Radiation integral . . . . .	84
3.3.3.3	Simplification of the calculation using relative order of magnitude and symmetry of SH radiation components . . . . .	86
3.3.3.4	Results: angular radiation diagrams . . . . .	88
3.3.3.5	Results: total SHG intensity polarization diagrams . . . . .	92
3.3.3.6	Discussion of the simulated $\rho$ and $\Delta$ . . . . .	95
3.3.4	SHG simulations in cornea . . . . .	99
3.3.4.1	Introduction . . . . .	99
3.3.4.2	In vivo structural imaging of the cornea by polarization-resolved second harmonic microscopy . . . . .	100
3.4	Discussion . . . . .	116

<b>4</b>	<b>Tendon biomechanics</b>	<b>119</b>
4.1	Experimental setup . . . . .	120
4.2	Proof of concept of biomechanical assays coupled with SHG imaging . . . .	122
4.2.1	Introduction . . . . .	122
4.2.2	Monitoring micrometer-scale collagen organization in rat-tail tendon upon mechanical strain using second harmonic microscopy . . .	123
4.3	Varying fibril ordering in tendon . . . . .	130
4.3.1	Introduction . . . . .	130
4.3.2	Polarization-Resolved Second-Harmonic Generation in Tendon upon Mechanical Stretching . . . . .	131
4.4	Discussion . . . . .	142



# Acknowledgements

From my point of view, the whole procedure of getting a Ph.D. degree is a rite of initiation to a specific social and professional community. While often considered as a personal engagement, it is by definition a social product, which many parties contribute to, both professionally and spiritually. My thesis is no exception.

For that reason, I owe my sincere gratitude to all the people who spent these three years by my side and who contributed to this work in many different, always priceless, ways.

First of all, I would like to thank my Ph.D. supervisor, Marie-Claire Schanne-Klein, who introduced me to the magic of nonlinear optics. Thank you for always supporting me both in professional and personal plan, especially for constantly persuading me that our scientific results are in fact something appreciable. As I wasn't always respecting deadlines, you sometimes had to work late in the evenings or even on weekends, reviewing my manuscript. For these hours stolen from you being with your family, I beg you pardon.

Further, I would like to thank Jean-Marc Allain from the Laboratory of Mechanics of Solids, who virtually was my second supervisor. You recurrently explained to me some basic mechanics that I never was good at. Thank you for the fruitful collaboration, and for your patience.

Yannick Goulam, Gaël Latour and Viet Tran, thank you for sharing with me these exciting research subjects. It was a pleasant time working together, and may I hope you appreciated it as well.

I'm indebted to Daniel Caldemaison and Vincent de Greef for the great traction devices, as well as to Géraldine Liot and Diane Zala for the rat tails. The integral part of my job basically consisted in stretching these rat tails on those traction devices, so this contribution cannot be underestimated.

I want to thank the members of jury, Sophie Brasselet and Pierre-François Brevet, who kindly accepted to come to the defence and to think about some tricky, but always relevant, questions and remarks. Especially, I thank my referees Celine Fiorini and François Treussart, who read the whole manuscript and even had to write a report on it.

I express my gratitude to all member of the Laboratory for Optics and Biosciences, and especially to:

- head of the laboratory Jean-Louis Martin for the responsive direction;
- secretaries Laure Lachapelle and Christelle Français for the invaluable help and administrative support for my missions and visa applications;
- Jean-Marc Sintès and Xavier Solinas, for helping us to make our experimental setup do what it should;
- Emmanuel Beaurepaire, François Hache, Manuel Joffre for fruitful discussion, support, and critical reading of journal papers;
- Max Zimmerley for valuable remarks and proofreading in English;
- Ph.D. students Thibault Vielle, Pierre Mahou, Lucille Mendonça, Stéphane Bancelin, Laura Antonucci, Laura Lobato, and not-anymore-Ph.D.-students Alexander Podzorov, Nicolas Olivier, Guillaume Labroille and Antoine Wojdyla, for the most friendly environment and the most scientific discussions ever;
- everyone...

The last but not the least, I would like to thank my family and my friends, who believed in me and supported me during these three years.

# Introduction

This manuscript gives an account of the application of polarization-resolved second harmonic generation microscopy (P-SHG) in collagenous tissues. The present work has been carried out in the Laboratory for Optics and Biosciences at Ecole Polytechnique (UMR7645 CNRS, U696 Inserm), Palaiseau, France, in the research group of Dr. Hab. Marie-Claire Schanne-Klein. The group possesses an extensive expertise in second harmonic generation (SHG) from collagen and connective tissues with various structural properties. This work goes in continuity with the group's general aim to deeper understand SHG in biological tissues. However, it tackles two new subjects for the laboratory which are polarization resolution of SHG signal, and application of SHG to biomechanical studies of connective tissue. In order to give a consistent introduction to the following manuscript, this section will be structured in the following way. First we will give the state of the art of P-SHG studies in 2009, when the Ph.D. work started. Secondly, we will list the objectives of this thesis. Finally, we will give a chapter-wise outline of the whole manuscript.

In 2009, SHG microscopy had already been established as an effective tool for connective tissue visualization due to its high specificity for fibrillar collagen. The technique was used for imaging of unstained collagenous tissues such as various tendons [1–16], skin [17–19], sclera [16, 20], cornea [21–24], cartilage [16, 25], invertebrate disks [26], fibrotic lung [27] and kidney [28], and others. Other biological sources of SHG, such as myosin in muscle sarcomeres [15, 29, 30], tubulin microtubules [31], starch grains [32, 33] and cellulose [34, 35] had been identified as well.

P-SHG is SHG refinement, which is almost exclusively intended to determine the anisotropy of SHG signals in tissues. By 2009, this anisotropy was measured in tendon and other collagen tissues [6, 7, 11, 13, 36], and several attempts had been performed to relate this anisotropy to the microstructure of collagen, either at molecular [15, 30, 37] or fibrillar [3] level. Accordingly, the anisotropy measured by P-SHG had been used as a discerning parameter between SHG-capable tissues with different microscopic structures, such as between tendons and muscles [15], or between collagen in healthy and tumoral [36, 37] or diseased [23, 38] tissue. Another topical application of P-SHG was to determine fibril orientation fields in collagenous tissues [39–41]. However, the determined orientations

usually coincided with those morphologically visible on images, and thus provided no new information.

P-SHG is often used in thick anisotropic tissues, such as tendon, so intensity and polarization changes due to birefringence and attenuation should be taken into account. However, in spite of increasing attention to P-SHG in 2009, the theoretical model interpreting P-SHG signal from collagen remained almost unchanged for three decades since its introduction by Roth and Freund in 1981 [2]. In particular, this model didn't account for the birefringence directly affecting P-SHG results.

Collagenous tissues have a crucial structural and mechanical role in organism, which makes it an important subject for biomechanical studies since 1970s [42–49]. A particular concern in these studies is the relationship between macroscopic properties and microscopic structure. SHG and P-SHG have a high intrinsic specificity to fibrillar collagen, which would make them perfect techniques to complete biomechanical measurement. However, to the best of our knowledge, no such experimental system coupling biomechanics with SHG microscopy had been reported by 2009.

Taking into consideration the state of the art in P-SHG in 2009, we chose the following objectives for this work.

1. Develop and test a comprehensive model of P-SHG in thick collagenous tissues.
2. Perform numerical simulations of SHG imaging in thick anisotropic tissues in order to have an independent reference to the experiment and to validate our understanding of SHG process in collagen.
3. Couple SHG/P-SHG microscopy to biomechanical assays in collagenous tissues.
4. Derive the relationship between P-SHG signal and structural parameters in collagenous tissues and test it in model tissues

The manuscript is structured in the following way.

- Chapter 1 gives a brief introduction to collagen synthesis and structure, as well as to biomechanical properties of macroscopic collagen assemblies. Collagen visualization techniques and associated challenges are equally discussed.
- Chapter 2 first deals with the bases of multiphoton microscopy (MPM). A detailed description of SHG principles is given afterwards. A particular attention is given to the tensorial nature of SHG origin in collagenous tissues. We also introduce a theoretical model linking SHG signal with structural disorder in collagen tissues.

- Chapter 3 deals with the influence of various light propagation effects on P-SHG microscopy in thick collagen tissues. This includes a description of the experimental setup for SHG imaging, followed by the experimental data, which are analyzed by a phenomenological model we developed to account for these effects. Additionally, the chapter presents *ab initio* numerical simulations of light propagation and harmonic generation in tendon and cornea.
- Chapter 4 presents results of biomechanical studies in rat-tail tendon, accompanied by SHG and P-SHG imaging, performed in collaboration with the group of Jean-Marc Allain at the Solid Mechanics Laboratory (Ecole Polytechnique - CNRS - MinesParisTech). It first introduces a proof of concept study, which demonstrates the possibility of coupling mechanical assays with simultaneous SHG microscopy in a single setup. Secondly, it presents our P-SHG measurements of the orientational order variations of collagen fibrils in a tendon upon controlled stretching.
- Finally, the Conclusion draws the bottom line for the thesis, paying special attention to the accomplished objectives, and to the contribution this work brings to the area of P-SHG studies of collagen.



# Chapter 1

## Collagen

This manuscript revolves around optical and mechanical properties of collagen assemblies in mammal tissues. The notions of collagen types, structure, synthesis, assembly and degradation are crucial for understanding macroscopic properties such as the remarkable optical transparency of cornea or peculiar strain-stress curves of tendon. In this chapter, starting from the section 1.1, we first present synthesis and structure of collagen from its genes and its smallest structure block – tropocollagen – to different levels of spatial organization in tissues. Secondly, in section 1.2, it will be discussed how higher levels of assembly condition the mechanical properties of tendon fibrils and fascicles. The section 1.3 is devoted to collagen conventional visualization techniques and to the associated challenges. These challenges are discussed in the context of connective tissue development and pathology diagnosis, and justify the development of SHG that is introduced in the next chapter. The conclusion to the chapter will be drawn in 1.4.

### 1.1 Structure and synthesis

#### 1.1.1 Collagen types

Collagen is the most abundant protein in human body, accounting for about 25% of total protein mass [50]. This protein is present in virtually all organs and is responsible for their mechanical properties, especially for tensile strength and rigidity. Collagen is a major component of such structural tissues as ligaments, tendons, fascia, cornea, bones and cartilage. It also assures the strength of vessels and skin.

There are almost 30 types of collagen, which differ in their amino-acid sequence, structure and function [50]. All these types have a triple-helical domain of various length as the main feature of the molecule, and structural differences are achieved via variations in higher orders of organization. It is noteworthy to distinguish fibrillar collagen family

(types I, II, III, V, ...) from the one that forms basement membranes (collagen type IV), the two showing remarkable difference in macromolecular assembly and function.

By far the most abundant collagen type is the fibrillar collagen type I, since it accounts for about 90% of all collagens in humans. Its synthesis will be described in details, since it is the main component of tendon and cornea, which this manuscript is centred around.

### 1.1.2 Collagen type I structure and synthesis

The elementary block of collagen type I is the correspondent tropocollagen protein  $[(\text{Gly-X-Y})_n]_3$ , which is the final step of collagen synthesis before it is assembled to produce larger structures (fibrils, fibers) in the extracellular matrix. The part of the helical domain in tropocollagen molecule is shown in Fig. 1.1. It is a 300 nm-long and 1.5 nm-thick tightly wound triple helix, consisting of three peptide chains, each forming a left-handed helix [51]. Two of them are identical and called  $\alpha 1$ -chain, and the third is called  $\alpha 2$ -chain.

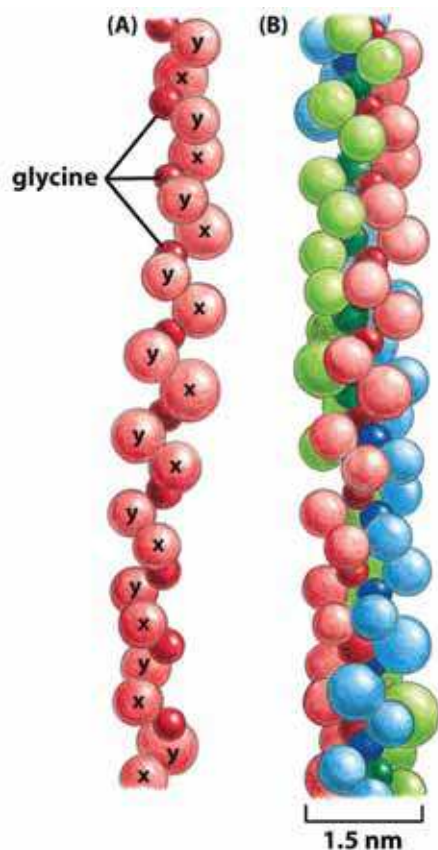


Figure 1.1: Schematic structure of collagen molecule. (a) Left-handed single helix, featuring glycine at every third position. X and Y can vary, though proline and hydroxyproline are frequent at X and Y positions respectively. (b) Right-handed triple helix with glycine amino acids pointing to the center of the assembly. Adapted from [50].

Every third amino acid in the strain is glycine, which has the smallest possible residue (only hydrogen atom)(Fig. 1.1 B). While the chains coil in helices, glycine occupies the

innermost position in the triple-chain assembly, which enables the three strands to come in contact and to form a compact collagen triple helix. Other amino acids in the strand can vary significantly, but the most abundant ones are proline and hydroxyproline, which are essential for stabilization of the triple helix (see the next subsection).

Collagen are produced by a class of cells named fibroblasts, which are additionally specialized depending on tissue, e.g. tenocytes in tendon and keratocytes in cornea. The synthesis is illustrated in Fig. 1.2. First, transcripts from COL1A1 and COL1A2 genes are translated directly into the lumen of the endoplasmic reticulum (ER) thanks to a short N-terminal signal sequence. The newly synthesized strands, called pro- $\alpha$ -chains, undergo post-transcriptional changes into the ER lumen: the signal sequence is cleaved, selected prolines and lysines are hydroxylated to produce hydroxyproline and hydroxylysine, and glycosylation of selected hydroxylysines is performed. Then, the three pro- $\alpha$  chains self-assemble into a procollagen triple helix. Hydroxylated amino acids help to stabilize the triple helix by hydrogen bonds they create between one another. After secretion via secretory vesicles, the cleavage of propeptides produces tropocollagen molecules consisting essentially of a single helical domain.

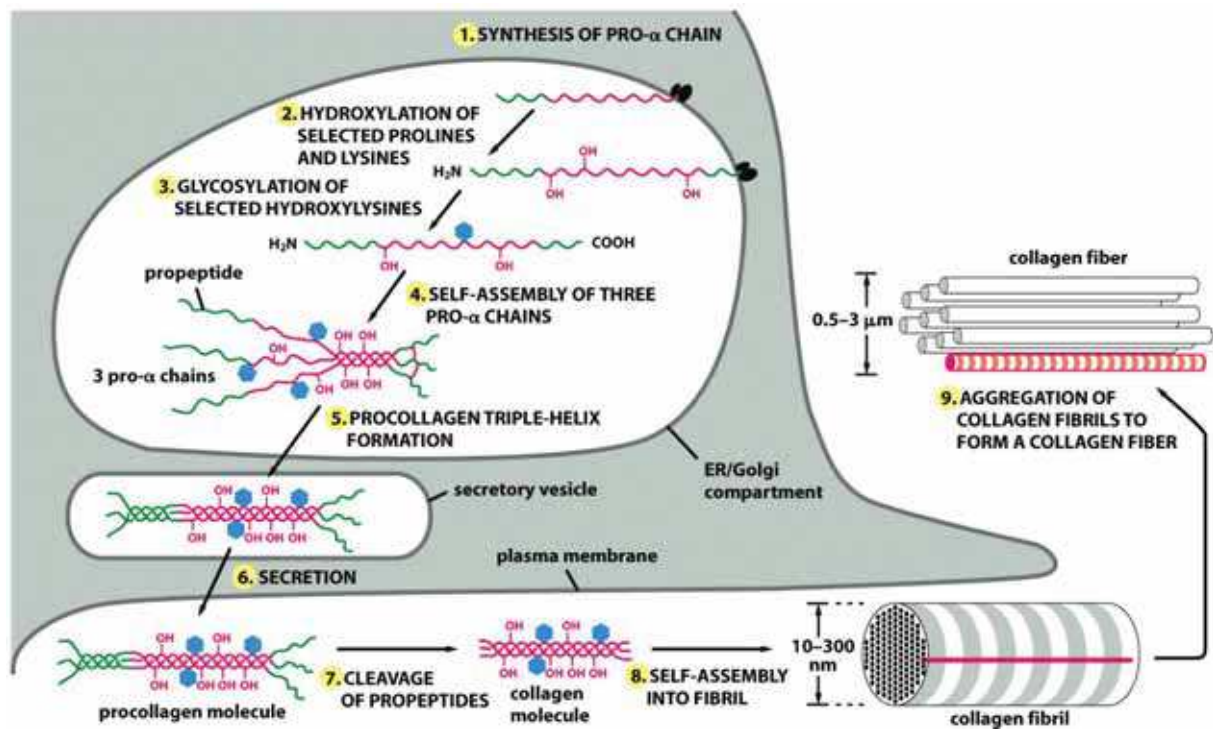


Figure 1.2: Pathway of collagen synthesis. Pro- $\alpha$ -chain synthesis (1) is followed by post-transcriptional modifications (2-3) and self-assembling into a triple helix (4-5). The procollagen is secreted (6), undergoes cleavage of terminal peptides (7) and self-assemble into fibrils (8). Further, fibrils aggregate to form thicker assemblies such as fibers and fascicles (9). Adapted from [50].

### 1.1.3 Hierarchical organization of collagen assemblies

In the previous subsection we described the synthesis of a collagen primitive structure which is the tropocollagen molecule. The next level of organization is the collagen fibril which is produced by self-assembly of tropocollagen molecules after the cleavage of propeptides. Self-assembly is followed by enzymatic cross-linking of lysine residues of constituent tropocollagen molecules, which is necessary to ensure tensile strength of the structure. Collagen fibrils may vary in diameter from 10 to 500 nm depending on tissue [52, 53]. In tendon, typical fibril diameter is about 100-300 nm, while in cornea it is near 30 nm. Different studies suggest that fibril diameter might be controlled by the stoichiometry of fibril-associated types of collagen (types IX, XI) [54], proteoglycan composition of tendon [55], and fibril polarity [56, 57].

Collagen molecules assembly within a fibril is not haphazard but possesses a particular order, both in longitudinal and transverse directions. All the molecules within a fibril have the same polarity (see Fig. 1.3 a). Longitudinal order can be seen on transmission electron microscopy (TEM) images, especially on those with negative staining (Fig. 1.3 b) which show a typical striated pattern with a period of 67 nm noted as  $D$ . This period corresponds to a shift between neighbouring molecules staggered in the assembly. As the molecule length is not a multiple of  $D$  ( $4D < L_{tropocollagen} < 5D$ ), there are regions with 5 overlapping molecules (overlap regions) and others with only 4 overlapping molecules (gap regions) (Fig. 1.3 b). The succession of these two series gives the observed banding. The transversal order has been extensively investigated using electron microscopy [58], nuclear magnetic resonance (NMR) [59] and X-Ray scattering [60–62]. These studies indicate the presence of both short-range crystalline order (Fig. 1.3 e) and liquid-like disorder with radial symmetry (Fig. 1.3 d).

In tendon, the fibrils reach 100-300 nm in diameter and are stacked in a parallel manner to form fibers and fascicles, measuring about 100-200  $\mu\text{m}$  in diameter. Fascicles are enforced by proteoglycans (up to 1% of tendon dry weight), which form networks orthogonal to fibril direction (see Fig. 1.4). Proteoglycans (PG) are large proteins with covalently attached highly hydrophilic glycosaminoglycan (GAG) chains. The substantial part of all collagen water content is associated with PG, forming a matrix which embeds fibrils and enhance their resistance to tensile and compression stress [65, 66]. Birefringence studies suggest that collagen fibers are arranged in bundles and fascicles in a helical manner [67].

In corneal stroma, accounting for 90% of corneal thickness, fibrils are thinner ( $< 30$  nm) and are organized in 2  $\mu\text{m}$ -thick lamellae with different orientations. The angle between two adjacent lamellae is typically  $\pi/3$  to  $\pi/2$  [52, 69, 70]. Theoretical and numerical

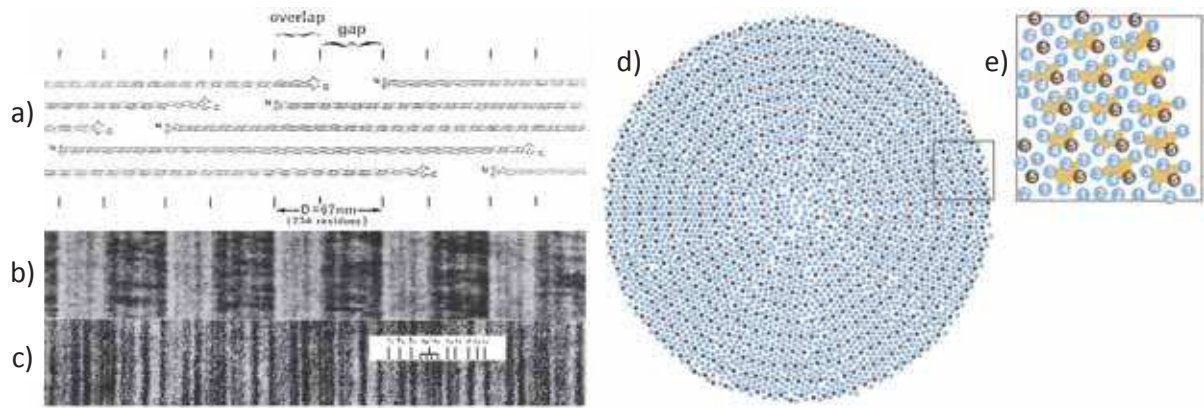


Figure 1.3: Structure of a collagen fibril. (a-c) Longitudinal order [63] and (d-e) lateral order [64] of collagen fibrils. (a) Fibrils feature a characteristic 67 nm periodicity, which is due to the presence of overlap and gap regions. TEM images with negative (b) and positive (c) staining. Dark-light banding with 67 nm period is better observed on negatively stained samples. (d) Lateral fibril organization has a quasi-crystalline structure with liquid-like disorder. (e) Elementary lattice for crystalline regions contains five molecules organized as in (a). Adapted from [63] and [64]

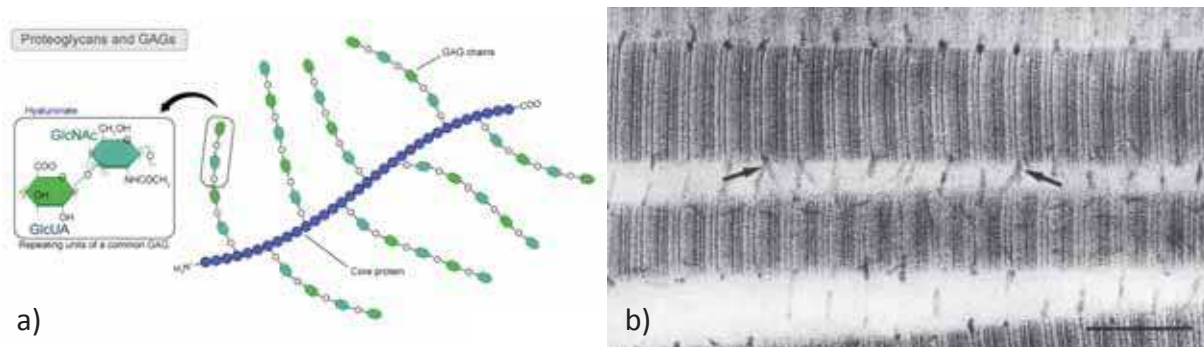


Figure 1.4: (a) Schematic representation of a proteoglycan chain. Courtesy of Pennsylvania State University. (b) Electron microscopy photograph of longitudinal section of collagen fibrils in rabbit outer sclera. Fixed in presence of Cuproline Blue. Proteoglycans appear as an array of positively stained filaments associated with the *D* bands of the collagen fibrils. Scale bar 150 nm. Adapted from [68]

studies were performed to show that the small diameter of fibrils in cornea and quasi-crystalline order in lamellae are crucial for the transparency of corneal stroma [69, 71]. Similar plywood collagen organization is observed in tadpole skin and mature bone.

## 1.2 Tendon biomechanics

The mechanical properties of tendons are dictated by their physiological function in the body. Their primary role in the organism is to transmit mechanical force between the muscles and the bones. Moreover, during the movement, the tendons have been shown to recuperate mechanical energy in the form of elastic contraction energy and then to release it, by analogy to a deformed spring [43, 72]. These properties, while conditioned by the

function, are conferred to tendons by its complex hierarchical structure, described in the previous section 1.1.

Tendon mechanics has been extensively studied since 1970s [43–48, 72]. Tendons are roughly unidimensional objects, so the natural mechanical assay on a tendon consists in stretching the tendon or its fascicles along their axis, and recording the induced stress as a function of applied strain. The obtained measurements are called "stress-strain curves" and can be either continuous or incremental.

Continuous curves are those obtained on a tendon continuously stretched at a given fixed speed. Incremental curves are those where a tendon is stretched by a fixed strain increment and then allowed to relax at a constant strain, and then stretched again and so on. Typical curves are displayed in the Fig. 1.5. In continuum mechanics, the continuous curves are used to define the constitutive equation  $\sigma(\epsilon)$  for an elastic medium. This equation establishes linkage between the stress  $\epsilon$  (tensile force per unit area) and the strain  $\sigma$  (relative deformation) in the medium. However, tendons are not purely elastic, but exhibit a strong viscoelastic behavior, which implies that the stress-strain curve depends not only on the strain, but also on the strain rate  $\dot{\epsilon} = \frac{d\epsilon}{dt}$ :

$$\sigma = \sigma(\epsilon, \dot{\epsilon}). \quad (1.1)$$

It means that a more general description of tendon mechanics would require stress-strain data at all  $\dot{\epsilon}$  rates. In practice, the dependence of the strain rate is often explicitly excluded when all the measurements within a study are performed at a constant strain rate.

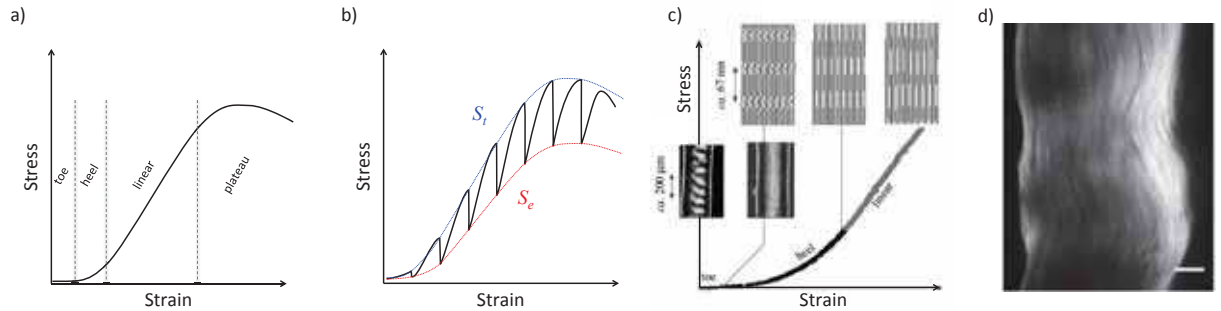


Figure 1.5: Schematic representation of stress-strain curves for tendon. (a) Continuous stress-strain curve, arbitrary units. (b) Incremental stress-strain curve. Upper points  $S_t$  represent total strain, while lower points  $S_e$  represent elastic component after relaxation. (c) Regions of a continuous stress-strain curve. Adapted from [48]. (d) SHG image of crimps in a relaxed rat tail tendon. Scale bar is 50  $\mu\text{m}$ .

Incremental curves give access to the relaxation at different strains. They probe the viscosity and the inner reconfigurations of the tissue. Indeed, they provide values for the elastic component of the stress, which is attained after relaxation ( $S_e$  in the Fig. 1.5),

and the total stress containing also the viscous component, which is attained at the end of a stretching period ( $S_t$  in the Fig. 1.5). Moreover, when mechanical assays are coupled with time-consuming imaging, this type of curve must be privileged over the continuous type, as the sample must reside in a stationary state during the imaging.

The continuous curve for the tendon has four distinct regions (see Fig. 1.5 a): a toe region, a heel region, a linear part and a plateau followed by rupture.

In its relaxed state, tendon features wavy structures, commonly referred to as crimps, undulations or wave-like structures (see Fig. 1.5 d). At small deformations, which correspond to the toe region, the tendon is stretched without significant increase in force, which is accompanied by straightening of these macroscopic crimps (see Fig. 1.5 c, toe region).

Further, in the heel region, the stiffness of tendon increases significantly with extension (see Fig. 1.5 c, heel region). X-ray scattering [47] and NMR [59] studies suggest that this part of the curve is characterized by microscopic kinks in gap regions of collagen fibrils, which are straightened upon loading. Misof et al. [47] proposed an entropic mechanism of kink straightening, which well explains the nonlinear behavior of the heel part.

The linear part includes both elastic and viscous deformation, which can be seen from the incremental curve (see Fig. 1.5 b). A model proposed by Puxkandl et al. [49] gives insight into the origin of this bimodal behavior on the linear region of the curve and allows one to quantify it. It considers tendon fascicle as collagen fibrils immersed in proteoglycan matrix (Fig. 1.6 a), where elasticity and viscosity come both from fibrils and fibril-matrix interaction. According to Puxkandl et al., a tendon can be represented by two instances of Kelvin model put in series, one for fibrils contribution and another one for that of proteoglycan matrix (Fig. 1.6 b). Several studies show that tendons can slowly recover from strain in linear region, so the stretching remains quasi-reversible [73, 74]. Finally, beyond the linear part, tendon yields and tears apart.

A typical stress-strain curve provides several relevant mechanical parameters, such as tangent modulus, maximal stress and strain to fail. These different parameters can vary significantly depending on tendon type and age, and can be a hallmark of various pathologies. Several studies suggest that decreased cross-linked efficiency results in much less maximal stress, and fibril length growing with age leads to increase of tangent modulus via increased shearing [49].

In spite of the wealth of mechanical and structural information on tendon, there is still no well-established and widely admitted picture accounting for all the details of its deformation. Tendon mechanics and its relation to structure remains of great interest for the treatment of tendon and ligaments injuries as well as a basic model for the biomechanics of other connective tissues.

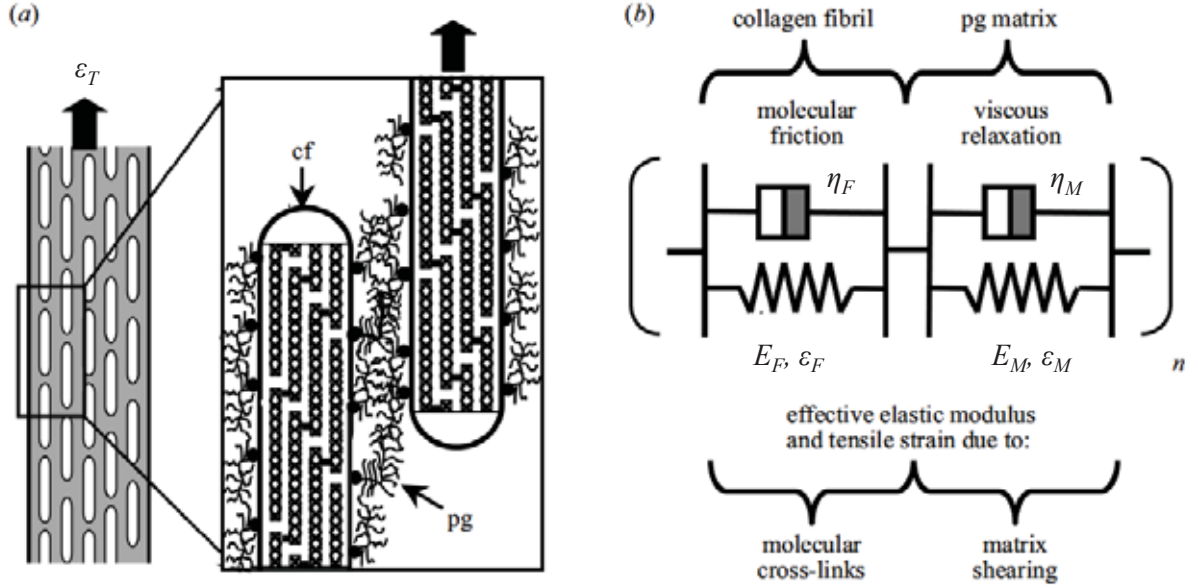


Figure 1.6: Viscoelastic model of tendon tensile response. (a) Collagen fibrils (cf) are embedded in a proteoglycan matrix (pg).  $\epsilon_T$  indicates the total strain applied to the tendon. (b) Kelvin model for fibril-matrix viscoelasticity.  $E$ ,  $\epsilon$  are elastic modulus and tensile strain, and  $\eta$  is viscosity.  $F$  and  $M$  indices stand for fibril and matrix, respectively. Adapted from [49].

### 1.3 Collagen visualization techniques and challenges

Systematic study of connective tissue, and in particular of collagen formation, presents a topical interest in biomedical domain. The different aspects of collagen metabolism, its structure and its interaction with cells and the rest of extracellular matrix (ECM) govern a variety of biological processes and pathologies, and the collagen visualization has a key role in their understanding. Collagen visualization and scoring is important for a variety of applications. As a diagnostic tool, it should help to evaluate various types of fibrosis, developing tumors, and burn recovery. Additionally, studies of biomimetic materials such as artificial collagen matrices require precise imaging of these complex structures.

In order to be efficiently implemented for the problems cited above, a visualization technique should meet several requirements. Notably, it should have low invasivity in order to be used *in vivo* and to maximally preserve the visualized specimen. 3D-capability is also important, especially for collagen scoring in thick samples and for analysis of complex structures such as artificial matrices. Additionally, apart from providing axial resolution, the technique should have large penetration depth to exploit its 3D capabilities. Finally, as collagen in tissue is accompanied by a number of other extracellular and cellular components, the visualization should also present specificity for collagen to discern it from the rest of the ECM.

In this section we briefly introduce the most common conventional techniques for visualization of collagen in tissues, and all of them show limitations from that point of

view. In contrast, second harmonic generation microscopy (SHG), which is the central topic of this manuscript, can provide all the advantages we've just cited as important. SHG properties, which impart these key features to the technique, will be described in details in the next chapter. However, in this section we introduce several challenges that are important for the present state of the art SHG microscopy. This will help to clarify the objectives of this work in the context of connective tissue studies, and make the transition to the rest of the manuscript.

### 1.3.1 Conventional visualization techniques

#### 1.3.1.1 Electron microscopy

Electron microscopy (EM) has been used to study the structure of collagen fibrils since 1940s [75, 76]. This technique has an extremely high resolution, which allowed, for example, to discover the 67 nm D-period of collagen fibrils which arises from staggering of tropocollagen molecules. More generally, electron microscopy is very useful to assess structural changes which occur at nanometre scale.

On the other hand, the electron microscopy has its limitations. First, a relatively complex preparation for biological tissues (dehydration, ultrathin sectioning, staining) and high doses of irradiation used to obtain images makes it inapplicable for *in vivo* studies. The complex sample preparation can also result in various imaging artefacts, which may give an erroneous data interpretation. Furthermore, electron microscopy images have a small field of view (FOV), thus providing only a local insight on the sample structure. A more comprehensive picture of the tissue in study thus requires preparing more samples and getting more images.

#### 1.3.1.2 Atomic force microscopy

Atomic force microscopy (AFM) is an imaging technique that uses a cantilever with a sharp tip to scan the surface of a specimen. AFM provides spatial resolution on the order of fractions of a nanometre, which competes with that of EM. In contrast with EM, AFM imaging is generally performed in air or in liquid, doesn't require any sample preparation, and is mild enough to image the surface of soft biological objects. AFM has been used to study collagen since 1990s [77–80]. AFM additionally enables force spectroscopy measurements, which allows for nanoscale stress-strain measurements. Notably, it has been used to perform mechanical assays on collagen molecules pulled out of collagen fibrils [81]. As it does not require specific sample preparation, AFM imaging can also be used to calibrate less-resolutive imaging techniques, as it was done for second harmonic imaging by comparing AFM images and corresponding second harmonic images [82, 83].

AFM produces images with extremely high resolution and additionally allows for getting 3D representation of sample surface. However, the scanning speed is generally low, and it may take up to several minutes to produce an image. AFM also has limitations due to its small field of view, even smaller than that of EM. Another drawback specific to AFM is that the tapered form of cantilever tip or too coarse tip can cause image artefacts while imaging steep walls and overhangs.

### **1.3.1.3 Polarized light microscopy**

Polarized light microscopy (PLM) exploits the sample's birefringence to produce image contrast. It has been extensively used to analyze different phases of liquid crystal ordering of different compounds, including collagen solutions in acid (see for instance [84–86]). PLM has long been established as an appropriate tool for visualizing and analysing crimps in tendon, as it reveals typical banding in crimped tendon with high contrast [87]. Additionally, PLM imaging of transverse tendon section was used to reveal helical organization of fibrils within tendon fascicles [67].

PLM has the advantage of being used without any particular sample preparation and for samples of different thicknesses. However, it doesn't have any specificity regarding different birefringent compounds and doesn't provide axial resolution.

### **1.3.1.4 Optical coherence tomography**

Optical Coherence Tomography (OCT) is an interferometric technique, which provides images with 3D-resolution in translucent and opaque tissues. Basically, the source of contrast in OCT is the reflectivity of a certain layer in tissue. OCT has been used to study the structure of the corneal stroma, and its different pathologies [88–93]. It also proved promising technique to study crimp morphology in tendon during mechanical load [94, 95].

OCT can provide decent axial resolution (about 1  $\mu\text{m}$ ) without using high-NA lenses, which gives it an advantage over confocal microscopy in precise imaging of relatively distant objects, such as retina imaging through the pupil [96, 97]. However, OCT lacks specificity for different compounds.

### **1.3.1.5 Histological and immunohistochemistry staining**

Histological staining (histochemistry) is based on specific coloration of biological tissues in order to provide contrast for optical visualization of its different constituents. Histological staining techniques remain the reference for identifying various pathologies in tissue. The staining is performed by various sets of dyes and preceded by a routine tissue preparation. A typical one consist of fixing the tissue (e.g. in formalin), embedding it in

paraffin wax (hardens the tissue block enabling sectioning), sectioning on a microtome, and rehydration. Instead of embedding in paraffin, the tissue can be frozen and cut by a cryomicrotome. Typical stains used for connective tissue study are HES (Haematoxylin-Eosin-Safran), Masson trichrome, and Picrosirius Red.

Histochemistry is a simple and low-cost technique, which is routinely used in laboratories and hospitals. On the other side, it provides low specificity to collagen, as all the ECM is stained similarly (besides Picrosirius Red that specifically enhances the birefringence of collagen, which can be observed by PLM). Additionally, as dyes must penetrate into the tissue to efficiently stain their targets, the tissue slice thickness is limited to somewhat  $\sim 2\text{-}5\ \mu\text{m}$ . It implies that the obtained images are essentially 2D. Finally, the tissue preparation procedure may perturb the morphology of the tissue and introduce image artefacts.

Another technique called immunohistochemistry (IHC) uses antibodies instead of chemical dyes to specifically mark proteins, carbohydrates and lipids. The presence of antibodies in tissue can be revealed by dedicated molecules bound to antibodies, such as chromogenic reporters and fluorescence reporters. In most cases IHC provides an unparalleled specificity, as antibodies can be obtained for virtually any antigen. However, due to very similar helical domains common to all collagens, the IHC staining of different collagens may be tricky in some tissues and may lack selectivity.

Immunohistochemistry is often used as it is relatively inexpensive and provides good specificity. However, the sample preparation for IHC contains numerous steps with inconsistent outcome, which makes it hardly reproducible and thus not quantitative. IHC also shares the drawbacks of histochemistry, which are notably the need in thin slices, and the tissue perturbation during the sectioning.

### 1.3.2 Challenges in collagen visualization

In contrast to conventional collagen imaging techniques, SHG microscopy can fulfil the demand for specific collagen visualization, 3D resolution, low invasivity and high imaging depth. However, while SHG has already proven to be a promising visualization modality for connective tissue study, there are at least two challenges to be undertaken in order to improve it and to provide new functionalities.

1. SHG microscopy potentially enables access to submicrometre scale organization of collagen assemblies via accurate polarization analysis of SHG signal (P-SHG). However, various phenomena such as scattering, attenuation and birefringence can impede these precise measurement. Thus, in order to understand and properly implement P-SHG modality, a comprehensive model taking account of different signal

perturbations should be developed. These theoretical considerations should also be tested by numerical calculations to evaluate influences of different factors.

2. Mechanical assays on collagenous tissues such as tendon, skin, *dura mater* helps to understand the origin of biomechanical response to applied strain, to the condition that a technique providing information on microscopic tissue organization is used simultaneously. As SHG and P-SHG are efficient techniques for assessing collagen morphology and microscopic structural features, they seem promising for complementing mechanical studies. Thus, such an experimental setup which couples mechanical assays with SHG microscopy should be developed, and the experimental approach needs to be validated.

These two challenges delimit the subject matter of this thesis and fully encompass its objectives, which we announced in the Introduction.

## 1.4 Conclusion

In this chapter we briefly presented the main aspects of collagen synthesis, molecular and supramolecular structure, and biomechanics. Moreover, we gave coverage of principal techniques of collagen visualization in tissues and cited their advantages and limitations for the biomedical use.

An increasing role in connective tissue study is entrusted to novel optical techniques, which can handle the increasing demand in low invasivity, increasing speed and high resolution. SHG microscopy perfectly meets these criteria and is valuable for collagen visualization in different tissues and upon different conditions. However, this nonlinear technique has a further potential which needs to be explored. In particular, P-SHG can provide additional information on internal organization of collagen structures, but requires adequate theoretical models to interpret experimental results. Additionally, SHG can be a suitable technique to be united with biomechanical studies, thus shedding the light on the origin of mechanical response in collagen tissues.

# Chapter 2

## Theoretical background of polarization-resolved SHG microscopy

### Introduction to multiphoton microscopy

Multiphoton microscopy (MPM), also known as nonlinear optical microscopy, is a class of optical imaging techniques which rely on various nonlinear processes occurring in nonlinear media. Since it was introduced in a milestone paper of Webb, Denk and Strickler [98], multiphoton microscopy gained more and more popularity in cellular and tissue biology because of its intrinsic 3D-capability, various available endogenous contrasts in tissues, and its small invasivity. In this section, some general features of multiphoton microscopy will be treated in section 2.1, followed by more detailed description of major contrasts used in MPM. Second harmonic generation (SHG) is a dominant topic of the present work, so it will be discussed in much more details and occupies the entire section 2.2. Tensorial response of collagen with respect to polarized excitation will be treated in the final section 2.3.

### 2.1 Principles and contrast mechanisms of multiphoton microscopy

By definition, multiphoton microscopy implements nonlinear optical interactions. This nonlinearity confers several advantages to multiphoton microscopy, such as optical sectioning, deep tissue penetration and small phototoxicity. However, these advantages have a price to pay, which is, notably, the need in extremely intensive electric field to be created in the sample.

The large variety of nonlinear optical interactions gives rise to a number of contrasts that can be used in nonlinear microscopy. In this section we will present two-photon

excited fluorescence (2PEF), third harmonic generation (THG) and coherent anti-Stokes Raman scattering (CARS). Simplified Jablonski diagrams for these processes are shown in the Fig. 2.1. Second harmonic generation (Fig. 2.1 a) will be briefly introduced as well, but its detailed description is given in the next section.

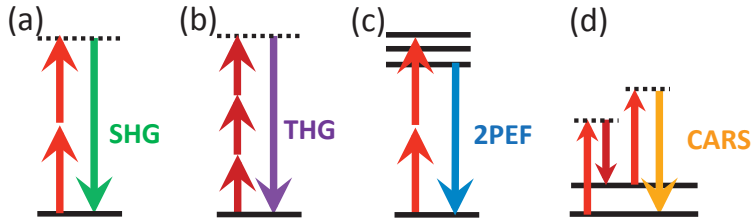


Figure 2.1: Simplified Jablonski diagrams for different types of multiphoton microscopies. (a) Second harmonic generation (SHG). (b) Third harmonic generation (THG). (c) Two-photon excited fluorescence (2PEF). (d) Coherent Anti-Stokes Raman Scattering (CARS).

### 2.1.1 Making intense fields

Classically, the appearance of nonlinear effects in optics signifies that electron response to sinusoidal excitation field becomes anharmonic. It happens when the perturbation field is large enough to be comparable with typical atomic electric field, which is  $E_{at} = e/a_0^2 \sim 10^{11}$  V/m [99]. A beam of a continuous laser light of 1 W, focused in a  $0.5 \mu\text{m} \times 0.5 \mu\text{m}$  spot will produce a field intensity of only about  $10^7$  V/m. Reaching higher intensities not only presents a technical challenge, but will also lead to energy flux and heat deposition much stronger than what biological tissues can tolerate. However, this problem is circumvented by using ultrashort pulse lasers. It allows one to increase peak intensities necessary for nonlinear processes to occur, while maintaining low average intensity. For example, a 100 mW 100 fs-pulsed laser with 80 MHz rate can provide peak intensity even larger than the atomic field, thus enabling all types of nonlinear interactions up to those leading to destruction of the tissue. Since the apparition of turn-key femtosecond lasers, such as a mode-locked Ti:Sa laser, nonlinear microscopy is gaining more and more popularity.

### 2.1.2 Optical sectioning

An outstanding and well-known property of multiphoton microscopy is its intrinsic optical sectioning. Sectioning means that the imaging system is able to resolve structures in the axial direction.

Let's consider a tightly focused beam in a medium with bulk fluorescence and discuss the  $z$ -resolution for single-photon excitation and for two-photon excitation. Single-photon

excited fluorescence (1PEF) scales linearly with the incident intensity, while 2PEF scales as the square of the incident intensity [99]. For a small volume of the excitation cone, the number of photons emitted will be  $\frac{dN^\omega(z)}{dSdz} \propto E^2$  for 1PEF, and  $\frac{dN^{2\omega}(z)}{dSdz} \propto E^4$  for 2PEF, where  $E$  is the excitation field. As the fluence is constant along the propagation direction, i.e.  $\int E^2 dS = C$  (we assume that there is no beam attenuation along the propagation), we can roughly take  $\tilde{E}(z)^2 \tilde{S}(z) = \tilde{C}$ ,  $\tilde{E}$  and  $\tilde{S}$  being the effective area of the beam section at  $z$  and the average field across this section. Thus, the number of photons emitted from a slab of thickness  $dz$  is  $dN^\omega(z) \propto dz \int E^2 dS = C dz$  for 1PEF, and  $dN^{2\omega}(z) \propto dz / \tilde{S}(z)$  for 2PEF. For 1PEF, each slab of uniformly fluorescent sample will produce the same number of photons. The integral  $\int dN^\omega(z) dz$  diverges, and one cannot say where a detected photon comes from. On the other hand, for a Gaussian beam we can easily calculate  $dN^{2\omega}(z)$ :

$$dN^{2\omega}(z) \propto \frac{dz}{\tilde{S}(z)} \propto \frac{dz}{1 + \frac{z^2}{z_R^2}}. \quad (2.1)$$

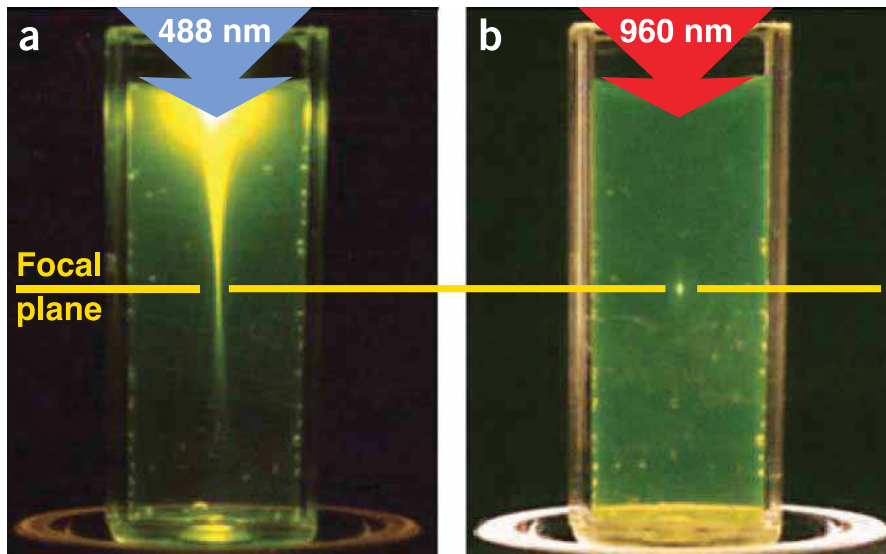


Figure 2.2: Fluorescence signal for conventional and two-photon excitation. (a) Excitation cone for linear excitation, with fluorophores efficiently excited outside the focal plane. (b) Two-photon excitation. Fluorophores are only efficiently excited at the focal point, due to squared dependence on excitation beam intensity. Adapted from [9].

Here, the integral  $\int dN^{2\omega}(z) dz$  converges, and most photons come from the region  $(-z_R, z_R)$ , naturally confined by Rayleigh length  $z_R$  on either side. This simple calculation is well illustrated by an iconic picture of multiphoton community (Fig. 2.2.) The actual value for the 2PEF resolution is readily defined from the focal field distribution. It is the size  $(1/e)$  of the point-spread function (PSF), which is the squared intensity of the

$$\begin{cases} \omega_{xy} = \frac{0.32\lambda}{\sqrt{2NA}}; & NA < 0.7 \\ \omega_{xy} = \frac{0.325\lambda}{\sqrt{2NA^{0.91}}}; & NA > 0.7 \end{cases} \quad \omega_z = \frac{0.532\lambda}{\sqrt{2}} \left[ \frac{1}{n - \sqrt{n^2 - NA^2}} \right]$$

Table 2.1: Estimation of 2PEF lateral ( $\omega_{xy}$ ) and axial ( $\omega_z$ ) resolution. adapted from [10]

focal field (quadrupled field). The obtained image is the convolution of fluorophores distribution with the PSF, and the PSF size determines the smallest detail resolved by the microscope. A good yet simple estimate for the  $1/e$  size of the 2PEF PSF is given in [10] (see Tab. 2.1).

Unlike conventional fluorescence microscopy, confocal microscopy can provide axial resolution. The excitation is still linear, but the detection path is modified by introducing a pinhole, which privileges the detection only of those photons that were emitted near the focal plane. The synergetic effect of tight focusing, which provides high lateral resolution, and the pinhole responsible for axial sectioning, ensures 3D-capability.

More detailed comparison of resolution and PSF between 1PEF and 2PEF can be found in [100].

### 2.1.3 Two-photon excited fluorescence (2PEF)

2PEF microscopy is far the most widespread nonlinear microscopy technique, and it was first made to be commercially available by Bio-Rad in 1996. Nowadays, a number of manufacturers (Zeiss, Leica, Nikon, Olympus, ...) produce commercial 2PEF microscopes. The process of simultaneous two-photon absorption was first described by Maria Goeppert-Mayer in her PhD thesis in 1931, and the first microscope was built in 1990 by Webb, Denk and Strickler in their lab at Cornell University [98].

Excitation by two photons with subsequent fluorescence (2PEF) is a nonlinear optical process, which is based on the probability of a fluorophore to be excited by simultaneous absorption of two photons in a single quantum event. Each photon carries about half of the energy necessary for the excitation of the fluorophore. The excitation is followed by the emission of a single fluorescence photon with energy lower than the excitation energy due to the Stokes shift, and typically higher than the energy of either photon used to excite the molecule. The diagram illustrating this process is shown in the Fig. 2.1 c. This process is dependent on the imaginary part of the third-order nonlinear susceptibility tensor, and the probability of 2PEF scales as the square of incident intensity [99].

Since 2PEF is a fluorescence imaging technique with 3D-resolution, exactly as the more conventional confocal microscopy, it is informative to compare their properties.

Typically, all the vast library of fluorophores used in confocal microscopy can be directly used for 2PEF. However, for many fluorophores their two-photon absorption spectra differ significantly from their single-photon counterpart due to different selection rules for single- and two-photon transitions. Moreover, two-photon excitation spectra are usually wider. On one hand, it can lead to the loss of selectivity if it is achieved by using different excitation wavelength to excite different fluorophores. On the other hand, while absorption spectra widen and overlap, the respective fluorescence emission spectra remain relatively well separated. It allows for simultaneous excitation of several fluorophores by a single wavelength and selectivity is achieved by choosing different spectral windows for fluorescence emission detection.

For a chosen wavelength and numerical aperture, the resolution of 2PEF is similar to that of confocal microscopy. While the confocal microscopy outperforms 2PEF by a factor of 2 at small depth in weakly-scattering tissue, in thick and scattering tissues 2PEF evens the score. First, the scattering in tissue is significantly higher for the single-photon excitation wavelength  $\lambda$  than for two-photon excitation wavelength  $2\lambda$  (for the same transition energy of the molecule), which results in more deteriorated PSF for confocal imaging. Secondly, scattering leads to lower fluorescence signal, which requires to further open pinhole, thus accepting photons from a wider layer near the focus and deteriorating the resolution.

Due to low phototoxicity, which is restrained to the focal volume, two-photon microscopy permits to further increase incident intensity and to efficiently excite endogenous fluorophores, which are generally much weaker than dedicated fluorescent dyes. The most common endogenous fluorophores in biological tissues are aromatic amino acids (tryptophan, tyrosine and phenylalanine), electron carriers (NADH, FAD) and structural proteins such as elastin and collagen. However, collagen fluorescence is weak compared to that of elastin, and it can be visualized much more efficiently by SHG microscopy.

An example of 2PEF image is displayed in Fig. 2.3. It shows a lung tissue affected by idiopathic lung fibrosis (ILF), which is a rare disease characterized by apparition of large collagen producing areas known as fibrotic foci. Two-photon excited fluorescence from endogenous fluorophores is shown in red, and green represents second harmonic generation from collagen fibers (see next section).

#### **2.1.4 Second and third harmonic generation**

Second harmonic generation was the first nonlinear optical process experimentally observed. It was demonstrated in 1961 by Franken et al. [101] soon after the invention of lasers. It has several applications across different areas of physics, and is often used in lasers to obtain new wavelengths. However, this manuscript focuses exclusively on SHG

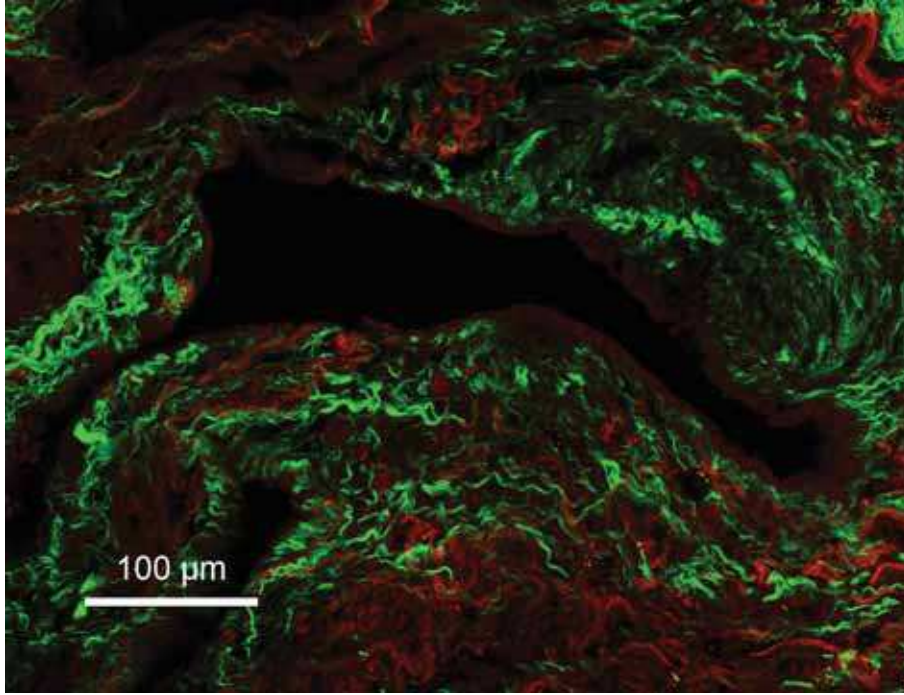


Figure 2.3: 2PEF/SHG image of human lung tissue attained with idiopathic lung fibrosis. Red is endogenous 2PEF primarily from NADH in cells and from elastin in the ECM. Green is SHG originating from fibrillar collagen. A fibrotic focus (green bean-shaped bundle of collagen fibrils) is visible in the upright corner above the alveolus (black cavity). Image taken with 20x 0.95NA objective, at 860 nm, 20 mW beam power. Lung sample from Hôpital Bichat/Inserm U700

application as a contrast in a multiphoton microscopy that is called second harmonic microscopy. SHG is specific to highly ordered structures such as those adopted by fibrillar collagen, and can be used in unstained biological tissues. SHG is the central topic of this manuscript, and its detailed description will be done in the next section.

Another promising contrast used in multiphoton microscopy is third harmonic generation (THG). It is a coherent nonlinear process of simultaneous scattering of three photons to produce a single photon with the energy equal to the sum of the three incident photons.

The technique relies on pulsed light with wavelength from 0.9 to 1.5  $\mu\text{m}$ , produced by infrared lasers or optical parametric oscillators (OPOs). Since it is a coherent process, its interpretation could be more difficult than that of incoherent 2PEF. The detected photons outcome depends on several factors, such as scatterers geometry, the form of radiation diagram and the scattering properties of the tissue. For example, there is no THG signal from a bulk sample with uniform nonzero third-order susceptibility  $\chi^{(3)}$ , due to the Gouy phase anomaly and resulting coherent cancellation of THG signal from different parts of the focal volume [99, 102, 103]. On the other hand, a high contrast is observed on the interfaces of two media with different  $\chi^{(3)}$ , such as water-oil interfaces [104, 105].

Since THG can visualize oil-water interfaces, it can reveal outer bilipid layer and nucleus surface, along with smaller organelles such as mitochondria [104]. In the context

of this manuscript, it is noteworthy that THG was used to image interfaces between subsequent collagen layers in corneal stroma [106]. It was attributed to different collagen fibril orientation in each collagen slab, resulting in different third-order susceptibilities  $\chi^{(3)}$  on the either sides of the interface [106].

### 2.1.5 Coherent anti-Stokes Raman Scattering

Coherent anti-Stokes scattering (CARS) in a scanning microscope was first demonstrated in 1982 by Duncan et al. [107], but it received no development until the end of the century, when it started to gain popularity. CARS relies on four-wave mixing, as shown in the Fig. 2.1 d, which is a third-order nonlinear process. This technique is more difficult to implement, since it requires 2 different excitation beams to be spatially aligned and temporally synchronized with high precision. The first is the pump field  $\omega_p$  which is involved twice (two red upward arrows in the Fig. 2.1 d) and the second is Stokes field  $\omega_s$  (smaller red downward arrow) involved once in the scattering event. This method allows for probing vibrational levels with efficient enhancement by the resonance at  $\omega_p - \omega_s$ . CARS microscopy also possesses an intrinsic 3D resolution, as its efficiency is proportional to  $I_{\omega_p}^2 I_{\omega_s}$  that is sufficient to ensure the optical sectioning (see subsection 2.1.2).

The advantage of CARS consists in chemical specificity attained with intrinsic axial resolution. Indeed, 3D-confinement of the excitation volume enables microscopy capabilities, while changing  $\omega_s$  provides spectral scanning of vibrational levels in the studied sample. However, in practice, obtaining pixel-wise spectra is time consuming, and often CARS is used with  $\omega_s$  set to a fixed vibrational frequency. For instance, it can be C-H bond stretching band at  $2840 \text{ cm}^{-1}$ , which allows for imaging of C-H rich lipid bodies.

## 2.2 Second Harmonic Generation microscopy

In this section we will first describe general principles of second harmonic generation in a medium, paying particular attention to the role of coherence in SHG process, and to the notion of resolution in SHG. After that, we will discuss the capability of collagen and its assemblies to efficiently generate second harmonic radiation.

### 2.2.1 Mechanisms and principles

#### 2.2.1.1 Physical origins

SHG is a nonlinear optical phenomenon where two photons at the same wavelength are scattered by a single molecule to produce a photon at half the wavelength. SHG is a coherent and instantaneous process (in contrast to 2PEF), which means that the phase

of the generated wave is strictly related to that of the incident field. In a more general case, the induced dipole  $p$  in such a molecule can be written as

$$p = [\alpha]E + [\beta]EE + [\gamma]EEE + \dots \quad (2.2)$$

Here,  $E$  is the incident field,  $[\alpha]$  is the linear polarizability of the molecule, and  $[\beta]$  and  $[\gamma]$  are first and second hyperpolarizabilities. The first term corresponds to the linear scattering, the second is responsible for SHG, and the third term governs THG. In the most general case, the polarizability and first and second hyperpolarizabilities are tensors with two, three and four dimensions respectively.

Harmonics generation can be illustrated by Lorentz oscillator model, treating the interaction of an electromagnetic wave with a bound electron. According to this model, an electron driven by the excitation field starts to oscillate and to generate the secondary wave. For a harmonic potential, the oscillation is sinusoidal with the same frequency  $\omega$  as the driving field. However, for large excitation fields, the real potential can differ significantly from harmonic one, which influences the oscillation signature. More precisely, such an oscillation contains contributions of harmonic frequencies, i.e.  $2\omega, 3\omega, \dots$  which are radiated more or less efficiently (see Fig. 2.4.)

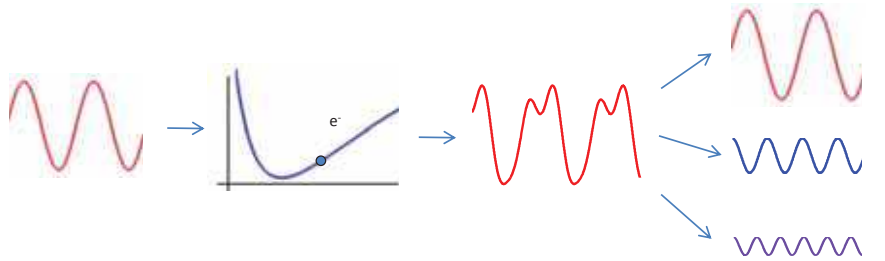


Figure 2.4: SHG from an electron in an anharmonic potential. The nonlinearly scattered wave contains harmonic components for double and triple frequencies.

In the case of symmetric potential, its Taylor series contains only even terms, which correspond to odd harmonics. It means that no second harmonic (fourth, sixth, ...) is possible in a centrosymmetric molecule.

### 2.2.1.2 The role of coherence in SHG

The coherent nature is the most prominent feature of SHG, which determines the rest of its properties. On one hand, the coherent amplification of signal from ordered and well-aligned structures makes that they are the only ones to efficiently produce SHG. It accomplishes the most important role of SHG in tissue microscopy, which is the specific

visualization of fibrillar collagens, tubulin microtubules, and sarcomeres in muscles without staining. On the other hand, this property significantly impedes both qualitative and quantitative interpretation of the SHG images, and even compromises the notion of resolution in SHG microscopy, as will be shown in the following item.

To illustrate the role of coherence, let's consider a simple example of the nonlinear scattering in two different media with the same number of scatterers within a small volume. The first volume contains harmonophores aligned along a specific direction, while in the second volume, the harmonophores are randomly oriented (see Fig. 2.5).

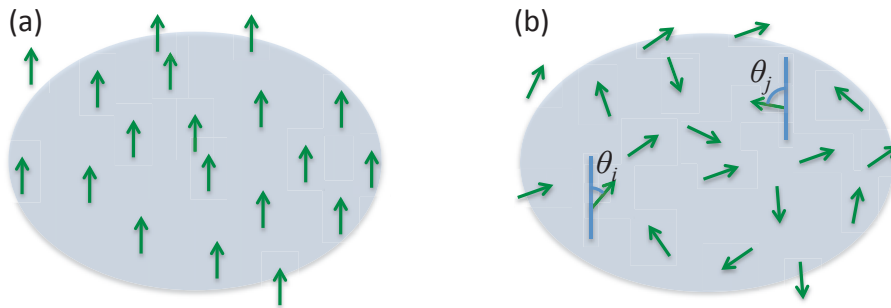


Figure 2.5: Schematic illustration of (a) second harmonic generation and (b) hyper-Rayleigh scattering.

We assume that the volume is small compared to the wavelength, so in the first case (Fig. 2.5 a) all the scatterers radiate in phase, and their contributions sum up coherently. The final radiated intensity (total or in a chosen direction) is therefore

$$I_{\text{SHG}} \propto \left( \sum E^2 \right)^2 \propto N^2 E^4, \quad (2.3)$$

where  $N$  is the number of scatterers and  $E$  is the excitation field. One can see that the intensity varies as the square of the number of molecules. It is actually this type of coherent amplification of second harmonic waves which is referred to as Second Harmonic Generation.

In the second medium, the second harmonic field radiated by each molecule along the direction of the incident field is proportional to  $\cos^3 \theta_i$ . Here,  $\theta_i$  is the angle between the orientation of the  $i$ th molecule and the polarization of the incident field. In such a medium, the total harmonic field is proportional to  $\sum_i E^2 \cos^3 \theta_i$ , which is a random variable for which the expected value is zero. In this case, the intensity is directly proportional to the

variance of the electric field, and reads:

$$\begin{aligned}
 I_{\text{HRS}} \propto \text{Var} [E_{2\omega}] &= E^4 \overline{\left( \sum_i \cos^3 \theta_i \right)^2} = \\
 &= E^4 \sum \overline{\cos^6 \theta_i} + 2E^4 \sum_{i,j \ i < j} \overline{\cos^3 \theta_i} \overline{\cos^3 \theta_j} = \frac{1}{7} N E^4.
 \end{aligned}
 \tag{2.4}$$

The bar over the terms signifies the expected value of a random variable. The intensity scales only linearly with the number of scatterers. This process is called hyper-Rayleigh scattering (HRS). For such an isotropic distribution of scatterers, their local density is usually much smaller than that in SHG capable tissues. In practice, the focal volume and the typical acquisition time in microscopy are too small to achieve detectable signal levels from isotropically distributed harmonophores.

This property can be interpreted as an illustration that SHG does not exist in a medium with central symmetry (explained in the previous item). Indeed, as all positions and orientations for molecules are equiprobable in such an isotropic medium, it possesses a central symmetry in a statistical sense (for the moment, we assume that the molecules are not chiral, i.e. the molecule and its spatially inverted copy differs only in orientation). It is thus natural that for large  $N$  the HRS intensity is statistically negligible compared to that of SHG.

### 2.2.1.3 Resolution: comparison between SHG microscopy and other techniques

In this part we will discuss the axial resolution of SHG microscopy in comparison with several widely-used techniques, such as conventional fluorescence microscopy, confocal microscopy and two-photon excited fluorescence microscopy. The two nonlinear techniques, SHG and 2PEF, provide intrinsic optical sectioning, while single-photon fluorescence microscopy does not, unless a pinhole is used.

The resolution aspect for fluorescence techniques was already treated in the previous section. Briefly, the main difference between linear and nonlinear fluorescence doping the latter of its 3D-capability, is that the nonlinear excitation is proportional to the square of excitation intensity, rather than scaling linearly with it. Thus, the optical sectioning in linear excitation is not intrinsic and should be ensured by a pinhole, which shapes the axial detection efficiency.

For incoherent microscopic techniques with axial resolution like confocal microscopy and two-photon excited microscopy, the resolution is associated to the point spread function (PSF) which is an image of a point source of contrast. The obtained image can be

interpreted as a convolution of the fluorophores distribution with the PSF, which gives to the PSF the significance of the smallest detail resolved by a technique.

The situation is more complex for the coherent SHG, as the recorded image depends not only on SHG intensities produced by individual scatterers, but also on their relative phase. As a consequence, the spatial distribution of harmonophores cannot be deduced in general case and requires some *a priori* assumptions about the sample and phase-matching conditions for the SHG wave. For example, small isolated objects, such as individual distant fibrils [5], are well resolved as there is no significant interference possible between distant sources due to the tight confinement of the field.

However, in the present work we mainly perform SHG in tendon and cornea, which are bulk and dense sources of SHG. To determine the resolution in this case, we will use a similar approach as for 2PEF resolution (see 2.1.3), looking at the total number of photons produced by the excitation and assessing the  $z$ -slab they primarily come from.

Let's consider a tightly focused beam in a medium with bulk SHG capability. The simulated intensity distribution for 0.95NA is shown in the Fig. 2.6 a and b.

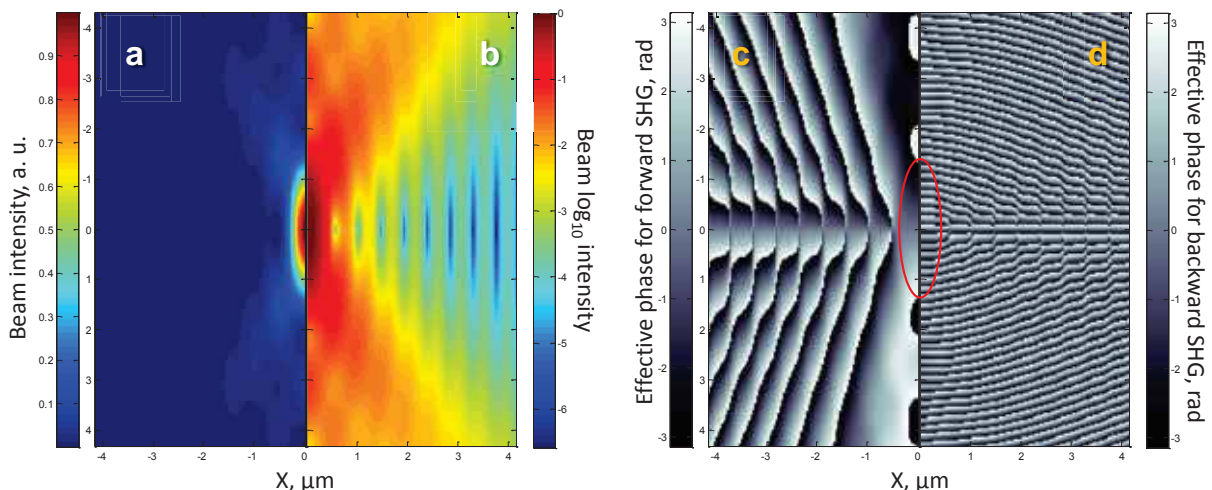


Figure 2.6: Fundamental beam intensity (a) and its decimal logarithm (b) in the  $(x, z)$  plane calculated for 0.95 NA. Effective phase distribution for forward SHG (with subtraction of  $2ik(z - z_0)$ ) (c) and backward SHG (with subtraction of  $-2ik(z - z_0)$ ) (d) in the  $(x, z)$  plane. Red ellipse at (c) and (d) indicates the approximate size of the focal spot. Black and white spots along the axial line in (c) correspond to regions where colormap value changes from  $-\pi$  to  $\pi$ , thus being zones of relatively constant phase in spite of their contrasted appearance.

For simplicity reasons, we will assume that the generated nonlinear dipole has only one component, which is parallel to the excitation field  $\mathbf{E}$ . For a chosen direction  $\mathbf{n} = \mathbf{k}^{2\omega}/k^{2\omega}$ , the detected SHG intensity is proportional to

$$I^{2\omega}(\mathbf{n}) \propto \left| \int \mathbf{E}(\mathbf{r})^2 e^{-i\mathbf{k}^{2\omega}\mathbf{r}} d^3\mathbf{r} \right|^2 = \left| \int |\mathbf{E}(\mathbf{r})|^2 e^{i2\phi(\mathbf{r})} e^{-i\mathbf{k}^{2\omega}\mathbf{r}} d^3\mathbf{r} \right|^2 \quad (2.5)$$

where  $\phi(\mathbf{r})$  is the phase of the incident field. One can possibly imagine such a perfectly coherent distribution of harmonophores and of the excitation beam phase, which makes the phase factor disappear. In this case we would observe the same dependence on field exponent as in conventional fluorescence microscopy, without any axial resolution. However, it is not the case in reality due to the relatively complex structure of the beam phase. It is thus clear that the signal formation and the total intensity depend strongly on phase distribution of the beam and the propagation direction. In a microscopy setup, the SHG can either be detected in the forward (trans, F-SHG) or backward (epi, B-SHG) direction, so we will consider these two cases to evaluate the effective resolution.

The forward direction, which coincides with the propagation direction of the incident field, privileges phase matching. Indeed, the phase difference between portions of SHG radiated from different slabs is compensated by the phase change of the fundamental wave acquired from propagation between these slabs. In the Fig. 2.6 c, one can see the phase distribution for squared field  $E_x^2$  with subtraction of  $2ikz$  term. This distribution represents the effective phase for the forward radiation. There are two cones of uniform phase, in front of and behind the focal point. The phase difference between these cones is about  $2\pi$ , which is twice the so-called Gouy phase. The Gouy phase change occurs at the focus, mostly within a 2-Rayleigh length-thick slab, which coincides approximately to the beam confinement in the  $z$  direction (Fig. 2.6 a). Hence, the diverging frontal and rear cones are approximately phase-matched, while the scatterers in the center of the beam are in opposite phase to the tails. In this situation, one may expect the signal to be efficiently produced even slightly outside the focal point. However, the phase matching conditions are additionally modified by the light dispersion in the medium ( $n_{2\omega} - n_\omega$ ), which reflects the difference in light velocities for fundamental and harmonic waves. This effect should decrease coherent amplification outside the focal point. For the case of back-propagating SHG, the effective phase distribution is displayed in Fig. 2.6 d. There are no zones of uniform phase, and there is no signal amplification, as the signal from a uniform sample undergoes destructive interference. However, for samples with non-uniform distribution of harmonophores, this geometry can probe spatial frequencies of approximately quarter the wavelength in the focal volume, so it can represent a potential interest for study of thin stratified media.

Rather than speaking of optical resolution in SHG microscopy, one can define a coherence length [2], which is the length over which the effective phase of signal formation changes by  $\pi$ :

$$l_c = \frac{\pi}{|\mathbf{k}_{2\omega} - 2\mathbf{k}_\omega|}. \quad (2.6)$$

Here,  $\mathbf{k}_{2\omega}$  indicates the wave vector of second harmonic in the direction of observation, while  $\mathbf{k}_\omega$  stands for the wave vector of excitation field, which is oriented along the

Type of contrast	Signal formation	Divergence
Conventional fluorescence	$\int  E ^2 d^3\mathbf{r} \propto \int dz$	diverges
Confocal fluorescence	$\int  E ^2 PSF_{pinhole} d^3\mathbf{r} \propto \int \frac{dz}{z^2}$	converges
2PEF	$\int  E ^4 d^3\mathbf{r} \propto \int \frac{dz}{z^2}$	converges
SHG	$\left  \int \mathbf{E}^2 d^3\mathbf{r} \right ^2 \propto \left  \int  E ^2 e^{i\phi} d^3\mathbf{r} \right ^2$	depends on phase
THG	$\left  \int \mathbf{E}^3 d^3\mathbf{r} \right ^2 \propto \left  \int  E ^3 e^{i\phi} d^3\mathbf{r} \right ^2$	$\sim 0$

Table 2.2: Origin of axial resolution for different imaging modes of contrast. Diverging integral for conventional fluorescence signifies absence of axial resolution. Converging integral implies axial resolution for confocal and two-photon excited microscopies. In SHG, the precise value of the integral depends on the scatterers distribution. For THG, there is no signal in bulk tissue due to Gouy phase.

excitation beam propagation. This formula gives a good estimation of  $l_c$  for the counterpropagative SHG beam (B-SHG), but requires the explicit introduction of the Gouy phase correction and index dispersion for the F-SHG beam [108, 109]. Instead, we can estimate F-SHG  $l_c$  directly from the calculated phase distribution. Finally, for 0.95NA we get  $l_c \approx l_{Rayleigh} \approx 3\lambda/2$  for the F-SHG (see Fig. 2.6 c), and  $l_c \approx \pi/4k_\omega = \lambda/8$  for the B-SHG (see Eq. 2.6 with  $\mathbf{k}_{2\omega} \approx -2\mathbf{k}_\omega$ ).

The Gouy phase is also a crucial factor in bulk THG. As can be deduced from few last paragraphs, the beam Gouy phase shift of  $\pi$  corresponds to  $3\pi$  for the effective forward THG. It makes the rear and frontal cones (see Fig. 2.6 c) of the opposite phase, and additionally cuts the focal volume in two parts interfering destructively. It is the reason why the THG is not produced in a bulk medium and usually requires an interface between media with different  $\chi^{(3)}$  [99, 110].

To summarize, the origins of resolution in different microscopy techniques for the bulk contrast source are presented in the table 2.2.

## 2.2.2 Origin of SHG in collagen

In the previous subsection we discussed the general principles of SHG, paying special attention to the coherent process of signal formation. In this part we will elucidate the origin of SHG in collagenous assemblies and emphasize the role of a regular hierarchical structure on the efficiency of this process. Hierarchy of SHG signal build-up in collagen is shown in the Fig. 2.7.

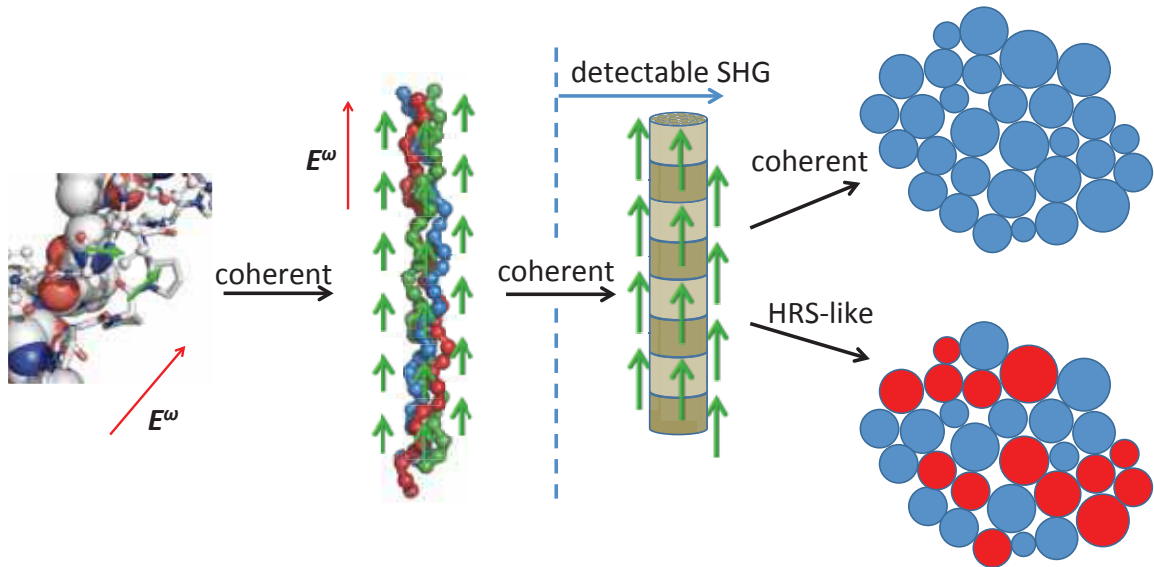


Figure 2.7: Origin of SHG in collagen tissues with hierarchical levels of SHG amplification in collagen. In this section, for the sake of simplicity the induced nonlinear dipoles in peptide bonds are assumed to be parallel to the excitation field.

The source of efficient second harmonic dipole in tropocollagen molecules has been attributed to the peptide bonds along the three chains constituting the helical structure [30,111–113]. The hypothesis that SHG is produced by the protein backbone rather than by the residues is supported by the fact that all types of collagens capable of hierarchical assembly (fibrillar types I, II, III, V, ...) produce SHG, while their amino-acid sequence differs significantly. In this context, a tropocollagen molecule can be considered as a set of second-order dipoles, which are situated along the three helices. While one can admit that a nonlinear response originates from a peptide bond, some studies show that the bond itself does not actually coincide to the induced nonlinear dipole direction [112,113].

When excited along the main axis of the triple helix, each bond contributes constructively to the SH signal produced by the molecule. The triple helix is therefore the first hierarchical level of SHG amplification for a peptide bond. However, as the length of the tropocollagen molecule is comparable to the wavelength, the amplification efficiency depends on the direction of signal detection [111]. In spite of the efficient coherent summation of peptide bond responses, neither individual collagen molecules nor isotropic distributions of these molecules are observable by SHG microscopy. Pena et al. demonstrated that there is no SHG produced from the basement collagen IV in connective tissue due to its virtually centrosymmetric organization [114]. However, Deniset-Besseau et al. showed that a much weaker HRS signal can be detected from concentrated collagen liquid solutions using higher excitation volume and much longer acquisition times than usually implemented in SHG microscopy setups [111].

The next level of collagen assembly — which is the assembly of individual molecules to produce fibrils — also amplifies the SHG signal significantly, as all molecules have the same orientation, or polarity, within the fibril [63]. This amplification has a qualitative impact on the SHG, as isolated fibrils are easily observed with SHG microscopy, unlike individual molecules.

Further, one can imagine two different scenarios for fibril assembly into a fascicle or bulk tissue. The first one would obey the same logic as previous two levels of assembly, i.e. the fascicle consists of aligned parallel fibrils with same polarity (same molecule orientation in each fibril with respect to the main axis of the fascicle). This case would produce fairly more amplified SHG signal than that from a single fibril.

Another possibility consists in organization in which each polar fibril randomly adopts either parallel or anti-parallel orientation with respect to the fascicle axis (random head-tail arrangement). Thus, the amplification of SHG in such a fascicle has a stochastic nature and is similar to the hyper-Rayleigh scattering of collagen (as described in 2.2.1.2), besides the fact that individual SH scatterers are collagen fibrils, not molecules. We suggest the name "HRS-like" amplification instead of coherent amplification to this process.

While there are evidences that collagen fibrils adopt a random head-tail organization in tendon [115], no data indicating either of two described scenarios are available for cornea.

## 2.3 Collagen tensorial response

In the previous section we extensively used the notion of a nonlinear dipole, which is induced in a moiety (also called "harmonophore") upon excitation by a fundamental field. To describe the coherent effects in SHG and signal amplification in collagen assemblies, we limited ourselves to molecules generating second harmonic along the polarization direction of the excitation field. This simple concept fully allowed us to explain the origin of SHG in collagenous tissues and to elucidate its main properties. However, in the context of SHG tensorial nature, which we first introduced in 2.2, this property corresponds solely to a single component of the hyperpolarizability tensor, which is  $\beta_{uuu}$  with  $u$  aligned with the excitation field. In general case, SHG-producing moiety has a wider set of tensor components, which depend on exact structure of the molecule. The different components of this tensor can be probed by polarization-resolved second harmonic generation (P-SHG). P-SHG consists in analysing SHG signal in tissue while varying the incident polarization. The SHG signal anisotropy can be quantified with a single parameter  $\rho$ , which we will discuss in details later in this section. P-SHG provides an additional contrast by measuring pixel-wise distribution of  $\rho$  in tissue, which gives access to the structure of the harmonophore assemblies.

P-SHG was successfully used to determine local fibril orientation within the tissue, which was demonstrated in [40, 41]. Several groups reported measurements of the  $\rho$  parameter in collagenous tissues [4, 6, 11, 13]. As different microscopic organization of nonlinear scatterers generally results in different P-SHG response, the parameter  $\rho$  can serve as a discerning variable to characterize different tissues or changes within a single type of tissue, which are accompanied by collagen reorganization. Notably, this approach was used to differentiate SHG from collagen and myosine [30], healthy and tumoral tissue [37, 116], and normal and diseased cartilage [38]. Some authors used the measured  $\rho$  values to determine helical pitch angles of peptide bonds within collagen molecules [15, 30], thus providing a link between SHG responses at peptide bond level and tissue level. As P-SHG is recently gaining more and more popularity, an effort was made by some groups to reduce both acquisition and image processing time while optimizing the precision of P-SHG analysis in tissues [117, 118]. Recent advanced model of P-SHG confirmed that the peptide bonds are sources of the nonlinear response in collagen [119].

In this section we briefly present the general tensorial properties of light scattering. Then, a substantial part of the section is dedicated to the hyperpolarizability of collagen molecules and macroscopic structures. Finally, we discuss on how the P-SHG can give an insight on the molecular organization on sub- $\mu\text{m}$  scale.

### 2.3.1 Tensorial formalism of medium polarization

Let's return to the Eq. 2.2 describing the polarization of a moiety in slightly different notations:

$$p_i = \alpha_{ij}E_j + \beta_{ijk}E_jE_k + \gamma_{ijkl}E_jE_lE_k + \dots \quad (2.7)$$

Here,  $p_i$  is the induced dipole moment including both linear and nonlinear parts,  $\alpha_{ij}$  is the linear polarizability tensor,  $\beta_{ijk}$  is the first hyperpolarizability tensor responsible for the SHG, and  $\gamma_{ijkl}$  is the second hyperpolarizability tensor responsible for the THG. The indices  $j, k, l$  are dummy indices, and we use the Einstein convention, performing a summation over indices appearing twice in a single term. The local field factors are omitted for simplicity.

Tensors are geometrical objects which are transformed in a specific way when the reference frame is changed. More precisely, a tensor  $T_{\alpha\beta\dots\gamma}$  in new basis will be transformed as follows:

$$\mathcal{T}_{\alpha'\beta'\dots\gamma'} = \mathcal{T}_{\alpha\beta\dots\gamma}e_{\alpha'}^{\alpha}e_{\beta'}^{\beta}\dots e_{\gamma'}^{\gamma}, \quad (2.8)$$

where  $e_{\gamma'}^{\gamma}$  governs the transformation between two frames. Here, upper and lower indices simply indicate old and new coordinates. Such a tensor is inherent to a moiety and is related to its geometric configuration and orientation. It implies that when seen from the

laboratory reference frame, two identical scatterers with different orientations will have two different tensors. It is useful to define such a tensor in the proper reference frame of the scatterer, preferably in a most convenient way. This will allow one to obtain the tensor in any reference frame by a known transformation.

A good example of molecules with strong  $\beta$  are push-pull molecules, where the charge transfer between donor and acceptor is only possible in one dimension. In this simplest case, the polarizability and all hyperpolarizabilities will have only one main component ( $\alpha_{uu}, \beta_{uuu}, \gamma_{uuuu}, \dots$ ) in the associated reference frame. This push-pull concept can be applied to describe qualitatively the SH response of peptide bonds.

While it is possible to define a hyperpolarizability tensor for an elementary scatterer such as a molecule or even a particular bond in a molecule, in practice this microscopic tensor is not accessible by optical measurements. Indeed, even a tightly focused beam contains many and many elementary scatterers, which are simultaneously excited by the driving field. Instead, the medium is characterized by an apparent nonlinear susceptibility, which results from summation of all elementary hyperpolarizability tensors in the focal volume:

$$\chi_{ijk}^{(2)} = \sum_{n \in V} \beta_{ijk, n}. \quad (2.9)$$

Here,  $\beta_{ijk}$  is the elementary scatterer's hyperpolarizability in the laboratory reference frame. It is obtained from the  $\beta_{IJK}$  tensor in the associated frame in the following way:

$$\beta_{ijk} = \beta_{IJK} T_i^I(\varphi, \theta, \psi) T_j^J(\varphi, \theta, \psi) T_k^K(\varphi, \theta, \psi). \quad (2.10)$$

The rotation matrix  $T$  between two reference frames reads

$$T(\varphi, \theta, \psi) = \begin{pmatrix} c_\varphi c_\psi - c_\theta s_\varphi s_\psi & -c_\varphi s_\psi - c_\theta c_\varphi s_\psi & s_\varphi s_\theta \\ c_\psi s_\varphi + c_\varphi c_\theta s_\psi & c_\varphi c_\theta c_\psi - s_\varphi s_\psi & -c_\varphi s_\theta \\ s_\theta s_\psi & c_\psi s_\theta & c_\theta \end{pmatrix} \quad (2.11)$$

with Euler angles  $\varphi$ ,  $\theta$  and  $\psi$  shown next to the formula.  $s$ 's and  $c$ 's signify sines and cosines of corresponding angles.

Here above, we related the microscopic hyperpolarizability tensor  $\beta$ , which describes the induced momentum of a single scatterer, to the macroscopic nonlinear susceptibility tensor  $\chi^{(2)}$ , which is appropriate for continuous media and which describes the volume density of induced dipoles (medium polarization). The hyperpolarizability describes the scatterer's interaction with the local field, while the nonlinear susceptibility describes the interaction of a continuous nonlinear medium with the average field.

### 2.3.2 Symmetries of collagen assemblies and nonlinear response tensors

In the most general case, the hyperpolarizability tensor describes how  $j$ th and  $k$ th components of two excitation fields at frequencies  $\omega_1$  and  $\omega_2$  contribute to the  $i$ th component of the scattered field at frequency  $\omega_1 + \omega_2$ . In full notation, the tensor is written as:

$$\beta_{ijk}(\omega_1 + \omega_2; \omega_1, \omega_2) \quad (2.12)$$

For an arbitrary scatterer, such a tensor may have as many as 27 independent components, although this number might be substantially reduced by different symmetries. First of all, we are not interested in sum-frequency generation for two arbitrary frequencies, but only in SHG, i.e. when  $\omega_1 = \omega_2 = \omega$ . In this case,  $\beta_{ijk}(\omega_1 + \omega_2; \omega_1, \omega_2)$  becomes  $\beta_{ijk}(2\omega; \omega, \omega)$ , which is invariant with respect to the permutation of two last indices. This fact reduces the number of independent components from 27 to 18.<sup>1</sup>

Further simplifications apply for the interaction in a lossless medium, which we suppose is the case for the tendon. It implies that all tensor components are real. Another substantial simplification is granted by Kleinman symmetry, which applies when all the involved frequencies ( $\omega$  and  $2\omega$ ) are far from resonance. It is a stronger requirement than the absence of losses. In collagen, light absorption bands are situated below 240 nm [7, 120], while we usually work at  $\lambda/2 = 430$ nm, which makes it reasonable to adopt this simplification. In some studies the Kleinman symmetry is shown to be precise within a few percent [113], while some other authors question the applicability of this symmetry for biological tissues [121]. When Kleinman symmetry is valid, the tensor components are basically frequency-independent, which allows to interchange all indices in  $\beta_{ijk}$  further reducing the number of independent components from 18 to 10.

Besides simplifications that come from general properties of SHG, there are those associated with the spatial symmetry of the medium. Fortunately, collagen assemblies are highly regular structures with high symmetry on different levels of organization. As the tropocollagen molecule consists of three almost identical helices, it possesses rotational symmetry  $C_3$ , and the tensor  $\beta_{\text{mol}}$  inherits it. For further simplicity, this symmetry is approximated with  $C_\infty$ . The Kleinman symmetry imposes invariance with respect to in-

---

<sup>1</sup>As SHG description with  $\beta_{ijk}$  becomes redundant, it is often substituted by a two-dimensional  $3 \times 6$  matrix  $d_{i,s}$ , which is basically a  $\beta_{ijk}$  with rearranged components [15, 30, 36, 41, 99]. In  $d_{i,s}$ ,  $i$  corresponds to the first index of  $\beta_{ijk}$ , while  $s$  corresponds to different combinations of  $j, k$  as shown below:

$$d_{i,s(j,k)} = \beta_{ijk}, \text{ where } s(j,k) = \begin{array}{c|ccc} j \setminus k & x & y & z \\ \hline x & 1 & 6 & 5 \\ y & 6 & 2 & 4 \\ z & 5 & 4 & 3 \end{array}. \quad (2.13)$$

terchanging of all three indices, explicitly ruling out chiral components, which makes that the medium effectively possesses  $C_{\infty v}$  symmetry. Additionally, the Kleinman symmetry reduces the number of independent tensor components for  $C_{\infty v}$  from 4 to 2.

$$\begin{array}{ll}
 C_{\infty v}, \text{ with Kleinman symmetry} & C_{\infty v}, \text{ w/o Kleinman symmetry} \\
 \beta_{xxx}, & \beta_{xxx}, \\
 \beta_{xyy} = \beta_{xzz} = & \beta_{xyy} = \beta_{xzz}, \\
 = \beta_{yxy} = \beta_{zxx} & \beta_{yxy} = \beta_{zxx}, \\
 = \beta_{yyx} = \beta_{zzx} & \beta_{yyx} = \beta_{zzx}
 \end{array} \quad (2.14)$$

Here and further in the manuscript, the  $x$  is the symmetry axis, unless other is stated.

### 2.3.3 Second harmonic response of collagen at molecular and fibrillar scale

In this subsection we will explore the tensorial nature of collagen taking into account its hierarchical structure and implementing the approach described above. The elementary sources of SHG in collagen are the peptide bonds in the protein backbone, which eventually determines the SHG response of the observable structures, such as bundles of collagen fibrils.

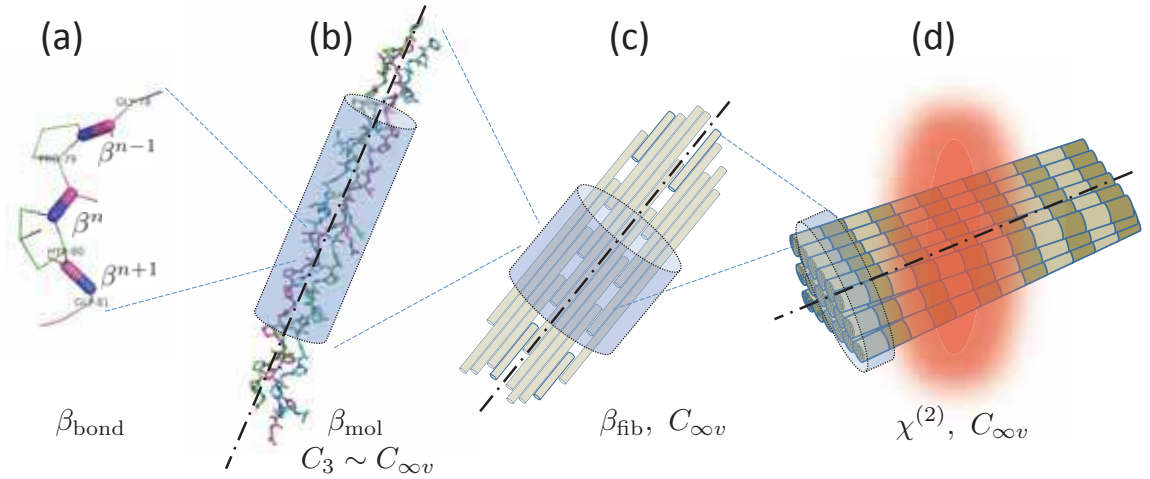


Figure 2.8: Nonlinear response tensors at different scales. (a) Part of the collagen alpha-chain, featuring Gly-Pro-Hyp-Gly sequence; peptide bonds are shown by blue-cyan sticks. (b) Part of tropocollagen molecule, which exhibits rotational symmetry  $C_3$ , which is often approximated by  $C_{\infty v}$ . (c) Collagen fibril equally possessing a  $C_{\infty v}$  symmetry. (d) Collagen fascicle with focused beam. The beam focal volume (red spot) encompasses one or two dozens of fibrils in tendon or about a hundred fibrils in cornea.

However, it is not always convenient to perform a direct transition from the elementary scatterer to the continuous medium according to Eq. 2.9. Instead of performing direct

summation over all amino-acids in the focal volume, one may separate the procedure in few steps, at each level calculating the intermediate tensor, e.g. for a collagen molecule and collagen fibril (see Fig. 2.8). It doesn't mean that one would be able to access these intermediate tensors by direct measurements, but instead this procedure yields tensors for more relevant building blocks for the collagen tissue. Additionally, these larger blocks may have a higher symmetry, and hence, a simpler form of tensor. Somewhere during this step-wise transformation one should switch from microscopic ( $\beta$ ) to continuous ( $\chi^{(2)}$ ) notations. However, this boundary is not clearly defined. Mostly by convenience in notations, we will however use hyperpolarizabilities for scales from the fibrillar level and below, and nonlinear susceptibility for the fascicles.

This multi-scale approach allows one to chose the most appropriate scale for the current needs. At every hierarchical level, the relevant tensors are those corresponding to the level of interest and to the level below. The first is as a matter of fact required to interpret the measured signal, and the second permits to gain insight into the variations of the former. Thus, when studying HRS signal from collagen, tensors for a single molecule and for a peptide bond become of a particular interest [111]. When studying individual fibril formation, the fibrillar and molecular tensors come to focus. Finally, in this work we address SHG in bulk tissues, so we are primarily interested by nonlinear susceptibility of tissue and hyperpolarizability of individual fibrils.

Hyperpolarizability tensor for the collagen molecule is obtained from the adequate elementary SHG-radiating block, that is the peptide bond [30]. For simplicity, it can be approximated by a push-pull molecule model, and in this case,  $\beta_{\text{mol}}$  reads:

$$\beta_{ijk, \text{mol}} = \sum_n \beta_{XXX, \text{bond}} T_i^X(\varphi_n, \theta_n) T_j^X(\varphi_n, \theta_n) T_k^X(\varphi_n, \theta_n). \quad (2.15)$$

Here capital letters stand for the associated reference of a push-pull moiety, and small letters stand for the reference associated with the tropocollagen molecule. The summation is performed over different peptide bonds in the molecule, and not over tensor components,  $\beta_{XXX, \text{bond}}$  being the only component of the elementary block's tensor. The pitch angles for different amino-acids are not equal, since their positions in  $[\text{Gly-X-Y}]_3$  blocks are not all equivalent. Additionally, the  $T_i^I$  matrix is simplified compared to the Eq. 2.11, as for a push-pull bond the angle  $\psi$  is irrelevant and can be set to any value. The  $C_{\infty v}$  symmetry of the tropocollagen limits the number of independent components to only two (as described in the previous subsection).

In spite of reproducing correctly the symmetry of the resulting molecular tensor, the model of SHG originating from non-interacting push-pull peptide bonds is not accurate. The proper calculation of the hyperpolarizability tensor for collagen molecule is not a trivial problem. Numerical simulations based on known molecular structure of tropocol-

lagen was recently performed by Tuer et al. [112, 122]. They explain that segmentation is needed to reasonably reduce the calculation time for hyperpolarizability tensor calculation. They also show that segmentation in individual effective amino acids doesn't offer sufficient precision and yields unrealistic results. The authors however were able to improve the situation by segmenting the molecule in larger blocks, containing 3-5 amino acids. As a conclusion, the best calculation would be a full triple helix simulation of hyperpolarizability tensor, which are still out of reach for modern calculation.

Hyperpolarizability of tropocollagen can further be used to calculate the tensor for a fibril. Neglecting the small helical angles of tropocollagen molecules within a fibril [123], one can also write the hyperpolarizability of a fibril consisting of  $N$  tropocollagen molecules in the following simple way:

$$\beta_{ijk, \text{fib}} = N\beta_{ijk, \text{mol}}. \quad (2.16)$$

Finally, performing a summation of contributions from all fibrils in the focal volume, we make a similar transition to the higher scale of fiber or fascicle. By convention, we consider that this transition marks the passage from microscopic notations to the macroscopic ones:

$$\chi_{ijk}^{(2)} = \sum_n \beta_{IJK, \text{fib}} T_i^I(\varphi_n, \theta_n) T_j^J(\varphi_n, \theta_n) T_k^K(\varphi_n, \theta_n) = N \langle \beta_{ijk, \text{fib}} \rangle_\Omega. \quad (2.17)$$

Here,  $\langle \cdot \rangle_\Omega$  stands for averaging over all orientations of contributing fibrils. In contrast to  $\beta$  tensors, which values are entangled within the value of  $\chi^{(2)}$  and cannot be accessed, the  $\chi^{(2)}$  tensor can be directly measured in tissue.

### 2.3.4 P-SHG signal for $C_{\infty v}$ symmetry

Absolute measurements of hyperpolarizability and nonlinear susceptibility are difficult, as they involve many loose parameters which cannot be precisely controlled. While providing absolute values, such measurements are usually still relative to compounds for which the hyperpolarizability tensor was independently measured previously (e.g. see [111]). On the contrary, it is rather straightforward to perform relative measurements of different components within a single susceptibility tensor, since the calibration is provided within the tensor (e.g. one of the components). For a tensor with  $n$  independent components  $\chi_1^{(2)}, \chi_2^{(2)}, \dots, \chi_n^{(2)}$ , there are  $n - 1$  ratiometric parameters:  $\frac{\chi_2^{(2)}}{\chi_1^{(2)}}, \frac{\chi_3^{(2)}}{\chi_1^{(2)}}, \dots, \frac{\chi_n^{(2)}}{\chi_1^{(2)}}$ .

For collagen within Kleinman approximation, there are only 2 independent components, so there is only one ratiometric parameter, which characterizes the tensor to within a constant factor. This value is often called the SHG anisotropy parameter  $\rho$  and can be

defined at different levels of hierarchy. For instance, we define  $\rho_{\text{fib}}$  for single fibril, and an effective  $\rho$  for the bulk tissue:

$$\rho_{\text{fib}} = \frac{\beta_{xxx, \text{fib}}}{\beta_{xyy, \text{fib}}} \quad \rho = \frac{\chi_{xxx}^{(2)}}{\chi_{xyy}^{(2)}}. \quad (2.18)$$

In the following, we will use  $\rho$  without an index to refer to SHG anisotropy parameter at tissue level, unless differently specified. When precise absolute measurement are unavailable, it is the only quantitative parameter that characterizes SHG from a sample with  $C_{\infty v}$  symmetry.

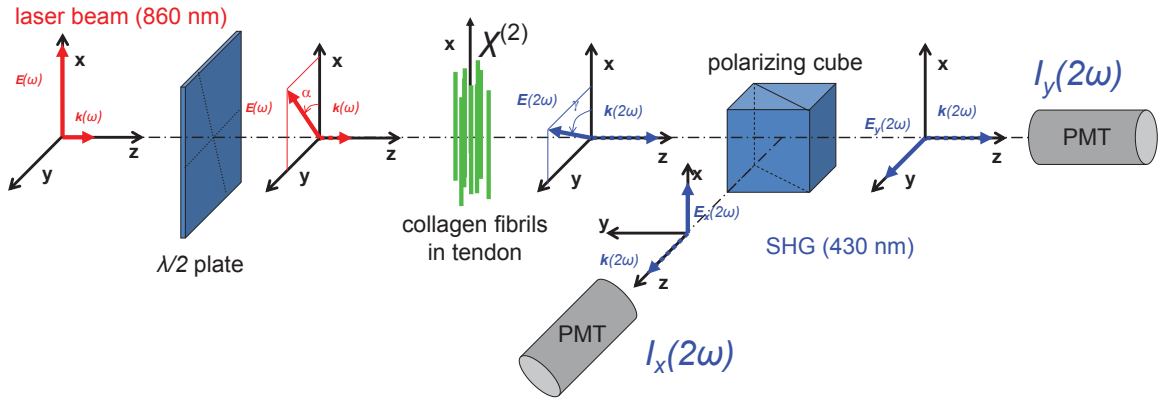


Figure 2.9: Scheme of polarization-resolved SHG experiment.

Let's discuss P-SHG signal for a tendon sample, considering a geometry which is typical for tendon SHG experiments [4, 13, 124] (see Fig. 2.9). A collagen fascicle with nonlinear susceptibility tensor  $\chi_{ijk}^{(2)}$  is placed within  $xy$  plane along the  $x$ -axis. The incident field propagates along  $z$ . The polarization of the incident beam lies within the sample plane, making an angle  $\alpha$  with the  $x$  axis, so that

$$E_x^\omega = E_0 \cos \alpha \quad (2.19)$$

$$E_y^\omega = E_0 \sin \alpha.$$

In this case, the radiated SHG intensities with  $x$  and  $y$  polarizations are:

$$I_x^{2\omega} \propto \left( \chi_{xxx}^{(2)} (E_x^\omega)^2 + \chi_{xyy}^{(2)} (E_y^\omega)^2 \right)^2 \propto (\rho \cos^2 \alpha + \sin^2 \alpha)^2 E_0^4 \quad (2.20)$$

$$I_y^{2\omega} \propto \left( \chi_{yxy}^{(2)} E_x^\omega E_y^\omega + \chi_{yyx}^{(2)} E_y^\omega E_x^\omega \right)^2 \propto \sin^2(2\alpha) E_0^4 \quad (2.21)$$

As it may be seen from above, the  $x$  SHG component is produced by either of incident polarizations independently. The  $y$  SHG field is only produced when the incident field has both  $x$  and  $y$  polarization components. The properties of  $z$  SHG are equivalent to that of

$y$ , but in this geometry there is no  $z$  excitation field, so there is no  $z$  SHG produced. The polar diagrams of  $I_x^{2\omega}$  and  $I_y^{2\omega}$  for  $\rho = 1.4$  are shown in the Fig. 2.10. One can see from the Eq. 2.20, that the ratio of intensities for  $\alpha = 0$  and  $\alpha = \pi/2$  gives the squared value for anisotropy parameter  $\rho$ . In practice, it allows one to extract  $\rho$  value from measured polarization diagrams by fitting the data accordingly to the Eq. 2.20.

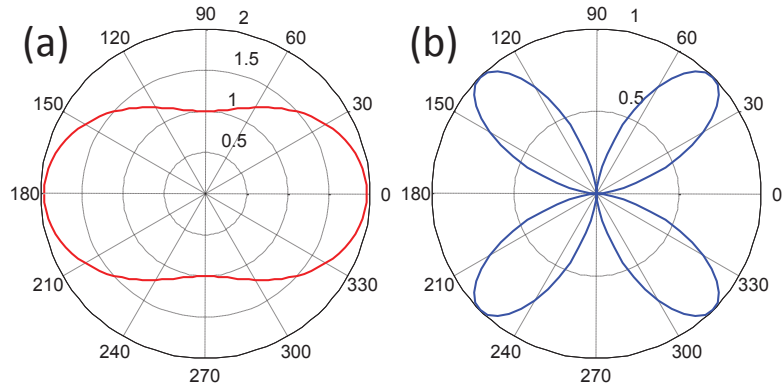


Figure 2.10: Polar diagram for SHG intensities along the tendon axis  $x$  (a) and along the orthogonal direction  $y$  (b) as a function of the polar direction  $\alpha$  of the excitation field. The diagrams are calculated for  $\rho = 1.4$ . Intensities are given in arbitrary units.

### 2.3.5 Tensorial response variation versus disorder in collagen fascicle

In this work, we are interested in measuring nonlinear susceptibility of the tissue, i.e. its response on the hierarchy level corresponding to the focal volume of our imaging system. In practice, this corresponds to clusters of few dozen fibrils in tendon (about a hundred for cornea), which may have orientational spread around the main axis (see Fig. 2.11 a). In this part we will explicitly derive the  $\chi^{(2)}$  tensor dependence on the angular spread of constituting fibrils to determine relationship between P-SHG responses at fibrillar level and tissue level. It should be noted, that this approach is different from that used by Plotnikov et al. [30], Tiaho et al. [15], and Su et al. [125], who directly link helical angle of peptide bond to the tissue nonlinear susceptibility. By doing this, the authors explicitly neglected any orientational disorder that collagen molecules may have within fibrils, or fibrils may have within fascicles. We believe that our approach is more appropriate, as it doesn't require additional hypotheses on the organization of molecules within fibrils.

The relationship between anisotropy parameters  $\rho_{\text{fb}}$  and  $\rho$  is derived by writing down the two independent components  $\chi_{xxx}^{(2)}$  and  $\chi_{xyy}^{(2)}$  according to the Eq. 2.17. For a fascicle consisting of fibrils oriented at different polar angles  $\theta$  and azimuthal angles  $\varphi$  to fascicle

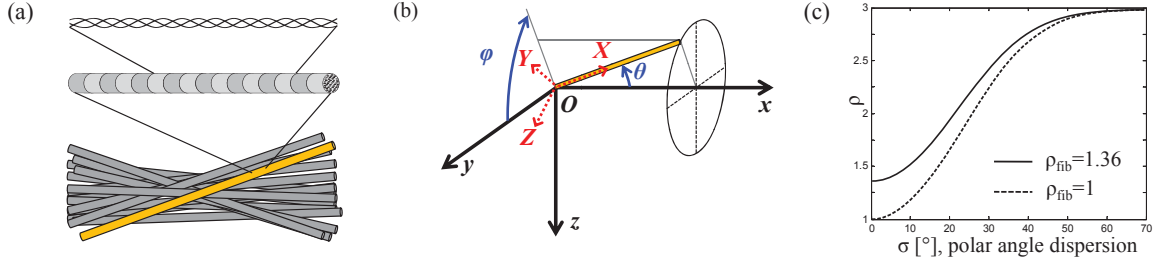


Figure 2.11: Orientational disorder in tendon. (a) Hierarchical structure of collagen, from molecule to fibril and fascicle. P-SHG probes the orientational distribution of fibrils within the fascicle. (b) Collagen fibril with  $(\theta, \varphi)$  orientation.  $(x, y, z)$  and  $(X, Y, Z)$  denote laboratory frame and fibril frame respectively. (c) Effective SHG anisotropy parameter  $\rho$  as a function of fibril orientation dispersion  $\sigma$  in the tendon fascicle for fibril parameter  $\rho_{\text{fib}} = 1$  and  $\rho_{\text{fib}} = 1.36$ .

axis (see Fig. 2.11 b), one can write:

$$\chi_{xxx}^{(2)} = N \langle \beta_{XXX} \cos^3 \theta + 3\beta_{XYY} \cos \theta \sin^2 \theta \rangle_{\varphi, \theta} \quad (2.22)$$

$$\chi_{xyy}^{(2)} = N \langle \beta_{XXX} \cos \theta \sin^2 \theta \cos^2 \varphi + \beta_{XYY} (\cos^3 \theta \cos^2 \varphi - 2 \cos \theta \sin^2 \theta \cos^2 \varphi + \cos \theta \sin^2 \varphi) \rangle_{\varphi, \theta}. \quad (2.23)$$

Here above, we used the fact that for Kleinman and  $C_{\infty v}$  symmetry the following relations hold:  $\beta_{XYY} = \beta_{YYX} = \beta_{YXY} = \beta_{XZZ}$ . We assume that fibrils are distributed uniformly with respect to the azimuthal angle  $\varphi$ . Further, we assume that the polar angle  $\theta$  is governed by some distribution  $g(\theta)$ , which reflects the angular spread of fibril orientation about the fascicle axis. In this case we obtain:

$$\chi_{xxx}^{(2)} = N\beta_{XXX} \langle \cos^3 \theta \rangle_g + 3N\beta_{XYY} \langle \cos \theta \sin^2 \theta \rangle_g \quad (2.24)$$

$$\chi_{xyy}^{(2)} = \chi_{yyx}^{(2)} = \chi_{yyx}^{(2)} = \frac{1}{2}N \left( \beta_{XXX} \langle \cos \theta \sin^2 \theta \rangle_g + \beta_{XYY} \left( 3 \langle \cos^3 \theta \rangle_g - \langle \cos \theta \rangle_g \right) \right) \quad (2.25)$$

and  $\chi_{ijk}^{(2)} = 0$  for all other components.

The SHG anisotropy parameter  $\rho$  writes:

$$\rho = \frac{\chi_{xxx}}{\chi_{xyy}} = \frac{\rho_{\text{fib}} \langle \cos^3 \theta \rangle_g + 3 \langle \cos \theta \sin^2 \theta \rangle_g}{\frac{3}{2} \langle \cos^3 \theta \rangle_g - \frac{1}{2} \langle \cos \theta \rangle_g + \frac{1}{2} \rho_{\text{fib}} \langle \cos \theta \sin^2 \theta \rangle_g}, \quad (2.26)$$

It is useful to introduce a spread parameter  $\delta$  as follows

$$\delta = 1 - \frac{\langle \cos^3 \theta \rangle_g}{\langle \cos \theta \rangle_g} = \frac{\langle \cos \theta \sin^2 \theta \rangle_g}{\langle \cos \theta \rangle_g} \quad (2.27)$$

which is positive if  $\theta$  is distributed around 0, and  $\delta \xrightarrow{\theta \rightarrow 0} 0$ . Hence, Eq. 2.26 can be rewritten as

$$\rho = \rho_{\text{fib}} + \frac{\frac{\delta}{2} (3 - \rho_{\text{fib}}) (\rho_{\text{fib}} + 2)}{1 - \frac{\delta}{2} (3 - \rho_{\text{fib}})}. \quad (2.28)$$

This equation shows different behavior for  $\rho_{\text{fib}} < 3$  (increases asymptotically to 3) or  $\rho_{\text{fib}} > 3$  (decreases asymptotically to 3). Given the values of  $\rho$  measured in our experiments and reported in the literature [4, 6, 7, 13, 15, 36, 111], we expect that  $\rho_{\text{fib}} < 3$  for rat-tail tendon fascicles. In that case, the effective parameter  $\rho$  increases with  $\delta$ , i.e. with disorder. The same trend has been reported in the particular case of a conical distribution at a fixed angle  $\theta$  when increasing  $\theta$  [112]. It is noteworthy, that the special point  $\rho_{\text{fib}} = 3$  is a consequence of symmetry of the fibril hyperpolarizability tensor (total number of components identical to  $\beta_{xyy,\text{fib}}$ ), and is not related to the dimension of fibril orientation distribution. For instance, this critical value  $\rho_{\text{fib}} = 3$  also appears for a planar fibril distribution, i.e. fibrils symmetrically spread in the  $xy$  plane around zero angle.

To further simplify the calculations, we now consider that the angle  $\theta$  exhibits a Gaussian distribution around  $x$ -axis,  $g(\theta) \propto e^{-\frac{\theta^2}{2\sigma^2}}$ , with distribution width  $\sigma = \sqrt{\langle \theta^2 \rangle_g}$ . For this Gaussian distribution,  $\delta$  can be written using Dawson's integral  $\xi(x) = e^{-x^2} \int_0^x e^{t^2} dt$ , which gives:

$$\delta = \frac{\langle \cos \theta \sin^2 \theta \rangle_\sigma}{\langle \cos \theta \rangle_\sigma} = \frac{2\xi(\sqrt{2}\sigma) - \xi(2\sqrt{2}\sigma)}{4\xi(\sqrt{2}\sigma)}. \quad (2.29)$$

Parameter  $\rho$  is then easily computed as a function of angular dispersion  $\sigma$  (see results in Fig. 2.11 c). Note that the Gaussian distribution approximation holds only for small angles ( $\sigma \lesssim \pi/4$ ), since  $\theta_{\text{max}}$  is limited to  $\pi$ . Other distributions, such as von Mises or Wrapped Normal distributions, may be considered for larger dispersions.

## 2.4 Conclusion

In this chapter we presented theoretical bases of P-SHG. We briefly introduced basic features and most prominent imaging modalities of multiphoton microscopy and discussed in details the properties of SHG microscopy and its origin in collagenous tissues. Finally, we described the tensorial nature of P-SHG signal in tissues and developed a theoretical model which links orientational order in tissue with its nonlinear susceptibility tensor.

SHG relies on simultaneous scattering of two excitation photons by a single harmonophore. We showed that coherence is of particular importance in SHG process, and it is responsible for efficient SHG amplification in samples with uniformly oriented harmonophores. As so, SHG is produced only in dense and highly ordered tissues. P-SHG from a molecule or a medium is characterized by a first hyperpolarizability or nonlinear susceptibility tensor, respectively. These tensors determine how efficiently the different

components of the excitation field produce SHG that is polarized along different coordinate axes. We introduced a theoretical model, which links the nonlinear susceptibility of a complex collagen structure to its building elements and their relative orientations. Notably, we showed how P-SHG measurements in tendon fascicle can provide information on the angular spread of collagen fibrils within the fascicle.

To conclude, SHG by itself proved to be an efficient probe for tissues organization. Additionally, P-SHG provides a promising structural imaging modality, which allows for quantifying fibril orientation and disorder in collagen tissue. While the image resolution is still diffraction-limited, P-SHG is sensible to structural properties at submicrometre scale, i.e. below optical resolution.

# Chapter 3

## Linear optical effects in polarization-resolved SHG microscopy

### Introduction

The SHG signal produced in a complex tissue by an excitation beam obviously depends both on the tissue, and on the beam propagation. Indeed, the focal field distribution can undergo dramatic changes in a dense, scattering tissue. Additionally and most importantly, if the tissue is anisotropic like tendon, these changes are different for incident polarizations along and perpendicular to the fascicle. However, up to now, little attention was given to this fact, and in the literature P-SHG images were usually processed according to Eqs. 2.19-2.21. In 1982, Roth et Freund [3] included a birefringence term in the model equation for SHG intensity, but this approach didn't receive thorough experimental validation, and is not applicable for tightly focused beams used in microscopy setups. More recently, Stoller et al. [6] explicitly neglected possible birefringence in the interpretation of their results, while the diagrams they obtained suggest its presence. Mansfield et al. [38] observed polarization-resolved SHG diagrams as a function of depth in tendon and cartilage, and touched upon possible contributions of birefringence and anisotropic attenuation. However, the P-SHG results were not treated accordingly, and no quantitative explanation was proposed to that account. In parallel to the course of this thesis, some papers were published reporting a more elaborated study of polarization scrambling [35] and birefringence [126].

In our work we clearly demonstrate that P-SHG measurements are prone to different perturbations in tissues due to linear propagation effects, that impede correct interpretation of P-SHG data in aligned rat-tail tendons. We therefore develop a comprehensive approach to correct P-SHG measurement for these artefacts.

In the first section we describe in details the experimental setup used for P-SHG measurements.

In the second section we present the results are given as an article that has been published in Optics Express. The article presents a phenomenological model which includes explicitly the effects we observed in tendon P-SHG imaging, and the experimental data which are interpreted using this model.

The third section is devoted to numerical simulations of the excitation beam propagation and SH generation. It includes both a theoretical part and the simulation results for tendon. Additionally, simulation results for cornea are presented in a form of a published article. This article reports experimental P-SHG data obtained by one of my colleagues, G. Latour, and their interpretation based on my numerical simulations.

Finally, in the fourth section we discuss the obtained experimental and theoretical results and draw some conclusions on the impact they can have on the modern state-of-art P-SHG imaging.

### 3.1 Experimental setup for simultaneous SHG/2PEF imaging

Here we describe the main part of our experimental setup. It allows for simultaneous acquisition of two-photon excited fluorescence and second harmonic generation, thus being a representative case of multiphoton microscopy instrumentation. The scheme of our multiphoton microscope is depicted in the Fig. 3.1.

The source of the excitation light is a mode-locked Titane:Sapphire femtosecond laser (Tsunami, Spectra-Physics) which is pumped with a continuous 5 W laser (Millenia, Spectra-Physics). The wavelength of the Ti:Sa laser is tunable between 700 *nm* and 990 *nm*. The pulses are cadenced at 82 MHz and have a duration of approximately 130 fs. The beam power varies from 500 mW at 730 nm to 250 mW at 970 nm, reaching its maximum of 800 mW at 790 nm. In our experiments we typically used 860 nm light, for which the beam power was about 700 mW.

The laser power delivered to the microscope is controlled by a half-wave plate succeeded by a Glan prism. The half-wave plate rotates the incident polarization before the Glan prism, changing the amount of light transmitted by the prism.

A shutter installed after the Glan prism blocks the beam unless the acquisition is performed, which limits the photo-damage undergone by the sample.

The beam scanning is performed by galvanometric mirrors (GSI-Lumonics). They change the angle of incidence of the beam on the objective, therefore laterally displacing

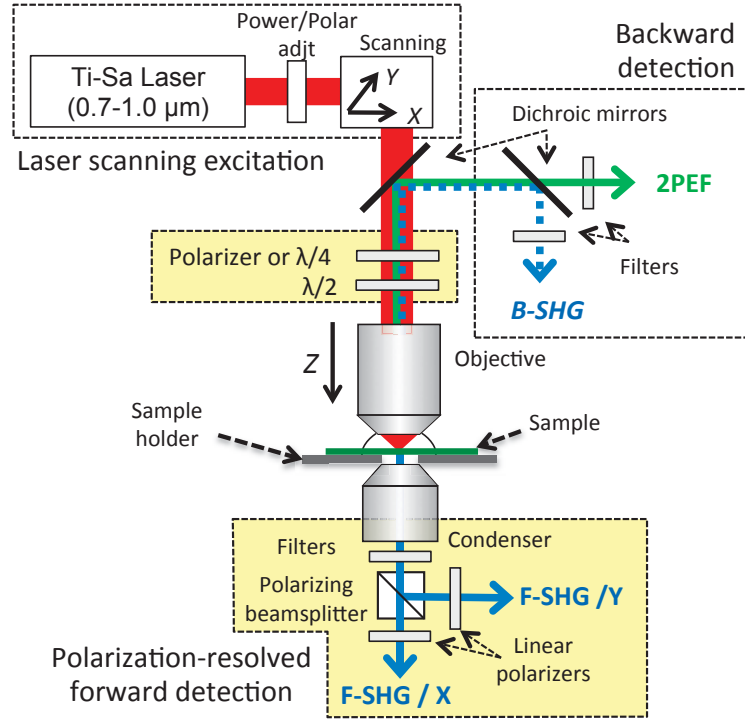


Figure 3.1: Experimental setup. Microscope consists of the following modules as depicted: excitation and scanning, incident polarization control, backward detection, and polarization-resolved forward detection. See description in the text.

the focal spot in the focal plane. The mirrors are optically coupled with the back pupil of the objective by an afocal system, which is also designed to expand the beam spot for full coverage of the pupil. The beam magnification is essential for exploiting the full numerical aperture of the objective.

Before hitting the objective, the beam passes through a dichroic mirror, which deflects the backward-emitted light, containing both SHG and 2PEF signal, to the epidetection module.

The polarization state of the light is controlled just before the objective. For the precise polarimetric measurement in the forward direction, an IR polarizer is used to eliminate non-negligible ellipticity (14%) originating from the dichroic and the galvanometric mirrors. The polarizer is oriented to deliver the maximum possible power. Then, the resulting linear polarization is rotated by an achromatic half-wave plate (MWPAA2-22-700-1000, CVI-Melles Griot). When performing polarimetric measurements in the backward direction, the polarizer is replaced by a quarter-wave plate to avoid polarization-specific blocking of the beam. The reason why  $\lambda/4$ -plate is not used in the forward direction is that in practice the polarizer allowed for almost perfect ellipticity elimination, while there was a remainder ellipticity of 5% with  $\lambda/4$ -plate.

The beam is focused at the sample by an objective. Since we usually work at 860 nm IR light with broad spectrum, the objective must be transparent for the infra-red light

and corrected for the chromatic aberrations. In our setup we use Olympus XLUMPFL 20x W/IR objective with 0.95 numerical aperture. It is a water-immersion objective transparent in infra-red, with working distance of 2 mm. It has a high NA, which ensures tight focusing, beneficial for the resolution (1.6  $\mu\text{m}$  axial and 0.4  $\mu\text{m}$  lateral FWHM resolution for 2PEF). At the same time, due to moderate magnification, it possesses a large field of view of about 500  $\mu\text{m} \times 500 \mu\text{m}$ . The vertical position of the objective, which corresponds to the axial coordinate of the focal spot, is controlled by a motor (Physik Instrumente M-126 DG) with a minimal step of 0.2  $\mu\text{m}$ .

There are two detection modules, in the forward and backward directions, each featuring two photomultiplier tubes (PMTs). The epidetection module allows for detecting backward-emitted 2PEF and back-scattered SHG light. In the module, the two modes of contrast are separated by a second dichroic mirror (FF458-Di01, Semrock). The forward detection module uses a polarization cube (BBPC-550, CVI-Melles Griot), which divides two orthogonal SHG polarizations towards two different PMTs. To ensure the quality of polarized light, we additionally put linear polarizers (03FPG021, CVI-Melles Griot) in front of each of these PMTs. For all PMTs, spectral filters are used to select the needed spectral component and to reject the other contributions. We used bandpass filter (Chroma HQ430/20) in SHG channels and coloured filters (Schott GG455) for 2PEF channels. Each channel was additionally equipped by one (backward detection) or two (forward detection) low-pass filters (FF01-680SP or FF01-720SP Semrock) to block the fundamental beam.

The whole system is controlled by a custom Labview interface developed in the laboratory. The module for polarization-resolved detection was developed by myself.

## 3.2 Experimental artefacts in thick anisotropic tissue

### Introduction

In this section we present a phenomenological model (i.e. based on the observed effects rather than on *ab initio* considerations) for P-SHG in rat-tail tendon. First, in this subsection we present a brief introduction to this model and to experimental results. Secondly, the detailed formalism, results and discussion are presented in a form of a journal article, as it has already been published in Optics Express.

The rat-tail tendon was chosen for our experiments because it is model tissue in collagen studies and in SHG experiments in particular, and it is easily obtained from rat tails. It has a simple structure as compared to other collagenous tissues. Indeed, it is virtually unidimensional, its dry content is 90% collagen and its hierarchical structure

possesses similar organization on all levels (parallel packing of molecules into fibrils and fibrils into fibers and fascicles).

In the article presented in this section we measured SHG polarization diagrams as a function of imaging depth in tendon. More precisely, for each position  $z_{obj}$  of the objective, we recorded SHG intensities along two polarization directions,  $I_x(\alpha, z_{obj})$  (along the tendon) and  $I_y(\alpha, z_{obj})$  (perpendicular to the tendon), as functions of incident linear polarization angle  $\alpha$ .

The obtained diagrams were then compared to those predicted by the Eqs. 2.20, 2.21 and discrepancies were observed. Notably, for a certain imaging depth  $\sim 30\mu\text{m}$  and angles  $\alpha \sim \pm\pi/4$  we observed minima of  $x$ -polarized SHG signal  $I_x(\alpha, z_{obj})$ , which could not be explained by the Eq. 2.20. We attributed this effect to tissue birefringence, which results in phase shift between the  $x$ - and  $y$ -components of the excitation field. Furthermore, we observed that SHG signal attenuation was stronger for incident polarization parallel to the tendon axis than for incident polarization perpendicular to the tendon axis. We referred to this effect as diattenuation, which is explained by anisotropic scattering of the excitation field. Finally, we demonstrated that a significant part of harmonic field initially radiated with  $x$ -polarization is detected in the  $y$ -polarization channel and vice versa. This is called polarization cross-talk, and is probably due to scattering on misaligned fibrils within the fascicle.

All these three effects were explicitly taken into account in the Eq. 2.20 to produce the following general equation of our phenomenological model:

$$I_x^{2\omega}(z) \propto \left| \rho e^{-\frac{z}{\Delta l_a}} \cos^2 \alpha e^{i\Delta\phi} + \sin^2 \alpha \right|^2 + \eta_{XY} e^{-\frac{z}{\Delta l_a}} |\sin 2\alpha|^2. \quad (3.1)$$

$\Delta\phi$  denotes the phase shift accumulated with depth between two incident orthogonal polarizations,  $\Delta l_a$  stands for excitation field diattenuation length, and  $\eta_{XY}$  shows the amount of  $I_y$  detected in the  $x$ -channel.

The measured diagrams  $I_x(\alpha, z_{obj})$  were fitted with the equation above to obtain the values for birefringence, diattenuation and polarization cross-talk. The simulated diagrams obtained with the extracted parameters are in excellent agreement with the experimental data, which signifies that our model correctly accounts for all observed effects affecting P-SHG in tendon.

### 3.2.1 Polarization-resolved Second Harmonic microscopy in anisotropic thick tissues

# Polarization-resolved Second Harmonic microscopy in anisotropic thick tissues

Ivan Gusachenko, Gaël Latour, Marie-Claire Schanne-Klein

Laboratory for Optics and Biosciences, Ecole Polytechnique, CNRS, INSERM U696,  
91128 Palaiseau, France

[marie-claire.schanne-klein@polytechnique.edu](mailto:marie-claire.schanne-klein@polytechnique.edu)

**Abstract:** We thoroughly analyze the linear propagation effects that affect polarization-resolved Second Harmonic Generation imaging of thick anisotropic tissues such as collagenous tissues. We develop a theoretical model that fully accounts for birefringence and diattenuation along the excitation propagation, and polarization scrambling upon scattering of the harmonic signal. We obtain an excellent agreement with polarization-resolved SHG images at increasing depth within a rat-tail tendon for both polarizations of the forward SHG signal. Most notably, we observe interference fringes due to birefringence in the SHG depth profile when excited at  $\pi/4$  angle from the tendon axis. We also measure artifactual decrease of  $\rho = \chi_{xxx}/\chi_{yyy}$  with depth due to diattenuation of the excitation. We therefore derive a method that proves reliable to determine both  $\rho$  and the tendon birefringence and diattenuation.

© 2010 Optical Society of America

**OCIS codes:** (180.4315) Nonlinear microscopy; (190.2620) Harmonic generation and mixing; (120.5410) Polarimetry; (170.3660) Light propagation in tissues; (170.6935) Tissue characterization

---

## References and links

1. P. J. Campagnola, A. C. Millard, M. Terasaki, P. E. Hoppe, C. J. Malone, and W. Mohler, "Three-Dimensional High-Resolution Second-Harmonic Generation Imaging of Endogenous Structural Proteins in Biological Tissues," *Biophys. J.* **82**, 493–508 (2002).
2. W. R. Zipfel, R. Williams, R. Christie, A. Nikitin, B. Hyman, and W. Webb, "Live tissue intrinsic emission microscopy using multiphoton-excited native fluorescence and second harmonic generation." *Proc. Natl. Acad. Sci. USA* **100**, 7075–7080 (2003).
3. A.-M. Pena, A. Fabre, D. Débarre, J. Marchal-Somme, B. Crestani, J.-L. Martin, E. Beaurepaire, and M.-C. Schanne-Klein, "Three-dimensional investigation and scoring of extracellular matrix remodeling during lung fibrosis using multiphoton microscopy." *Microsc. Res. Tech.* **70**(2), 162–170 (2007).
4. M. Strupler, M. Hernest, C. Fligny, J.-L. Martin, P.-L. Tharaux, and M.-C. Schanne-Klein, "Second Harmonic Microscopy to Quantify Renal Interstitial Fibrosis and Arterial Remodeling," *J. Biomed. Optics* **13**, 054041 (2008).
5. S. V. Plotnikov, A. Millard, P. Campagnola, and W. Mohler, "Characterization of the myosin-based source for second-harmonic generation from muscle sarcomeres," *Biophys. J.* **90**, 328–339 (2006).
6. F. Tiaho, G. Recher, and D. Rouède, "Estimation of helical angle of myosin and collagen by second harmonic generation imaging microscopy," *Opt. Express* **15**(19), 12286–12295 (2007).
7. A. Deniset-Besseau, J. Duboisset, E. Benichou, F. Hache, P.-F. Brevet, and M.-C. Schanne-Klein, "Measurement of the second order hyperpolarizability of the collagen triple helix and determination of its physical origin." *J. Phys. Chem. B* **113**(40), 13437–13445 (2009).
8. V. Nucciotti, C. Stringari, L. Sacconi, F. Vanzi, L. Fusi, M. Linari, G. Piazzesi, V. Lombardi, and F. S. Pavone, "Probing myosin structural conformation in vivo by second-harmonic generation microscopy," *Proc. Natl. Acad. Sci. USA* **107**(17), 7763–7768 (2010).
9. S. Roth and I. Freund, "Second harmonic generation in collagen," *J. Chem. Phys.* **70**(04), 1637–1643 (1979).

10. P. Stoller, K. Reiser, P. Celliers, and A. Rubenchik, "Polarization-modulated second harmonic generation in collagen," *Biophys J.* **82**(6), 3330–3342 (2002).
11. P. Stoller, P. Celliers, K. Reiser, and A. Rubenchik, "Quantitative second-harmonic generation microscopy in collagen," *Appl. Opt.* **42**(25), 5209–5219 (2003).
12. R. Williams, W. R. Zipfel, and W. Webb, "Interpreting second-harmonic generation images of collagen fibrils," *Biophys. J.* **88**, 1377–1386 (2005).
13. A. Erikson, J. Örtengren, T. Hompland, C. de Lange Davies, and M. Lindgren, "Quantification of the second-order nonlinear susceptibility of collagen I using a laser scanning microscope," *J. Biomed. Optics* **12**(4), 044002 (2007).
14. X. Han, R. M. Burke, M. L. Zettel, P. Tang, and E. B. Brown, "Second harmonic properties of tumor collagen: determining the structural relationship between reactive stroma and healthy stroma," *Opt. Express* **16**(3), 1846–1859 (2008).
15. J. C. Mansfield, C. P. Winlove, J. Moger, and S. J. Matcher, "Collagen fiber arrangement in normal and diseased cartilage studied by polarization sensitive nonlinear microscopy," *J. Biomed. Optics* **13**(4), 044020 (2008).
16. D. Aït-Belkacem, A. Gasecka, F. Munhoz, S. Brustlein, and S. Brasselet, "Influence of birefringence on polarization resolved nonlinear microscopy and collagen SHG structural imaging," *Opt. Express* **18**(14), 14859–14870 (2010).
17. O. Nadiarnykh, and P. J. Campagnola, "Retention of polarization signatures in SHG microscopy of scattering tissues through optical clearing," *Opt. Express* **17**, 5794–5806 (2009).
18. M. Strupler, A.-M. Pena, M. Hernest, P.-L. Tharaux, J.-L. Martin, E. Beaurepaire, and M.-C. Schanne-Klein, "Second harmonic imaging and scoring of collagen in fibrotic tissues," *Opt. Express* **15**(7), 4054–4065 (2007).
19. R. Boyd, *Nonlinear optics* (Academic press, London, 2003).
20. N. J. Kemp, H. N. Zaatari, J. Park, H. G. Rylander, and T. E. Milner, "Form-biattenuance in fibrous tissues measured with polarization-sensitive optical coherence tomography (PS-OCT)," *Opt. Express* **13**(12), 4611–4628 (2005).
21. J. Park, N. J. Kemp, H. G. Rylander, and T. E. Milner, "Complex polarization ratio to determine polarization properties of anisotropic tissue using polarization-sensitive optical coherence tomography," *Opt. Express* **17**(16), 13402–13417 (2009).
22. N. Olivier and E. Beaurepaire, "Third-harmonic generation microscopy with focus-engineered beams: a numerical study," *Opt. Express* **16**(19), 14703–14715 (2008).
23. P. Schön, M. Behrmdt, D. Aït-Belkacem, H. Rigneault, and S. Brasselet, "Polarization and phase pulse shaping applied to structural contrast in nonlinear microscopy imaging," *Phys. Rev. A* **81**(1), 013809 (2010).
24. X. D. Wang, and L. H. V. Wang, "Propagation of polarized light in birefringent turbid media: A Monte Carlo study," *J. Biomed. Optics* **7**, 279–290 (2002).
25. R. LaComb, O. Nadiarnykh, S. Carey, S. and P. J. Campagnola, "Quantitative second harmonic generation imaging and modeling of the optical clearing mechanism in striated muscle and tendon," *J. Biomed. Optics* **13**, 021109 (2008).
26. T. Boulesteix, A. Pena, N. Pagès, G. Godeau, M.-P. Sauviat, E. Beaurepaire, and M. Schanne-Klein, "Micrometer scale ex vivo multiphoton imaging of unstained arterial wall structure," *Cytometry* **69A**(1), 20–26 (2006).

## 1. Introduction

Second Harmonic Generation (SHG) microscopy is an efficient imaging technique to visualize the three-dimensional (3D) distribution of fibrillar collagen in biological tissues [1, 2]. Incident circular polarization is usually used since it enables imaging of fibrils independently of their orientation in the focal plane. This approach is particularly relevant for quantitative biomedical studies such as fibrosis scoring [3, 4]. However, fibrillar collagen exhibits a structural anisotropy that may be interesting to characterize for many applications. For that purpose, polarization-resolved SHG provides complementary information about the 3D distribution of nonlinear dipoles within the focal volume [5, 6, 7, 8]. The usual approach is to measure the ratio  $\rho$  of the two main tensorial components of the nonlinear response, considering a cylindrical symmetry for fibrillar collagen [9, 10, 11, 12, 13, 14]. This ratio depends on the orientational distribution of the collagen triple helices and on the orientation of the nonlinear dipoles (along the peptidic bonds) within the triple helix.  $\rho$  therefore provides information about the ordering of collagen molecules or fibrils within the focal volume. It has been measured in various collagenous tissues and showed a wide dispersion of values (1.2 to 2.6). Comparison of healthy and pathological tissue however requires to characterize the accuracy of  $\rho$  measure-

ments and their sensitivity to various artifacts. In particular, the anisotropy of many collagenous tissues may affect polarization-resolved SHG experiments as reported in tendons [10, 15, 16]. Polarization-resolved image processing improved when taking into account diattenuation [15] and birefringence [10, 16]. Furthermore, polarization scrambling due to scattering has been shown in tendons and other biological tissues [17].

The aim of this paper is therefore to thoroughly characterize the linear propagation effects that affect polarization-resolved SHG experiments in anisotropic tissues and to develop a reliable method to determine  $\rho$  in collagenous tissues. For this purpose, we first develop a theoretical model that fully accounts for birefringence, diattenuation and polarization scrambling upon scattering. We then record polarization-resolved SHG images in rat-tail tendons that is a model tissue composed of aligned collagen fibrils. We finally compare simulated and experimental data that show an excellent agreement and give insight into the linear and nonlinear optical properties of the tendon. Most notably, we observe interference fringes in the SHG depth profiles when excited at  $\pi/4$  angle from the tendon axis, and artifactual decrease of  $\rho$  with depth due to diattenuation of the excitation. We conclude that the correction for these effects enables a reliable determination of  $\rho$ .

## 2. Experimental setup

### 2.1. Tendon preparation

Tendons were extracted from Sprague-Dawley rat-tails (female,  $\approx 300\text{g}$ ), centrifugated at 4700 rpm and stored at  $4^\circ$  in phosphate buffer saline (PBS). Imaging was performed within a few days using a water-immersion objective. Tendons were first labelled with fluorescent latex beads to enable precise location of the tissue surface ( $1\mu\text{m}$  diameter, L1030, Sigma-Aldrich). After rinsing, they were fixed at both extremities and stretched to get rid of the crimps and facilitate alignment of the fibrillar pattern along the  $x$  direction of the microscope stage. They were kept in PBS on a glass coverslip that maintained them in the focal plane of the microscope.

### 2.2. Imaging setup

Multiphoton imaging was performed using a custom-built laser scanning microscope [18] as depicted in fig. 1.a. Excitation was provided by a femtosecond Titanium-sapphire laser tuned at 860 nm and scanned in the  $xy$  directions using galvanometric mirrors. It was focused in the tendon using a water-immersion 20x, 0.95 NA objective that resulted in typically  $0.4\mu\text{m}$  lateral and  $1.6\mu\text{m}$  axial resolution near the sample surface. Power was adjusted to 10-15 mW at the focus using a rotating half waveplate and a Glan prism that filtered out  $y$ -polarization before entering the microscope setup. Nonlinear optical signals were detected using photon-counting photomultiplier tubes and appropriate spectral filters to reject the laser excitation (FF01-680SP, Semrock) and select two-photon excited fluorescence (2PEF) signal (GG455 high-pass filter, Schott) or SHG signal (HQ430/20 interferential filter, Chroma). 2PEF was detected in the backward direction and SHG in the forward direction. Multimodal images were recorded using 100 to 200 kHz pixel rate,  $0.4$  to  $0.8\mu\text{m}$  pixel size and 1 to  $2\mu\text{m}$   $z$ -step. They were combined using Matlab and ImageJ softwares as shown in fig. 1.c. Note that there is a slight index mismatch between the tendon ( $n = 1.5$ ) [20] and water ( $n = 1.33$ ), so that the depth  $z$  within the tendon is related to the lens displacement  $dz_{lens}$  by:  $z = dz_{lens} n_{tendon}/n_{water}$ .

### 2.3. Polarization-resolved measurements

The laser polarization at the back pupil of the objective was approximately along the  $x$  direction but exhibited a 14% ellipticity due to the optical components within the microscope (9% ellipticity without the dichroic mirror for epi-detection). We therefore inserted an infrared polarizer

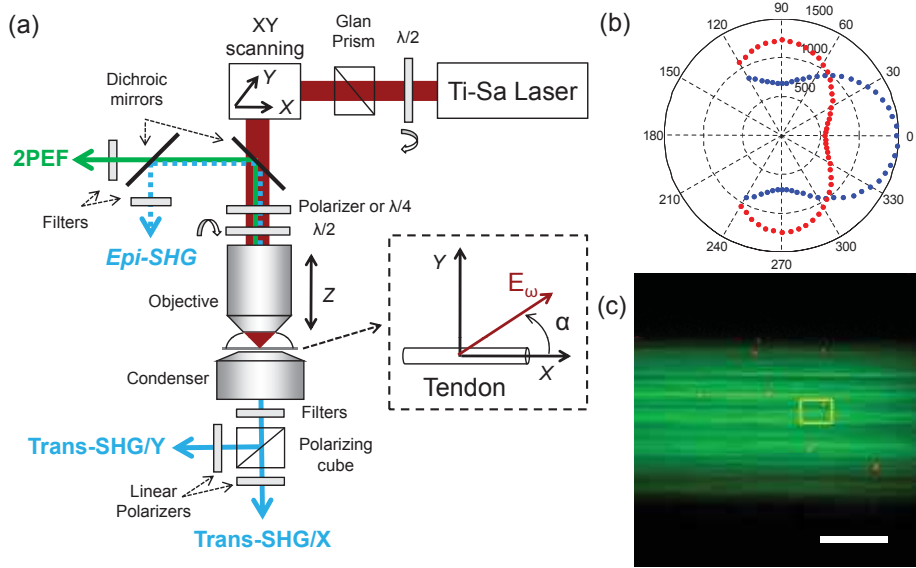


Fig. 1. Experimental setup. (a) Laser scanning multiphoton microscope showing polarization-resolved detection of forward SHG signal and epi-detection of 2PEF signal and possibly of SHG signal. The insert displays the incident electric field relative to the tendon geometry in the focal plane. (b)  $x$ - and  $y$ -polarized forward 2PEF signal from a fluorescent slide for variable incident polarization angles. The ratio of the 2 maxima is used for calibration of polarization-resolved SHG signals. (c) Combined 2PEF (red) and SHG (green) image of a tendon labeled with fluorescent latex beads. The image is the summation of 15 images acquired  $2\mu\text{m}$  apart from the tendon upper surface, with enhanced contrast. The yellow box shows a typical Region of Interest used for plotting depth-polar diagrams as in fig. 5. Scale bar:  $50\mu\text{m}$ .

and achieved an ellipticity less than 1% with small scanning angles. This linear polarization was tuned from  $-\pi/3$  to  $\pi/3$  (usually with  $\pi/12$  steps) by rotating an achromatic half waveplate (MWPAA2-22-700-1000, CVI-Melles Griot) placed just before the objective (see fig. 1.a). Forward SHG signals were analyzed using a polarizing beamsplitter cube (BBPC-550, CVI- Melles Griot). To improve the extinction ratio of the  $x$ - and  $y$ -polarized detection channels, linear polarizers (03FPG021, CVI- Melles Griot) were set in front of the detectors. The relative transmission of these two channels was calibrated using a fluorescent slide (Chroma): we took advantage of the isotropy of the setup within the  $xy$  plane and compared the  $x$ -polarized signal to the  $y$ -polarized one excited with polarizations shifted by  $\pi/2$  angle (see fig.1.b). The ratio of both channels was typically 1.1. Calibration was performed before every experiment and enabled quantitative comparison between  $x$ - and  $y$ -polarized signals.

### 3. Theoretical background

#### 3.1. Polarization-resolved SHG

Let's consider the nonlinear optical interaction of the incident laser beam with a rat-tail tendon. The polarization induced in the medium by the electric field  $\mathbf{E}$  is given by:

$$P_i = \chi_{ij}^{(1)} E_j + \chi_{ijk}^{(2)} E_j E_k \quad (1)$$

where we considered only the first- and second-order electric susceptibility tensors  $\chi^{(1),(2)}$ . Rat-tail tendon is commonly assumed to have a cylindrical symmetry ( $C_{6v}$  symmetry) [9, 10, 7], which reduces the number of independent nonvanishing  $\chi^{(2)}$  components. Moreover, we assume that the Kleinman symmetry is valid as usually considered because of the nonresonant character of the interaction. Within these approximations, there are only 2 independent nonvanishing  $\chi^{(2)}$  tensorial components:  $\chi_{xxx}$  and  $\chi_{xyy} = \chi_{xzz} = \chi_{yyx} = \chi_{zxx} = \chi_{yzy} = \chi_{zzx}$ , where  $x$  represents the main axis of the tendon [19]. Considering a laser beam propagating in the  $z$  direction with a linear polarization at angle  $\alpha$  to the tendon lying in the  $xy$  plane (see fig. 1.a), the electric fields reads:  $E_x^\omega = E_0 \cos \alpha$  and  $E_y^\omega = E_0 \sin \alpha$  near the focus and induces a SH polarization:

$$\begin{aligned} P_x^{2\omega} &\propto (\chi_{xxx} \cos^2 \alpha + \chi_{xyy} \sin^2 \alpha) E_0^2 \\ P_y^{2\omega} &\propto (\chi_{xyy} \sin 2\alpha) E_0^2 \end{aligned} \quad (2)$$

which radiates at frequency  $2\omega$ . In this paper, we are interested in ratiometric measurement of the second-order response and we consider the ratio of the two independent tensorial components of the second-order susceptibility:  $\rho = \chi_{xxx}/\chi_{xyy}$ . This ratio provides insight into the orientational distribution of the collagen molecules within the focal volume. It is taken to be real in the Kleinman approximation. The SH intensity detected for each polarisation then reads:

$$I_x^{2\omega} = K |\rho \cos^2 \alpha + \sin^2 \alpha|^2 \quad (3a)$$

$$I_y^{2\omega} = K |2 \sin \alpha \cos \alpha|^2 \quad (3b)$$

where  $K$  is a constant merging various parameters such as setup geometry and squared incident beam intensity  $I_0^2$ . Polar diagrams of eq. (3) are displayed in fig. 2.a and b using  $\rho = 1.4$ . A common method to determine  $\rho$  from polarization-resolved SH experiments is to fit  $I_x^{2\omega}$  using eq. (3a).

In the following, we propose a more general method. Since  $I_x^{2\omega}$  and  $I_y^{2\omega}$  are even functions of  $\alpha$  and contain only even powers of trigonometric functions, they can be represented as a sum of  $\cos 2n\alpha$  functions:

$$I_x^{2\omega} = A \cos 4\alpha + B \cos 2\alpha + C \quad (4a)$$

$$I_y^{2\omega} = \frac{K}{2} (-\cos 4\alpha + 1) \quad (4b)$$

where

$$A = \frac{K}{2} \left( \frac{\rho - 1}{2} \right)^2 \quad (5a)$$

$$B = 2K \left( \frac{\rho - 1}{2} \right) \left( \frac{\rho + 1}{2} \right) \quad (5b)$$

$$C = \frac{K}{2} \left( \frac{\rho - 1}{2} \right)^2 + K \left( \frac{\rho + 1}{2} \right)^2 \quad (5c)$$

In that framework, one can notice that:

$$\rho^2 = \frac{A + B + C}{A - B + C} \quad (6)$$

This expression enables the determination of  $\rho$  from polarization-resolved SH data by fitting  $I_x^{2\omega}$  using eq. (4a). The advantage of this method is that it can take into account various physical effects that appear to modify the expression of  $I_x^{2\omega}$  but not its representation as a sum of  $\cos 2n\alpha$  functions. These physical effects will be presented in the following sections and the new expressions of the  $A, B$  and  $C$  parameters will be derived.

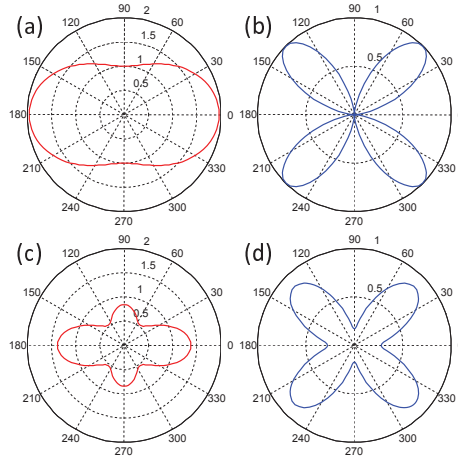


Fig. 2. Simulated polar diagrams of polarization-resolved SH intensity generated by a tendon aligned along  $x$  axis. The angle represents the direction of the excitation polarization to the tendon direction (see fig. 1.a). (a)  $I_x^{2\omega}$  and (b)  $I_y^{2\omega}$  in a non-birefringent, non-scattering medium without diattenuation (see eq. (2)). (c)  $I_x^{2\omega}$  and (d)  $I_y^{2\omega}$  at  $24\mu\text{m}$  depth considering birefringence ( $\Delta n = 0.0066$ ), diattenuation ( $\Delta I_a = 175\mu\text{m}$ ) and polarisation cross-talk due to scattering ( $\eta_{xy} = 0.13$ ) (see Eq. (11)).  $\rho = 1.40$  in all simulations.

### 3.2. Tendon birefringence

In the former derivation of  $I^{2\omega}$ , we have assumed that the electric field propagation takes place in an isotropic medium. Nevertheless, the tendon is considered to exhibit a  $C_{6v}$  symmetry, so that the permittivity tensor  $\epsilon_0 \left(1 + \chi_{ij}^{(1)}\right)$  has two different components and the tendon is analogous to a uniaxial birefringent crystal. Indeed, it has been reported that birefringence  $\Delta n = n_e - n_o$  attains  $5 \cdot 10^{-3}$  [20, 21] in tendon. As a consequence, the  $x$  (extraordinary wave) and  $y$  (ordinary wave) excitation field components undergoes a relative phase retardation when propagating within the tendon. SH intensity then reads:

$$I_x^{2\omega}(z) = K \left| \rho \cos^2 \alpha e^{i\Delta\phi} + \sin^2 \alpha \right|^2 = K \left( |\rho \cos^2 \alpha + \sin^2 \alpha|^2 + \frac{\rho}{2} \sin^2 2\alpha (\cos \Delta\phi - 1) \right) \quad (7a)$$

$$I_y^{2\omega}(z) = K \left| \sin 2\alpha e^{i\frac{2\pi(n_e+n_o)}{\lambda}z} \right|^2 = K |\sin 2\alpha|^2 \quad (7b)$$

where  $\Delta\phi = \frac{4\pi(n_e-n_o)z}{\lambda}$  accounts for the birefringence in the excitation propagation (SHG intensity is unaffected by birefringence in the harmonic propagation). Note that  $z$  represents the depth in tendon at which SH takes place: due to index mismatch,  $z = dz_{lens} n_{tendon} / n_{water}$ , where  $dz_{lens}$  is the microscope lens displacement from the tendon upper surface.

These expressions show that  $I_y^{2\omega}$  is unaffected by birefringence, while  $I_x^{2\omega}$  has a supplement-

tary term compared to eq. (4). Decomposing  $I_x^{2\omega}$  in the  $\cos 2n\alpha$  basis, we get:

$$A_{biref} = K \left[ \frac{1}{2} \left( \frac{\rho-1}{2} \right)^2 + \frac{\rho}{4} (1 - \cos \Delta\phi) \right] \quad (8a)$$

$$B_{biref} = 2K \left( \frac{\rho-1}{2} \right) \left( \frac{\rho+1}{2} \right) \quad (8b)$$

$$C_{biref} = K \left[ \frac{1}{2} \left( \frac{\rho-1}{2} \right)^2 + \left( \frac{\rho+1}{2} \right)^2 - \frac{\rho}{4} (1 - \cos \Delta\phi) \right] \quad (8c)$$

One observes that  $B_{biref} = B$  and  $A_{biref} + C_{biref} = A + C$ , so that  $\rho$  can be determined using eq. 6 as in section 3.1. To get better insight into the effect of birefringence, we have plotted in fig. 3 the variation of  $I_x^{2\omega}$  and  $I_y^{2\omega}$  as a function of the incident polarization angle  $\alpha$  for increasing depth within the tendon. Comparison of model calculations with and without birefringence shows that birefringence results in interference fringes in the  $x$ -polarized SH intensity  $I_x^{2\omega}$  when excited with a linear polarization at  $\pi/4$  from the tendon axis, as shown by the  $\cos \Delta\phi$  term in eq. 7a (see  $z$ -profiles in 3.k and 3.n).

### 3.3. Polarization cross-talk

We have assumed yet that propagation occurs in an optically perfect medium. However, tendon is a scattering medium like most biological tissues. It results in the decrease of the excitation intensity since scattered light is not intense enough to induce a nonlinear response. This effect, that may be different for  $x$ - and  $y$ -polarized incident light, will be considered in the next section. Here, we are interested in the effect of light scattering on the harmonic beam polarization. When propagating in an anisotropic scattering medium, a wave with well-defined polarization accumulates scrambling over its polarization direction since scattering processes slightly rotate the polarization direction. As a consequence, a small amount of SH light that is initially polarized along  $y$  is detected in the  $x$ -polarized channel and vice versa. Let  $\eta_{XY}$  (resp.  $\eta_{YX}$ ) be the amount of that polarization "cross-talk" from  $y$  detection channel to  $x$  detection channel (resp. from  $x$  to  $y$ ), so  $I_x^{2\omega}$  reads:

$$I_x^{2\omega}(z) = K |\rho \cos^2 \alpha + \sin^2 \alpha|^2 + \eta_{XY} K |\sin 2\alpha|^2 \quad (9a)$$

$$I_y^{2\omega}(z) = \eta_{YX} K |\rho \cos^2 \alpha + \sin^2 \alpha|^2 + K |\sin 2\alpha|^2 \quad (9b)$$

Decomposing  $I_x^{2\omega}$  in the  $\cos 2n\alpha$  basis, we obtain:

$$A_{pol} = K \left[ \frac{1}{2} \left( \frac{\rho-1}{2} \right)^2 - \frac{\eta_{XY}}{2} \right] \quad (10a)$$

$$B_{pol} = 2K \left( \frac{\rho-1}{2} \right) \left( \frac{\rho+1}{2} \right) \quad (10b)$$

$$C_{pol} = K \left[ \frac{1}{2} \left( \frac{\rho-1}{2} \right)^2 + \left( \frac{\rho+1}{2} \right)^2 + \frac{\eta_{XY}}{2} \right] \quad (10c)$$

Once again,  $B_{pol} = B$  and  $A_{pol} + C_{pol} = A + C$ , and  $\rho$  can be determined as before. Fig. 3.b and g show that the angular profiles of  $I_x^{2\omega}$  and  $I_y^{2\omega}$  are slightly modified by polarization cross-talk.

### 3.4. Diattenuation in tendon

Multiphoton microscopy uses near-infrared excitation which minimizes absorbance and scattering in biological tissues. Nevertheless, light scattering and spherical aberrations cause focal

volume deterioration upon propagation within the tendon, which results in smaller excitation intensity and weaker SH signal. For simplicity, we assume that the excitation intensity undergoes exponential attenuation with depth. Due to the tendon anisotropy, the effective attenuation lengths for  $I_x^\omega$  and  $I_y^\omega$  are different and the excitation light experiences diattenuation. These attenuation lengths will be noted as  $l_a^e$  and  $l_a^o$  to account for the uniaxial symmetry of the tendon. We assume that diattenuation of the SH signal is negligible because signal forward-detection in multiphoton setups is not much sensitive to light scattering and aberrations.  $I_{x,y}^{2\omega}$  then reads:

$$I_x^{2\omega}(z) = K \left| \rho \cos^2 \alpha e^{-\frac{z}{l_a^e}} + \sin^2 \alpha e^{-\frac{z}{l_a^o}} \right|^2 = K e^{-\frac{2z}{l_a^e}} \left| \rho e^{-\frac{z}{\Delta l_a}} \cos^2 \alpha + \sin^2 \alpha \right|^2 \quad (11a)$$

$$I_y^{2\omega}(z) = K \left| \sin 2\alpha e^{-\frac{z}{2l_a^e}} e^{-\frac{z}{2l_a^o}} \right|^2 = K e^{-\frac{2z}{l_a^e}} e^{-\frac{z}{\Delta l_a}} |\sin 2\alpha|^2 \quad (11b)$$

where  $\frac{1}{\Delta l_a} = \frac{1}{l_a^e} - \frac{1}{l_a^o}$ . The expression of the  $A$ ,  $B$  and  $C$  parameters are the same as in eq. 5 with the modified parameters:  $K \rightarrow K e^{-\frac{2z}{l_a^e}}$  and  $\rho \rightarrow \rho e^{-\frac{z}{\Delta l_a}}$ . Consequently, once  $\Delta l_a$  is known,  $\rho$  can be determined in a similar way as in section 3.1. Note that this approach can be generalized to an arbitrary diattenuation profile  $f_a(z) = f_a^x(z)/f_a^y(z)$  by using the transformation  $\rho \rightarrow \rho f_a(z)$  in eq. 6. Fig. 3.c, h and m show the modifications of  $I_x^{2\omega}$  and  $I_y^{2\omega}$  induced by diattenuation. In particular,  $z$ -profiles for an incident polarization parallel (resp. perpendicular) to the tendon exhibit a  $l_a^e$  (resp.  $l_a^o$ ) exponential decay.

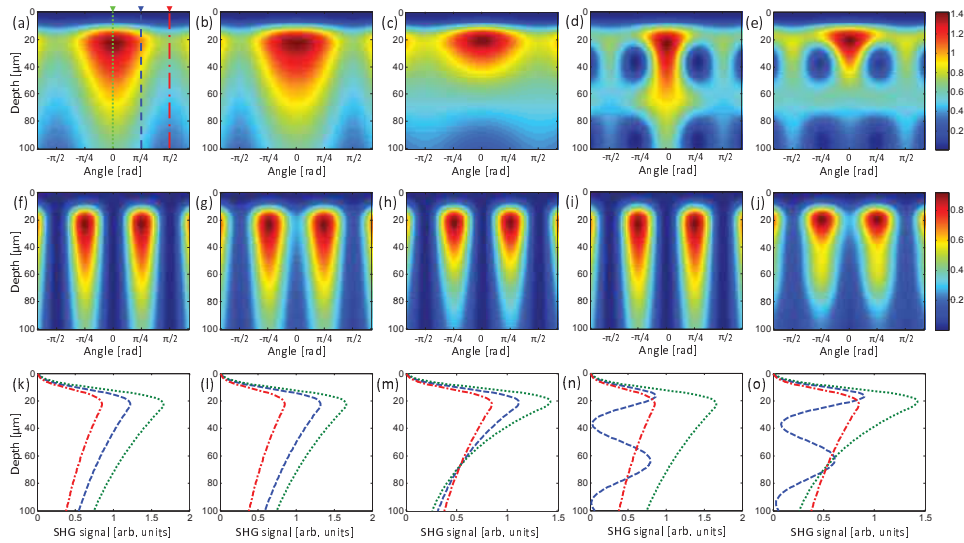


Fig. 3. Numerical calculation of polarization-resolved SH intensity as a function of incident polarisation angle  $\alpha$  (see fig. 1) and depth  $z$  within tendon for different parameters. (a)-(e)  $I_x^{2\omega}$ , (f)-(j)  $I_y^{2\omega}$  and (k)-(o)  $z$ -profiles of  $I_x^{2\omega}$  for  $\alpha = 0$  (green dotted line),  $\alpha = \pi/4$  (blue dashed line) and  $\alpha = \pi/2$  (red dash-dot line). (a), (f), (k) tendon with uniform depth-attenuation:  $l_a^e = l_a^o = 190\mu\text{m}$ . (b), (g), (l) tendon with polarization cross-talk:  $\eta_{xy} = 0.13$ ,  $\eta_{yx} = 0.2$  (constant with depth). (c), (h), (m) tendon with diattenuation:  $l_a^e = 91\mu\text{m}$  and  $l_a^o = 190\mu\text{m}$ . (d), (i), (n) tendon with birefringence  $\Delta n = 0.0066$ . (e), (j), (o) tendon with diattenuation, birefringence and polarisation cross-talk (same parameters).  $\rho$  is equal to 1.40 for all calculations.

### 3.5. Combined effects of birefringence, polarization cross-talk and diattenuation

When taking into account all the effects introduced above, we obtain the following expression:

$$I_x^{2\omega}(z) = Ke^{-\frac{2z}{l_a^e}} \left( \left| \rho e^{-\frac{z}{\Delta a}} \cos^2 \alpha e^{i\Delta\phi} + \sin^2 \alpha \right|^2 + \eta_{XY} e^{-\frac{z}{\Delta a}} |\sin 2\alpha|^2 \right) \quad (12)$$

Fig. 2.c and d display the polar diagrams of this expression along with the similar expression for  $I_y^{2\omega}$ . They clearly look very different from the polar diagrams a and b plotted from the simplified model (eq. 3). It shows that determination of  $\rho$  using eq. 3a is hazardous. Conversely,  $I_x^{2\omega}$  can still be decomposed as a sum of  $\cos 2n\alpha$  functions as in eq. 4a: the parameters  $A_{eff}, B_{eff}$  and  $C_{eff}$  are obtained by combining the effects of birefringence (eq. 8) and polarization cross-talk (eq. 10) only, and considering the modified parameters:  $K \rightarrow Ke^{-\frac{2z}{l_a^e}}$ ,  $\rho \rightarrow \rho e^{-\frac{z}{\Delta a}}$  and  $\eta_{XY} \rightarrow \eta_{XY} e^{-\frac{z}{\Delta a}}$ . In that framework,  $\rho$  can be determined as follows:

$$\rho^2 e^{-\frac{2z}{\Delta a}} = \frac{A_{eff} + B_{eff} + C_{eff}}{A_{eff} - B_{eff} + C_{eff}} \quad (13)$$

given that  $z$ -profiles of  $I_x^{2\omega}$  for  $\alpha = 0$  and  $\frac{\pi}{2}$  can be used to determine  $l_a^e$  and  $l_a^o$  (or  $f_a(z)$  in a more general case).

The right hand side of fig. 3 displays the  $x$ - and  $y$ -polarized SH signal given by eq. 12: diattenuation is revealed by differences in  $z$  attenuation for incident polarization parallel and perpendicular to the tendon axis, birefringence by oscillations in the  $z$ -profile at  $\pi/4$  polarization angle from the tendon axis and polarization cross-talk by deformation of the angular profiles. In order to better evidence the latter two effects, we introduce the parameter  $\Delta$  that sorts out the contributions of  $\Delta\phi$  and  $\eta_{XY}$  to  $A_{eff}$  and  $C_{eff}$ :

$$\Delta(z) = \frac{C - 3A - \sqrt{(A+C)^2 - B^2}}{2(A - B + C)} \quad (14a)$$

$$\Delta(z) = f_a \left[ \eta_{XY} - \frac{\rho}{2} (1 - \cos \Delta\phi) \right] \quad (14b)$$

At a given depth, contributions of birefringence and polarization cross-talk are intrinsically mixed, but information on these effects can be obtained by analysis of  $\Delta$  depth variation.

## 4. Results

Fig. 4 displays typical  $x$ - and  $y$ -polarized SHG images obtained at various depths within a tendon for an incident beam polarized at  $\pi/4$  from the tendon axis. Transverse profiles show that the SHG signal is higher at the tendon edges as expected because of the cylindrical shape of the tendon: attenuation of the excitation beam is more effective in the center of the section when the incident light propagates along a larger distance within the tendon. However, the  $x$ - and  $y$ -polarized SHG transverse profiles exhibit different behaviour as a function of the depth from the tendon upper surface. In fig. 4.a and b, the  $x$ -polarized SHG image is more attenuated than the  $y$ -polarized SHG image at the tendon center, whereas it is not the case in fig. 4.c and d. Moreover, the  $x$ -polarized SHG image at  $57\mu\text{m}$  (fig. 4.c) displays more signal at the center than at intermediate positions along the transverse profile. This complex behaviour is characteristic for birefringence effects. The  $x$  and  $y$  components of the  $\pi/4$ -polarized incident beam experience different optical indices when propagating within the tendon and accumulate a relative phase shift. The tensorial components of the nonlinear response excited by the  $x$  and  $y$  components of the  $\pi/4$ -polarized incident beam then interfere in a constructive or destructive

way, depending on the propagation distance within the tendon. It results in interference fringes in the depth profile of the SHG signal for incident excitation mixing up  $x$  and  $y$ -polarization components. These fringes appear only in  $x$ -polarized SHG images because they result from the coherent summation of two tensorial components excited along  $x$  and  $y$  polarizations respectively (see eq. 2). Conversely,  $y$ -polarized SHG images are not sensitive to birefringence because they probe only one tensorial component.

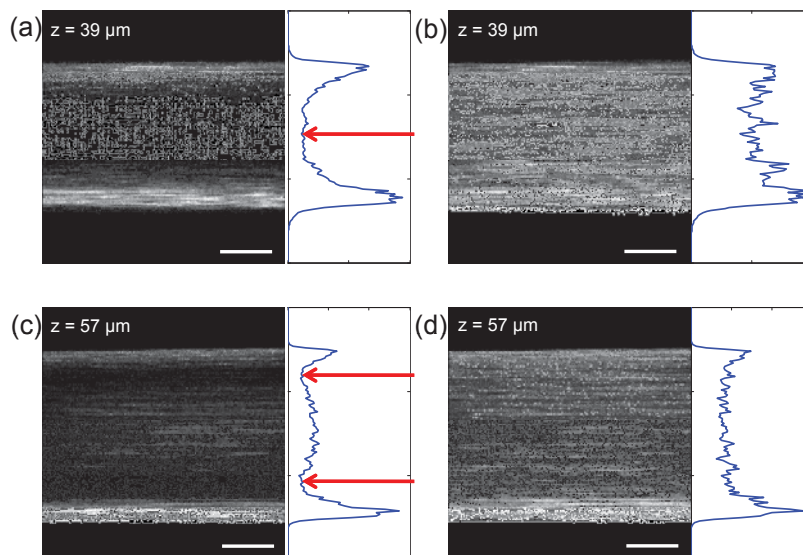


Fig. 4. Polarization-resolved SH images of a tendon upon excitation polarized at  $\pi/4$  from the tendon axis. (a)-(c)  $x$ - and (b)-(d)  $y$ -polarized SH images and transverse profiles of a tendon aligned along  $x$  axis at (a)-(b)  $39 \mu\text{m}$  depth and (c)-(d) at  $57 \mu\text{m}$  depth from the tendon upper surface.  $x$ -polarisation images shows dark fringes (red arrows), whereas  $y$ -polarisation has almost uniform intensity profile in the tendon center. Scale bar:  $50 \mu\text{m}$ .

To get a better insight into the physics of polarization-resolved SHG images, we carried out SHG experiments at increasing depth within the tendon. Fig. 5.a and b display typical  $x$ - and  $y$ -polarized SHG signals in  $28 \times 20 \mu\text{m}$  regions of interest such as the one depicted in fig. 1.a. The depth profile of the 2PEF signal from the latex beads is also displayed in fig. 5.c. It enables the location of the tendon surface  $z_0$  that corresponds to the maximum of the 2PEF peak. The specific patterns observed in the SHG images were consistently observed in all our samples provided that the ellipticity of the incident polarization was negligible. Practically, experiments performed without a linear polarizer at the back pupil of the objective lens exhibited a non symmetrical pattern relative to the tendon axis ( $\alpha = 0$ ).

Fig. 5.f displays  $z$ -profiles of the  $x$ -polarized SHG signal for various incident polarization angles. Interference fringes characteristic for birefringence in the excitation propagation are clearly observed for an incident polarization at  $\pi/4$  angle to the tendon axis. The distance between the two maxima is  $\delta z \approx 47 \mu\text{m}$ . In a first approximation, it is related to the birefringence phase shift by  $\Delta n = \lambda/2\delta z$ . It gives:  $\Delta n \approx 0.008$  (after index mismatch correction), in qualitative agreement with reported birefringence in tendon [20, 21]. It will be determined more precisely later on. Diattenuation of the laser excitation is suggested by the  $z$ -profiles of the  $x$ -polarized SHG signal at  $0$  and  $\pi/2$  angles. Exponential fitting gives the following attenuation

lengths for  $x$  and  $y$  incident polarizations :  $l_a^e = 91\mu\text{m}$  and  $l_a^o = 190\mu\text{m}$  (see fig. 6.a).

Finally, fig. 5.d and e display  $I_x^{2\omega}$  and  $I_y^{2\omega}$  at the surface of the tendon ( $z = z_0$ ) where birefringence and diattenuation effects do not apply. We therefore fit our data using eq. 9 that accounts only for polarization cross-talk due to light scattering (or equivalently, using eq. 12 with  $z = 0$  and  $\Delta\phi = 0$ ). We observe that the experimental data are better fitted using eq. 9 than in the simplified approach (eq. 3). It shows that polarization cross-talk due to light scattering significantly distorts the polarization pattern at the tendon surface.

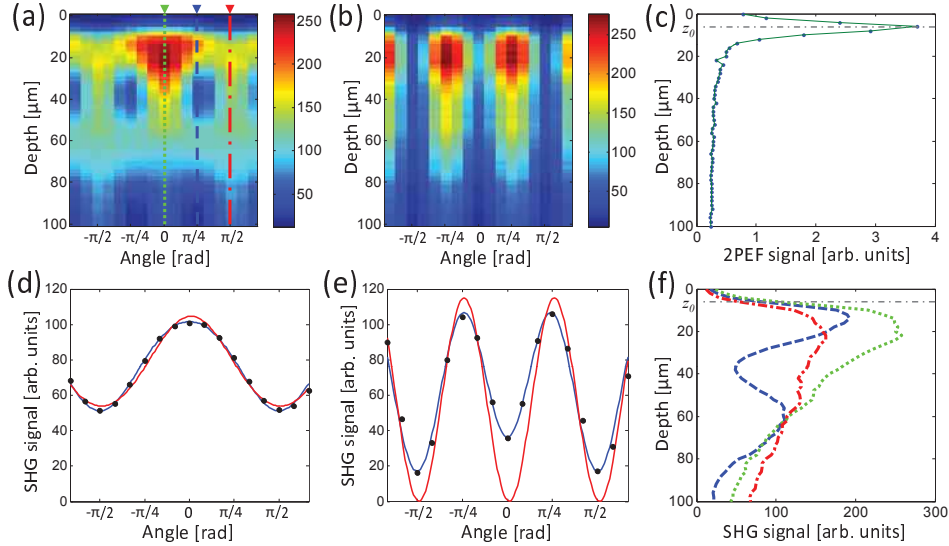


Fig. 5. Experimental polarization-resolved SH intensity from a tendon. (a)  $I_x^{2\omega}$  and (b)  $I_y^{2\omega}$  as a function of incident polarisation angle  $\alpha$  (see fig. 1) and lens displacement. (c)  $z$ -profile of fluorescence signal from latex beads, peaking at the tendon surface  $z_0$ . (d)  $I_x^{2\omega}(\alpha)$  and (e)  $I_y^{2\omega}(\alpha)$  at the tendon surface (black dots), along with fits using the simplified approach (eq. 3, red line) or accounting for polarization cross-talk (eq. 9, blue line). (f) experimental  $z$ -profiles of  $I_x^{2\omega}$  for  $\alpha = 0$  (green dotted line),  $\alpha = \pi/4$  (blue dashed line) and  $\alpha = \pi/2$  (red dash-dot line).

Altogether, these experimental observations show that the usual approach with eq. 3 does not satisfactorily account for polarization-resolved SHG imaging in thick tendons. Birefringence, diattenuation and polarization cross-talk due to scattering must all be taken into account to explain experimental data. Accordingly, we used eq. 4 with parameters  $A_{eff}$ ,  $B_{eff}$  and  $C_{eff}$  to fit our data. Note that we introduced an angular shift  $\alpha_0$  to account for possible slight misalignment of the tendon axis from  $x$  direction ( $-2^\circ < \alpha_0 < 2^\circ$  for all our data). We then calculated  $\rho e^{\frac{\Delta\phi}{\Delta a}}$  by use of eq. 13. This value was subsequently corrected for diattenuation using  $l_a^e = 91\mu\text{m}$  and  $l_a^o = 190\mu\text{m}$  obtained from exponential fitting of  $I_x^{2\omega}(\alpha = 0)$  and  $I_x^{2\omega}(\alpha = \pi/2)$ . Both the raw and corrected values of  $\rho$  are depicted in fig. 6.b. Diattenuation correction successfully removes the artifactual variation of  $\rho$  with depth and enables the reliable determination of this parameter:  $\rho = 1.40 \pm 0.03$ . Moreover, as already stated, this approach is applicable to any attenuation profile  $f_a(z)$ . To fully characterize the optical response of our sample, we also calculated the parameter  $\Delta(z)$  from eq. 14a and plotted its depth profile in fig. 6.c. Eq. 14b shows that the values at the maxima ( $\Delta\phi = 2\pi k$  with  $k$  integer) reduce to  $\eta_{xy}$ . The first maximum is obtained at the tendon surface:  $\eta_{xy} = 0.13$ . The second maximum is zero which shows that

$e^{\frac{-z}{l_a}} \eta_{xy}$  is negligible  $\approx 60\mu\text{m}$  deep within the tendon. We then consider that  $\eta_{xy}$  diminishes exponentially from 0.13 to 0 within the first  $40\mu\text{m}$  from the surface and we get  $\Delta n = 0.0066$  by fitting our data using eq. 14b ( $\Delta n = 0.0074$  without any index mismatch correction).

Finally, to verify the consistency of our data processing, let's compare our experimental data (fig. 5.a and b) to the simulations using our experimentally determined parameters for birefringence, diattenuation and polarization cross-talk (fig. 3.e and j). The theoretical and experimental intensity maps are in excellent agreement which proves that our theoretical approach satisfactorily reproduces polarization-resolved SHG experiments in tendons.

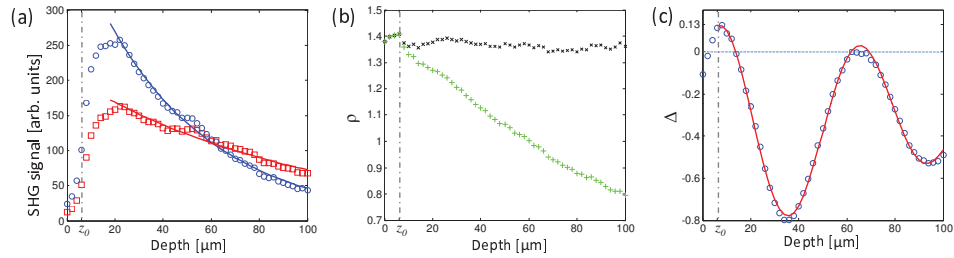


Fig. 6. Determination of tendon characteristic parameters from experimental SH depth-profiles. (a)  $I_x^{2\omega}(\alpha=0)$  (blue dots) and  $I_x^{2\omega}(\alpha=\pi/2)$  (red squares) showing diattenuation: the solid lines correspond to exponential fitting with  $l_a^e = 91\mu\text{m}$  and  $l_a^o = 190\mu\text{m}$ . (b)  $\rho$  determined from polarization-resolved SHG measurements with (black) and without (green) correction for diattenuation. (c)  $\Delta$  parameter evidencing birefringence (oscillations), polarization cross-talk due to scattering (non-vanishing value at the tendon surface) and diattenuation (exponential attenuation with depth). The solid line represents fitting with the following parameters:  $\Delta n = 1.40$ ,  $\eta_{xy} = 0.13$  near the surface and  $\Delta l_a = 134\mu\text{m}$ .

## 5. Discussion

In this paper, we developed a method to account for linear propagation effects affecting the polarization when determining  $\rho$  by polarization-resolved SHG experiments. Previous works studied the effects of diattenuation [15] and birefringence [10, 16] separately, but they did not propose an approach accounting for both effects and enabling the determination of  $\rho$  at any depth. Our model considers birefringence and diattenuation along the excitation beam propagation and polarization cross-talk due to scattering of the SHG signal. Our experimental results show that this model perfectly fits our data on rat-tail tendons and enables the reliable determination of  $\rho$ . We also observed interference fringes in the SHG depth profiles which show unambiguously that birefringence affects polarization-resolved SHG microscopy. Our model may be refined by numerical simulations of the field distribution within the focal volume using a vectorial approach to properly describe the polarizations [22]. Such a calculation would account for polarization mixing through the high numerical aperture objective lens [22, 23] and for deformation of the focal volume due to birefringence. The description of the polarization may also be further refined by using Mueller matrices and tracking Stokes vectors through the tendon [24]. The advantage of our model however is to include all the characteristic features of the biological sample in a phenomenological approach, including light scattering or depolarization. It presumably explains why it shows an excellent agreement with our experimental data and proves relevant to determine optical parameters of rat-tail tendon.

Our data gives insight into both the linear and nonlinear optical response of the tendon. It first enables the determination of the tendon birefringence at the excitation wavelength. We obtain  $\Delta n = 6.6 \cdot 10^{-3}$  in good agreement with recently reported values measured in a more

direct way using Optical Coherence Tomography (OCT) ( $\Delta n = 5.3 \cdot 10^{-3}$ ) [20, 21]. We also measure the diattenuation at  $860\text{nm}$ ,  $\Delta l_a = 175\mu\text{m}$ , and the polarization cross-talk due to scattering,  $\eta_{xy} = 13\%$ . Our measured values seem reasonable considering usual optical properties in biological tissues. Previous work also reported polarization scrambling in tendon that could be reduced by optical clearing [17]. Our phenomenological parameter  $\eta_{xy} = 13\%$  amounts to an average SHG polarization rotation of about  $20^\circ$ . It shows that the SHG polarization is reasonably well preserved in the forward direction although propagation to the detector takes place over several scattering lengths. Indeed, forward detection picks up mainly quasi-ballistic photons and the polarization of these photons is not strongly modified. Similarly, the measured attenuation lengths ( $l_a^e = 91\mu\text{m}$  and  $l_a^o = 190\mu\text{m}$ ) are in good agreement with our previous measurements in rat-artery [26] and the diattenuation shows qualitative agreement with previously reported measurements in rat-tail tendon using OCT ( $\Delta l_a = 125\mu\text{m}$  [20, 21]) or in horse flexor tendon using SHG microscopy ( $\Delta l_a = 480\mu\text{m}$  [15]). Note that the precise determination of these parameters depends on the tendon index considered for index mismatch correction. Finally, as intended from these polarization-resolved SHG experiments, they determine the ratio  $\rho$  of the two main tensorial components of the tendon second-order susceptibility. We obtain  $\rho = 1.40 \pm 0.03$  from the experimental data displayed in fig. 5. Similar values in the range 1.3 to 1.5 were consistently obtained in all our samples. The reproducibility of these measurements is excellent considering the dispersion of tissue properties in biological samples. Slight differences from one tendon to the other may moreover be attributed to differences in the tendon preparation, particularly in the tendon stretching, that could affect the 3D distribution of fibrils at a submicrometric scale.

Most importantly, our measurements show that the raw value of  $\rho$  varies a lot with depth as depicted in fig. 6.b. It decreases from 1.40 at the surface of the tendon to 0.8 at  $\approx 90\mu\text{m}$  depth within the tendon. These data proves that correction for diattenuation is essential for reliable measurements of  $\rho$  in thick anisotropic tissues and that our model provides an efficient correction along the full stack of data. We expect that the determination of  $\rho$  deeper in the tissue would be hampered because of the low signal to noise ratio. When possible, the most reliable method is to perform polarization-resolved measurements at the sample surface to get rid of diattenuation and birefringence effects.

Finally, note that this method is also applicable to epidetected SHG signals. In that configuration, the infrared polarizer set before the half waveplate at the back pupil of the objective has to be replaced by a quarter waveplate set at a suitable angle to correct for incident ellipticity without rejecting some epi-SHG signal (see fig. 1.a). Polarization analysis of this epidetected SHG signal is a complex task because of the presence of the waveplates. Furthermore, backward-detected SHG is highly affected by scattering and related polarization distortion [25, 17]. However, SHG polarization analysis was required here for properly characterizing the different linear optical effects that may affect the determination of  $\rho$ . Once this study is completed, the total SHG intensity can be fitted like the  $x$ -polarized component as a sum of  $\cos 2n\alpha$  functions, using an expression similar to eq. 12. Favourably, this configuration does not require the alignment of the tendon axis relative to polarization analysis.

## 6. Conclusion

In this paper, we combined model calculation and experiments in rat-tail tendon to characterize linear optical effects that affect the polarization in polarization-resolved SHG experiments. We evidenced that birefringence, diattenuation and polarization scrambling upon scattering significantly distort the SHG response for tunable incident linear polarizations. In particular, birefringence results in interference fringes in the depth profile of the SHG signal excited with polarization at  $\pi/4$  angle from the tendon axis. Most importantly, diattenuation results in an ar-

tifactual decrease of  $\rho$  with the depth within the tendon. To address these problems, we derived a method to process polarization-resolved SHG data and we successfully retrieved relevant optical parameters in rat-tail tendon. This method is applicable to any anisotropic sample that exhibits SHG signals, including other collagenous tissues and presumably skeletal muscles. It may also be generalized to other nonlinear optical processes, that is 2PEF, THG, CARS or SRS polarization-resolved microscopies. Altogether, our work proves unambiguously that uncorrecting for polarization distortion results in misleading determination of the tensorial nonlinear response in anisotropic thick tissues.

### **Acknowledgements**

We gratefully acknowledge G. Liot from Institut Curie, Université Paris XI, for providing us with the rat-tails, X. Solinas and J.-M. Sintès for technical implementation of the setup, A. de Martino, E. Beaurepaire and D. Débarre for fruitful discussions, and F. Hache for critical reading of this manuscript. G. Latour was supported by RTRA-Triangle de la Physique.

## 3.3 Numerical simulations

### Introduction

This section is devoted to numerical simulations of SHG by a strongly focused beam in collagenous tissues. This quantitative analysis is intended to extend the phenomenological model described in the previous section of this chapter. Although the latter is robust, simple and accounts for all observed artefactual processes, it has the drawback to of being deduced for a scalar field, i.e. for low numerical aperture. However, SHG microscopy usually relies on strongly focused beams to provide decent axial resolution. Hence, the case of high numerical aperture (NA 0.95) should be explicitly treated in a numerical model to study the influence it could have on the interpretation of P-SHG signal.

The section is organized as follows. First, we give an overview of main stages of simulation and describe the geometry for which the simulation is performed. Second part is devoted to the numerical simulation of beam focal field in a birefringent medium which emulates the tendon. This part deals with the theoretical derivation of the calculation, which is followed by numerical results, and algorithmic issues are presented in the Appendix. The third part is devoted to the simulation of dipole radiation in a birefringent medium and has similar internal organization. Finally, the fourth part presents the results for the SHG simulation in cornea.

#### 3.3.1 Overview of SHG simulation in tendon

Apart from the SHG anisotropy, our experimental polarimetric results reveal three main effects which influence polarization diagrams in rat-tail tendons. They are birefringence, diattenuation that is mainly due to scattering, and polarization cross-talk that is also governed by anisotropic scattering. The latter two processes involving scattering should be treated using appropriate statistical methods [127–130]. On the contrary, the light propagation in birefringent medium without scattering is purely deterministic and its calculation is more straightforward. In this work, we restrain numerical simulations to the case of non-scattering medium.

This simulation aims to reproduce the experimental results obtained in the previous section. Thus, we will calculate the diagrams for the radiated SHG intensity as a function of the angle  $\alpha$  of incident linear polarization and the imaging depth in tendon, which will be determined by the  $z$ -position of the objective  $z_{obj}$ . The general scheme of calculation is displayed in Fig. 3.2. As a starting point for the simulation, we take the field distribution on the back pupil of the objective. Then, for a fixed  $z_{obj}$  we simulate propagation from the objective to the interface between water and tendon by the angular spectrum method

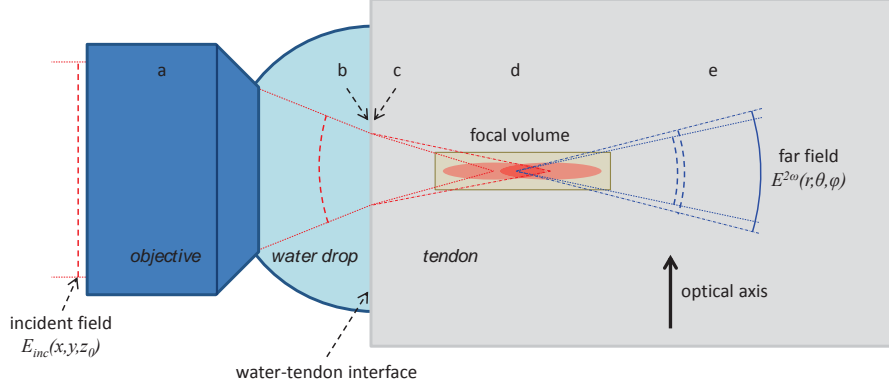


Figure 3.2: Scheme of SHG calculation in a birefringent tendon. (a) Plane incident wave is mapped onto a converging spherical wave by a model objective lens. (b) Field distribution just before the water-tendon interface is calculated using angular spectrum method [131]. (c) Field beyond the interface is obtained using appropriate boundary conditions based on [132]. (d) Focal field in birefringent medium (tendon) is calculated using model described in [132]. (e) Radiation in birefringent medium is calculated based on [133, 134].

[131]. After that, boundary conditions are used to obtain the field in the tendon near the surface. The focal field distribution is then calculated by a method similar to that of [131] which uses different field propagators for ordinary and extraordinary waves [132]. The obtained field distribution near the focal volume is used to calculate the induced nonlinear polarization. Finally, the SH radiation in the birefringent medium is calculated using Clemmow scaling method [133, 134]. This whole procedure is performed for all  $z_{obj}$ , and the diagrams  $I_{\alpha,z}$  are produced.

### 3.3.2 Focal field calculation in birefringent media

#### 3.3.2.1 Field propagation in a uniform medium. Angular spectrum representation.

To get the field distribution in the beam focused by an objective one can use angular spectrum representation, which is described in chapter 3 of [131]. Central result of that chapter is that the field  $\mathbf{E}$  near the beam focus can be expressed through the far-field  $\mathbf{E}_\infty$  at a reference sphere of radius  $f$  (focal distance of the objective) centred at  $z = 0$

$$\mathbf{E}(x, y, z) = \frac{ir e^{-ikr}}{2\pi} \iint_{(k_x^2 + k_y^2) \leq k^2} \mathbf{E}_\infty(k_x, k_y) e^{i[k_x x + k_y y + k_z z]} \frac{1}{k_z} dk_x dk_y. \quad (3.2)$$

Here,  $k_z(k_x, k_y) = \sqrt{k^2 - k_x^2 - k_y^2}$  is the longitudinal component of wave vector, and  $r = \sqrt{x^2 + y^2 + z^2}$ . The integral is calculated over a circle of radius  $k$ , since we ne-

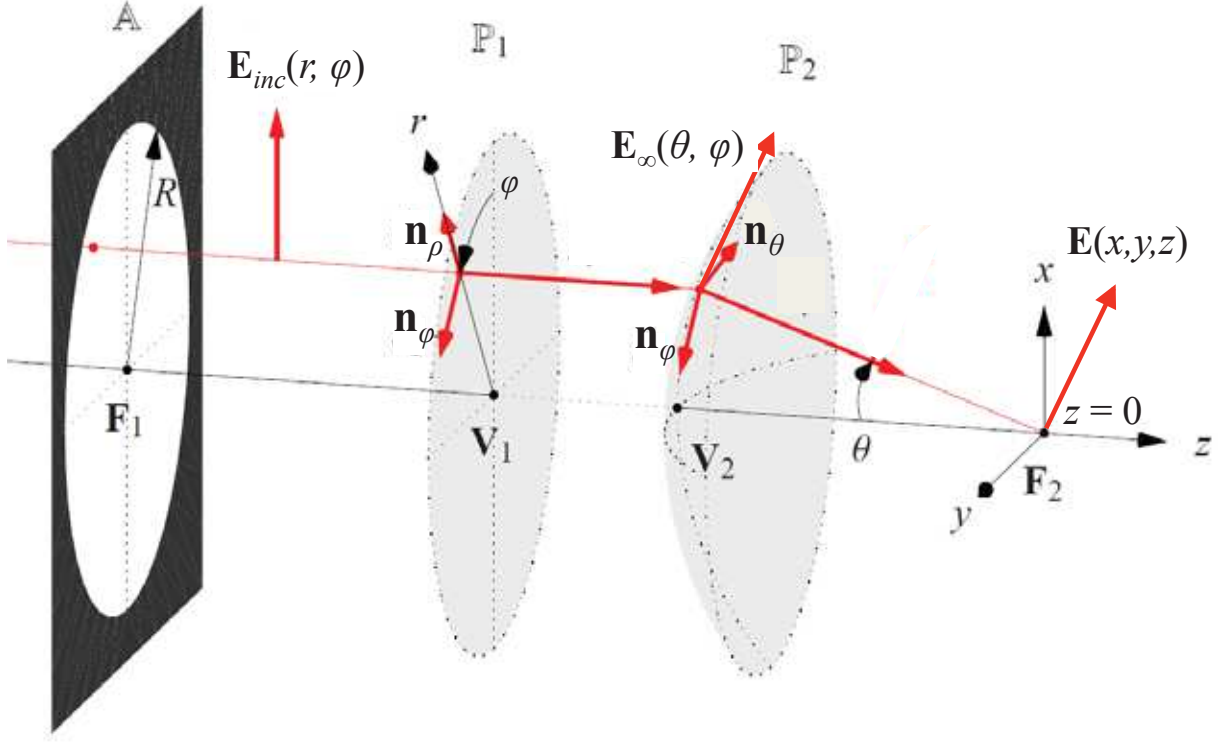


Figure 3.3: Scheme of focal field calculation by angular representation method.  $\mathbf{n}_\varphi$  and  $\mathbf{n}_\rho$  unit vectors are mapped onto  $\mathbf{n}_\varphi$  and  $\mathbf{n}_\theta$ .  $\mathbb{A}$  is the back pupil,  $\mathbb{P}_1$  and  $\mathbb{P}_2$  are the principal planes of the objective. The beam is focused into the point  $F_2 = (0, 0, 0)$ . Adapted from [135].

glect evanescent waves with imaginary  $k_z$ . Moreover, for a real lens the solid angle of illumination is always smaller than  $2\pi$ , and we replace  $k$  by  $k_{max} = k \frac{NA}{n}$ .

The far-field  $\mathbf{E}_\infty$  is obtained from the incident field  $\mathbf{E}_{inc}$  using a model lens, which transforms a plane wave into a spherical wave converging to  $z = 0$ , which is the focal point.

$$\mathbf{E}_\infty = \left[ t^s [\mathbf{E}_{inc} \cdot \mathbf{n}_\varphi] \mathbf{n}_\varphi + t^p [\mathbf{E}_{inc} \cdot \mathbf{n}_\rho] \mathbf{n}_\theta \right] \sqrt{\frac{n_1}{n_2} \cos \theta} \quad (3.3)$$

Here,  $\mathbf{n}_\varphi$ - and  $\mathbf{n}_\rho$ -projections of the incident field in cylindrical coordinate system are mapped onto  $\mathbf{n}_\varphi$ - and  $\mathbf{n}_\theta$ -components in spherical system for converging wave. The factor  $\sqrt{\frac{n_1}{n_2} \cos \theta}$  ensures energy flux conservation.  $t^s$  and  $t^p$  are Fresnel transmission coefficients. The scheme illustrating this mapping is displayed in the Fig. 3.3

We suppose that our incident beam is linearly polarized in  $xy$  plane with  $\alpha$  angle to  $x$  axis, and collimated at the rear principal plane  $\mathbb{P}_1$ . Its intensity profile is Gaussian with waist  $w_0$ . While choosing  $w_0$ , one should make a trade-off between high resolution (efficiently filled back aperture for large  $w_0$ ) and tolerable energy loss on the back aperture  $\mathbb{A}$  (small  $w_0$ ). Typically,  $w_0$  is comparable to the aperture radius [131]. Moreover, we

suppose the lens to be optically cleared, which means that Fresnel coefficients  $t^s$  and  $t^p$  are equal to 1. Finally, one can deduce the expression for  $\mathbf{E}_\infty$  as a function of  $\theta$  and  $\varphi$ :

$$\begin{aligned}
E_\infty^x(\theta, \varphi) &= E_0 e^{-\frac{f^2 \sin^2 \theta}{w_0^2}} \left( [1 - \cos^2 \varphi (1 - \cos \theta)] \cos \alpha + \cos \varphi \sin \varphi (\cos \theta - 1) \sin \alpha \right) \sqrt{\frac{n_1}{n_2} \cos \theta} \\
E_\infty^y(\theta, \varphi) &= E_0 e^{-\frac{f^2 \sin^2 \theta}{w_0^2}} \left( \cos \varphi \sin \varphi (\cos \theta - 1) \cos \alpha + [1 - \sin^2 \varphi (1 - \cos \theta)] \sin \alpha \right) \sqrt{\frac{n_1}{n_2} \cos \theta} \\
E_\infty^z(\theta, \varphi) &= -E_0 e^{-\frac{f^2 \sin^2 \theta}{w_0^2}} (\cos \varphi \sin \theta \cos \alpha + \sin \varphi \sin \theta \sin \alpha) \sqrt{\frac{n_1}{n_2} \cos \theta}.
\end{aligned} \tag{3.4}$$

After expressing  $\theta$  and  $\varphi$  via  $k_x$  and  $k_y$ , one can calculate  $\mathbf{E}$  by introducing the equations 3.4 into Eq. 3.2.

### 3.3.2.2 Field in a birefringent medium

After propagation from the objective through the immersion medium, the beam strikes the interface with the tendon and further propagates through it. We model the tendon as a uniaxial birefringent medium, so there will be an ordinary and an extraordinary wave propagating through the tissue. To model the light propagation in birefringent medium we follow the formalism proposed by Hacyan and Jáuregui [132], which is described below with small modifications relevant to our implementation.

The Maxwell equations in the absence of free charges and currents are

$$\begin{aligned}
\nabla \cdot \mathbf{B} &= 0, & \nabla \times \mathbf{E} + \frac{\partial \mathbf{B}}{\partial t} &= 0, \\
\nabla \cdot \mathbf{D} &= 0, & \nabla \times \mathbf{H} - \frac{\partial \mathbf{D}}{\partial t} &= 0,
\end{aligned} \tag{3.5}$$

where  $\mathbf{D} = \hat{\epsilon} \cdot \mathbf{E}$  and  $\mathbf{B} = \mu \mathbf{H}$ . For a birefringent medium, the linear susceptibility writes:

$$\hat{\epsilon} = \epsilon_\perp \mathbf{1} + (\epsilon_\parallel - \epsilon_\perp) \mathbf{s} \mathbf{s}, \tag{3.6}$$

where  $\mathbf{s}$  is a unitary vector along the optical axis of the medium, and  $\epsilon_\parallel$  and  $\epsilon_\perp$  are permittivities parallel and perpendicular to the axis, respectively. One can show that solutions for Maxwell equations 3.5 for ordinary and extraordinary monochromatic waves are

$$\mathbf{E}^o = -i\omega \mathbf{s} \times \nabla \psi^o, \quad \mathbf{E}^e = -\frac{1}{\epsilon_\perp} \nabla (\mathbf{s} \cdot \nabla \psi^e) - \mu \omega^2 \psi^e \mathbf{s}, \tag{3.7}$$

where  $\psi^o$  and  $\psi^e$  are Hertz potentials meeting the two equations:

$$\begin{aligned}\epsilon_{\perp}\mu\omega^2\psi^o + \nabla^2\psi^o &= 0, \\ \epsilon_{\perp}\epsilon_{\parallel}\mu\omega^2\psi^e + \nabla \cdot \hat{\epsilon} \cdot \nabla\psi^e &= 0.\end{aligned}\tag{3.8}$$

The general solutions of 3.8 for  $z > 0$  are

$$\psi^{(o,e)}(x, y, z) = \frac{1}{2\pi} \int \int dk_x dk_y e^{ik_x x + ik_y y + ik_z^{(o,e)} z} \tilde{\psi}^{(o,e)}(k_x, k_y),\tag{3.9}$$

where  $\tilde{\psi}^{(o,e)}(k_x, k_y)$  is the Fourier transform of  $\psi^{(o,e)}(x, y, z=0)$  (for example, near the interface with another medium).  $k_z^{(o,e)}$  in the expression above are solutions to the following equations:

$$\begin{aligned}\epsilon_{\perp}\mu\omega^2 - \mathbf{k}^o \cdot \mathbf{k}^o &= 0 \\ \epsilon_{\perp}\epsilon_{\parallel}\mu\omega^2 - \mathbf{k}^e \cdot \hat{\epsilon} \cdot \mathbf{k}^e &= 0.\end{aligned}\tag{3.10}$$

Although  $\tilde{\psi}^{(o,e)}(k_x, k_y; z) = \tilde{\psi}^{(o,e)}(k_x, k_y) e^{ik_z^{(o,e)} z}$  is not a 3D Fourier transform, its dependence on  $z$  allows for manipulating it like if it were. Essentially, it means that we can substitute  $z$  derivative in  $(x, y, z)$ -space by a factor  $ik_z$  in  $(k_x, k_y; z)$ -space. Indeed,

$$\begin{aligned}\mathcal{F}\left[\frac{\partial\psi}{\partial z}\right](k_x, k_y; z) &= \frac{1}{2\pi} \iint e^{-ik_x x - ik_y y} \left( \frac{1}{2\pi} \iint ik_z e^{ik'_x x + ik'_y y + ik_z z} \tilde{\psi}(k'_x, k'_y) dk'_x dk'_y \right) dx dy \\ &= \iint ik_z(k'_x, k'_y) \tilde{\psi}(k'_x, k'_y) e^{ik_z(k'_x, k'_y) z} \delta(k_x - k'_x) \delta(k_y - k'_y) dk'_x dk'_y \\ &= ik_z \tilde{\psi}(k_x, k_y) e^{ik_z z} = ik_z \tilde{\psi}(k_x, k_y; z).\end{aligned}\tag{3.11}$$

One can thus rewrite 3.7 in the form

$$\tilde{\mathbf{E}}^o = \omega \mathbf{s} \times \mathbf{k}^o \tilde{\psi}^o(\mathbf{k}^o), \quad \tilde{\mathbf{E}}^e = \left[ \frac{1}{\epsilon_{\perp}} (\mathbf{s} \cdot \mathbf{k}^e) \mathbf{k}^e - \mu\omega^2 \mathbf{s} \right] \tilde{\psi}^e(\mathbf{k}^e).\tag{3.12}$$

Focal fields  $\mathbf{E}^o$  and  $\mathbf{E}^e$  are obtained from  $\tilde{\psi}^{(o,e)}(k_x, k_y; z)$  using 3.12 and subsequent Fourier Transform. The total field  $\mathbf{E}$  in the medium is:

$$\mathbf{E} = \mathbf{E}^o + \mathbf{E}^e = (E_x^e; E_y^e + E_y^o; E_z^o + E_z^e) = (E_x; E_y; E_z).\tag{3.13}$$

By definition, there is no ordinary wave component  $E_x^o$  along the optical axis.

If we consider an  $x$ -polarized planar wave incident on a birefringent medium with optical axis  $x$ , it will obviously create only an extraordinary wave in the medium. Identically, the  $y$ -polarized one will only create an ordinary wave. However, in the case of tight focus-

ing discussed in this section, a wave with any polarization incident on a high-NA objective will produce all the five components from the Eq. 3.13, both ordinary and extraordinary ones, and along  $x$ ,  $y$  and  $z$ .

Due to linearity of Maxwell equations, the field  $\mathbf{E}_{1+2}$  created by the sum of two incident fields  $\mathbf{E}_{inc,1} + \mathbf{E}_{inc,2}$  is equal to the sum of fields  $\mathbf{E}_1$  and  $\mathbf{E}_2$  created independently by  $\mathbf{E}_{inc,1}$  and  $\mathbf{E}_{inc,2}$ . It allows us to choose two basis incident fields  $\mathbf{E}_{inc,1,2}$  and to calculate  $\mathbf{E}_{1,2}$ , which can be used to reproduce focal field from any incident polarization. To simplify the calculations, we choose

$$\mathbf{E}_{inc,1} = \mathbf{E}_{inc,\parallel} = E_0 \mathbf{e}_x \quad (3.14)$$

$$\mathbf{E}_{inc,2} = \mathbf{E}_{inc,\perp} = E_0 \mathbf{e}_y \quad (3.15)$$

and we will use  $E_{i,\parallel,\perp}$  to denote field components produced by  $\mathbf{E}_{inc,\parallel,\perp}$ . Should it be emphasized that all these components, except for  $E_{x\parallel}$ , have both ordinary and extraordinary components, as seen from the Eq. 3.13. Notably, for an incident field polarized at angle  $\alpha$  to the  $x$ -axis, the focal field writes

$$\mathbf{E}_\alpha = (E_{x\parallel} \cos \alpha + E_{x\perp} \sin \alpha, E_{y\parallel} \cos \alpha + E_{y\perp} \sin \alpha, E_{z\parallel} \cos \alpha + E_{z\perp} \sin \alpha) \quad (3.16)$$

where

$$\begin{aligned} E_{x\parallel,\perp} &= E_{x\parallel,\perp}^e \\ E_{y\parallel,\perp} &= E_{y\parallel,\perp}^o + E_{y\parallel,\perp}^e \\ E_{z\parallel,\perp} &= E_{z\parallel,\perp}^o + E_{z\parallel,\perp}^e \end{aligned} \quad (3.17)$$

It means that we have to calculate 10 field distributions. However, it is expected that  $E_{y\perp}^o$  and  $E_{x\parallel}^e$  are much larger than all other components, so the fields produced by  $\mathbf{E}_{inc,\parallel}$  and  $\mathbf{E}_{inc,\perp}$  are "mostly" ordinary and extraordinary.

### 3.3.2.3 Boundary conditions between isotropic and birefringent media

As seen from the Eq. 3.9, the calculation of  $\psi^{o,e}(x, y, z)$  and therefore of  $\mathbf{E}^{o,e}$  requires the values of  $\psi^{o,e}(x, y, z = 0)$  near the interface between the birefringent medium (tendon) and the isotropic medium (immersion, water). These values must be obtained from the incident field using appropriate boundary conditions between two media. From the work of Hacyan and Jáuregui [132] we also deduce boundary conditions for ordinary and extraordinary Hertz potentials. For an interface between a uniform medium with permittivity  $\epsilon_1$  and birefringent medium with permittivity tensor defined in the Eq. 3.6 one

obtains

$$\begin{aligned}\tilde{\psi}^o &= 2 \frac{[\mathbf{e}_z \times (\mathbf{Q} + \mathbf{S})] \cdot \tilde{\mathbf{E}}^{\mathbf{I}}}{(\mathbf{Q} + \mathbf{S}) \cdot [(\mathbf{P} + \mathbf{R}) \times \mathbf{e}_z]}, \\ \tilde{\psi}^e &= -2 \frac{[\mathbf{e}_z \times (\mathbf{P} + \mathbf{R})] \cdot \tilde{\mathbf{E}}^{\mathbf{I}}}{(\mathbf{Q} + \mathbf{S}) \cdot [(\mathbf{P} + \mathbf{R}) \times \mathbf{e}_z]}\end{aligned}\quad (3.18)$$

where

$$\begin{aligned}\mathbf{P} &= \omega(\mathbf{s} \times \mathbf{k}^o)_\perp, \quad \mathbf{Q} = \epsilon_\perp^{-1}(\mathbf{s} \cdot \mathbf{k}^e)\mathbf{k}_\perp - \mu\omega^2\mathbf{s}_\perp \\ \mathbf{R} &= \frac{\omega}{\mu k_z}[(\mathbf{s} \cdot \mathbf{k}^o)\mathbf{e}_z \times \mathbf{k}_\perp] - \frac{\epsilon_\perp \omega^3}{k_z}[\mathbf{e}_z \times \mathbf{s}] + \frac{\epsilon_\perp}{\epsilon_1 k_z}(\mathbf{e}_z \cdot [\mathbf{s} \times \mathbf{k}_\perp])\mathbf{k}_\perp, \\ \mathbf{S} &= \frac{\omega^2}{k_z}(s_z \mathbf{k}_\perp - k_z^e \mathbf{s}_\perp) + \frac{1}{\epsilon_1 k_z}[(\mathbf{s} \cdot \mathbf{k}_\perp k_z^e) - s_z k_\perp^2]\mathbf{k}_\perp,\end{aligned}\quad (3.19)$$

where  $\tilde{\mathbf{E}}^{\mathbf{I}}$  is the Fourier transform of the incident field  $\mathbf{E}^{\mathbf{I}}$ .

The implementation of these numerical calculations is presented in the Appendix.

### 3.3.2.4 Results and discussion

In 3D SHG microscopy, the  $z$ -position of the imaged slab usually refers to the  $z$  coordinate of the objective. However, the objective displacement  $\Delta z_{\text{obj}}$  and the resulting displacement of the focal point in the sample  $\Delta z_{\text{sample}}$  are generally not equal. Their difference depends on the index mismatch between the immersion medium, for which the objective is designed (water,  $n_{\text{water}=1.33}$ ) and the sample  $n_{\text{sample}}$ . In paraxial approximation,  $\Delta z_{\text{sample}} = \Delta z_{\text{obj}} \frac{n_{\text{sample}}}{n_{\text{water}}}$ , so they are equal when the indices are matched. In the following, for the sake of simplicity, we will write that the beam is focused at  $Z \mu\text{m}$  if  $z_{\text{obj}} = Z \mu\text{m}$ , and  $z_{\text{obj}} = 0$  corresponds to a beam focused at the water-tendon interface.

**Intensity distribution** The calculated beam intensity distribution for two tendon indices ( $n^o = 1.33$  and  $n^o = 1.5$ ) and for two incident linear polarization (parallel and perpendicular to the tendon axis) is shown in the Fig. 3.4. The index  $n^o = 1.33$  is chosen to provide a case of index-matched propagation, while index  $n^o = 1.5$  corresponds to values reported for tendon [136]. As explained previously, we use notations  $E_{i,\parallel,\perp}$  for focal field components resulting from the incident field  $E_{\text{inc},\parallel,\perp}$ . Intensities are calculated for objective position  $z_{\text{obj}} = 50 \mu\text{m}$ . Birefringence is set to  $\Delta n = n^e - n^o = 0.007$ , as reported for tendon in the previous section and in [136, 137]. Within each of two sets with different  $n^o$ , intensities are normalized to the maximal intensity of the field  $E_{x\perp}$ . Intensities for  $n^o = 1.33$  are larger than those for  $n^o = 1.5$  by factor of 1.441. Indeed, the focal volume is deteriorated for  $n^o = 1.5$  due to spherical aberrations, which result in a larger FWHM.

As in both cases the total beam energy flux is the same, larger FWHM for  $n^o = 1.5$  leads to smaller intensity.

The largest components produced by  $E_{\text{inc},\parallel}$  and  $E_{\text{inc},\perp}$  are  $E_{x\parallel}$  and  $E_{y\perp}$ , as expected (Fig. 3.4 (a, d) and (h, k)). The intensity of  $z$ -polarized fields attains up to 9% (Fig. 3.4 l) of that of the main components, while the intensities of  $E_{y\parallel}$  and  $E_{x\perp}$  do not exceed 1% (Fig. 3.4 e). Due to high numerical aperture, the wave created by  $E_{\text{inc},\parallel}$  ( $E_{\text{inc},\perp}$ ) is not purely extraordinary (ordinary), but has a small contribution of its orthogonal counterpart. However, for simplicity, we will refer to the field produced by  $E_{\text{inc},\parallel}$  (incident field parallel to the tendon axis), as the extraordinary component, and to that produced by  $E_{\text{inc},\perp}$  (incident field perpendicular to tendon axis) as the ordinary component.

The shape of the focal field distribution is less regular for  $n^o = 1.5$  than for  $n^o = 1.33$  due to spherical aberrations originating from the index mismatch on the surface. However, the extraordinary components for  $n^e = 1.337$  are also distorted due to an index slightly different from 1.33. For the case of  $n^o = 1.5$ , the secondary (smaller) components are axially displaced with respect to the main components.

**Phase distribution and birefringence** As can be seen from the Fig. 3.4, the effect of birefringence on the intensity of focal field is limited. However, the birefringence influences the relative phase between the ordinary and extraordinary parts of the beam, as they perceive different indices,  $n^o$  and  $n^e$ , during the propagation. The effect of birefringence is observed in the  $x$  component of the nonlinear polarization (see Eq. 2.20), as was shown in the previous section:

$$P_x^{2\omega} \propto \rho E_x^2 + E_y^2. \quad (3.20)$$

Indeed, when the phase difference between squared ordinary field  $E_y^2$  and extraordinary field  $E_x^2$  is  $\pi$ , the two terms interfere destructively. It then produces remarkable dark spots on polarization-depth diagrams (see previous section). The phenomenological model described in the previous section relies on the assumption that  $x$  and  $y$  field components overlap completely and have uniform phase difference across the focal volume, which is not strictly true.

In this simulation, we calculate the phase shift within the focal volume as the complex phase of the product  $\arg((E_{x\parallel}^2)^\dagger E_{y\perp}^2)$ . To simplify, we don't take  $E_{x\perp}$  and  $E_{y\parallel}$  into account, as their intensity is less than 1% of that for the main components. The average phase across the focal volume is weighted by the overlap of the two components which is calculated as  $|E_{x\parallel}|^2 |E_{y\perp}|^2$ . The phase is averaged over a zone  $\mathcal{S}$  which encompasses 90%

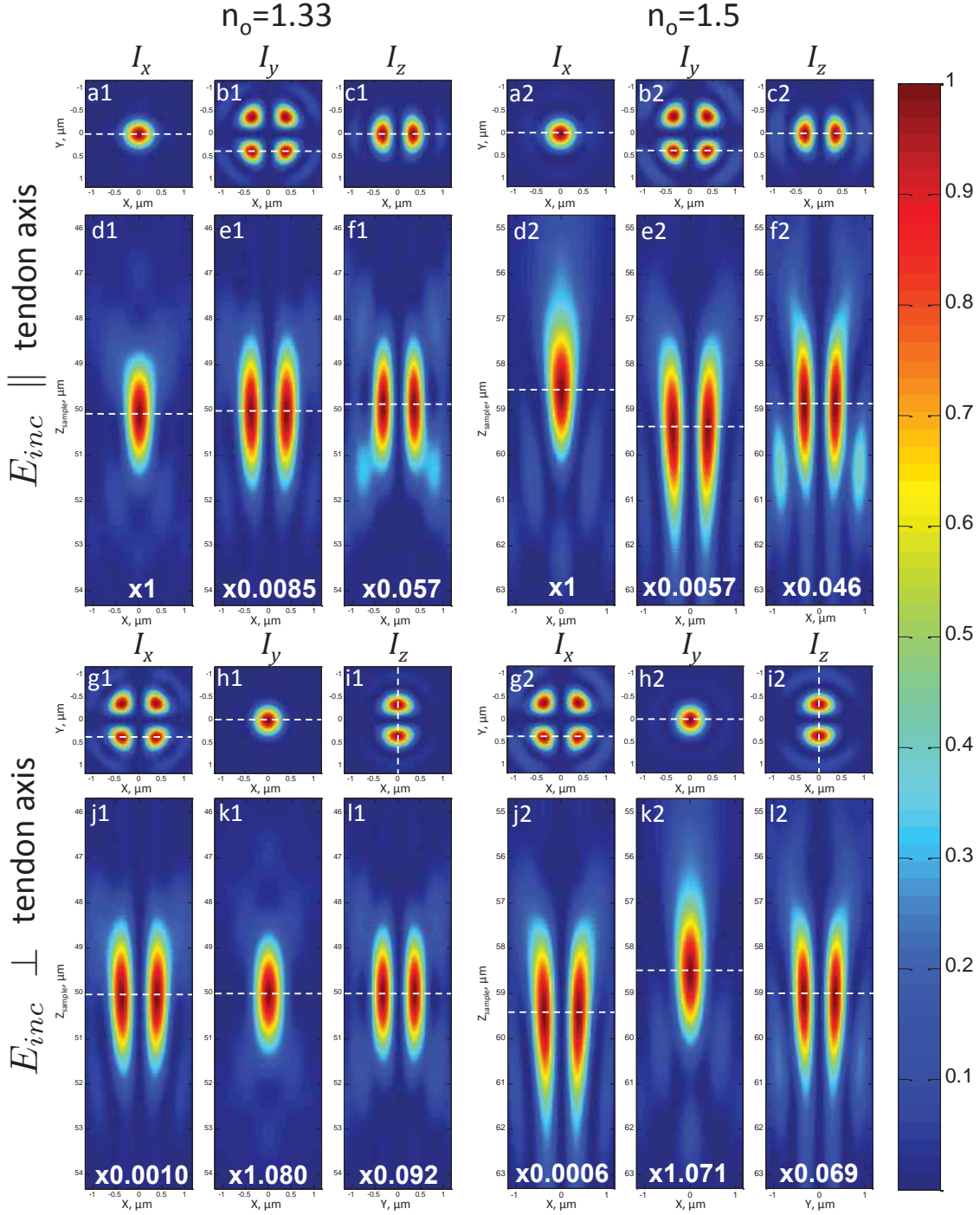


Figure 3.4: Intensity distribution of simulated focal field for 0.95 NA objective in birefringent medium normalized to the  $x$  component of  $x$ -polarized incident field  $I_{x\parallel}$  (a, d). The objective  $z$ -coordinate is  $z_{obj} = 50 \mu\text{m}$ . (a, d, g, j)  $x$ -polarized component; (b, e, h, k)  $y$ -polarized component; (c, f, i, l)  $z$ -polarized component. Calculations for (a1-l1)  $n^o = 1.33$ ; (a2-l2)  $n^o = 1.5$ ; (a-f) incident beam polarized along the tendon optical axis; (g-l) incident beam polarized perpendicularly to the tendon axis. I profile (a-c, g-i) in the  $xy$  plane; (d-f, j-k) in the  $xz$  plane; (l) in the  $yz$  plane. White dotted lines on  $xy$  slices indicate  $xz$  slice position, and vice versa. Numbers indicate the intensity factor with respect to  $I_{x\parallel}$  intensity. Intensities for  $n^o = 1.33$  are larger than those for  $n^o = 1.5$  by factor of 1.441. The difference in  $z$ -position between  $n^o = 1.33$  and  $n^o = 1.5$  is due to different index mismatch.

of the overlap. More precisely, the zone  $\mathcal{S}$  is defined as the smallest region for which:

$$\frac{\iiint_{\mathcal{S} \subset \mathbb{R}^3} |E_{x\parallel}|^2 |E_{y\perp}|^2 d^3\mathbf{r}}{\iiint_{\mathbb{R}^3} |E_{x\parallel}|^2 |E_{y\perp}|^2 d^3\mathbf{r}} = 0.9 \quad (3.21)$$

and the average phase at a certain depth is calculated in the following way:

$$\overline{\Delta\phi} = \frac{\iiint_{\mathcal{S}} \arg((E_{x\parallel}^2)^\dagger E_{y\perp}^2) |E_{x\parallel}|^2 |E_{y\perp}|^2 d^3\mathbf{r}}{\iiint_{\mathcal{S}} |E_{x\parallel}|^2 |E_{y\perp}|^2 d^3\mathbf{r}}. \quad (3.22)$$

This spatial overlap is calculated as a function of focusing depth in Fig. 3.5 f. One can see that ordinary and extraordinary components don't separate significantly over the whole simulated range (up to 80  $\mu\text{m}$  depth). Remarkably, the separation is more pronounced for the case  $n^o = 1.33$  than for  $n^o = 1.5$ . It can be understood as in the second case the relative difference in index mismatch between ordinary and extraordinary waves is marginal ( $1.507 - 1.33 = 0.177$  and  $1.5 - 1.33 = 0.170$ ), while it is substantial in the first case (0.007 for extraordinary, while the ordinary is index-matched).

The phase shift between  $(E_{x\parallel})^2$  and  $(E_{y\perp})^2$  within the focal volume is shown in Fig. 3.5 a-d. In each subfigure (a-d), the inner region corresponds to the phase variation within the zone  $\mathcal{S}$  with respect to the average phase  $\overline{\Delta\phi}$  over this zone. The average phase corresponds to zero of the colorbar, and its absolute value is given in the bottom of each subfigure. The outer region has the gray level corresponding to zero (average phase) to simplify perception. The phase shift in the head of the beam is larger than that in its tail. One can see from the scale bars that the phase dispersion across  $\mathcal{S}$  is roughly two-times larger at 50  $\mu\text{m}$  than at 25  $\mu\text{m}$ . However, it is approximately of the same extent for  $n^o = 1.33$  and for  $n^o = 1.5$ .

The phase difference averaged across the focal volume as a function of focusing depth is shown in Fig. 3.5 e. Phase shift  $\pi$ , which corresponds to destructive interference, occurs near  $\sim 27\text{-}30 \mu\text{m}$ , as observed experimentally. Notably, the phase difference accumulated with depth between extraordinary and ordinary polarization depends on the index of the medium. Indeed, in paraxial approximation the phase shift between squared fields at a fixed  $z_{\text{sample}}$  can be written as

$$\Delta\phi = 2\frac{2\pi}{\lambda} \Delta n z_{\text{sample}} = \frac{4\pi}{\lambda} \Delta n z_{\text{obj}} \frac{n_{\text{sample}}}{n_{\text{water}}}. \quad (3.23)$$

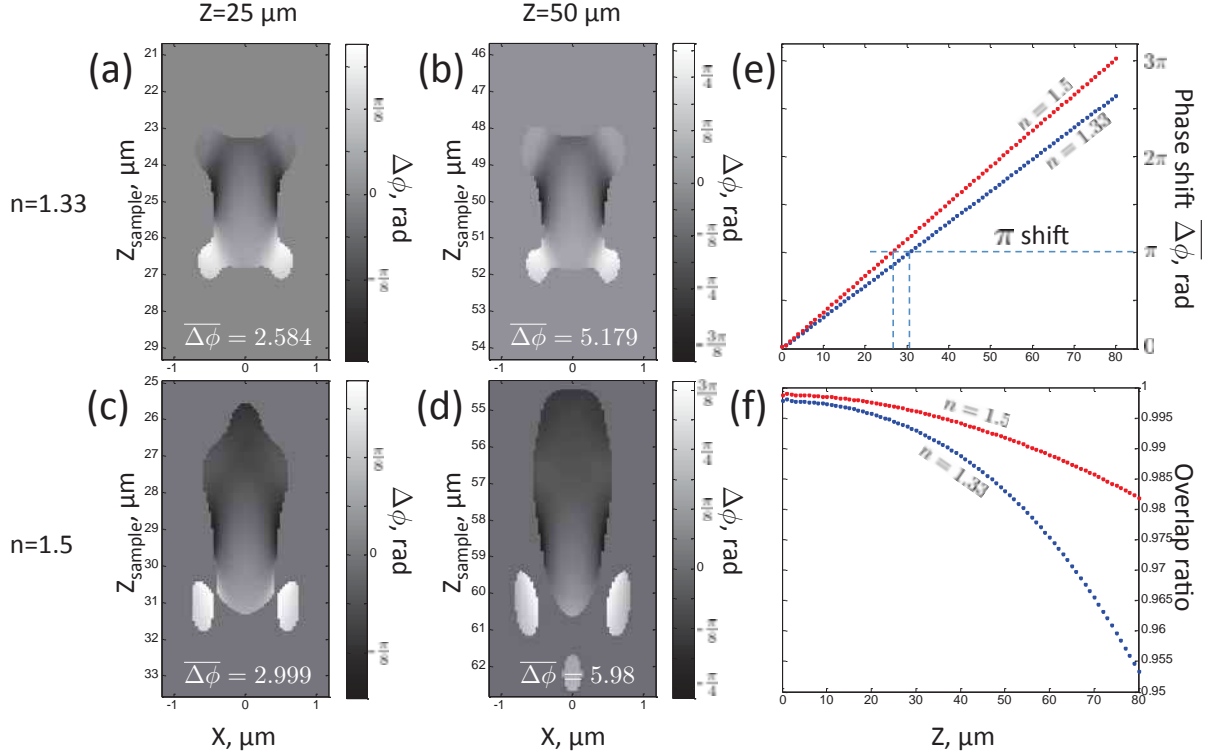


Figure 3.5: (a-d) Simulated phase shift between squared  $x$ - and  $y$ -polarized fields produced by  $E_{inc,x}$  and  $E_{inc,y}$  within the zone encompassing 90% of fields overlap. Calculation (a, b) for  $n^o = 1.33$ ; (c, d) for  $n^o = 1.5$ ; (a, c) at  $25 \mu\text{m}$  focusing depth; (b, d) at  $50 \mu\text{m}$  focusing depth. (e) Averaged phase shift between  $(E_{x\parallel})^2$  and  $(E_{y\perp})^2$  as a function of focusing depth for  $n^o = 1.33$  (blue) and  $n^o = 1.5$  (red). (f) Overlap between ordinary and extraordinary components as a function of focusing depth for  $n^o = 1.33$  (blue) and  $n^o = 1.5$  (red).

It is proportional to both medium index and birefringence. Fitting data in Fig. 3.5 e with this equation one can get  $\Delta n \approx 0.0071$  for  $n^o = 1.33$  and  $\Delta n \approx 0.0072$  for  $n^o = 1.5$  which is very close to the value used for calculation in spite of non-paraxial focusing.

**Conclusion** To conclude, we calculated the focal field distribution in a birefringent medium for a tightly focused beam and characterized the phase shift between ordinary and extraordinary waves. The phase shift is not uniform within the focal volume, and its average is proportional to the depth of focusing as expected. The birefringence obtained from the simulated data is in perfect agreement with the value used for calculation, which means that paraxial approximation can be used for extracting birefringence from the experimental data. Additionally, slight separation of focal volumes is observed at larger depths. The effect of the birefringence on the focal field intensity distribution is minimal and is due to additional spherical aberrations it creates.

### 3.3.3 SH radiation in tendon

#### 3.3.3.1 Radiation of a punctual dipole in a birefringent medium

The focal field calculated in the previous subsection is used to calculate the induced polarization at double frequency. For the field  $\mathbf{E} = (E_x, E_y, E_z)$  the polarization is the following:

$$\begin{aligned} P_x^{(2\omega)} &= \chi_{xxx}^{(2)} E_x^2 + \chi_{xyy}^{(2)} E_y^2 + \chi_{xyy}^{(2)} E_z^2, \\ P_y^{(2\omega)} &= 2\chi_{xyy}^{(2)} E_x E_y, \\ P_z^{(2\omega)} &= 2\chi_{xyy}^{(2)} E_x E_z. \end{aligned} \quad (3.24)$$

where  $x$  is the direction along the tendon fascicle. The simple structure of the nonlinear susceptibility tensor has been discussed in the second chapter of this manuscript. While the induced polarization is easily calculated, the analytic calculation of radiation produced by this polarization density in a birefringent medium is not a trivial task.

The mathematical formulation of the radiation problem consists in the following. In order to find radiated intensity one has to derive a particular far-field solution of Maxwell equations

$$\begin{aligned} \nabla \times \mathbf{E} &= -\frac{\partial \mathbf{B}}{\partial t} \\ \nabla \times \mathbf{H} &= \mathbf{J}_S + \frac{\partial \mathbf{D}}{\partial t} \end{aligned} \quad (3.25)$$

in the medium with the following constitutive equations:

$$\mathbf{D} = \varepsilon_0 \mathbf{E} + \mathbf{P} = \begin{pmatrix} \epsilon_{\parallel} & 0 & 0 \\ 0 & \epsilon_{\perp} & 0 \\ 0 & 0 & \epsilon_{\perp} \end{pmatrix}, \quad \mathbf{B} = \mu \mathbf{H}. \quad (3.26)$$

$\epsilon_{\parallel} = n_e^2$  and  $\epsilon_{\perp} = n_o^2$  are dielectric permittivities along and perpendicular to the axis of symmetry, as introduced in section 3.3.2.2. In the equations above,  $\mathbf{J}_S = \frac{\partial \mathbf{P}^{(2\omega)}}{\partial t}$  is the source current, produced by induced polarization  $\mathbf{P}^{(2\omega)}$ . This polarization that creates radiation is present only in the focal volume.

The particular solution can be easily found if the fundamental solution is known. Indeed, if one knows the field  $\mathbf{E}^j(\mathbf{r})$  radiated by a punctual dipole  $\mathbf{p}^j = \mathbf{e}_j \delta(\mathbf{r})$ , the solution is obtained as

$$\mathcal{E}_i^j = \iiint E_i^j(\mathbf{r} - \mathbf{r}') P_j^{(2\omega)}(\mathbf{r}') d\mathbf{r}'. \quad (3.27)$$

For an isotropic medium, the fundamental solution represents the field radiated by a punctual dipole, and it is known to be a spherical wave with amplitude of the form  $e^{ikr}/kr$ .

In a uniaxial medium, a radiating dipole can be split into two components (parallel and perpendicular to the optical axis) for which radiation is expected to be different due to anisotropy. An elegant solution for dipole radiation in uniaxial medium was proposed by Clemmow [133, 134]. The method relies on known solutions for field in vacuum and is based on different scaling of these solutions in birefringent medium for TE and TM waves. Accordingly, it is known as Clemmow scaling method. For a birefringent medium, TE is equivalent to ordinary and TM is equivalent to extraordinary.

Below, we present electromagnetic field radiated by  $x$ -,  $y$ -, and  $z$ -oriented dipole as given in [133]. Additionally, expressions are simplified by applying far-field approximation. All fields are written down in spherical coordinate system associated with the axis of beam propagation (and SHG detection)  $z$ . For a dipole oriented along tendon axis  $x$ , its radiation is purely a TM (extraordinary) wave. However, the radiation of a dipole perpendicular to the tendon axis is neither pure TM nor pure TE, but is a mixture of two. It is shown by Clemmow that such a punctual dipole can be split into two spatial distributions of dipole density, so that each one generates exclusively TE or TM wave [134]. In the following, the electric field is given in units of  $\frac{k^2}{4\pi}\sqrt{\mu_0/\varepsilon_0}\sqrt{\epsilon_\perp}$ , so this factor is omitted in the expressions. We also introduce the effective radius-vectors for ordinary ( $\epsilon_\perp \mathbf{r}$ ) and extraordinary ( $\mathbf{R}$ ) waves, and their lengths  $\sqrt{\epsilon_\perp}r$  and  $R$ , respectively.

$$\begin{aligned}\mathbf{R} &= (\sqrt{\epsilon_\parallel}x, \sqrt{\epsilon_\perp}y, \sqrt{\epsilon_\perp}z), & R &= \sqrt{\epsilon_\parallel x^2 + \epsilon_\perp(y^2 + z^2)}; \\ \sqrt{\epsilon_\perp} \mathbf{r} &= \sqrt{\epsilon_\perp}(x, y, z), & \sqrt{\epsilon_\perp} r &= \sqrt{\epsilon_\perp}(x^2 + y^2 + z^2).\end{aligned}\tag{3.28}$$

Radiated field for an  $x$ -oriented dipole reads:

$$\begin{aligned}E_\theta &= i \cos \theta \cos \varphi \frac{\epsilon_\parallel r^2}{R^2} \frac{e^{ikR}}{kR} = T_\theta^{e,x} \frac{e^{ikR}}{kR} \\ E_\varphi &= -i \sin \varphi \frac{\epsilon_\parallel r^2}{R^2} \frac{e^{ikR}}{kR} = T_\varphi^{e,x} \frac{e^{ikR}}{kR}\end{aligned}\tag{3.29}$$

where  $\theta$  and  $\varphi$  are polar and azimuthal angles in the spherical coordinate reference frame associated with  $z$ -axis, with the ray  $\varphi = 0$  along the  $x$ -axis (see Fig. 3.6).  $k = 2\pi/\lambda$  is the wavenumber in vacuum. Here,  $\frac{e^{ikR}}{kR}$  is the propagative term for the extraordinary wave, and  $T_{\theta,\varphi}^{e,x}$  encompass angular dependence of  $\varphi$  and  $\theta$  components of the extraordinary wave generated by a punctual dipole along  $x$ .

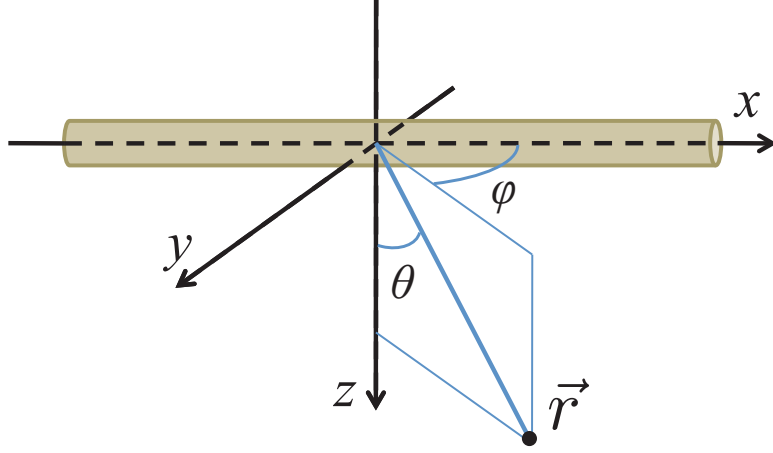


Figure 3.6: Coordinates in tendon reference frame.  $x$ -axis is the symmetry axis of the tendon. Positive  $z$ -axis corresponds to the direction of beam propagation. The ray  $\theta = 0$  coincides with  $z > 0$ , and  $\varphi$  is measured with respect to the  $xz$  plane.

Radiated field for a  $y$ -oriented dipole reads:

$$\begin{aligned}
 E_\theta &= -i \frac{\sin \theta}{\sin^2 \theta \sin^2 \varphi + \cos^2 \theta} \left( \sin^2 \varphi \frac{e^{ik\sqrt{\epsilon_\perp} r}}{k\sqrt{\epsilon_\perp} r} + \cos^2 \theta \cos^2 \varphi \frac{\epsilon_\parallel r^2}{R^2} \frac{e^{ikR}}{kR} \right) = \\
 &= T_\theta^{o,y} \frac{e^{ik\sqrt{\epsilon_\perp} r}}{k\sqrt{\epsilon_\perp} r} + T_\theta^{e,y} \frac{e^{ikR}}{kR} \\
 E_\varphi &= -i \frac{\sin \theta \cos \theta \sin \varphi \cos \varphi}{\sin^2 \theta \sin^2 \varphi + \cos^2 \theta} \left( \frac{e^{ik\sqrt{\epsilon_\perp} r}}{k\sqrt{\epsilon_\perp} r} - \frac{\epsilon_\parallel r^2}{R^2} \frac{e^{ikR}}{kR} \right) = \\
 &= T_\varphi^{o,y} \frac{e^{ik\sqrt{\epsilon_\perp} r}}{k\sqrt{\epsilon_\perp} r} + T_\varphi^{e,y} \frac{e^{ikR}}{kR}.
 \end{aligned} \tag{3.30}$$

Radiated field for a  $z$ -oriented dipole reads:

$$\begin{aligned}
 E_\theta &= -i \frac{\sin \theta}{\sin^2 \theta \sin^2 \varphi + \cos^2 \theta} \left( \sin^2 \varphi \frac{e^{ik\sqrt{\epsilon_\perp} r}}{k\sqrt{\epsilon_\perp} r} + \cos^2 \theta \cos^2 \varphi \frac{\epsilon_\parallel r^2}{R^2} \frac{e^{ikR}}{kR} \right) = \\
 &= T_\theta^{o,z} \frac{e^{ik\sqrt{\epsilon_\perp} r}}{k\sqrt{\epsilon_\perp} r} + T_\theta^{e,z} \frac{e^{ikR}}{kR} \\
 E_\varphi &= -i \frac{\sin \theta \cos \theta \sin \varphi \cos \varphi}{\sin^2 \theta \sin^2 \varphi + \cos^2 \theta} \left( \frac{e^{ik\sqrt{\epsilon_\perp} r}}{k\sqrt{\epsilon_\perp} r} - \frac{\epsilon_\parallel r^2}{R^2} \frac{e^{ikR}}{kR} \right) = \\
 &= T_\varphi^{o,z} \frac{e^{ik\sqrt{\epsilon_\perp} r}}{k\sqrt{\epsilon_\perp} r} + T_\varphi^{e,z} \frac{e^{ikR}}{kR}
 \end{aligned} \tag{3.31}$$

The expressions on the right side highlight that Eqs. 3.29-3.31 behave the same way:  $\frac{e^{ik\sqrt{\epsilon_\perp} r}}{k\sqrt{\epsilon_\perp} r}$  and  $\frac{e^{ikR}}{kR}$  are propagative terms for ordinary and extraordinary waves, respectively, while  $T_{\theta,\varphi}^{e,o;x,y,z}$  are specific for  $x$ -,  $y$ -, and  $z$ -oriented dipoles (with  $T_{\theta,\varphi}^{o,x} = 0$ ).

### 3.3.3.2 Radiation integral

In order to calculate the total fields, one has to integrate these fundamental solutions over the radiating volume as shown in the Eq. 3.27:

$$\begin{aligned} \mathcal{E}_{\theta, \varphi}^i(\mathbf{r}) = & \iiint T_{\theta, \varphi}^{o,i}(\mathbf{r} - \mathbf{r}') P_i^{(2\omega)}(\mathbf{r}') \frac{e^{-ik\sqrt{\epsilon_{\perp}}|\mathbf{r} - \mathbf{r}'|}}{k\sqrt{\epsilon_{\perp}}|\mathbf{r} - \mathbf{r}'|} d^3\mathbf{r}' + \\ & + \iiint T_{\theta, \varphi}^{e,i}(\mathbf{r} - \mathbf{r}') P_i^{(2\omega)}(\mathbf{r}') \frac{e^{-ik|\mathbf{R} - \mathbf{R}'|}}{k|\mathbf{R} - \mathbf{R}'|} d^3\mathbf{r}'. \end{aligned} \quad (3.32)$$

We choose the origin  $\mathbf{r} = 0$  somewhere in the radiative volume. The vector  $\mathbf{r}$  denotes points in the far-field zone, while  $\mathbf{r}'$  denotes points in the excitation volume where the nonlinear polarization is induced, so  $r \gg r'$ . In this case,  $|\mathbf{r} - \mathbf{r}'|$  can be developed in Taylor series by the powers of  $\mathbf{r}'/r$ . In the dipole approximation we keep only the first term:

$$|\mathbf{r} - \mathbf{r}'| = \sqrt{(\mathbf{r} - \mathbf{r}')^2} = \sqrt{r^2 - 2\mathbf{r} \cdot \mathbf{r}' + r'^2} \approx r - \mathbf{n} \cdot \mathbf{r}'. \quad (3.33)$$

We suppose that for a chosen  $\mathbf{r}$ , all functions of  $|\mathbf{r} - \mathbf{r}'|$  are constant across the radiative volume except for rapidly varying exponentials. Introducing 3.33 in the integral 3.32, we obtain

$$\begin{aligned} \mathcal{E}_{\theta, \varphi}^i(r; \theta, \varphi) = & T_{\theta, \varphi}^{o,i}(\theta, \varphi) \frac{e^{ik\sqrt{\epsilon_{\perp}}r}}{k\sqrt{\epsilon_{\perp}}r} \iiint P_i^{(2\omega)}(\mathbf{r}') e^{-ik\sqrt{\epsilon_{\perp}}\mathbf{n} \cdot \mathbf{r}'} d^3\mathbf{r}' \\ & + T_{\theta, \varphi}^{e,i}(\theta, \varphi) \frac{e^{ikR}}{kR} \iiint P_i^{(2\omega)}(\mathbf{r}') e^{-ik\mathbf{N} \cdot \mathbf{R}'} d^3\mathbf{r}' \\ = & \mathcal{E}_{\theta, \varphi}^{o,i}(r; \theta, \varphi) + \mathcal{E}_{\theta, \varphi}^{e,i}(r; \theta, \varphi) \end{aligned} \quad (3.34)$$

where  $\mathbf{N} = \mathbf{R}/R$ . The scalar integrals  $\mathcal{P}_o^i(\theta, \varphi) = \iiint P_i^{(2\omega)}(\mathbf{r}') e^{-ik\sqrt{\epsilon_{\perp}}\mathbf{n} \cdot \mathbf{r}'} d^3\mathbf{r}'$  and  $\mathcal{P}_e^i(\theta, \varphi) = \iiint P_i^{(2\omega)}(\mathbf{r}') e^{-ik\mathbf{N} \cdot \mathbf{R}'} d^3\mathbf{r}'$  reflect the angular efficiency of SH radiation by a given focal distribution of induced polarization  $P_i^{(2\omega)}$ . Additionally, the angular dependence is shaped by  $T_{\theta, \varphi}^{o,i}$  terms.

The angular intensity distribution is calculated as the sum of squared absolute values for  $\theta$ - and  $\varphi$ -projections of the electric field.

$$\mathcal{I}(r; \theta, \varphi) = |\mathcal{E}_{\theta}^{o,y} + \mathcal{E}_{\theta}^{o,z} + \mathcal{E}_{\theta}^{e,x} + \mathcal{E}_{\theta}^{e,y} + \mathcal{E}_{\theta}^{e,z}|^2 + |\mathcal{E}_{\varphi}^{o,y} + \mathcal{E}_{\varphi}^{o,z} + \mathcal{E}_{\varphi}^{e,x} + \mathcal{E}_{\varphi}^{e,y} + \mathcal{E}_{\varphi}^{e,z}|^2 \quad (3.35)$$

One can see from Eq. 3.34 that the cross-terms between ordinary and extraordinary components contain the factor  $e^{ik(r\sqrt{\epsilon_{\perp}} - R)}$ , which oscillates as a function of  $r$ . For the propagation along  $z$ -axis, the extraordinary wave has an effective index close to  $n_e$ , so the oscillation period is about  $\lambda/(n_e - n_o)$ . For a birefringence of 0.007 it gives about  $120 \mu\text{m}$ , which for a  $500 \mu\text{m}$ -thick tendon is equivalent to several periods. It is thus reasonable to

consider ordinary and extraordinary waves mutually incoherent, which allows neglecting these cross-terms.

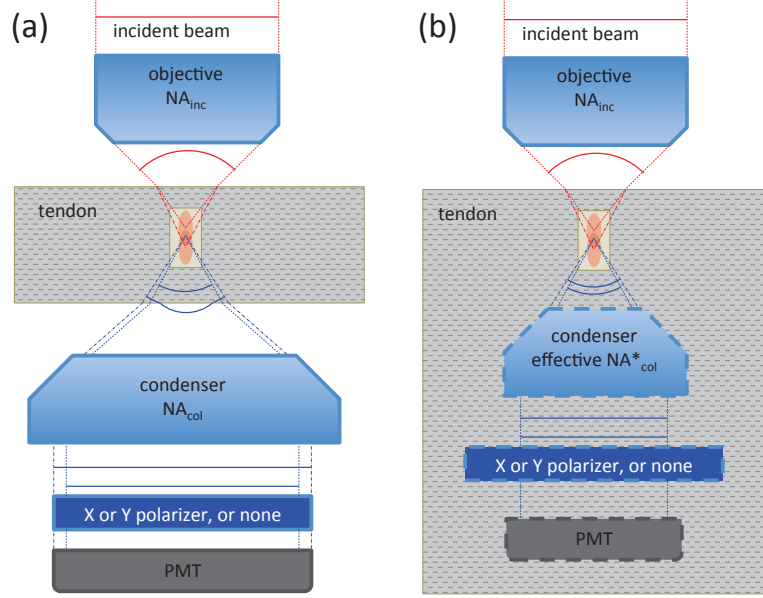


Figure 3.7: Two possible schemes for total intensity calculation. (a) The detector is situated after the tendon-water interface. Angular SHG radiation diagrams are altered by the interface. (b) The effective detector is situated within the tendon.

In a real experimental setup, the radiation diagrams  $\mathcal{I}(r; \theta, \varphi)$  in tendon are altered on the tendon-water interface, which precedes the detectors (Fig. 3.7 a). Calculating angular diagrams outside the tendon would require the explicit introduction of such an interface between birefringent and isotropic media. An alternative way is to assume that the SHG signal is detected by a virtual detector situated within the tendon (Fig. 3.7 b). If we neglect the internal reflection, the total intensity in either configuration is the same, but the original diagrams  $\mathcal{I}(r; \theta, \varphi)$  are more informative than those changed by the interface, as they reflect the actual phase matching properties. We adopt the latter configuration (Fig. 3.7 b), for which the total radiated intensity for a given angle  $\alpha$  of the incident beam polarization and for a given  $z_{obj}$  is calculated as follows:

$$I(\alpha, z_{obj}) = r^2 \iint \mathcal{I}(r; \theta, \varphi) \Big|_{\alpha, z_{obj}} \sin \theta d\theta d\varphi. \quad (3.36)$$

As the angular coordinates further need to be discretized for numerical implementation, we will use  $n_x, n_y$  instead of  $(\theta, \varphi)$  in the following, so that  $\mathcal{E}(r; \theta, \varphi) = \mathcal{E}(r; n_x, n_y)$ .

$n_x$ ,  $n_y$  and  $n_z$  are defined as

$$\begin{aligned} n_x &= \sin \theta \cos \varphi \\ n_y &= \sin \theta \sin \varphi \\ n_z &= \cos \theta. \end{aligned} \tag{3.37}$$

### 3.3.3.3 Simplification of the calculation using relative order of magnitude and symmetry of SH radiation components

In the section 3.3.2 devoted to the beam focusing in a birefringent medium, it was shown that as much as six components are required to reproduce the focal field created by an arbitrary incident polarization:  $E_{x\parallel}$ ,  $E_{y\parallel}$ ,  $E_{z\parallel}$ ,  $E_{x\perp}$ ,  $E_{y\perp}$ ,  $E_{z\perp}$ .

For induced polarization density it implies:

$$P_x^{(2\omega)} \propto \rho \left( E_{x\parallel} \cos \alpha + E_{x\perp} \sin \alpha \right)^2 + \left( E_{y\parallel} \cos \alpha + E_{y\perp} \sin \alpha \right)^2 + \left( E_{z\parallel} \cos \alpha + E_{z\perp} \sin \alpha \right)^2 \tag{3.38}$$

$$P_y^{(2\omega)} \propto 2 \left( E_{x\parallel} \cos \alpha + E_{x\perp} \sin \alpha \right) \left( E_{y\parallel} \cos \alpha + E_{y\perp} \sin \alpha \right) \tag{3.39}$$

$$P_z^{(2\omega)} \propto 2 \left( E_{x\parallel} \cos \alpha + E_{x\perp} \sin \alpha \right) \left( E_{z\parallel} \cos \alpha + E_{z\perp} \sin \alpha \right) \tag{3.40}$$

where  $\alpha$  is the angle between the incident field polarization and tendon axis. Instead of calculating numerically  $P_i^{(2\omega)}$  and resulting radiation for every  $\alpha$  of the incident field, one can calculate the radiation for a finite number of quadratic terms  $E_{i,\parallel,\perp} E_{j,\parallel,\perp}$  and use it to instantly obtain radiation at any given  $\alpha$  according to Eqs. 3.38-3.40. In the light of previous paragraph, one would need to calculate both ordinary and extraordinary integrals  $\mathcal{P}^o$  and  $\mathcal{P}^e$  for as many as 17 quadratic terms such as  $E_{x\parallel} E_{x\parallel}$ ,  $E_{x\parallel} E_{x\perp}$ , ... etc. (9 terms from Eq. 3.38, 4 from Eq. 3.39 and 4 from Eq. 3.40). In the following, we will designate these integrals  $\mathcal{E}\mathcal{E}^{o,e}$ , such as, for example (see Eq. 3.34):

$$\mathcal{E}\mathcal{E}_{x\parallel,x\perp}^o = \iiint E_{x\parallel} E_{x\perp} e^{-ik\sqrt{\epsilon_\perp} \mathbf{nr}'} d^3\mathbf{r}' \tag{3.41}$$

$$\mathcal{E}\mathcal{E}_{y\parallel,z\perp}^e = \iiint E_{y\parallel} E_{z\perp} e^{-ik\mathbf{NR}'} d^3\mathbf{r}' \tag{3.42}$$

However, as it was shown previously (see Fig. 3.4 on page 78), the six field components differ significantly in intensity, which allows one to choose principal and additional components. According to the intensities obtained in focal field simulations, we separate

the field components into three orders of magnitude:

$$\begin{aligned}
E_{x\parallel}, E_{y\perp} &: \text{order 0} \\
E_{z\parallel}, E_{z\perp} &: \text{order 1} \\
E_{y\parallel}, E_{x\perp} &: \text{order 2}
\end{aligned} \tag{3.43}$$

where order 0 corresponds to the strongest field. When multiplied one by another, they are arranged in five orders as follows:

$$\begin{aligned}
E_{x\parallel}^2, E_{y\perp}^2, E_{y\perp}E_{x\parallel} &: \text{order 0} \\
E_{x\parallel}E_{z\parallel}, E_{x\parallel}E_{z\perp} &: \text{order 1} \\
E_{z\parallel}^2, E_{z\parallel}E_{z\perp}, E_{z\perp}^2, E_{x\parallel}E_{x\perp}, E_{y\parallel}E_{y\perp}, E_{x\parallel}E_{y\parallel}, E_{x\perp}E_{y\perp} &: \text{order 2} \\
E_{x\perp}E_{z\parallel}, E_{x\perp}E_{z\perp} &: \text{order 3} \\
E_{y\parallel}^2, E_{x\perp}^2, E_{x\perp}E_{y\parallel} &: \text{order 4}
\end{aligned} \tag{3.44}$$

We should note that this separation is not strict, and additionally may depend on the numerical aperture of the objective. In practice, this approach allows for estimating contributions from different components. For example, one may compare scalar field approximation (only 0 order enabled) with vectorial focusing (all 5 orders enabled). Also, it is possible to qualitatively assess contributions of  $E_{z\perp,\parallel}$  fields (1<sup>st</sup> order) and smaller  $E_{x\perp}$  and  $E_{y\parallel}$  fields (2<sup>nd</sup> order).

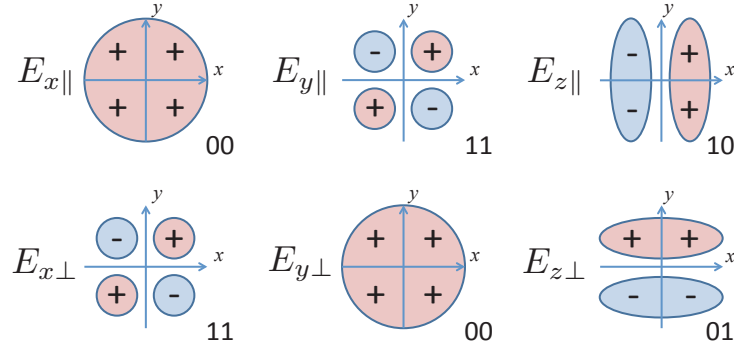


Figure 3.8: Symmetry of the focal field with respect to the inversion of  $x$  and  $y$  coordinates. The two largest components  $E_{x\parallel}$  and  $E_{y\perp}$  are symmetric with respect to both inversions, smallest components  $E_{x\perp}$  and  $E_{y\parallel}$  are fully antisymmetric. Intermediate  $E_z$  components are symmetric with respect to one inversion and antisymmetric with respect to the other.

The calculation of integrals  $\mathcal{E}\mathcal{E}^o$  and  $\mathcal{E}\mathcal{E}^e$  can also be simplified by considering the symmetry of the focal field components. According to our simulations, the focal field components are either symmetric or antisymmetric with respect to  $x$  and  $y$  coordinate inversion. The symmetries for field components are shown in the Fig. 3.8. We denote

symmetry class with two digits, one for each mirror plane, 0 standing for symmetric and 1 for antisymmetric behavior with respect to axis inversion. For example, class 01 signifies that the function is symmetric with respect to  $x$ -coordinate inversion (plane of mirror symmetry  $y = 0$ ), and antisymmetric with respect to  $y$ -coordinate inversion (plane of inversion symmetry  $x = 0$ ).

The symmetries for terms written in 3.44 can be easily deduced and are shown below:

$$\begin{aligned}
E_{x\parallel}^2, E_{x\perp}^2, E_{y\parallel}^2, E_{y\perp}^2, E_{z\parallel}^2, E_{z\perp}^2, E_{y\perp}E_{x\parallel}, E_{x\perp}E_{y\parallel} &: \text{class 00} \\
E_{z\parallel}E_{x\parallel}, E_{z\perp}E_{x\perp} &: \text{class 01} \\
E_{z\parallel}E_{x\perp}, E_{z\perp}E_{x\parallel} &: \text{class 10} \\
E_{z\perp}E_{z\parallel}, E_{x\parallel}E_{x\perp}, E_{x\parallel}E_{y\parallel}, E_{y\perp}E_{y\parallel}, E_{y\perp}E_{x\perp} &: \text{class 11}
\end{aligned} \tag{3.45}$$

Now let's consider, for example, the value of  $\mathcal{E}\mathcal{E}^o$  for inverted  $x$ -coordinate (mirror plane  $y = 0$ ):

$$\mathcal{E}\mathcal{E}^o(r; -n_x, n_y) = \frac{e^{ik\sqrt{\epsilon_{\perp}}r}}{k\sqrt{\epsilon_{\perp}}r} \iiint \mathfrak{C}\mathfrak{C}(x', y', z') e^{-ik\sqrt{\epsilon_{\perp}}(-x'n_x + y'n_y + z'n_z)} d^3\mathbf{r}' \tag{3.46}$$

$$= \frac{e^{ik\sqrt{\epsilon_{\perp}}r}}{k\sqrt{\epsilon_{\perp}}r} \iiint \mathfrak{C}\mathfrak{C}(-x'', y'', z'') e^{-ik\sqrt{\epsilon_{\perp}}(x''n_x + y''n_y + z''n_z)} d^3\mathbf{r}''. \tag{3.47}$$

Here,  $\mathfrak{C}\mathfrak{C}$  is one of the quadratic field terms shown in 3.44, such as, for example,  $E_{x\parallel}E_{y\perp}$ . In the equation above we changed variables as follows:  $\mathbf{r}'' = (-x', y', z')$ . One can see that the value  $\mathcal{E}\mathcal{E}^o$  inherits the symmetry of  $\mathfrak{C}\mathfrak{C}$  term. Hence, it is only necessary to numerically calculate radiation terms  $\mathcal{E}\mathcal{E}^{o,e}$  for a single quadrant, for example  $x > 0, y > 0$ , as the values in other quadrants can be deduced according to 3.45. In order to obtain all necessary components for SH radiation produced at a fixed  $z_{obj}$  and at any polarization angle  $\alpha$  of the incident field, one must numerically calculate 34 integrals (17 for both ordinary and extraordinary components) in a single quadrant ( $x > 0, y > 0$ ). Finally, the angular diagrams  $\mathcal{I}(\theta, \varphi)|_{\alpha, z=z_{obj}}$  are obtained using symmetry (Eq. 3.45) and angular dependence (Eqs. 3.38-3.40).

The summary of calculation data flow is represented in Fig. 3.9.

### 3.3.3.4 Results: angular radiation diagrams

In this section we present the results of our numerical calculations for angular intensity distribution  $\mathcal{I}(\theta, \varphi)$  of SHG radiation.

SHG radiation was calculated for different sets of tendon optical parameters. First parameter is the tendon birefringence, for which values  $\Delta n = 0$  and  $\Delta = 0.007$  were used. While  $\Delta n = 0.007$  corresponds to the values experimentally measured in tendon [136, 138,

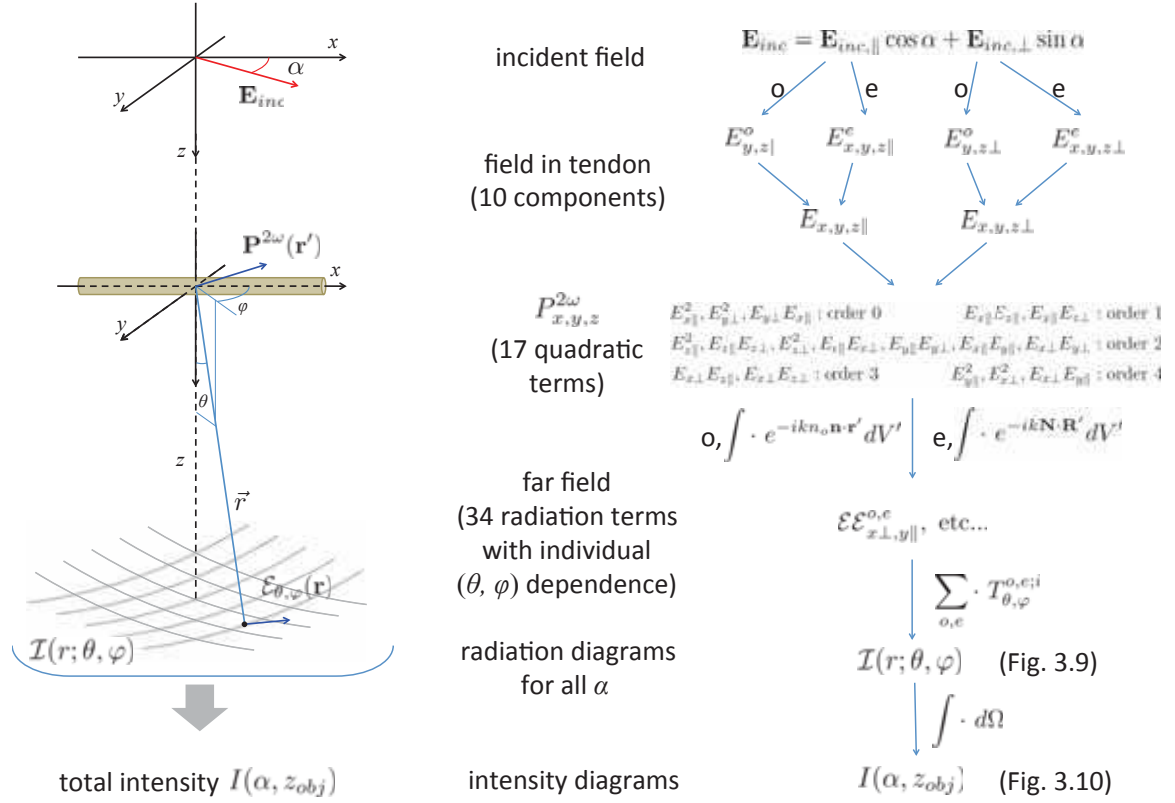


Figure 3.9: Data flow of P-SHG numerical calculation. For two components  $E_{inc,\parallel}$ ,  $E_{inc,\perp}$  of the incident field, 10 components  $E_{i;\parallel,\perp}^{o,e}$  of focal field are calculated in tendon. The focal field creates  $\mathbf{P}_i^{2\omega}$ , which contains 17 quadratic terms of different order and symmetry. Each of this term produces an ordinary  $\mathcal{E}\mathcal{E}^o$  and an extraordinary  $\mathcal{E}\mathcal{E}^e$  radiation component (34 total). Radiation diagrams  $\mathcal{I}(\theta, \varphi)$  for any chosen  $\alpha$  are then calculated using these components  $\mathcal{E}\mathcal{E}$  and their respective angular dependences  $T_{\theta,\varphi}^{o,e;i}$ . Integration of  $\mathcal{I}(\theta, \varphi)|_{\alpha, z_{obj}}$  over the solid angle of radiation produces intensity diagrams  $I(\alpha, z_{obj})$ .

139], the value  $\Delta n = 0$  was chosen to comparatively assess the effect of birefringence on the determination of other optical parameters, such as anisotropy parameter  $\rho = \frac{\chi_{xxx}^{(2)}}{\chi_{xyy}^{(2)}}$ . The simulations were performed for two different indices  $n_o = 1.33$  and  $n_o = 1.5$ , as explained previously. As the radiation process involves interaction of waves at  $\omega$  (incident wave) and  $2\omega$  (SH wave), the phase-matching conditions and hence, the SHG efficiency, depend on medium dispersion  $d = n_{2\omega} - n_\omega$ . In our simulations we used  $d = 0$  and  $d = 0.05n_o$  (5% dispersion). The 5% value corresponds to values reported in literature [140], while  $d = 0$  was used for comparison. SHG anisotropy parameter was fixed to 1.36, which corresponds to values obtained using our phenomenological approach [138]. The simulations were thus performed for a total of 8 sets of parameters, as shown in table 3.1.

The simulated angular SHG radiation diagrams at different imaging depths and different angles of the incident field polarization are shown in the Fig. 3.10. The diagrams are displayed for three different polarization angles  $\alpha = 0$  (a,d),  $\alpha = \pi/4$  (b,e) and  $\alpha = \pi/2$

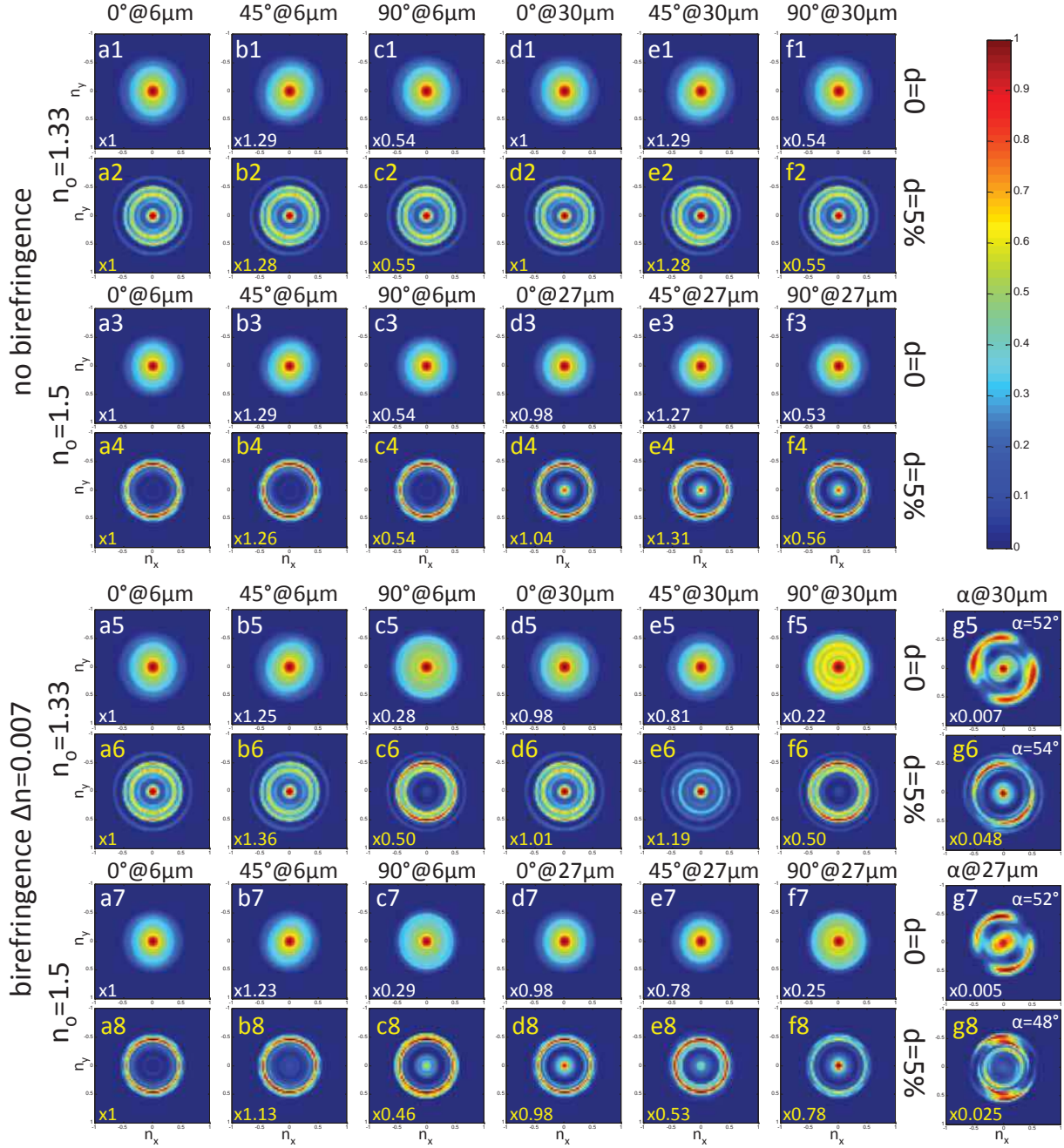


Figure 3.10: Simulated SHG radiation angular diagrams  $\mathcal{I}(n_x, n_y)$  as functions of  $n_x = \sin \theta \cos \varphi$  and  $n_y = \sin \theta \sin \varphi$  for the 8 parameter sets listed in Tab. 3.1 and for two different imaging depths  $z_{obj,1}$  and  $z_{obj,2}$ .  $z_{obj,1}$  was set to  $6 \mu\text{m}$  and corresponds to imaging plane in the proximity of tendon-water interface.  $z_{obj,2}$  corresponds to the depth where the phase shift between incident squared fields  $(E_x^\omega)^2$  and  $(E_y^\omega)^2$  attains  $\pi$ . Accordingly, it was set to  $30 \mu\text{m}$  for the cases with  $n_o = 1.33$  and to  $27 \mu\text{m}$  for the cases with  $n_o = 1.5$ . Intensities within a set (a-g) are normalized to the maximal intensity in (a), and relative intensities are shown in the bottom-left corner. (a) Diagrams for incident field polarized at  $\alpha = 0$  to tendon axis, at the depth  $z_{obj,1}$ . (b) Diagrams for  $\alpha = \pi/4$ ,  $z_{obj,1}$ . (c) Diagrams for  $\alpha = \pi/2$ ,  $z_{obj,1}$ . (d) Diagrams for  $\alpha = 0$ ,  $z_{obj,2}$ . (e) Diagrams for  $\alpha = \pi/4$ ,  $z_{obj,2}$ . (f) Diagrams for  $\alpha = \pi/2$ ,  $z_{obj,2}$ . (g) Radiation diagrams created by  $P_x^{2\omega}$  at  $z_{obj,2}$  at angle  $\alpha$  for which maximal intensity extinction is obtained ( $\alpha$  shown at the upper right corner). These diagrams (g) are not observed directly. Odd (1, 3, 5, 7) and even (2, 4, 6, 8) rows correspond to non-dispersive and dispersive ( $d = 5\%$ ) parameter sets, respectively.

1 : $\Delta n = 0$	2 : $\Delta n = 0$	3 : $\Delta n = 0$	4 : $\Delta n = 0$
$d = 0$	$d = 5$	$d = 0$	$d = 5$
$n = 1.33$	$n = 1.33$	$n = 1.5$	$n = 1.5$
5 : $\Delta n = 0.007$	6 : $\Delta n = 0.007$	7 : $\Delta n = 0.007$	8 : $\Delta n = 0.007$
$d = 0$	$d = 5$	$d = 0$	$d = 5$
$n = 1.33$	$n = 1.33$	$n = 1.5$	$n = 1.5$

Table 3.1: Parameter sets used for simulation of SHG radiation intensity. The set #8 presumably reproduces actual tendon optical parameters.

(c,f), and for two different imaging depths  $z_{obj,1} = 6\mu\text{m}$  and  $z_{obj,2} = 30\mu\text{m}$  or  $27\mu\text{m}$ .  $z_{obj,2}$  corresponds to the depth where a  $\pi$  phase shift between  $(E_x^\omega)^2$  and  $(E_x^\omega)^2$  is attained, which results in extinction of induced  $x$ -polarization  $P_x^{(2\omega)}$  for a certain  $\alpha$ . This depth is  $30\mu\text{m}$  for  $n_o = 1.33$  and  $27\mu\text{m}$  for  $n_o = 1.5$ , as given by Fig. 3.5 e in section 3.3.2

The diagrams for  $\Delta n = 0$  and for water-matched index  $n = 1.33$  (a1-f2) have fairly similar form within a set, varying only in relative amplitude. It can be understood, as first, the medium is isotropic with respect to propagation, which removes dependence on polarization angle  $\alpha$ , and second, the index matching removes possible dependence on the depth  $z_{obj}$ . For the non-birefringent case of  $n = 1.5$  the diagrams are slightly different at different depths (a3-c4 compared to d3-f4), which is due to spherical aberrations altering the focal field distribution.

While diagrams for the non-dispersive case (a1-f1, a3-f3) present strong forward emission with maximum along  $\theta = 0$ , the diagrams for 5% dispersion have additional annular parts (a2-f2) or consist exclusively of a conical lobe (a4-c4) with possibly a central lobe (d4-f4). For the non-dispersive case, the incident beam and generated SH beam are phase-matched for the forward radiation, while dispersion changes the phase-matching conditions and hence the polar angle of optimal SH radiation.

Angular diagrams for sets with birefringence  $\Delta n = 0.007$  (a5-f8) vary considerably within a single set and are more complex than those for  $\Delta n = 0$ . For a given depth and index and without dispersion, diagrams for  $\alpha = 0$  and  $\alpha = \pi/2$  have slightly different forms (a5 compared to c5, d5 to f5, a7 to c7, d7 to f7). While  $\alpha = 0$  diagrams have a wide central lobe,  $\alpha = \pi/2$  diagrams show additional rings which are particularly neat in (f5). As one can see from the Eq. 2.20-2.21, the incident field polarized both at  $\alpha = 0$  and  $\alpha = \pi/2$  induces exclusively the  $P_x^{(2\omega)}$  term. The wave it radiates is an extraordinary wave, while incident waves for  $\alpha = 0$  and  $\alpha = \pi/2$  are extraordinary and ordinary waves, respectively. Thus, a particular phase matching between an incident ordinary beam and

an induced extraordinary SH wave creates annular modulations of radiation intensity. This effect is more pronounced for  $n_o = 1.33$  and for the larger depth. The complex structure of diagrams for dispersive sets makes their interpretation more difficult.

Quantitatively, the effect of birefringence is observed by comparing maximal intensity on a diagram (number in the corner) for  $\alpha = \pi/4$  between  $z_{obj,1}$  and  $z_{obj,2}$  (b to e). While pairs (a,d) and (c,f) have approximately the same intensity, b and e differ significantly. It is explained by the extinction of  $P_x^{(2\omega)}$  term due to birefringence. (e6 has a thin lobe of high peak intensity but limited total intensity of similar magnitude as e8).

Diagrams (g5-g8) in the Fig. 3.10 represent the  $x$ -polarized SH intensity when the  $P_x^{(2\omega)}$  term is most efficiently extinguished. It happens for a certain  $\alpha$  when the terms  $\rho E_0 \cos^2 \alpha$  and  $E_0 \sin^2 \alpha$  are perfectly balanced. This angle  $\alpha$  is shown in the upper-right corner of diagrams. These angular diagrams are relatively irregular because they result from the residual dipole distribution produced by the difference of almost identical focal fields.

### 3.3.3.5 Results: total SHG intensity polarization diagrams

In this paragraph we present  $z$ -diagrams of calculated total intensity  $I(\alpha, z_{obj}) = \iint \mathcal{I} d\Omega|_{\alpha, z_{obj}}$  for SHG radiation in tendon. These numerical simulations of the radiated SHG intensity were performed to test the applicability of the phenomenological model of section 3.2 for the case of tight focusing in a birefringent medium. To that end, we applied our phenomenological model to the simulation results in the same way as it was applied to the experimental data.

We use Eq. 3.1 considering no diattenuation, because it is absent in our simulations:

$$I(\alpha, z_{obj}) \propto |\rho \cos^2 \alpha e^{i\Delta\phi} + \sin^2 \alpha|^2 + \eta_{XY} |\sin 2\alpha|^2. \quad (3.48)$$

Here,  $\Delta\phi$  is the phase shift due to birefringence. In our phenomenological approach [138], Eq. 3.1 was used to fit the intensity polarized along  $x$ -axis, and  $\eta_{XY}$  was used to take into account possible contribution of  $y$ -polarized components. In the present case, we use this equation to fit total intensity diagrams, containing  $x$ - and  $y$ -polarized signals. It means that  $\eta_{XY}$  should have unity value. We will refer to it simply as  $\eta$ . The parameters we extract from the fit are  $\rho$  and

$$\Delta = \eta - \frac{\rho}{2}(1 - \cos \Delta\phi). \quad (3.49)$$

The latter unites the relative contribution of  $y$ -polarization,  $\eta$ , and oscillations due to birefringence (see detailed derivation in [138]).

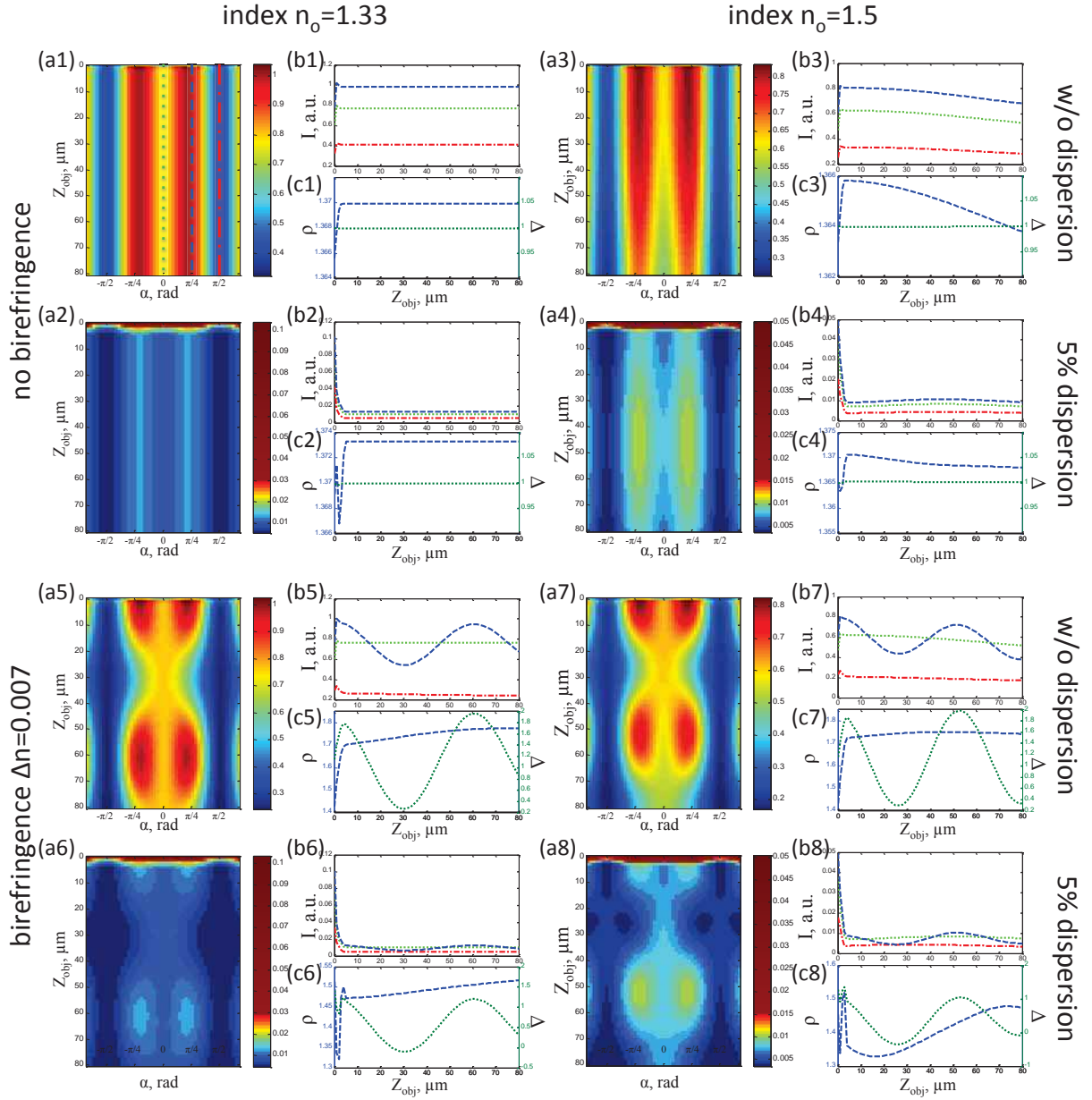


Figure 3.11: Simulated total SHG intensity in tendon as a function of incident polarization angle  $\alpha$  and of imaging depth  $z_{obj}$  for the 8 parameter sets listed in Tab. 3.1. Imaging depth  $z_{obj}$  varied between 0 and 80  $\mu\text{m}$ . (a) SHG intensity  $I(\alpha, z_{obj})$  as a function of incident field polarization angle  $\alpha$  and imaging depth  $z_{obj}$ . (b) SHG intensity depth profiles along  $\alpha = 0$  (green dotted line),  $\alpha = \pi/4$  (blue dashed line) and  $\alpha = \pi/2$  (red dash-dot line). (c) Anisotropic parameter  $\rho$  and parameter  $\Delta$  as a function of  $z_{obj}$ .  $\rho$  and  $\Delta$  are extracted from the intensity diagrams as explained in [138]. Contrast is enhanced for images (a6) and (a8).

Figure 3.11 shows numerically simulated total SHG intensity and parameters extracted from the simulated data according to the phenomenological model. The results are provided for the 8 parameter sets listed in Tab. 3.1. Simulated forward-emitted SHG intensities as functions of polarization angle  $\alpha$  and scanning depth  $z_{obj}$  are shown in subfigures (a1-a8). Subfigures (b1-b8) show depth intensity profiles for incident polarization angles  $\alpha = 0$  (green dotted line),  $\alpha = \pi/4$  (blue dashed line) and  $\alpha = \pi/2$  (red dash-dot line). Lines corresponding to these profiles are shown on the intensity diagram (a1). Subfigures (c1-c8) show parameters  $\rho$  and  $\Delta$  as extracted by fitting with the phenomenological model.

**Non-birefringent case:  $\Delta n = 0$ .** First we consider simulations for the non-birefringent cases  $\Delta n = 0$  (1-4). Diagram for the non-dispersive and index-matched case ( $d = 0$ ,  $n = 1.33$ ) (a1) shows constant intensity as a function of  $z_{obj}$  as expected, as the confinement of the focal field is well preserved at larger depths due to the water-tendon index matching. For the non-dispersive case with index mismatch ( $d = 0$ ,  $n = 1.5$ ) (a3) a slight signal attenuation is observed with depth, as focal volume deteriorates due to spherical aberrations. Diagrams for both dispersive cases (a2, a4) shows a peak of intensity at the water-tendon interface and a constant (a2) or slowly varying (a4) intensity as a function of depth beyond the interface. This steep intensity decrease is due to the altered phase-matching conditions within the beam, which results in destructive interference of SHG signals radiated from frontal and rear halves of the beam. On the surface, when the SHG from the frontal half is not compensated, the resulting efficiency is much higher. The interfacial peak is up to 10 times weaker than intensities for non-dispersive cases (a1, a3). The intensity beyond the surface is up to 100 times weaker as compared to the diagrams without dispersion.

$\rho$  and  $\Delta$  for non-birefringent sets are shown in (c1-c4). The  $\rho$  values are very close to the value 1.36 used for simulations. The small difference is probably due to the contribution of  $z$ -field, which is not taken into account in the phenomenological model. For four cases (c1-c4) the parameter  $\Delta$  is equal to 1 at all  $z_{obj}$ , as expected from Eq. 3.49 when  $\Delta n = 0$ .

**Birefringent case:  $\Delta n = 0.007$ .** Now we will discuss simulation results for sets with birefringence  $\Delta n = 0.007$  (5-8). The intensity diagrams (1-4) are different from those without birefringence, notably because of visible periodic variations as a function of  $z_{obj}$ . The oscillating behavior of intensity is evidenced on depth intensity profiles (b5-b7) for incident angle  $\alpha = \pi/4$  (blue dashed line). A slight attenuation is observed with depth for  $n_o = 1.5$  (a7) due to spherical aberrations which deteriorate focusing. Identically to the non-birefringent sets (1-4), the polarization diagrams for two dispersive cases (a6, a8)

exhibit an interfacial intensity peak and much weaker SHG signal beyond the interface. According to [136,138,140], the set #8 is expected to reproduce tendon optical parameters. However, in the experiment we don't observe any intensity peak on the surface, but a smooth increase of intensity instead. We suppose this happens due to a less dense surface layer consisting of loose fibrils. In other words, the collagen density and  $\chi^{(2)}$  also vary smoothly near the surface from zero to their respective value within the tendon.

$\rho$  and  $\Delta$  parameters for birefringent sets are plotted in (c5-c8). Unlike the non-birefringent cases (1-4), the values of  $\rho$  vary with depth and differ significantly from the value 1.36 used for calculations ( $\sim 1.7$  for c5 and c7,  $\sim 1.5$  for c6,  $\sim 1.35-1.5$  for c8). Additionally, the high values of  $\Delta$  for (c5, c6, c7) cannot be explained by the Eq. 3.49, as it predicts values less or equal to unity. However, the oscillating behavior, which is due to the birefringence, is well reproduced. The fitting of  $\Delta$  as a function of  $z_{obj}$  by a cosine function provides measured values for birefringence, which coincide with great precision with the  $\Delta n = 0.007$  used for calculation: 0.007 for c5, 0.0071 for c6, 0.0072 for c7, 0.0071 for c8 (for  $n_o = 1.5$  (c7, c8)  $\Delta n$  values were corrected according to Eq. 3.23).

### 3.3.3.6 Discussion of the simulated $\rho$ and $\Delta$

**Reconsideration of the phenomenological model.** In order to understand why  $\rho$  and  $\Delta$  differ significantly from the expected values, we need to reconsider the phenomenological model in the light of derived solutions for the radiated SH field. According to the Eqs. 3.24, 3.38, 3.39 and using only the largest terms  $E_{x\parallel}$  and  $E_{y\perp}$  we can write for the induced polarization:

$$\begin{aligned} P_x^{(2\omega)} &\propto \rho E_{x\parallel}^2 \cos^2 \alpha + E_{y\perp}^2 \sin^2 \alpha \\ P_y^{(2\omega)} &\propto E_{x\parallel} E_{y\perp} \sin 2\alpha. \end{aligned} \quad (3.50)$$

As it was shown in the focal field simulations (3.3.2), the  $E_{x\parallel}$  and  $E_{y\perp}$  fields have almost identical magnitudes for each of the cases  $n_o = 1.33$  and  $n_o = 1.5$  (see Fig. 3.4). According to Eqs. 3.36, the total radiated intensity at a given  $\alpha$  writes:

$$\begin{aligned} I|_{\alpha, z_{obj}} &\propto \iint |\mathcal{P}^e|^2 d\Omega + \iint |\mathcal{P}^o|^2 d\Omega = \\ &= \iint |\rho \mathcal{E} \mathcal{E}_{x\parallel, x\parallel}^e \cos^2 \alpha + \mathcal{E} \mathcal{E}_{y\perp, y\perp}^e \sin^2 \alpha|^2 d\Omega + \iint |\mathcal{E} \mathcal{E}_{x\parallel, y\perp}^o \sin^2 \alpha|^2 d\Omega. \end{aligned} \quad (3.51)$$

We remind that  $\mathcal{E} \mathcal{E}_{x\parallel, x\parallel}^e$ , for example, is the extraordinary wave radiation efficiency of the term  $E_{x\parallel}^2$  (see Eqs. 3.41, 3.42). The equation above is an elaborate analogue of the Eq. 3.48, with  $\eta = 1$ .

While all the three terms  $E_{x\parallel}^2$ ,  $E_{y\perp}^2$  and  $E_{x\parallel}E_{y\perp}$  have almost identical magnitude, it is generally not true for  $\mathcal{E}\mathcal{E}_{x\parallel,x\parallel}^e$ ,  $\mathcal{E}\mathcal{E}_{y\perp,y\perp}^e$  and  $\mathcal{E}\mathcal{E}_{x\parallel,y\perp}^o$  as they correspond to different types of phase-matching conditions (see Fig. 3.12). Indeed, the term  $\mathcal{E}\mathcal{E}_{x\parallel,x\parallel}^e$  is the type 0 (extraordinary SH wave generated by two extraordinary incident waves),  $\mathcal{E}\mathcal{E}_{y\perp,y\perp}^e$  is the type I (extraordinary SH wave generated by two ordinary incident waves), and  $\mathcal{E}\mathcal{E}_{x\parallel,y\perp}^o$  is the type II (ordinary SH wave generated by one ordinary wave and one extraordinary wave).

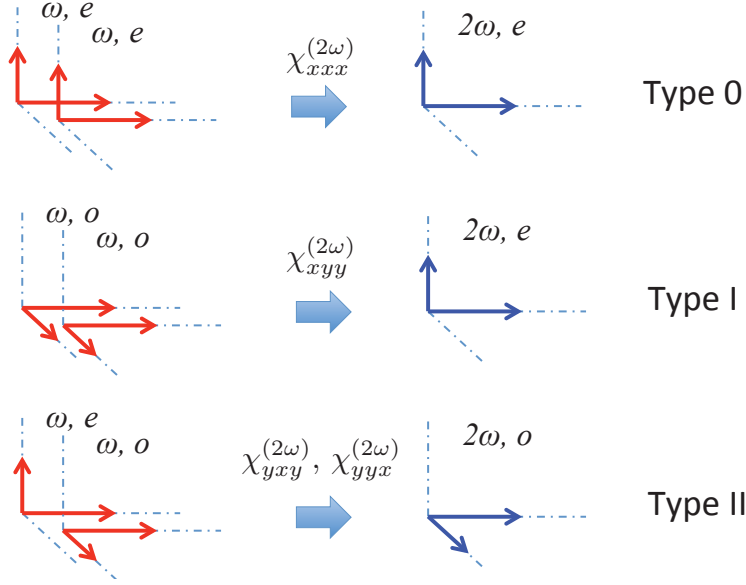


Figure 3.12: Possible types of SHG in tendon by analogy to phase-matching types in birefringent crystals. Type 0 corresponds to generation of an extraordinary wave by two extraordinary waves (governed by  $\chi_{xxx}^{(2\omega)}$  tensorial component). Type I corresponds to generation of an extraordinary wave by two ordinary waves ( $\chi_{xyy}^{(2\omega)}$ ). Type II corresponds to generation of ordinary wave by one extraordinary and one ordinary wave ( $\chi_{yxy}^{(2\omega)}$  and  $\chi_{yyx}^{(2\omega)}$ ).

When fitting the Eq. 3.51 with 3.48, instead of actual values  $\rho = 1.3$  and  $\eta = 1$  we will extract apparent values  $\rho_{app}$  and  $\eta_{app}$ :

$$\rho_{app} = \rho \frac{\iint |\mathcal{E}\mathcal{E}_{x\parallel,x\parallel}^e|^2 d\Omega}{\iint |\mathcal{E}\mathcal{E}_{y\perp,y\perp}^e|^2 d\Omega} \quad (3.52)$$

$$\eta_{app} = \frac{\iint |\mathcal{E}\mathcal{E}_{x\parallel,y\perp}^o|^2 d\Omega}{\iint |\mathcal{E}\mathcal{E}_{y\perp,y\perp}^e|^2 d\Omega} \quad (3.53)$$

If we record  $I(\alpha, z_{obj}) = I_x(\alpha, z_{obj}) + I_y(\alpha, z_{obj})$ , we know that  $\eta$  in Eq. 3.48 is unity, so measuring the apparent  $\eta_{app}$  delivers directly the relative efficiency of types II and I, which is  $r_I^{\text{II}} = \frac{\iint |\mathcal{E}\mathcal{E}_{x\parallel,y\perp}^o|^2 d\Omega}{\iint |\mathcal{E}\mathcal{E}_{y\perp,y\perp}^e|^2 d\Omega}$ . Thus, this value can only be measured when the detection is

not resolved in polarization [141] or when  $I_x$  and  $I_y$  intensities are detected simultaneously in different channels which are properly calibrated [138].

On the contrary, it follows from Eq. 3.52 that  $\rho$  cannot be measured separately from the relative efficiency of types 0 and I, which is  $r_I^0 = \frac{\iint |\mathcal{E}\mathcal{E}_{x\parallel,x\parallel}^e|^2 d\Omega}{\iint |\mathcal{E}\mathcal{E}_{y\perp,y\perp}^e|^2 d\Omega}$ . The latter can only be estimated from simulations based on known optical parameters of the tendon, but cannot be measured independently. In this case, the II-to-I efficiency  $r_I^{II}$  which can be both measured and simulated, indicates whether the optical parameters were chosen correctly. However, this indication relies on the assumption that the numerical model reproduces the phase-matching behavior within the required precision.

Both efficiencies  $r_I^0$  and  $r_I^{II}$  reflect the phase-matching within the focal volume, so they depend primarily on the birefringence  $\Delta n$  and the dispersion  $d$  which directly influence the phase-matching conditions. For zero birefringence, both  $r_I^0$  and  $r_I^{II}$  are unities as the ordinary and extraordinary waves have exactly the same indices. The absolute efficiency can vary upon dispersion, but it doesn't influence ratiometric measurements. Unity relative efficiencies result in precise determination of  $\rho$  and  $\Delta$  from the polarization diagrams (see c1-c4 at Fig. 3.11). For birefringence  $\Delta n = 0.007$  and for zero dispersion, for both indices we observe  $\rho \sim 1.7$  and  $\Delta$  up to 2 (c5, c7), which signifies that  $r_I^0$  is about  $1.7/1.36 \approx 1.25$ , and  $r_I^{II}$  is as high as  $\sim 2$ . For both dispersive sets (c6, c8), the measured parameters are closer to the values used for calculations, which signifies that  $r_I^0$  and  $r_I^{II}$  are closer to one. Finally, for the case which is expected to reproduce tendon optical parameters (c8,  $\Delta n = 0.007$ ,  $n = 1.5$ ,  $d = 5\%$ ), the values of  $\rho_{app}$  and  $\eta_{app}$  are relatively close to the set values. Indeed,  $\Delta$  is close to 1 near its maxima (see Eq. 3.49), and  $\rho$  is close to 1.36 beyond the tendon surface.

The apparent values  $\rho_{app}$  and  $\Delta$  obtained in the simulations have to be compared to the experimental results. Considering the experimental data for tendon presented in the previous section 3.2 and in our paper [138], the phenomenological model provided  $\eta_{app} \sim 1.2 - 1.4$  (using  $x$  and  $y$  channel calibration, not discussed in the paper), which is slightly different from that of Fig. 3.11 c8, but close to that of the dispersive case with  $n_o = 1.33$  (c6). Even if the relative efficiencies are not explicitly related one to another, we suppose that the set #6, for which the simulated  $r_I^{II}$  is close to that observed in experiment, can be used to estimate  $r_I^0$ . Hence, the uncertainty on experimentally measured  $\rho$  can also be estimated from this set. The apparent  $\rho_{app}$  in this case is 8-10% larger than the one introduced in the calculation, and we suppose it is roughly the same for measured  $\rho$ .

The true values of  $n_o$  and  $d$  in the tendon may also differ slightly from those we chose for the simulation. It implies that, for example, choosing smaller dispersion may give the simulated  $\eta_{app}$  closer to that measured in tendon. However, this hypothesis requires

extensive simulations to reproduce the  $\rho_{app}$  and  $\Delta$  curves for a large number of parameter sets near  $n_o = 1.5$  and  $d = 5\%$ , in order to study the dependence of  $r_I^0$  and  $r_I^{II}$  on these parameters. Finally, precise independent measurements of tendon optical parameters, such as birefringence, refractive index and dispersion, along with simulations, would allow to estimate  $r_I^0$  and hence, the real  $\rho$  in tendon.

**Polarization cross-talk due to vectorial focusing.** In section 3.2 we showed that fitting the  $x$ -polarized SHG intensity with the Eq. 3.48 allows one to measure the extent of polarization cross-talk, i.e. the part of  $y$ -polarization detected in the  $x$ -channel. We assumed that this effect was due to scattering on slightly misaligned fibrils within the fascicle. However, in the case of tight focusing with high-NA objectives, one can assume that the field emitted by an induced polarization  $P_y^{(2\omega)}$  within a wide cone will bring non-negligible contribution to the  $x$ -field after refocusing on the detectors. In order to assess this possible contribution of vectorial focusing in a non-scattering medium we calculated the intensity detected in the  $x$ -channel  $I_x(\alpha, z_{obj})$  and applied the Eq. 3.48 to obtain  $\eta$  parameter.

For these calculations we used two sets with no birefringence ( $\Delta n = 0$ ) and an index  $n = 1.5$ : one with and one without dispersion. It corresponds to the sets #3 and #4 in Tab. 3.1. We used  $z_{obj} = 50\mu\text{m}$ . While the radiation is forward-directed within a relatively narrow lobe for the non-dispersive case #3 (see Fig. 3.10 a3-f3), it is spread within a wide cone with aperture of about  $30^\circ$  for the dispersive case #4 (see Fig. 3.10 a4-f4). Hence, the scrambling should be significantly larger for the set #4. The calculations gave  $\eta \sim 10^{-4}$  for the narrow forward-directed emission of the set #3 and  $\eta \sim 10^{-3}$  for the case #4. While cross-talk is approximately ten times larger for the field radiated in a wide cone, as expected, it is still two orders of magnitude smaller than the value  $\eta \sim 0.1$  we measured in tendon (see previous section and [138, 139]). It proves that the scrambling observed experimentally is not due to the vectorial focusing. Thus, the polarization-resolved detection can bring additional information about polarization cross-talk, which cannot be obtained only by measuring  $I = I_x + I_y$ . To conclude, the ideal configuration that allows for obtaining the maximum of information is polarization-resolved excitation coupled with detection split into two properly calibrated channels for  $x$ - and  $y$ -polarized SHG.

### 3.3.4 SHG simulations in cornea

#### 3.3.4.1 Introduction

In this subsection we present numerical simulations of SHG in cornea. A short outline of our results is given here, while the detailed results and discussion will be given in our published article that we present in the next paragraph.

Cornea is a transparent collagenous tissue, which accounts for the 2/3 of the refractive power in a mammalian eye. It is organized in 1-3  $\mu\text{m}$  thick lamellae of aligned collagen fibrils, typically 30 nm in diameter, embedded in an aqueous matrix. The angles between fibril directions in adjacent lamellae are typically  $\sim \pi/3$ - $\pi/2$ . Due to local anisotropy of this tissue and to the intrinsic SH signal it can generate, P-SHG is a promising technique for structural imaging of unstained corneal samples.

We performed P-SHG measurements in human and rat corneas and applied our phenomenological model described previously to the obtained polarimetric data. While the  $\chi^{(2)}$  formalism in general, and our phenomenological model in particular deal with homogeneous media such as tendon, the model proved to be robust even for the case of lamellar non-homogeneous structure of cornea. In particular, the application of this phenomenological model allowed us to determine with good precision the interfaces between adjacent lamellae and fibril orientation within lamellar domains. Interestingly, the parameter  $\rho$  measured at the interface of two adjacent lamellae was smaller than that within the lamellae. This fact seems in contradiction with our theoretical calculations in the chapter 2 (see Eq. 2.28), which predict larger  $\rho$  for samples with orientation disorder. In fact, this behavior is related to the phase shift at the beam focus that is observed with tightly focused beams (Gouy phase shift). SHG electric fields radiated from anterior and posterior parts of the beam focus exhibit an effective phase difference of about  $\pi/2$ . As a consequence, the contributions from the two lamellae apart from the interface are in quadrature rather than in phase, so that they contribute independently to the SHG signal. One may alternatively consider that they add in an incoherent manner rather than in a coherent one, which results in a smaller  $\rho$ .

While the output data provided by the model allows for determining lamella interfaces, it should be noted that the hypothesis of a uniform  $\chi^{(2)}$  used in the model doesn't hold when the beam is focused between two lamellae. In this case, the model output parameters, such as  $\rho$ , do not represent real values in tissue, and should be regarded accordingly.

In order to understand the behavior of SHG process in the vicinity of interlamellar interface we performed numerical simulations as described in the two previous subsections. In contrast to tendon, which is uniformly birefringent, cornea are made of thin birefringent slabs oriented quasi arbitrarily. It means that in each slab there is a different set of

ordinary and extraordinary waves, and phase aspects of the focal field distribution and harmonic generation can be very subtle. However, the cornea is globally non-birefringent, as due to arbitrary lamellae orientations, the average phase shift is globally zero. For the sake of simplicity, for these simulations, we assumed that cornea is also locally non-birefringent. Accordingly, we set the birefringence to zero. The simulated intensity diagrams were fitted with the phenomenological model to obtain parameters of interest, such as  $\rho$ , fibril orientation  $\phi$  and the indicator of fit quality  $R^2$ .

The numerical results we obtained reproduced both qualitatively and quantitatively the measured data. In particular, we showed that the angle  $\phi$  of fibril direction within a lamella exhibits a steep transition between lamellae. Furthermore,  $R^2$  parameter attains its minima near the interface, which shows that the model does not reproduce correctly the SHG near the interface of two slabs with different  $\chi^{(2)}$  tensors. Finally, the simulations proved that the intensity diagrams near the interface corresponds to a  $\rho$  smaller than used for simulations, which is explained by the Gouy phase shift within the focal volume.

As a conclusion, our phenomenological model can be fruitfully used to analyze P-SHG data in cornea, providing information on fibril directions within the lamellae and on precise  $z_{obj}$ -coordinates of the interfaces. It also provides values for the anisotropy parameter  $\rho$  within the lamellae, though these values should be interpreted with caution because of phase-matching considerations described previously.

#### **3.3.4.2 In vivo structural imaging of the cornea by polarization-resolved second harmonic microscopy**

# ***In vivo* structural imaging of the cornea by polarization-resolved second harmonic microscopy**

**Gaël Latour,<sup>1</sup> Ivan Gusachenko,<sup>1</sup> Laura Kowalczyk,<sup>2</sup> Isabelle Lamarre,<sup>1</sup> and Marie-Claire Schanne-Klein<sup>1,\*</sup>**

<sup>1</sup>Laboratory for Optics and Biosciences, École Polytechnique—CNRS—INSERM, 91128 Palaiseau, France

<sup>2</sup>Laboratory for Applied Optics, ENSTA ParisTech—École Polytechnique—CNRS, 91761 Palaiseau, France

\*marie-claire.schanne-klein@polytechnique.edu

**Abstract:** The transparency and mechanical strength of the cornea are related to the highly organized three-dimensional distribution of collagen fibrils. It is of great interest to develop specific and contrasted *in vivo* imaging tools to probe these collagenous structures, which is not available yet. Second Harmonic Generation (SHG) microscopy is a unique tool to reveal fibrillar collagen within unstained tissues, but backward SHG images of cornea fail to reveal any spatial features due to the nanometric diameter of stromal collagen fibrils. To overcome this limitation, we performed polarization-resolved SHG imaging, which is highly sensitive to the sub-micrometer distribution of anisotropic structures. Using advanced data processing, we successfully retrieved the orientation of the collagenous fibrils at each depth of human corneas, even in backward SHG homogenous images. Quantitative information was also obtained about the submicrometer heterogeneities of the fibrillar collagen distribution by measuring the SHG anisotropy. All these results were consistent with numerical simulation of the polarization-resolved SHG response of cornea. Finally, we performed *in vivo* SHG imaging of rat corneas and achieved structural imaging of corneal stroma without any labeling. Epi-detected polarization-resolved SHG imaging should extend to other organs and become a new diagnosis tool for collagen remodeling.

© 2011 Optical Society of America

**OCIS codes:** (180.4315) Nonlinear microscopy; (120.5410) Polarimetry; (190.4160) Multiharmonic generation; (170.3880) Medical and biological imaging; (170.4470) Ophthalmology.

---

## **References and links**

1. R. F. Guthoff, A. Zhivov, and O. Stachs, "In vivo confocal microscopy, an inner vision of the cornea - a major review," *Clin. Experiment. Ophthalmol.* **37**(1), 100–117 (2009).
2. M. Gora, K. Karnowski, M. Szkulmowski, B. J. Kaluzny, R. Huber, A. Kowalczyk, and M. Wojtkowski, "Ultra high-speed swept source OCT imaging of the anterior segment of human eye at 200 kHz with adjustable imaging range," *Opt. Express* **17**(17), 14880–14894 (2009).
3. G. Latour, G. Georges, L. S. Lamoine, C. Deumié, J. Conrath, and L. Hoffart, "Human graft cornea and laser incisions imaging with micrometer scale resolution full-field optical coherence tomography," *J. Biomed. Opt.* **15**(5), 056006 (2010).
4. J. H. Krachmer, M. J. Mannis, and E. J. Holland, *Cornea*, 2nd ed. (Mosby, 2005).
5. K. Plamann, F. Aptel, C. L. Arnold, A. Courjaud, C. Crotti, F. Deloison, F. Druon, P. Georges, M. Hanna, J.-M. Legeais, F. Morin, É. Mottay, V. Nuzzo, D. A. Peyrot, and M. Savoldelli, "Ultrashort pulse laser surgery of the cornea and the sclera," *J. Opt.* **12**(8), 084002 (2010).
6. M. Hao, K. Flynn, C. Nien-Shy, B. E. Jester, M. Winkler, D. J. Brown, O. La Schiazza, J. Bille, and J. V. Jester, "In vivo non-linear optical (NLO) imaging in live rabbit eyes using the Heidelberg Two-Photon Laser Ophthalmoscope," *Exp. Eye Res.* **91**(2), 308–314 (2010).
7. P. J. Campagnola, A. C. Millard, M. Terasaki, P. E. Hoppe, C. J. Malone, and W. A. Mohler, "Three-dimensional high-resolution second-harmonic generation imaging of endogenous structural proteins in biological tissues," *Biophys. J.* **82**(1), 493–508 (2002).

8. W. R. Zipfel, R. M. Williams, R. Christie, A. Y. Nikitin, B. T. Hyman, and W. W. Webb, "Live tissue intrinsic emission microscopy using multiphoton-excited native fluorescence and second harmonic generation," *Proc. Natl. Acad. Sci. U.S.A.* **100**(12), 7075–7080 (2003).
9. D. W. Piston, B. R. Masters, and W. W. Webb, "Three-dimensionally resolved NAD(P)H cellular metabolic redox imaging of the in situ cornea with two-photon excitation laser scanning microscopy," *J. Microsc.* **178**(1), 20–27 (1995).
10. A. T. Yeh, N. Nassif, A. Zoumi, and B. J. Tromberg, "Selective corneal imaging using combined second-harmonic generation and two-photon excited fluorescence," *Opt. Lett.* **27**(23), 2082–2084 (2002).
11. M. Han, G. Giese, and J. Bille, "Second harmonic generation imaging of collagen fibrils in cornea and sclera," *Opt. Express* **13**(15), 5791–5797 (2005).
12. S.-W. Teng, H.-Y. Tan, J.-L. Peng, H.-H. Lin, K. H. Kim, W. Lo, Y. Sun, W.-C. Lin, S.-J. Lin, S.-H. Jee, P. T. C. So, and C.-Y. Dong, "Multiphoton autofluorescence and second-harmonic generation imaging of the ex vivo porcine eye," *Invest. Ophthalmol. Vis. Sci.* **47**(3), 1216–1224 (2006).
13. N. Morishige, T. Nishida, and J. J. Jester, "Second harmonic generation for visualizing 3-dimensional structure of corneal collagen lamellae," *Cornea* **28**(Suppl 1), S46–S53 (2009).
14. P. Matteini, F. Ratto, F. Rossi, R. Cicchi, C. Stringari, D. Kapsokalyvas, F. S. Pavone, and R. Pini, "Photothermally-induced disordered patterns of corneal collagen revealed by SHG imaging," *Opt. Express* **17**(6), 4868–4878 (2009).
15. F. Aptel, N. Olivier, A. Deniset-Besseau, J.-M. Legeais, K. Plamann, M.-C. Schanne-Klein, and E. Beaurepaire, "Multimodal nonlinear imaging of the human cornea," *Invest. Ophthalmol. Vis. Sci.* **51**(5), 2459–2465 (2010).
16. N. Olivier, F. Aptel, K. Plamann, M.-C. Schanne-Klein, and E. Beaurepaire, "Harmonic microscopy of isotropic and anisotropic microstructure of the human cornea," *Opt. Express* **18**(5), 5028–5040 (2010).
17. J. M. Bueno, E. J. Gualda, A. Giakoumaki, P. Pérez-Merino, S. Marcos, and P. Artal, "Multiphoton microscopy of ex vivo corneas after collagen cross-linking," *Invest. Ophthalmol. Vis. Sci.* **52**(8), 5325–5331 (2011).
18. M. Strupler, A.-M. Pena, M. Hernest, P.-L. Tharaux, J.-L. Martin, E. Beaurepaire, and M.-C. Schanne-Klein, "Second harmonic imaging and scoring of collagen in fibrotic tissues," *Opt. Express* **15**(7), 4054–4065 (2007).
19. A. Deniset-Besseau, J. Duboisset, E. Benichou, F. Hache, P.-F. Brevet, and M.-C. Schanne-Klein, "Measurement of the second-order hyperpolarizability of the collagen triple helix and determination of its physical origin," *J. Phys. Chem. B* **113**(40), 13437–13445 (2009).
20. R. Lacombe, O. Nadiarnykh, S. S. Townsend, and P. J. Campagnola, "Phase Matching considerations in Second Harmonic Generation from tissues: Effects on emission directionality, conversion efficiency and observed morphology," *Opt. Commun.* **281**(7), 1823–1832 (2008).
21. M. Strupler and M.-C. Schanne-Klein, "Simulating second harmonic generation from tendon—do we see fibrils?" in *Biomedical Optics*, OSA Technical Digest (CD) (Optical Society of America, 2010), paper BTuD83.
22. M. Rivard, M. Laliberté, A. Bertrand-Grenier, C. Harnagea, C. P. Pfeiffer, M. Vallières, Y. St-Pierre, A. Pignolet, M. A. El Khakani, and F. Légaré, "The structural origin of second harmonic generation in fascia," *Biomed. Opt. Express* **2**(1), 26–36 (2011).
23. F. Tiaho, G. Recher, and D. Rouède, "Estimation of helical angles of myosin and collagen by second harmonic generation imaging microscopy," *Opt. Express* **15**(19), 12286–12295 (2007).
24. P. Stoller, K. M. Reiser, P. M. Celliers, and A. M. Rubenchik, "Polarization-modulated second harmonic generation in collagen," *Biophys. J.* **82**(6), 3330–3342 (2002).
25. O. Nadiarnykh and P. J. Campagnola, "Retention of polarization signatures in SHG microscopy of scattering tissues through optical clearing," *Opt. Express* **17**(7), 5794–5806 (2009).
26. I. Gusachenko, G. Latour, and M.-C. Schanne-Klein, "Polarization-resolved Second Harmonic microscopy in anisotropic thick tissues," *Opt. Express* **18**(18), 19339–19352 (2010).
27. S. Brasselet, D. Ait-Belkacem, A. Gasecka, F. Munhoz, S. Brustlein, and S. Brasselet, "Influence of birefringence on polarization resolved nonlinear microscopy and collagen SHG structural imaging," *Opt. Express* **18**(14), 14859–14870 (2010).
28. S. Psilodimitrakopoulos, S. I. C. O. Santos, I. Amat-Roldan, A. K. N. Thayil, D. Artigas, and P. Loza-Alvarez, "In vivo, pixel-resolution mapping of thick filaments' orientation in nonfibrillar muscle using polarization-sensitive second harmonic generation microscopy," *J. Biomed. Opt.* **14**(1), 014001 (2009).
29. W.-L. Chen, T.-H. Li, P.-J. Su, C.-K. Chou, P. T. Fwu, S.-J. Lin, D. Kim, P. T. C. So, and C.-Y. Dong, "Second harmonic generation chi tensor microscopy for tissue imaging," *Appl. Phys. Lett.* **94**(18), 183902 (2009).
30. V. Nucciotti, C. Stringari, L. Sacconi, F. Vanzì, L. Fusi, M. Linari, G. Piazzesi, V. Lombardi, and F. S. Pavone, "Probing myosin structural conformation in vivo by second-harmonic generation microscopy," *Proc. Natl. Acad. Sci. U.S.A.* **107**(17), 7763–7768 (2010).
31. S. V. Plotnikov, A. C. Millard, P. J. Campagnola, and W. A. Mohler, "Characterization of the myosin-based source for second-harmonic generation from muscle sarcomeres," *Biophys. J.* **90**(2), 693–703 (2006).
32. E. E. B. A. Directory, 18th ed. (European Eye Bank Association, 2010).
33. P. Réfrégier, M. Roche, and S. Brasselet, "Precision analysis in polarization-resolved second harmonic generation microscopy," *Opt. Lett.* **36**(11), 2149–2151 (2011).
34. J. C. Mansfield, C. P. Winlove, J. Moger, and S. J. Matcher, "Collagen fiber arrangement in normal and diseased cartilage studied by polarization sensitive nonlinear microscopy," *J. Biomed. Opt.* **13**(4), 044020 (2008).
35. L. J. Bour, "Polarized light and the eye" in *Visual Optics and Instrumentation*, W. N. Charman, ed. (CRC Press, 1991), Vol. 1, Chap. 13.
36. L. Novotny and B. Hecht, *Principles of Nano-Optics* (Cambridge University Press, 2006).
37. W. Radner, M. Zehetmayer, R. Aufreiter, and R. Mallinger, "Interlacing and cross-angle distribution of collagen lamellae in the human cornea," *Cornea* **17**(5), 537–543 (1998).

## 1. Introduction

The cornea is the outer part of the eye that protects against external injuries and contributes to 2/3 to the eye refractive power. Commercially available techniques, such as confocal reflectance microscopy [1] or optical coherence tomography (OCT) [2,3], enable three-dimensional (3D) cell-scale imaging of cornea. However, these techniques lack specificity or contrast when looking at the collagen organization of the corneal stroma. The stroma represents 90% of the corneal thickness and is composed of more than 250 stacked collagen lamellae that are 1-3  $\mu\text{m}$  thick [4]. Each lamella forms 10-100  $\mu\text{m}$  wide domains that are comprised of 30 nm diameter collagen fibrils organized into a hexagonal lattice. This highly organized structure is responsible for both the transparency and the mechanical strength of the cornea. It may be disrupted in case of a variety of injuries and pathologies (e.g. keratoconus) [4] or after laser surgery [5]. It is therefore of great interest to develop *in vivo* imaging techniques that provide structural and quantitative information about the corneal stroma.

Multiphoton microscopy (MPM) has been shown to enable 3D imaging of biological tissues with similar resolution as the other optical techniques mentioned above. Strong two-photon excited fluorescence (2PEF) signals can be obtained from exogenous labels and *in vivo* tracking of fluorescent microspheres was recently reported in rabbit corneas [6]. However, it is of great interest to take advantage of endogenous MPM signals to image *unstained* corneas [7,8]. MPM has been shown to provide *ex vivo* specific and contrasted images of unstained corneas by using Second Harmonic Generation (SHG) and Third Harmonic Generation (THG) signals to complement usual 2PEF signals [9–17]. THG signals are related to micrometer-sized optical heterogeneities and are obtained at the lamellar interfaces [16]. However, THG signals are mainly detected in the forward direction, which is not appropriate for *in vivo* imaging. SHG is a coherent second order nonlinear signal that probes dense non-centrosymmetrical macromolecular structures such as fibrillar collagen [7,8,18,19]. Since the diameter of stromal collagen fibrils is much smaller than the optical resolution, collagen fibrils are not resolved in the SHG images of cornea. Accordingly, backward SHG (B-SHG) images can be considered as nearly homogeneous with speckle-like background at the micrometer scale [11,13,15]. However, forward SHG (F-SHG) images exhibit striated features that are attributed to complex coherent processes within the focal volume with different phase-matching conditions than in the B-SHG images [20–22]. These striated features are generally considered to indicate the orientation of the lamellar domains [11,13,15,16]. Therefore, SHG microscopy has been mainly limited to forward imaging in excised corneas up until now, since only F-SHG images seem to provide information about the stromal architecture. Application of THG or SHG microscopy to *in vivo* imaging may take advantage of internal reflections at the eye optical interfaces to image forward-radiated signals in an epi-configuration; however, these back-scattered signals are quite low and direct utilization of B-SHG signals is the most promising technique for *in vivo* imaging.

This work aims to implement polarization-resolved B-SHG microscopy to retrieve orientation information about the 30 nm-diameter stromal collagen fibrils and to enable *in vivo* structural imaging of cornea without any labeling. Polarization resolved techniques are indeed highly sensitive to the sub-micrometer distribution of anisotropic elementary components within a sample, much below the optical resolution, as routinely exploited in ellipsometry measurements. Polarization-resolved SHG microscopy was first developed in rat-tail tendons [23–27] and in skeletal muscle [25,28–31] to determine orientation maps. It was also used in *ex vivo* corneas using a forward detection configuration to study thermal disruption of the collagen lamellae [14]. However, polarization-resolved SHG microscopy was never used to visualize the 3D organization of nanometer-sized fibrils in an epi-configuration until now.

The paper is organized as follows; we first introduce experimental implementation of polarization-resolved SHG and theoretical background based on tensorial formalism of nonlinear optics. We also perform numerical simulations to understand the construction of the polarization-resolved SHG signals from stacked adjacent lamellae. We then show that this method successfully retrieves the orientation and anisotropy of the collagenous lamellar domains in human excised corneas both from F-SHG and B-SHG signals. Most importantly, we perform *in vivo* polarization-resolved SHG imaging of rat corneas and demonstrate that our method also applies to that configuration. Finally, we discuss the robustness and interest of this approach and we propose further *in vivo* studies.

## 2. Materials and methods

### 2.1. Polarization-resolved SHG microscopy

MPM imaging was performed using a custom-built laser scanning upright microscope, based on a femtosecond titanium-sapphire laser (Tsunami, Spectra-Physics) and photon-counting detection (P25PC photomultiplier tubes, Electron Tubes) [15,18,26] (Fig. 1A). High numerical aperture water immersion objectives (20x, NA 0.95 or 60x, NA 1.2, Olympus) were used to achieve lateral and axial spatial resolutions of  $0.4 \times 1.6$  or  $0.3 \times 0.9 \mu\text{m}^2$  at 860 nm near the sample surface. B-SHG and 2PEF signals were detected in the backward direction for *in vivo* imaging, while in *ex vivo* corneas, F-SHG signals were also collected. We used suitable spectral filters to reject the excitation laser beam (FF01-680/SP and FF01-720/SP, Semrock), and select the 2PEF emission (GG455 and GG400 high-pass filters at 730 and 860 nm respectively, Schott) or the SHG signal (Hg01-365 and FF01-427/10 interferential filters respectively, Semrock). Multimodal image stacks were recorded using 200 to 300 kHz pixel rate with 0.5 to 0.8  $\mu\text{m}$  pixel size, and 0.5  $\mu\text{m}$  (fine lamellar studies) to 10  $\mu\text{m}$  (structural

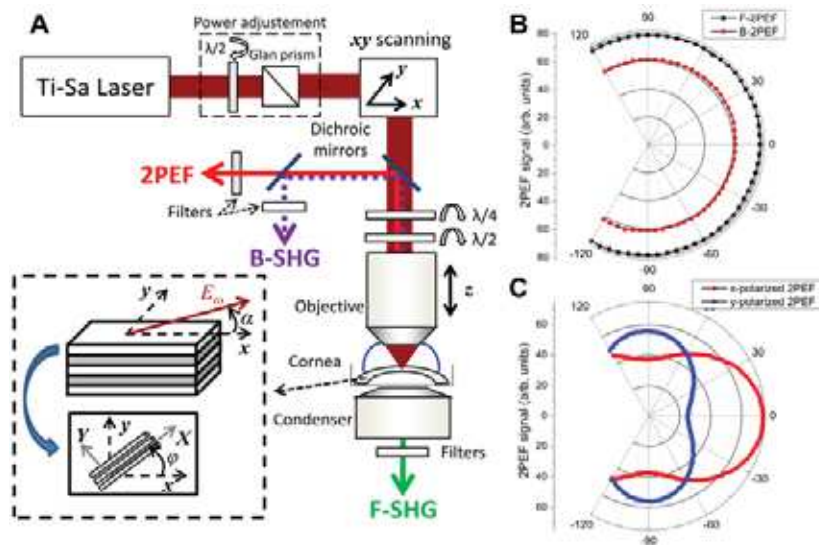


Fig. 1. Experimental setup. (A) Laser scanning microscope with rotating waveplates to control the polarization state of the excitation beam. Orientation of the linearly polarized excitation relative to the cornea morphology in the laboratory frame is indicated in the inset. 2PEF and B-SHG are detected in the backward direction as required in *in vivo* experiments. F-SHG is also detected in *ex vivo* experiments and correlated to polarimetric B-SHG data. (B) Forward and backward 2PEF signals from a fluorescent slab versus orientation of the linearly-polarized excitation, showing variations smaller than 3.2%. (C) Polarization-resolved 2PEF signal from a fluorescent slab versus orientation of the linearly-polarized excitation using polarization sensitive forward detection showing that the maximum 2PEF signal consistently corresponds to  $x$  or  $y$  polarization of the excitation beam.

information through the whole corneal thickness) axial steps. Laser power at the objective focus was typically 20 to 85 mW.

Polarization-resolved SHG was performed using two motorized achromatic waveplates inserted at the back pupil of the objective (Fig. 1A). A quarter waveplate was first used either to switch to quasi-circular polarization or to correct the 14% ellipticity that is mainly introduced by galvanometric mirrors and dichroic mirror and to obtain a well-defined linear polarization (5% residual ellipticity after correction). A half waveplate was then used to control the orientation of this linear polarization. Polarization-resolved SHG was carefully calibrated as previously reported [26]. We verified that forward and backward 2PEF signals from a fluorescent slab (Chroma), exhibited variations smaller than 3.2% when the linear excitation was rotated (Fig. 1B). The absolute polarization angle of the laser excitation was also verified before each experiment by analyzing the polarization of 2PEF signals using a polarizing beamsplitter and linear polarizers in the forward detection module (Fig. 1C). Circularly polarized excitation was sometimes used to obtain SHG images of collagen lamellae with similar efficiency whatever their orientation in the focal plane. Equivalently, we summed all the SHG images obtained with linearly polarized excitation tuned from  $-90^\circ$  to  $90^\circ$  every  $10^\circ$ .

## 2.2. Human cornea preparation

The study was conducted according to the tenets of the Declaration of Helsinki and French legislation for scientific use of human corneas, using 7 human corneas, obtained from the French Eye Bank (BFY, Paris, France), which were unsuitable for transplantation [32]. They exhibited an endothelial cell density between 1850 and 2450 cell/mm<sup>2</sup> (mean value: 2130 cell/mm<sup>2</sup>) that is above the viability threshold fixed at 2000 cell/mm<sup>2</sup> for all the corneas except one [32]. They were stored at 31°C in CorneaMax medium (Eurobio, France) until the experiment. A custom-built holder was used for SHG imaging that clamped the sclera and preserved the cornea. This holder was inserted in a Petri dish with refined thickness to optimize the F-SHG signal detection. Corneas were immersed in a storage medium without red phenol (#7002\_WORP, Stem Alpha, France) to prevent tissue drying during SHG imaging. They were slightly edematous as shown by their increased thickness (typically 700  $\mu$ m) compared to physiological corneal thickness (around 500  $\mu$ m).

## 2.3. Ex vivo porcine eyeball imaging

Freshly enucleated pig eyes were obtained from a local slaughterhouse (Etablissement Guy Harang, France) and stored in Hanks' Balanced Salt Solution (Sigma) until experiment. MPM imaging was performed within 12 hours after the death using a molded agarose gel to hold the eyeball. A gel tear substitute (Lacrigel, Europhta, Monaco) was used to maintain optical contact between the eye and the immersion objective (1.340 refractive index in the visible range at 22°C as measured with Abbe refractometer).

## 2.4. In vivo rat cornea imaging

Experiments were conducted in accordance with the Association for Research in Vision and Ophthalmology (ARVO) Statement for the Use of Animals in Ophthalmic and Vision Research. Male three-month old ( $n = 1$ ) and one-year old ( $n = 1$ ) Wistar rats were purchased from Janvier (Le Genest-Saint-Isle, France) and roomed for one week before inclusion in the study. For experiments, rats were anesthetized by intramuscular injection of a mixture of Ketamine (100 mg/kg) and Xylazine (10 mg/kg). The rat was then placed on a plate under the microscope and, after local anesthetic (tetracaine) instillation, the eye was flattened with a coverslip mounted on a custom-built mechanical device. Optical contact was maintained with ophthalmic gel as for porcine eyeballs.

### 3. Polarization-resolved SHG: theoretical background and numerical simulation

#### 3.1. Theoretical background and data processing

The SH response of a medium is characterized by the second order nonlinear susceptibility tensor  $\chi^{(2)}$ . This tensor is obtained as the averaged response of small collagen fibrils aligned in domains within lamellae and it reflects the direction of collagen fibrils in these domains. Assuming that fibrillar collagen exhibits a cylindrical symmetry and that Kleinmann symmetry applies [19,24], it exhibits only two independent components:  $\chi_{xxx}$  and  $\chi_{xyy} = \chi_{xzz} = \chi_{yxy} = \chi_{yzz} = \chi_{yyx} = \chi_{zzx}$ , where  $X$  is the direction of the collagen fibrils (see Fig. 1A). An incident electric field  $E_\theta$  then induces the following SH radiation in the fibril frame  $XYZ$ :

$$E_X^{2\omega} \propto [\chi_{xxx} \cos^2(\alpha - \varphi) + \chi_{xyy} \sin^2(\alpha - \varphi)] E_0^2 \quad (1a)$$

$$E_Y^{2\omega} \propto [\chi_{xyy} \sin 2(\alpha - \varphi)] E_0^2 \quad (1b)$$

where  $\alpha$  and  $\varphi$  stand for the laser excitation polarization angle and the fibril orientation angle, respectively, with respect to a fixed direction in the laboratory frame (axis  $x$  in Fig. 1A). This formalism is valid because the collagen lamellae are parallel to the surface of the cornea so that the collagen fibrils and the incident electric field are both within the focal plane. The total SH intensity is then given by

$$I^{2\omega} = K \left( \left| \rho \cos^2(\alpha - \varphi) + \sin^2(\alpha - \varphi) \right|^2 + \left| \sin 2(\alpha - \varphi) \right|^2 \right) \quad (2)$$

where  $K$  is a constant merging the squared incident intensity and setup geometrical parameters. Two quantitative parameters appear in this expression: (i) the angle  $(\alpha - \varphi)$  of the laser excitation polarization to the collagen fibrils axis within lamellar domains; (ii) the ratio  $\rho = \frac{\chi_{xxx}}{\chi_{xyy}}$ , which reflects the anisotropy of the nonlinear response of these lamellar domains.

This approach is valid for both B-SHG and F-SHG signals.

Equation (2) can be expressed as a sum of Fourier components  $\cos 2n(\alpha - \varphi)$ , with  $n = 0, 1, 2$  [24,26,33]. This is an efficient way to process the experimental data and determine the SHG anisotropy parameter  $\rho$  even in the presence of optical artifacts due to diattenuation or birefringence in the propagation of the laser excitation [25–27,34]:

$$I^{2\omega} = A \cos 4(\alpha - \varphi) + B \cos 2(\alpha - \varphi) + C \quad (3)$$

As previously derived [26], the SHG anisotropy ratio  $\rho$  is then calculated as

$$\rho = \sqrt{\frac{A+B+C}{A-B+C}} \quad (4)$$

where we have omitted diattenuation correction since there is no diattenuation in the corneal stroma (data not shown). This expression applies even in birefringent media, which may be the case in corneal stroma [35].

Equation (3) was then used to fit the SHG signal in every pixel of the images as a function of the polarization angle of the laser excitation. Image processing was performed automatically using custom-written Matlab script applicable to 3D image stacks with polarimetric information for each pixel (4D data stacks). In order to optimize the signal to noise ratio, the polarization-resolved SHG images were first binned to obtain  $8 \times 8$  to  $13 \times 13 \mu\text{m}^2$  pixel areas. These enlarged regions of interest (ROI) remain smaller than the lamellar domains that extend over  $10 \mu\text{m}$  wide in the anterior stroma to more than  $100 \mu\text{m}$  wide in the

posterior part. Our script then determined for every ROI the angle  $\varphi$  of the collagen fibrils to a reference direction in the laboratory frame, the SHG anisotropy parameter  $\rho$  and the coefficient of determination  $R^2$  which quantifies the goodness of the fitting procedure ( $0 < R^2 < 1$ ).

### 3.2. Numerical simulation of the anisotropy parameter variation with depth

The parameter  $\rho$  is related to the anisotropy of the SH response in *homogenous* lamellar domains composed of aligned nanometric collagen fibrils. Generally speaking, the nonlinear susceptibility formalism is relevant for locally uniform tissue structures. However, two adjacent lamellae with different orientations and consequently different  $\chi^{(2)}$  can contribute together to the SH response when the beam is focused at the interface between them. This configuration occurs at every lamellar interface when scanning along the depth of the cornea. It is expected to induce distortions of the polarimetric diagrams and to hinder the correct determination of the parameters  $\rho$  and  $\varphi$  since the SH response is not uniform throughout the focal volume.

We performed numerical simulation of the depth profile of SHG signals while scanning through an interlamellar interface so as to have a better quantitative understanding of the variation of  $\rho$  and  $\varphi$  in our experimental data. The electric field distribution near the beam focus was calculated using the angular spectrum method [36] for a 1.2 numerical aperture objective (axial FWHM  $\approx 0.9 \mu\text{m}$ ). The second order polarization was calculated at every node of the discretized focal volume, considering two different orientations of the  $\chi^{(2)}$  tensor for the two lamellae, with  $\rho = 1.3$ . The total SH electric fields radiated in different solid angles were then calculated and the total F-SHG intensity was finally obtained for all polarization directions of the excitation beam. These model calculations resulted in distorted polarization diagrams at interfaces due to the contributions of both lamellae. These diagrams were fitted in the same way as our experimental data using Eq. (3). The resulting effective SHG anisotropy parameter  $\rho_{\text{eff}}$  is depicted in Fig. 2A as a function of the angle between two lamellar domains and of the depth position of the lamellar interface within the focal volume.  $\rho_{\text{eff}}$  exhibits a minimum at the interface between two lamellae (for a depth equal to 0 in the simulation), whatever the angle between the two adjacent lamellae. The depth profiles of the effective parameters  $\rho_{\text{eff}}$  and  $\varphi_{\text{eff}}$  for two lamellae at  $60^\circ$  is detailed in Fig. 2B. In addition to the decrease of the  $\rho_{\text{eff}}$  values,  $\varphi_{\text{eff}}$  switches steeply from the direction of the first lamella to the direction of the second one while the goodness of the fit  $R^2$  displays a minimum.

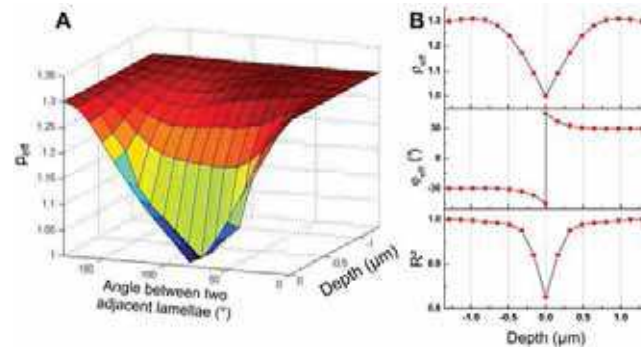


Fig. 2. Numerical simulation of effective SHG anisotropy parameter  $\rho_{\text{eff}}$  across a lamellar interface. (A) Effective SHG anisotropy ratio  $\rho_{\text{eff}}$  obtained by fitting with Eq. (3) simulated polarimetric diagrams with contributions of two adjacent lamellae.  $\rho = 1.3$  within a unique lamella and  $\rho_{\text{eff}}$  varies with the depth of the lamellar interface within the focal volume and with the relative angle of the two lamellae orientations. (B) Simulated depth profiles of the SHG anisotropy ratio ( $\rho_{\text{eff}}$ ), of the orientation of the collagen lamellar domains ( $\varphi_{\text{eff}}$ ) and of the coefficient of determination ( $R^2$ ) for two adjacent lamellae with  $60^\circ$  relative angle.

## 4. Results

### 4.1. Cornea multiphoton imaging

Typical B-SHG and F-SHG images from *ex vivo* human corneas are displayed in Figs. 3A-B. Image stacks in the whole corneal thickness are shown in [Media 1](#). As previously reported, F-SHG images are characterized by striated spatial features, while B-SHG images are nearly homogeneous at the micrometer scale, with speckle-like background interrupted by linear cracks with much smaller signal. Similar features are observed in transverse reconstructions of F-SHG and B-SHG images (Figs. 3C-D and [Media 2](#)). B-SHG images therefore do not directly provide any structural information about the corneal stroma. We have, however, measured that the F-SHG to B-SHG intensity ratio is close to 1 after normalization of both detection channels, so that B-SHG signals are quite large signals. Structural information may therefore be obtained from these signals by performing polarization-resolved SHG microscopy since we expect larger SHG signals when the incident excitation field is aligned with the collagen fibrils. F-SHG and B-SHG polarization-resolved signals are both recorded by rotating the incident polarization as depicted in Fig. 4. We then developed a specific method to process these data based on the tensorial nonlinear optics formalism.

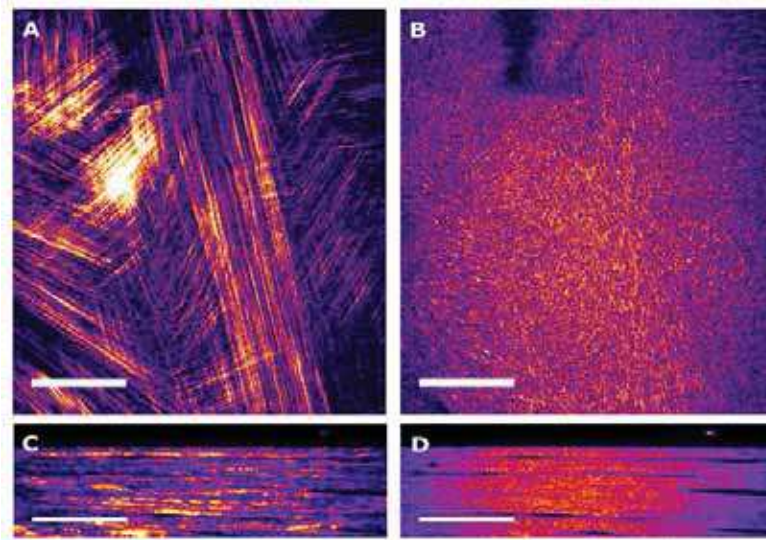


Fig. 3. F-SHG and B-SHG images of posterior stroma from human corneas. (A) F-SHG and (B) B-SHG images obtained as the sum of all the raw images acquired with tunable linear incident polarization (60x 1.2 NA objective, scale bar: 30  $\mu\text{m}$ , false colors) ([Media 1](#)). (C) F-SHG and (D) B-SHG  $xz$  reconstruction from the previous data volume ([Media 2](#)). Striated features (A) and stacked organization (C) are clearly visible in F-SHG images while B-SHG images (C) and (D) are spatially homogenous in.

### 4.2. Determination of fibril orientations

Figure 4 displays typical polarimetric diagrams for the highlighted ROIs in the SHG images. The fits give  $R^2$  values that are close to 1 and consistent for F-SHG and B-SHG signals. It is worth noting that the angle  $\varphi$  (Fig. 4B) corresponds to the orientation of the striated features that appear in F-SHG images (Fig. 4A). It confirms that these striated features reveal the orientation of the collagen fibrils in stromal lamellar domains. In a few ROIs, the  $R^2$  values were lower and fitting F-SHG and B-SHG signals provided different parameters. This discrepancy is related to the specific structures observed in these ROIs. The F-SHG image shows two distinct networks of striated features that seem to be superimposed in the focal volume. It means that the excitation beam was focused at the interface between two lamellae

and that SHG radiation from these two adjacent lamellae was collected together. These two contributions lead to a distortion of the polarization-resolved SHG profile and the fibril orientation cannot be determined unambiguously in such ROIs.

In order to further evaluate the relevance of our method, the angle  $\varphi$  was superimposed on the SHG images, using arrows with length proportional to the  $R^2$  value (Figs. 5A-B). When  $R^2$  values were below an arbitrary threshold (typically 0.7), the results of the fits were discarded. This image processing was performed along the whole depth of the corneal stroma and gave consistent results (Media 3). We observe that the fibrils orientations determined by this approach are (i) the same for F-SHG and B-SHG images although these images exhibit different structures, (ii) in good agreement with the orientations of the micrometric features

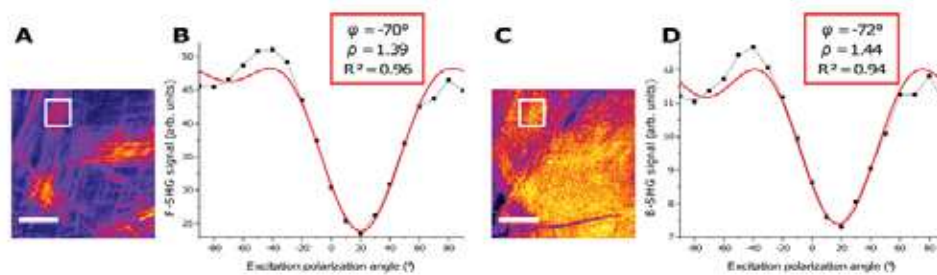


Fig. 4. Polarimetric diagrams from F-SHG and B-SHG images of posterior stroma from human corneas. (A) F-SHG and (C) B-SHG images obtained as the sum of all the raw images acquired with tunable linear incident polarization (20x 0.95 NA objective, scale bar: 50  $\mu\text{m}$ , false colors). (B) F-SHG and (D) B-SHG averaged intensity in the highlighted ROIs versus the angular direction  $\alpha$  of the incident linear polarization. Fits of F-SHG and B-SHG polarimetric diagrams using Eq. (3) (red color) provide the same orientation  $\varphi$  of the collagen lamellar domains and the same SHG anisotropy ratio  $\rho$  with a high coefficient of determination  $R^2$  (see insets).

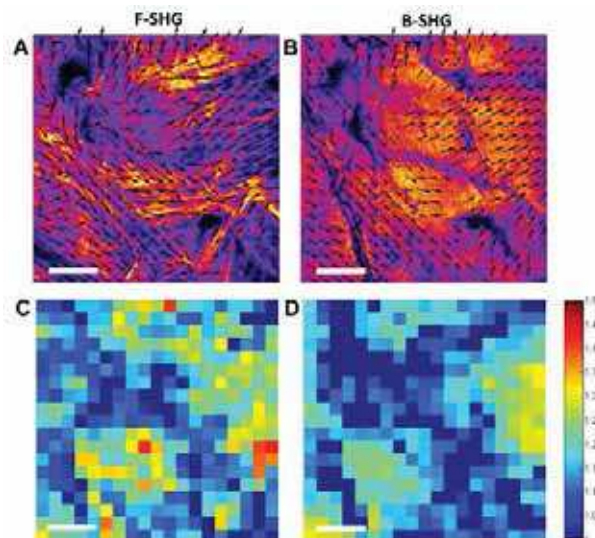


Fig. 5. Orientation maps and SHG anisotropy ratio obtained from polarimetric SHG imaging. (A) F-SHG and (B) B-SHG images of human corneal stroma superimposed with arrows indicating the orientation of collagen fibrils in the lamellar domains calculated from polarimetric diagrams in  $13 \times 13 \mu\text{m}^2$  ROIs using Eq. (3). The arrow lengths scale as  $R^2$  and results are displayed only when  $R^2 > 0.7$ . Maps of the SHG anisotropy ratio  $\rho$  obtained in the same way from (C) F-SHG and (D) B-SHG data. Scale bar: 50  $\mu\text{m}$ . Excitation: 75 mW at 860 nm with a 20x 0.95 NA objective. (Media 3)

revealed in F-SHG images. It shows that polarization-resolved SHG microscopy enables the determination of the collagen fibril orientations within the corneal lamellae using epi-detected signals although raw B-SHG images are spatially homogenous.

The robustness of this approach was characterized as a function of the depth and of the  $R^2$  threshold value (Fig. 6). The greater the  $R^2$  threshold value, the smaller the number of retained ROIs, as expected. The goodness of the fit also gradually deteriorates with depth, which is mainly due to the slight decrease of the SHG signal with depth. While a  $R^2 > 0.9$  threshold appears to be too restrictive because of the weak number of retained ROIs,  $R^2$  thresholds between 0.5 and 0.7 provide a satisfactorily mapping of the angle  $\varphi$  without incongruous results. Using a  $R^2 > 0.7$  threshold, the mean  $R^2$  is  $0.92 \pm 0.07$  (resp.  $0.84 \pm 0.06$ ) and 91% (resp. 63%) of the ROIs are retained for F-SHG images (resp. B-SHG images). It shows that our fitting procedure is robust enough to determine the collagen fibril orientation in the lamellar domains at each depth in the cornea.

This approach also enables the determination of the SHG anisotropy parameter  $\rho$  that shows values between 1.1 and 1.4 in both detection directions (see Figs. 5 C-D).

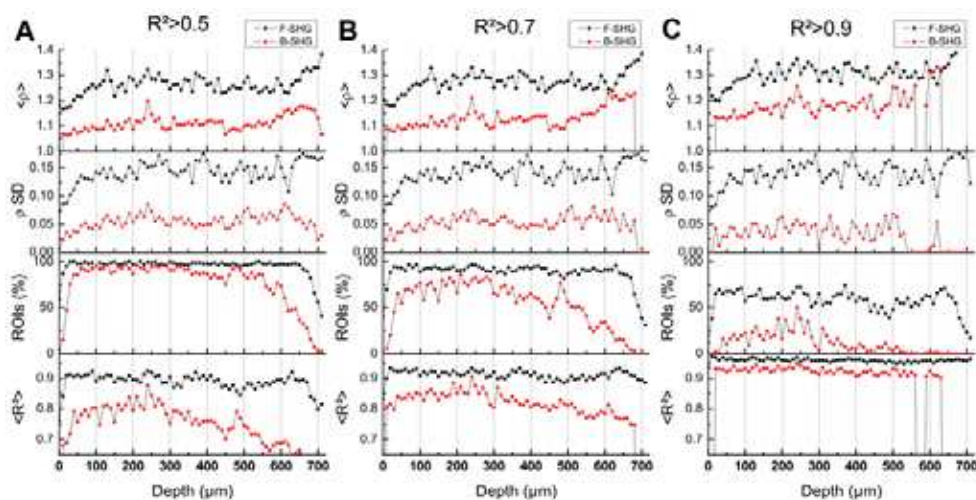


Fig. 6. **Optimization of polarimetric image processing.** Depth profiles of the mean SHG anisotropy ratio ( $\langle \rho \rangle$ ), its standard deviation ( $\rho \text{ SD}$ ), the percentage of retained ROIs above the  $R^2$  threshold (ROIs (%)) and the mean coefficient of determination ( $\langle R^2 \rangle$ ) as obtained from polarization-resolved SHG images, using Eq. (3) with a  $R^2$  threshold equal to (A) 0.5, (B) 0.7 and (C) 0.9.  $13 \times 13 \mu\text{m}^2$  ROIs are processed in  $170 \times 170 \mu\text{m}^2$  F-SHG (black) and B-SHG (red) images over the whole corneal thickness.

#### 4.3. Depth profiles of SHG intensity, SHG anisotropy and lamellar domain orientation

Depth profiles of the SHG signals were measured using a 60x, NA 1.2 objective to increase the axial resolution and to better resolve the lamellae. These measurements were performed in the posterior stroma where the lamellae are thicker and wider. Transverse reconstructions of the anisotropy parameter  $\rho$  show a stacked organization both for F-SHG data (Fig. 7A) and for B-SHG data (Fig. 7B). This feature is better characterized when looking at the depth profiles of the total SHG intensity, of parameter  $\rho$ , of angle  $\varphi$ , and of the  $R^2$  values that are plotted together in Fig. 7C for the  $8.5 \times 8.5 \mu\text{m}^2$  ROI underlined in the image profiles.

Depth profiles of angle  $\varphi$  exhibit plateaus that extend over a few microns and are followed by steep transitions to other plateaus at a quite different angle. This behavior is consistent with the organization of lamellar domains in corneal stroma. The average angular shift between two adjacent lamellae is  $60^\circ \pm 22^\circ$  in this corneal sample, in good agreement with the value determined by electron microscopy from corneal slices [37].

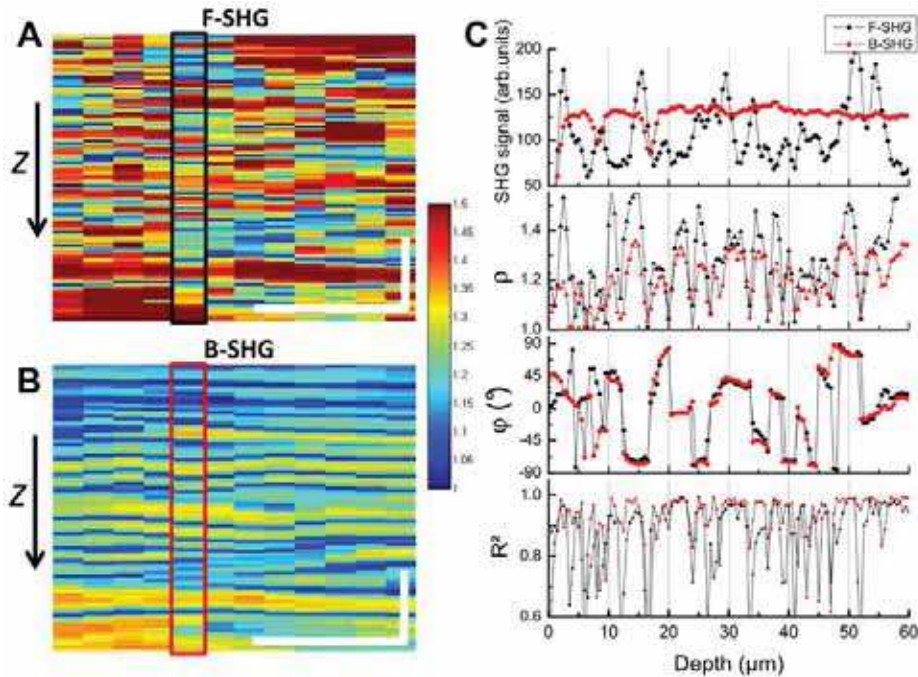


Fig. 7. Depth profiles of polarimetric SHG data in the posterior stroma of a human cornea. SHG anisotropy ratio  $\rho$  along a transverse section obtained from (A) F-SHG and (B) B-SHG polarization-resolved data using  $8.5 \times 8.5 \mu\text{m}^2$  ROIs and  $0.5 \mu\text{m}$   $z$ -steps. Scale bars:  $20 \mu\text{m}$ . Excitation: 20 mW at 860 nm with a  $60\times$  1.2 NA objective. (C) Depth profiles of the total SHG intensity summed for all linear incident polarizations (SHG signal), of the SHG anisotropy ratio ( $\rho$ ), of the orientation of the collagen lamellar domains ( $\phi$ (°)) and of the coefficient of determination ( $R^2$ ), in forward (black) and backward (red) configurations. A low  $R^2$  threshold (0.5) has been used for this data set.

The SHG anisotropy parameter  $\rho$  also exhibits strong depth variations, with maxima (resp. minima) corresponding to the plateaus (resp. steep variations) in the angle  $\phi$  profiles. It means that  $\rho$  has local maxima within the lamellae and minima between lamellae. This behavior is consistent for F-SHG and B-SHG data although B-SHG provides slightly smaller  $\rho$  than F-SHG.

The F-SHG intensity profile also reflects the stacked organization of stromal lamellae. Correlation with angle  $\phi$  profiles show that the intensity maxima are found within the lamellae. This result is in good agreement with previous work that compared SHG and THG intensity depth profiles [15,16]. It is worth noting that the B-SHG intensity profile is much smoother than the F-SHG one. Similarly, transverse reconstructions of B-SHG image stacks do not show the stromal stacked organization observed in F-SHG ones (Media 2). This further substantiates the development of polarization-resolved SHG microscopy for epi-detected imaging.

Finally,  $R^2$  depth profiles exhibit maxima that are correlated with the plateaus of the angle  $\phi$ , the  $\rho$  maxima, and the F-SHG intensity maxima. The goodness of the fit is therefore higher within the lamellae. Meanwhile, the minima of the  $R^2$  values correlate with the interface between two adjacent lamellae, in agreement with our previous considerations about the fitting accuracy (Fig. 2). Here again, these results are consistent for F-SHG and B-SHG data although B-SHG provides slightly higher  $R^2$  values than F-SHG. This behavior is attributed to the difference in coherence lengths for F-SHG and B-SHG. B-SHG microscopy is characterized by a smaller coherence length and probes smaller axial regions than F-SHG microscopy. It is consequently expected to be sensitive to the interface region between two lamellae over a thinner axial extent.

#### 4.4. Ex vivo eyeball imaging

Intact porcine eyeballs were imaged using polarization-resolved SHG microscopy as a first step toward *in vivo* imaging. Spatially homogeneous B-SHG images were observed as in the *ex vivo* human corneas [11,13,17]. By using the same image processing as above, the orientation and the SHG anisotropy of the different lamellar domains were successfully retrieved for the whole 800  $\mu\text{m}$ -deep cornea (Fig. 8 and Media 4). No comparison was possible with F-SHG signals, which could not be detected in that configuration. Nevertheless, we verified that our results were consistent with physiological data. In particular, the spatial extent of the retrieved lamellar domains was smaller in the anterior stroma than in the posterior one, as expected. Moreover, the high  $R^2$  values certified the goodness of the fitting procedure: using a  $R^2 > 0.7$  threshold, 81% of the binned pixels were retained with  $\langle R^2 \rangle = 0.8 \pm 0.07$ .

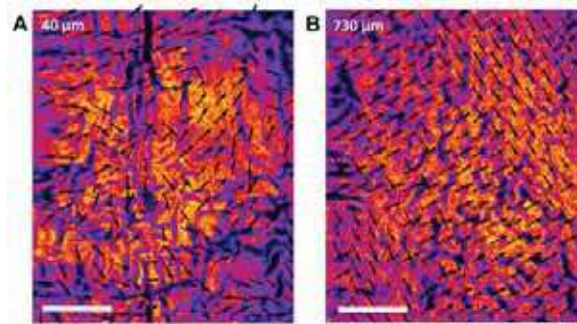


Fig. 8. *Ex vivo* polarization-resolved SHG imaging of intact porcine eyeball. B-SHG images at (A) 40 and (B) 730  $\mu\text{m}$  depth, superimposed with the orientation maps of lamellar domains determined from polarimetric data for  $R^2 > 0.7$ . Scale bar: 50  $\mu\text{m}$ . Excitation: 70 mW at 730 nm with 20x 0.95 NA objective, at 300 kHz pixel rate. Image processing is performed for 13 x 13  $\mu\text{m}^2$  ROIs (Media 4).

#### 4.5. In vivo imaging

Finally, we performed *in vivo* corneal imaging in anesthetized Wistar rat. A custom-built aplanation device was applied to prevent the eye from any movement as in *in vivo* reflectance confocal microscopy. The pixel acquisition rate was also increased to 300 kHz, or typically a

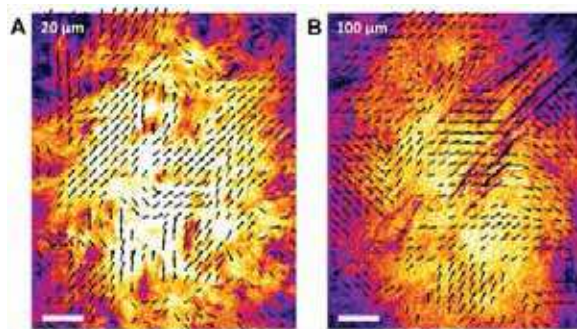


Fig. 9. *In vivo* polarization-resolved SHG imaging from rat cornea. B-SHG images at (A) 20 and (B) 100- $\mu\text{m}$  depth, superimposed with the orientation maps of collagen fibrils in lamellar domains determined from polarimetric data for  $R^2 > 0.7$ . Scale bar: 50  $\mu\text{m}$ . Excitation: 85 mW at 860 nm with a 20x 0.95 NA objective, at 300 kHz pixel rate. Image processing is performed for 13 x 13  $\mu\text{m}^2$  ROIs (Media 5)

few tenths of a second per frame. *In vivo* B-SHG images of the rat cornea were similar to images obtained in *ex vivo* rat eyeball (data not shown). After data processing of SHG polarimetric data, the orientation and the anisotropy of the collagen fibrils in the lamellar domains were successfully retrieved in the whole thickness of the cornea (around 150  $\mu\text{m}$  thick) (Fig. 9 and Media 5) with good statistics: using a  $R^2 > 0.7$  threshold, 70% of the binned pixels were retained with  $\langle R^2 \rangle = 0.85 \pm 0.07$ .

## 5. Discussion

### 5.1. Polarization-resolved SHG of the corneal stroma

In this work, we implemented polarization-resolved SHG imaging to probe the orientation of 30 nm-diameter collagen fibrils in lamellar domains within corneas. The main advantage of our approach is its applicability to both forward and backward detections, opening the way to structural quantitative *in vivo* microscopy. Raw B-SHG images of corneal stroma are indeed spatially homogenous and do not provide any structural information about the collagen lamellae distribution. F-SHG images from excised corneas exhibit striated patterns that reveal the collagen fibril distribution within the lamellae, but they cannot be recorded in *in vivo* configuration. In that context, our approach takes advantage of the enhanced SHG response of collagen fibrils when aligned along the excitation electric field. F-SHG and B-SHG images are recorded for various polarization directions of the laser excitation and suitable data processing retrieves the collagen orientation in every pixel of the SHG images. Fitting of polarimetric data is based on the tensorial formalism of second order nonlinear optics and takes into account possible birefringence of the cornea, which may distort the excitation polarization. The anisotropy of the SHG response in any ROI of the cornea is also measured through the parameter  $\rho$ . It is quite low ( $\rho = 1.1-1.4$ ), but it appears to be sufficient to determine orientations using Eq. (3), provided that the excitation polarization is well-defined. It is therefore mandatory to correct any ellipticity of the incident beam and to carefully control the rotating angle of the incident polarization.

Our results demonstrate that this new modality is (i) reliable since the retrieved orientation maps are the same for F-SHG and B-SHG images and are in good agreement with the direct visualization of lamellar domain orientations in raw F-SHG images; (ii) robust and efficient since it enables the structural characterization of the lamellar domains along the whole thickness of the corneal tissue with good fitting accuracy (high  $R^2$  values) (Fig. 5 and Media 3); (iii) applicable to intact eyeballs (Fig. 8 and Media 4) and to *in vivo* imaging of rat corneas (Fig. 9 and Media 5).

### 5.2. Comparison between experimental data and numerical simulation

The susceptibility tensor  $\chi^{(2)}$  formally applies to a homogenous medium while the cornea is composed of stacked collagen lamellae. In particular, the SHG collected signals may have contributions from two adjacent lamellae. Accordingly, we observed specific features in the depth profiles of the parameters  $\varphi$ ,  $\rho$  and  $R^2$  obtained when fitting experimental polarization-resolved SHG signals (Fig. 7). Interfaces between lamellae were accurately located thanks to the steep changes of the lamellar domain orientation angle  $\varphi$ . We consistently observed a decrease of  $R^2$  at the same depths. Interestingly, the  $\rho$  depth profiles also exhibited minima at the lamellae interfaces, which means that a heterogeneous SH response in the focal volume results in a lower effective  $\rho$ .

Numerical simulations are in excellent agreement with these experimental results (see Fig. 2B). They fully reproduce the experimental variations of all the parameters through a lamellar interface. Such an excellent agreement cannot be obtained by just averaging the SH anisotropy from two lamellae in the focal volume. Indeed, the peculiar depth profiles we observed experimentally are due to the specific axial phase profile of the excitation beam. Tightly focused beams exhibit a phase shift at the beam focus that is the so-called Gouy phase shift [36]. Practically, the effective phase shift between the front and the back halves of the excitation beam, which illuminate two different lamellae, is about  $\pi/2$ . It means that the

contributions from the two lamellae apart from the interface are in quadrature rather than in phase, so that they contribute independently to the SH response. In other words, they add in an intensity-like manner rather than in a coherent one. This results in a lower effective  $\rho$ .

Finally, our numerical simulations demonstrate that (i) measurement of the orientation of the collagen fibrils in the lamellar domains by polarization-resolved SHG microscopy is robust even near the interface between two lamellae where the polarization diagrams are distorted; (ii) measurement of the SHG anisotropy parameter  $\rho$  must be performed away from any interface in a homogenous region of the cornea to avoid artifacts due to heterogeneities; (iii) variation of the SHG anisotropy parameter  $\rho$  is related to heterogeneities of the fibrillar collagen organization within the focal volume. The latter consideration may be used to study pathological disorders in the cornea, which are characterized by an alteration of the fibril organization inside the lamellae. Measurements of  $\rho$  should also enable monitoring of either corneal reshaping after corneal graft or corneal wounding after any injury.

### 5.3. *In vivo* imaging

Altogether, the main advantage of polarization-resolved SHG microscopy is its applicability to *in vivo* imaging. Our data demonstrates that clear B-SHG images are obtained in anesthetized rats despite the vital movements and that the orientation of the collagen lamellar domains can be retrieved. We estimated that the lateral corneal movements during the acquisition of a polarization-resolved image at a given depth (10 seconds for 18 angular positions) were around a few microns. We therefore processed the SHG data using  $13 \times 13 \mu\text{m}^2$  ROIs that are larger than the corneal movements and small enough compared to the typical lamellae width. Axial movements could not be experimentally determined because B-SHG images were homogenous. However, in case of axial movements, two or more lamellae would contribute to the SHG signal and data fitting would exhibit lower  $R^2$  than for *ex vivo* imaging of immobilized eyeball. Since  $R^2$  are similar in both configurations, we expect that axial movements are marginal and do not disrupt the determination of lamellar domain orientations.

Further *in vivo* studies would require a few improvements of the acquisition conditions. First, the acquisition time could be reduced by degrading the image resolution and increasing the pixel size rather than averaging the signal over large ROIs. The number of polarization-resolved images could also be reduced by using greater angular steps. It would, however, require carefully optimizing the angular step number and total acquisition time to determine the orientation of the lamellar domains with reasonable accuracy [33]. Second, immobilization of the rat eye could be improved by designing a user-friendly system as already used in confocal microscopy; possible artifacts due to fast eye motion could be also corrected by use of suitable image processing to reconstruct undistorted images as reported for confocal microscopy [38]. Third, further studies are necessary to precisely evaluate the maximum power to be used to avoid any tissue damage and ensure cell viability, although no alteration of the stromal collagen was observed during our experiments. Regarding the other ocular tissues such as lens and retina, we expect that our technique is quite safe since the laser is focused in the cornea, similarly to what is routinely performed with pulsed lasers for corneal surgery.

## 6. Conclusion

In this paper, we demonstrated a new method to visualize the structural organization of the cornea without any staining and in an epi-detection configuration that is appropriate for *in vivo* imaging. Our approach merges polarimetric and SHG microscopies to provide quantitative data about the main direction and the heterogeneity of the collagen fibrils distribution. It takes advantage of the high sensitivity of polarimetry for optically anisotropic structures, even below the optical resolution, such as for the 30 nm-diameter stromal collagen fibrils. Using polarization-resolved SHG, we mapped the 3D distribution of collagen lamellae at each depth in human corneas and obtained an excellent agreement with numerical simulations. We also performed *in vivo* SHG imaging of rat corneas and demonstrated that our

approach enables structural imaging of corneal stroma without any labeling and despite the vital movements.

This method opens avenues for preclinical ophthalmological studies, which require dynamic follow-up of corneal lamellar structure in a variety of injuries or pathologies. It should also find applications to *in vivo* diagnosis of human corneal dystrophies or to corneal healing monitoring after keratoplasty or refractive surgery. More generally, epi-detected polarization-resolved SHG imaging can provide quantitative structural information about the 3D organization of collagen fibrils within any tissue. We therefore expect that this new method will extend to other organs and become a new diagnosis tool for collagen remodeling.

### **Acknowledgments**

The authors gratefully acknowledge I. Sourati and P. Sabatier from the “Banque Française des Yeux” for providing the human corneas, X. Solinas and J.-M. Sintès for technical implementation of the setup, K. Plamann, E. Beaurepaire and D. Débarre for fruitful discussions, and M. Zimmerley and F. Hache for critical reading of the manuscript. G. L. was supported by “RTRA-Triangle de la Physique” and “Fondation Berthe Fouassier—Fondation de France.” L. K. was supported by ANR NOUGAT ANR-08-TecSan-012.

### 3.4 Discussion

In this chapter we discussed linear optical effects that can affect SHG measurements in thick collagenous tissues. First, to account for these effects when processing P-SHG data, we presented a simple and robust phenomenological model. Furthermore, we performed simulations of SHG in tendon and cornea in the case of tight focusing, starting from the incident field distribution on the back pupil of the objective and ending with angular diagrams of SHG radiation.

The phenomenological model was very useful as it allowed us to easily take into account all the discrepancies we observed in measured polarization diagrams with respect to those predicted by a simpler commonly used model. However, this model is based solely on P-SHG experimental observations, which served both for deriving the model and deducing from this model the parameters of interest. It means that this model still needs to be validated by independent measurements of optical parameters or by direct simulations of the SHG in the tissue with known linear and nonlinear optical parameters.

In order to have an independent reference for P-SHG experiments, and to account for the tight focusing geometry, we performed numerical simulations of SHG. Interestingly, the most important results drawn from the numerical simulations were not due to the tight focusing, which was one of the reasons to perform the simulations. Indeed, we showed that auxiliary fields which are absent in the scalar case ( $E_z$  and  $E_y$  created by an  $x$ -polarized excitation beam) were rather small, and their effect on the polarization diagrams  $I(\alpha, z_{obj})$  and on the measured SHG anisotropy parameter  $\rho$  was minimal.

In contrast, we showed that the birefringence and the optical index dispersion can affect  $\rho$  measurements in more dramatic and less predictable way than we expected. The birefringence was partially taken into account in the phenomenological model, as it introduced a phase difference between ordinary and extraordinary fields, participating together to create the  $x$ -component of the induced polarization  $P_x \propto \rho E_x^2 + E_y^2$ . However, it was shown in our simulations that the difference in focal field phase distribution between ordinary and extraordinary waves could additionally change relative efficiencies of SHG. When birefringence is present, the index dispersion also has a crucial role in the phase-matching within the beam. To the best of our knowledge, this subtle effect of birefringence has never been observed nor discussed in the context of SHG in tissues up to now. Though, it has a direct analogy to the phase matching types for SHG in birefringent nonlinear crystals, which are well known for decades.

We also showed that this difference in SHG efficiency for different phase-matching geometries has a direct consequence on the determination of  $\rho$  in the tissue. Combining the phenomenological model 3.1 and the expressions for the relative SHG efficiencies 3.52, one can deduce the measured  $\rho_{app}$ :

$$\rho_{app} = \rho e^{-\frac{z}{\Delta l_a}} \frac{\iint |\mathcal{E}\mathcal{E}_{x||,x||}^e|^2 d\Omega}{\iint |\mathcal{E}\mathcal{E}_{y\perp,y\perp}^e|^2 d\Omega}. \quad (3.54)$$

It shows that the determination of the true anisotropy parameter  $\rho$  on the tissue scale  $\rho$  is affected by two independent effects. The first is the diattenuation, which is due to different attenuation lengths for 2 polarizations and is characterized by a diattenuation length  $\Delta l_a$ . The second is the birefringence  $\Delta n$ , which results in different phase-matching conditions for the SH waves generated by ordinary or extraordinary excitation fields. It is noteworthy, that besides these two effects, diattenuation and birefringence, measuring  $\rho$  on each lower scale of collagen structure ( $\rho_{\text{fib}}$  or  $\rho_{\text{mol}}$ ) introduces additional uncertainty in the determination of anisotropy parameter.

The diattenuation is progressively accumulated with depth, so it is negligible in thin collagen samples and near the surface. In thick tissues, it can be measured from the  $z$ -diagrams and corrected for. However, it is not the case for the birefringence. While the accumulated average phase shift between the ordinary and extraordinary polarizations is negligible for thin samples, the alteration of relative SHG efficiencies due to birefringence is present at any depth and cannot be measured directly.

The simulation results for tendon have also consequences on the interpretation of SHG from cornea. While the cornea is macroscopically non-birefringent, it is birefringent locally. Thus, within a lamella, the different phase-matching conditions for ordinary and extraordinary waves can also result in different SHG efficiencies, which introduces error on  $\rho$  measurements. More generally, the effect of altered SHG efficiency due to birefringence is present as soon as the collagen assembly occupies a significant part of the focal volume. It should be the case not only for dense collagen tissues such as tendon, but even for thin or isolated fibers and fibril bundles in skin, vessels, fascia and other dense connective tissues.

In spite of substantial complexity of SHG in collagen, for which some aspects are revealed in our studies, we believe that further work could improve the robustness and accuracy of nonlinear tensor measurements. Notably, further numerical simulations of phase matching within the focal volume as a function of dispersion and birefringence should be performed to study the influence of these parameters on SHG efficiency. Additionally, precise independent measurements of tendon optical parameters such as index, dispersion and birefringence should be performed.

The numerical simulations described in this work are generally very time-consuming for typical desktop CPUs and require intensive computation solutions such as clusters or general-purpose calculation GPUs. For example, on the mid-range GPU we used, the calculation time for one set of parameters was about 3 hours, which is few times longer

than the real experiment. In this context we believe that further increase of calculation speed should be considered. For example, taking into account that the diagrams  $I(\alpha, z_{obj})$  are obtained by integrating angular radiation diagrams  $\mathcal{I}(\theta, \varphi)$  over the solid angle, the resolution (number of points) of the latter directly influences the calculation time. However, as we are eventually interested in the total intensity, we expect that satisfactory precision can be achieved with relatively small number of points. Hence, the influence of the number of points in  $\mathcal{I}(\theta, \varphi)$  on the resulting precision should be studied to reduce the calculation time.

To conclude, we demonstrated the complexity of P-SHG image processing in collagenous tissues, first by a phenomenological model and then by direct numerical simulations. Our results show that the experimental data are affected with most of the tissue optical parameters, such as birefringence, index dispersion, diattenuation and polarization cross-talk. Further numerical simulations and independent measurement of tissue index, dispersion and birefringence are required to increase the precision on the determined SHG anisotropy parameter  $\rho$ . Nevertheless, our study already provides a comprehensive understanding of P-SHG images and enables the determination of SHG anisotropy with reasonable accuracy.

# Chapter 4

## Tendon biomechanics

### Introduction

The relationship between microscopic organization and its macroscopic manifestation resulting in mechanical features is a great concern in connective tissue study. Advances in this respect should help clinical studies dealing with tendon and ligament injuries, and should provide clues for creating new biomimetic materials. Tendon is a model tissue for these studies, as it has simple unidirectional geometry, for which mechanical assays are straightforward. Tendon has unique mechanical properties, which are conferred by its microscopic structure and hierarchical organization. These properties have been widely studied in particular on rat-tail tendons, not least because they are easily extracted from rat tails which are widely available. However, to gain further insight on the origin of mechanical response and get information on the reorganization of tissue upon stretching, the mechanical assays must be coupled to techniques providing complementary information on the microscopic scale.

Several studies implementing incremental stretching assays coupled with imaging have been reported. Confocal microscopy has been used to track cell nuclei in a stretched tendon [142]. Crimp straightening and apparition during stretching and relaxation have been monitored by optical coherence tomography (OCT) [95]. Earlier, Misof et al. [47] reported stress-strain measurements with simultaneous X-ray scattering to evidence increasing lateral order in tendon during stretching.

SHG proved highly specific for imaging fibrillar collagen, which makes it a perfect tool for morphological studies. Additionally, SHG efficiency strongly depends on the packing properties of collagen molecules, thus providing a promising way to assess changes in structural order associated with tissue deformation. P-SHG gives to this inherent feature a quantitative aspect, allowing one to measure nonlinear susceptibility tensor variations associated with disorder, as shown in chapter 2 (2.3.5). Hence, SHG microscopy is a

perspective technique to provide complementary microscopic information during tendon mechanical assays.

To the best of our knowledge, no such study involving both SHG imaging and mechanical assays has been reported up to now. Thus, we performed a proof of concept implementation of simultaneous loading and SHG imaging of tendon. Besides the demonstration of feasibility of the method, we studied crimps behavior during load-relaxation cycles in rat-tail tendons. Furthermore, on an improved experimental setup allowing for polarization-resolved detection, we performed P-SHG in stretched tendon in order to monitor anisotropy parameter  $\rho$  upon tissue reorganization. These studies were performed in collaboration with J.-M. Allain and V. Tran from the Solids Mechanics Laboratory at Ecole Polytechnique (CNRS - MinesParisTech).

This chapter is organized as follows. In the first section will be presented the two experimental setups, which were developed for the proof of concept and for the P-SHG experiment, respectively. The second section is devoted to our results on coupling mechanical assays in rat-tail tendons with SHG imaging. The experimental results obtained together with one of my colleagues Y. Goulam Houssen are presented in the form of an article published in Journal of Biomechanics [143]. In the third section we present P-SHG experiments carried out in tendon during incremental stretching, also in the form of an article, which is published in Biophysical Journal [139]. Finally, in the fourth section the obtained results will be discussed.

## 4.1 Experimental setup

Stress-strain measurements on tendon were performed on two different implementations of our experimental setup. Both setups were implemented on the base of the multiphoton microscope described in 3.1. They share the excitation part and the epidetection path, but differ in forward detection path and mechanical devices used for tendon traction. The corresponding schemes and images are displayed in the Fig. 4.1.

The first setup (Fig. 4.1 a-c) uses a custom traction device developed by D. Caldemaison from Solid Mechanics Laboratory, Ecole Polytechnique, installed in the place of the sample stage. It allows for uniaxial asymmetrical traction of tendon, as it features only a single motor on one side, the other side being immobile (see Fig. 4.1 a). The force is measured using a 10N load cell (XFL225D10, FGP Sensors), and the displacement is measured by a displacement sensor. Small metal plates with a pin are used to attach the tendon, which extremities are coiled around the pin and glued with cyanacrylate to the plates. The plates are then fixed by two traction heads, one mobile and one immobile. The forward SHG detection block is removed to let enough place for the traction device installation, and detection for both SHG (collagen in tendon) and 2PEF (fluorescence

from latex beads) is performed in the backward direction. As the stretching is asymmetrical, slight adjustment of the tendon lateral position is required to always image the same region of the tendon fascicle. Characteristic patterns in SHG images are used as references to identify this region.

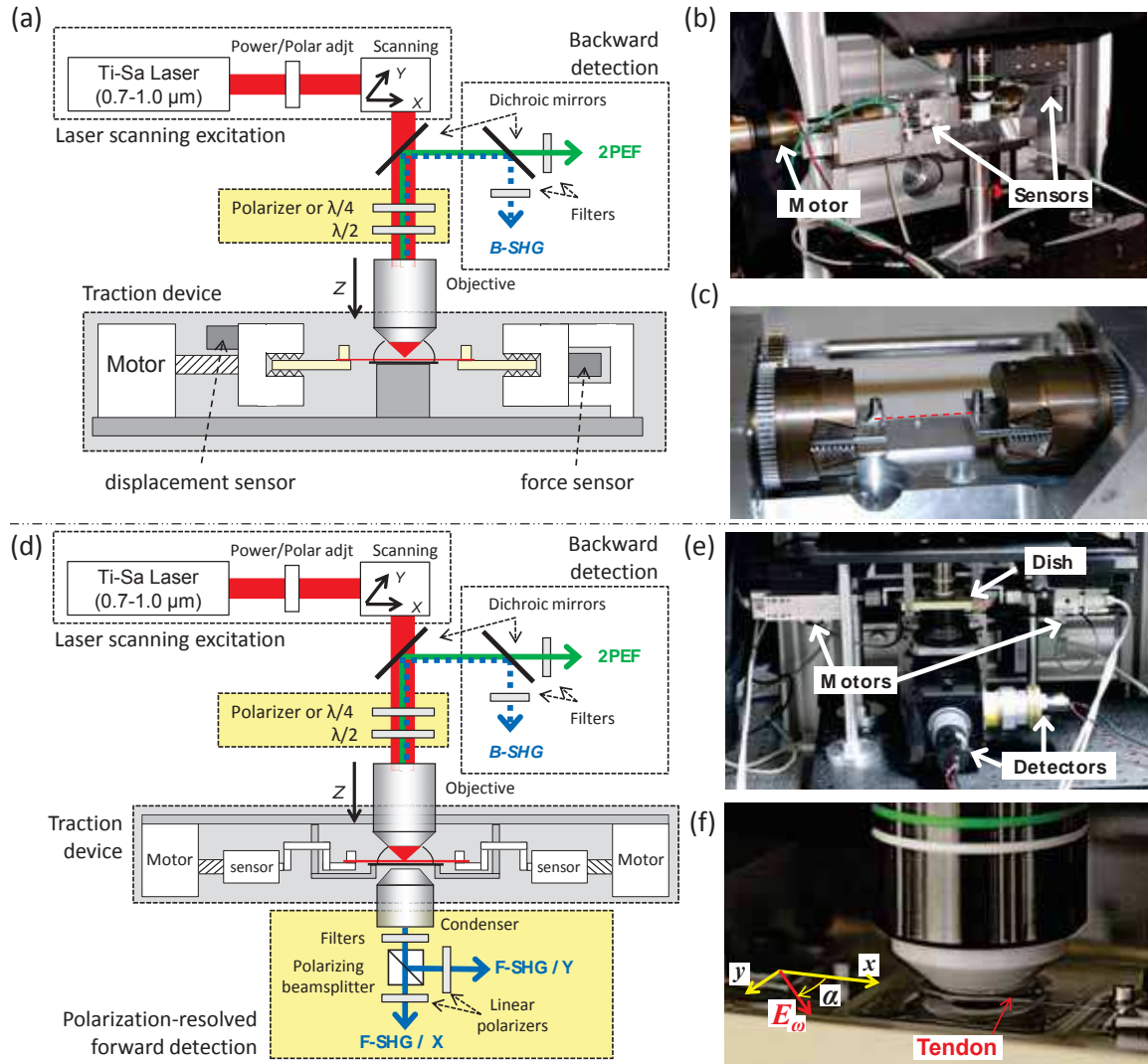


Figure 4.1: Experimental setups for biomechanical studies. (a-c) Asymmetric traction device used for the proof of concept experiment. (d-f) Symmetric traction device for P-SHG measurement. (a, d) Scheme of the setup. (b, e) General view of the setup. (c, f) Close view of the sample holder with attached tendon. Red dashed line in (c) indicates the tendon.

The traction device in the second setup (Fig. 4.1 d-f) represents an improvement of the first one. First, it has two motors (drl42pa2g-04; Oriental Motor, Tokyo, Japan), one on each side of the tendon, which are moving with equal speed and enable symmetrical stretching. Secondly, it has two force sensors (k1563-100N; Scaime, Annemasse, France) to increase precision. Finally, its specific design with a transparent basin allows for detection of forward-emitted SHG, which is resolved into  $x$ - and  $y$ -polarizations in the detection

module (described in 3.1). Backward detection is also possible and is usually used for detection of 2PEF from fluorescent latex beads labelling tendon. Due to symmetrical stretching, the zone of interest in the center of tendon thus remains immobile, which is verified by looking at specific pattern created by fluorescent beads.

## 4.2 Proof of concept of biomechanical assays coupled with SHG imaging

### 4.2.1 Introduction

In this section we report continuous monitoring of rat-tail tendon during stretch/relaxation cycles by SHG microscopy. In this paragraph we give a brief outline of the results, which are detailed immediately after in the form of a journal article.

We performed series of stress-relaxation cycles at increasing maximal strain (2%, 4%, 5%, 8% and 12%). In a series, for a maximal strain of, for example, 2%, the loading path in percent was 0-1-2-1-0-1-2-1-0-... (see Fig. 2 in the article in 4.2.2). The maximum stress we observed for a series at a given maximal strain increases linearly with this strain as expected. More interestingly, we observed hysteresis in the stress-strain curve during the first cycle of a series with a new maximal strain, but not for the following cycles. It means that the stretching and relaxation parts of the curve do not coincide for the first cycle. It evidences that tendon undergoes structural reorganization when stretched further than during former few cycles. Equivalently, it means that the equilibrium length of a relaxed tendon increases after a preconditioning to a new maximal strain.

The loading cycles were accompanied by SHG imaging of crimp morphology. Crimp pattern is typical for tendons in relaxed state, and has a pseudo-periodical aspect, so the average crimp period can be a relevant parameter to quantify the tendon relaxation (see Fig. 3 in the article in 4.2.2). In each cycle of each series at increased maximal strain, we measured the crimps period at zero strain that corresponded to the relaxed state of tendon. For example, for a cycle 0-1-2-3-4-3-2-1-0 we measured the crimp period twice, at the first and at the last 0% strain. We observed a decrease in crimp period at zero strain with the maximal strain in series. Indeed, each new maximal strain results in a new preconditioning of tendon, i.e. in longer length in relaxed state. When relaxed back to zero, longer tendons are naturally more crimped.

To conclude, we implemented the first mechanical assays in tendon with simultaneous SHG imaging, to the best of our knowledge. We showed that SHG imaging at microscopic scale and mechanical measurements at macroscopic scale give consistent results (see Fig. 2f and 3h in the article in 4.2.2). This multiscale approach showed that ten-

don is preconditioned to a new structural state when it is stretched to a higher extent. Additionally, we showed that crimp period could be a relevant parameter to quantify the tendon relaxation. Indeed, the crimp period reveals inner mechanisms of microstructural reorganization, and therefore is a good candidate to distinguish mechanical models of the tendons.

#### **4.2.2 Monitoring micrometer-scale collagen organization in rat-tail tendon upon mechanical strain using second harmonic microscopy**



Contents lists available at ScienceDirect

Journal of Biomechanics

journal homepage: [www.elsevier.com/locate/jbiomech](http://www.elsevier.com/locate/jbiomech)  
[www.JBiomech.com](http://www.JBiomech.com)

## Monitoring micrometer-scale collagen organization in rat-tail tendon upon mechanical strain using second harmonic microscopy

Y. Goulam Houssen<sup>a,b,c</sup>, I. Gusachenko<sup>a,b,c</sup>, M.-C. Schanne-Klein<sup>a,b,c</sup>, J.-M. Allain<sup>b,d,\*</sup>

<sup>a</sup> Ecole Polytechnique, Laboratory for Optics and Biosciences, 91128 Palaiseau, France

<sup>b</sup> CNRS, 91128 Palaiseau, France

<sup>c</sup> INSERM U696, 91128 Palaiseau, France

<sup>d</sup> Ecole Polytechnique, Solid Mechanics Laboratory, 91128 Palaiseau, France

### ARTICLE INFO

#### Article history:

Accepted 6 May 2011

#### Keywords:

Second harmonic generation  
Collagen  
Preconditioning  
Mechanical properties  
Tendon

### ABSTRACT

We continuously monitored the microstructure of a rat-tail tendon during stretch/relaxation cycles. To that purpose, we implemented a new biomechanical device that combined SHG imaging and mechanical testing modalities. This multi-scale experimental device enabled *simultaneous* visualization of the collagen crimp morphology at the micrometer scale and measurement of macroscopic strain–stress response. We gradually increased the ultimate strain of the cycles and showed that preconditioning mostly occurs in the first stretching. This is accompanied by an increase of the crimp period in the SHG image. Our results indicate that preconditioning is due to a sliding of microstructures at the scale of a few fibrils and smaller, that changes the resting length of the fascicle. This sliding can reverse on long time scales. These results provide a proof of concept that continuous SHG imaging performed simultaneously with mechanical assay allows analysis of the relationship between macroscopic response and microscopic structure of tissues.

© 2011 Elsevier Ltd. All rights reserved.

### 1. Introduction

The relationship between microscopic macromolecular organization and macroscopic biomechanical properties is a general concern in collagenous tissues. Tendon is a model system in that respect; it is almost unidirectional and does not require biaxial loading in biomechanical studies. It is a highly structured tissue designed for force transmission from muscle to skeleton, mainly composed of type I collagen that forms fibrils of around 200 nm diameter. These fibrils assemble into fibers that further form fascicles with a crimped pattern (Kastelic et al., 1978). This hierarchical organization is responsible for the biomechanical properties of the tissue.

The macroscopic mechanical properties of tendon are fairly well known (Abrahams, 1967; Ker, 2007). Quasi-static stretching of rat-tail tendon gives a non-linear response, with a toe region in the first few percent of strain, followed by a linear region. However, the relationship between these properties and the structure at lower scales (such as fibers or fibrils) remains a subject of strong interest (Puxkandl et al., 2002; Fratzl, 2003; Screen et al., 2004; Gupta et al., 2010). The initial toe region is

attributed to a straightening of the initially crimped collagen fibrils (Rigby et al., 1959; Viidik and Ekholm, 1968; Hansen et al., 2002; Franchi et al., 2007). The linear region is considered as the response when the collagen fibrils are aligned in the direction of traction, so it is associated with an extension of collagen fibers combined with a sliding of the fibrils in their proteoglycan matrix (Fratzl, 2003). Tendons subjected to cycles of stretch/relaxation exhibit a hysteretic stress–strain relationship (Fung, et al., 2009). This is attributed to a rearrangement of the proteoglycan matrix around the collagen fibrils (Puxkandl et al., 2002; Redaelli et al., 2003).

Further insight into these microscopic processes requires continuous monitoring of tendon microstructure during mechanical assays. In that respect, few studies using semi-continuous optical imaging of tendon stretching have been reported. Confocal microscopy has been used to track labeled cell nucleus in tendons (Screen et al., 2004). Optical Coherence Tomography (OCT) has been used to monitor the straightening of tendon crimps with applied tensile strain (Hansen et al., 2002). The latter technique provides images of unlabeled collagen fibrils, but with limited contrast because of its low specificity. In that context, Second Harmonic Generation (SHG) microscopy is a valuable technique to investigate the microstructure of collagenous tissues. SHG is a multiphoton mode of contrast at exactly half the excitation wavelength that is highly specific for dense noncentrosymmetric media, such as fibrillar collagen (Freund et al., 1986; Campagnola

\* Corresponding author at: Ecole Polytechnique, Solid Mechanics Laboratory, 91128 Palaiseau, France. Tel.: +33 1 69335812; fax: +33 1 69335706.

E-mail address: [allain@lms.polytechnique.fr](mailto:allain@lms.polytechnique.fr) (J.-M. Allain).

et al., 2002; Stoller et al., 2002; Zoumi et al., 2002; Cox et al., 2003; Zipfel et al., 2003; Strupler et al., 2007; Deniset-Besseau et al., 2009). As a coherent nonlinear optical process, it is an effective *structural* probe of the micrometer-scale collagen macromolecular organization (Pena et al., 2005; LaComb et al., 2008; Rivard et al., 2011). Moreover, it is characterized by intrinsic three-dimensional (3D) resolution like two-photon excited fluorescence (2PEF). SHG microscopy hence enables 3D visualization of intact tendons by recording stacks of optically sectioned images with typically 1–3  $\mu\text{m}$  axial resolution. It has been shown to provide high-contrast images of the characteristic crimped pattern of this tissue (Stoller et al., 2002; Stoller et al., 2003; Williams et al., 2005; Erikson et al., 2007; Legare et al., 2007; Gusachenko et al., 2010). SHG imaging has recently been used to visualize damage in tendons after fatigue tests, and proved efficient in providing 3D maps of fiber orientations (Fung et al., 2010).

This paper reports the development of multi-scale experiments to monitor *simultaneously* the microstructural organization of tendon and its macroscopic mechanical response. To that end, we perform mechanical measurements while imaging optical sections of a whole tendon fascicle using SHG microscopy and analyzed the stress–strain relationship versus the crimp morphology. To the best of our knowledge, continuous monitoring of tendon microstructure during multiple loading cycles has not been reported yet. We observe that cyclic stretch/relaxation at increasing strains leads to a shift of the toe region accompanied by an increase of the crimp spatial period. Our data confirm that the toe region is due to the straightening of the crimps, and that the linear region is due to the fibrils sliding.

The paper is organized as follows: the next section is devoted to a detailed description of the experimental methods; then we present our mechanical measurements and SHG images for increasing cyclic stretching; we finally discuss the mechanical data through changes of the microstructure morphology.

## 2. Materials and methods

### 2.1. Rat-tail tendon preparation and clamping to the testing device

The tendons were extracted from Sprague Dawley rat tails (female, 250–300 g,  $n=3$ ). The tails were kept frozen until dissection. Incisions were made at the tapered end of the tails using pliers to pull out the tendon fascicles gently. The tendons were rinsed in phosphate buffered saline (PBS) and centrifuged at 4700 rpm ( $3 \times 10$  min) to remove all other tissue components. The tendon

fascicles were stored in PBS at 4 °C and used within a few days for the experiments.

Tendon fascicles were attached to the testing device as depicted in Fig. 1. They were glued with cyanoacrylate onto a metallic plate ( $20 \times 20 \times 1$  mm<sup>3</sup>) and coiled on rods inserted in the plate, in an almost symmetric manner to limit any boundary effect due to gluing (see Fig. 1C). The fascicles were suspended vertically and allowed to rotate freely before gluing to a second plate, to minimize initial torsion. We always gently manipulated the tendon fascicles to avoid uncontrolled stretching and maintained them in PBS to prevent drying (except for the ends). The plates were then firmly clamped to small screw-tightened grips within the testing device. The distance between the grips was adjusted to maintain the tendon fascicles almost horizontal, with 1–2 mm of deflection at most. This initial deflection is due to the fascicle weight and cannot be avoided without stretching the fascicle. During all experiments, the tendon fascicles were immersed in PBS using a glass cover-slip just under the sample (see Fig. 1A and B). In some experiments, the tendon fascicle was labeled with fluorescent latex beads (1  $\mu\text{m}$  diameter, L1030, Sigma-Aldrich) to monitor local strains.

### 2.2. Multiphoton imaging

The tendon microstructure was observed by putting the testing device in place of the stage in a custom-built laser scanning microscope (see Fig. 1A and B; Strupler et al., 2007). Tendons were illuminated in an upright geometry using circularly-polarized excitation at 860 nm from a femtosecond titanium–sapphire laser (Spectra-Physics). SHG and 2PEF signals were recorded in two photon-counting epi-detection channels using appropriate dichroic mirrors and spectral filters (Strupler et al., 2007). We used a  $20 \times 0.95$  NA water objective with typically 0.40  $\mu\text{m}$  (lateral)  $\times$  1.6  $\mu\text{m}$  (axial) resolution near the sample surface. SHG images were recorded using 200 kHz pixel rate and 0.8  $\mu\text{m}$  pixel size, with typically 50 mW excitation power. We verified that we always imaged the same region of the tendon fascicle using characteristic patterns in the SHG images as references. When necessary, we slightly shifted the microscope stage to compensate for small lateral displacements during loading cycles. Adjustment of the objective focus was usually required because of slight axial displacement of the tendon fascicle. In some experiments, z-stacks of combined SHG and 2PEF images were acquired along the full thickness of the tendon fascicle (every 2  $\mu\text{m}$ ). No photo-damage of the tendon was observed under these experimental conditions.

SHG images were analyzed using ImageJ software (W. Rasband, NIH) to estimate the crimp period (distance measurements along the tendon axis).

### 2.3. Mechanical testing

Mechanical tests were performed at room temperature using a uniaxial RAITH® testing device. The force was measured using a 10 N load cell (XFL225D10, FGP Sensors) with 1% accuracy. Stress was obtained as the force divided by the initial cross-sectional area, assuming a cylindrical shape of the tendon fascicle. Typical diameter was 400  $\mu\text{m}$ , as obtained from SHG image-stacks recorded before stretching. Strain was obtained as the ratio of the grips displacement divided by the initial length of the tendon fascicle (typically 26 mm). Displacement and force values were measured every second. The fascicles were stretched at 10  $\mu\text{m/s}$  constant strain rate (around  $3 \times 10^{-2}\%$  s<sup>-1</sup>).

To investigate possible slipping, we compared the grips displacement to the local displacement on the tendons through the tracking of ink labels, separated by

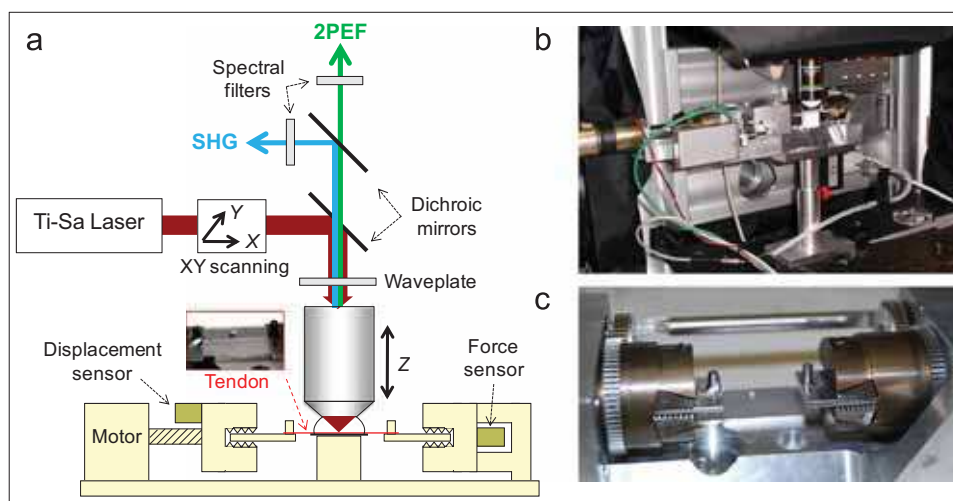


**Fig. 1.** Experimental setup. (a) Scheme of the laser scanning microscope and the traction device. (b) Picture of the traction device under the objective, showing the tendon immersed in water on a glass coverslip and supported by a teflon base. (c) Zoomed view of the tendon fascicle mount and the grips.

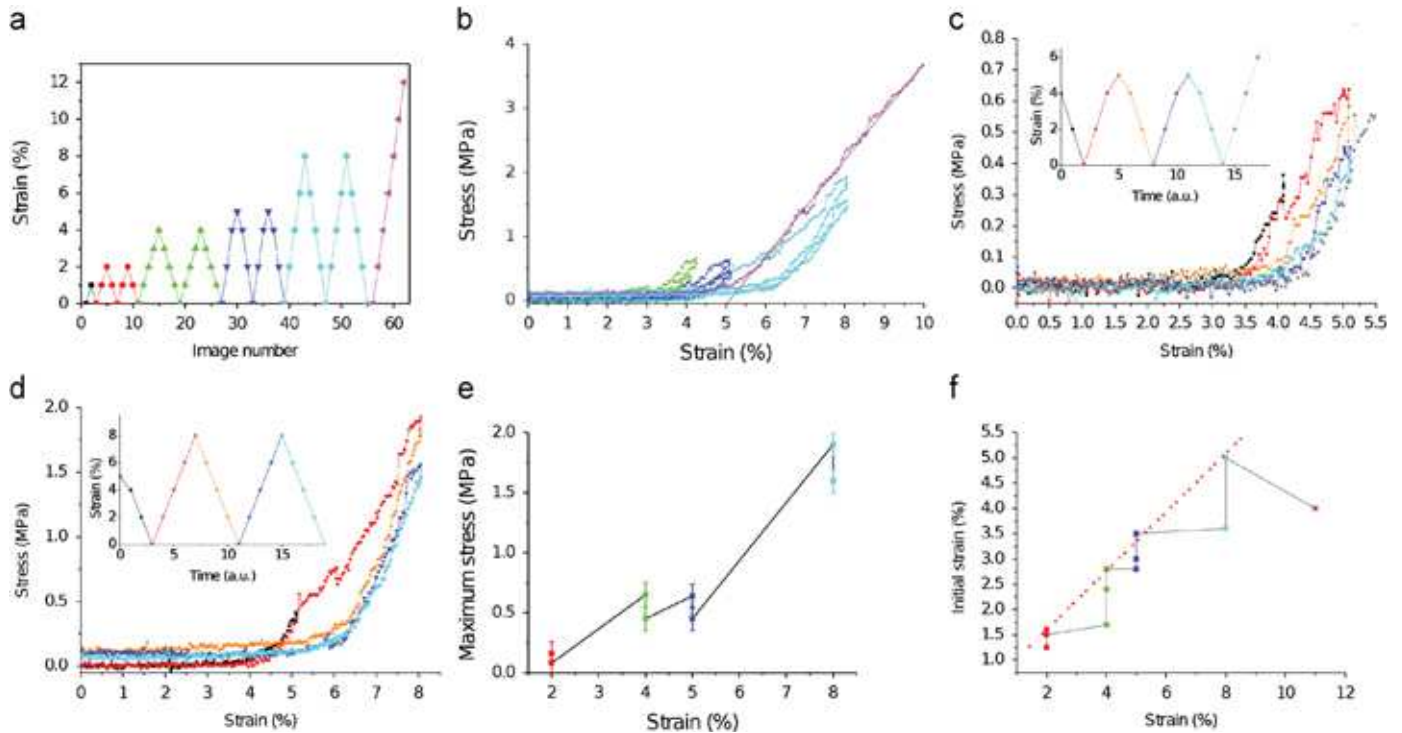


**Fig. 2.** Mechanical behavior of a tendon fascicle. (a) Loading path versus the image number; each color is associated with one ultimate strain. (b) Stress–strain curves for the whole loading path. (c)–(d) Stress–strain curves for a series of cycles at 5% and 8% ultimate strain, with color codes as indicated in the insert. (e) Maximum stress per cycle versus the ultimate strain. (f) Initial measurable strain versus the ultimate strain. (For interpretation the references to color in this figure legend, the reader is referred to the web version of this article.)

10 mm and imaged under a binocular microscope. No significant difference was observed. However, we noticed that significant torsion could occur if the tendon fascicle torsion was not carefully minimized before gluing.

Typical loading path was composed by successive series of two stretch/relaxation cycles at the same ultimate strain (see Fig. 2A). The ultimate strains of the series were progressively increased up to breaking. The traction device was immobilized during image acquisition.

### 3. Results

#### 3.1. Stress–strain relationship

Typical strain–stress measurements are displayed in Fig. 2. Fig. 2A shows the loading path made up of successive series at increasing ultimate strains (2, 4, 5, 8, and 12%). Each point corresponds to a typically 40 s pause for SHG imaging. Fig. 2B shows the measured stresses for the whole loading path. We observe similar stress–strain curves to those previously reported (Rigby et al., 1959), with an initial toe-region followed by a linear part at larger strains, which can be clearly defined in our case as strains higher than 6%. The curves shift to the right as we gradually increase the ultimate strain in the series. For example, the curves for 5% ultimate strain (in blue) seem to be a translation to higher strains of the curves for 4% ultimate strain (in green). The only exception to this observation is the last curve (in magenta). We attribute this backward shift at 12% to a longer pause (about 5 min) at 0% strain before stretching to 12%.

The observed stresses are quite reproducible in our experiments but they are significantly lower than previously reported ones (Hansen et al., 2002; Sionkowska and Wess, 2004; Screen et al., 2005). The slope of the linear part gives an equivalent Young modulus of 75 MPa (considering the last stretching up to 12% strain). This quantitative discrepancy may come from uncontrolled strain application during fascicle preparation. We think however that it is most likely due to the storage in PBS solution,

which was reported to lead to fascicle swelling and subsequent artificial increase of the fascicle cross-section for stress calculation (Legerlotz et al., 2010). Moreover, we corroborated that fresh tendon fascicles give similar results to previously frozen ones. Our setup also enabled us to monitor the motion of the tendon surface by imaging fluorescent beads. We verified in this way that there was no excessive torsion and that the macroscopic strain corresponded to the local strain, at least for the first stretching.

Fig. 2B and C focus on the stress–strain relationship for the series with ultimate strains of 5% and 8%, respectively. We also include, for clarity, the last relaxation of the previous series (in black) and the first stretch of the next series (in grey). The set of curves illustrates preconditioning; the curves shift slowly to the right, reaching lower stresses for the same strain for the second cycle. The modification of the stress–strain relationship is strongest during the first stretch of a series. The stresses in the first relaxation and in the second cycle at this ultimate strain are very close, and cannot be easily distinguished given our sensor resolution. Thus we performed only two cycles per series at a given ultimate strain.

To quantify more precisely the preconditioning, we measured the maximum stress reached in each cycle (Fig. 2E) and the minimal strain at which we could measure a significant stress (Fig. 2F). These two quantities could be defined in all the cycles, whereas we could not determine a linear part for cycles with small ultimate strain. As there are two cycles per series, there are two maximum stresses per ultimate strain in Fig. 2E. The maximal stress of the second cycle of a series is always smaller than that of the first cycle, illustrating preconditioning. As expected, we see that the ultimate stress increases with the ultimate strain, although this increase is not homogeneous—for example, the ultimate stresses for 4% and 5% ultimate strains are similar.

Fig. 2F displays the lowest strains at which the stress is significantly different from the noise versus the ultimate strain. This quantity characterizes the onset of the toe-region of the

stress–strain curve. As strain is measured with respect to the initial length of the fascicle, it can be considered as the change in the resting length of the tendon fascicle; the larger the lowest strain, the longer the fascicle. Since a series includes two stretches and two relaxations, there are four points for each ultimate strain, although in most cases the last three ones are indistinguishable. We call this value the limit lowest strain for a given series. It is reached after the first stretch for each series and increases linearly with the ultimate strain of the series (dotted line in Fig. 2F). Linear fitting gives a slope of 0.58 and a lowest strain of 0.44%.

Fig. 2F appears as a stair-shaped curve. The lowest strain indeed increases abruptly between the first stretch and the first relaxation in a series. Then, when the ultimate strain is increased for a new series, the first stretch has not been preconditioned, and the lowest strain does not change. Consequently, the points are almost indistinguishable and the curve in Fig. 2F moves horizontally. The last point at 12% ultimate strain is lower since we allowed the tendon fascicle to relax for 5 min.

### 3.2. Crimp evolution

In order to connect the macroscopic biomechanical behavior of tendon to its microscopic collagen organization, we paused and recorded SHG images at every point on the loading path. Typical images are displayed in Fig. 3A–E and correspond to positions emphasized by orange circles in the loading path depicted in Fig. 3F. These images show  $\approx 2\text{--}3\ \mu\text{m}$  thick transverse sections within the intact tendon. They display a fibrillar pattern characteristic for the collagen macromolecular organization in agreement with previous reports (Stoller et al., 2003; Williams et al., 2005; Erikson et al., 2007). They do not directly show the fibers within the tendon fascicles, but correspond to interference patterns. The SHG signal indeed results from the coherent

summation of the SHG response of all the fibrils within the focal volume and is more or less intense depending on the relative position and orientation of these fibrils (LaComb et al., 2008; Rivard et al., 2011; Strupler and Schanne-Klein, 2010).

In most of our experiments, the tendon fascicle exhibited small but well defined crimps at 0% strain (Fig. 3A). At the ultimate strain of a cycle, the fascicle was always straight, with no visible crimped pattern in intact tendons (Fig. 3B and D). In broken tendons, we observed a stretched region in the center and a crimped region near the tendon edge in the same image. During stretching, the crimps disappear at a given strain, and then reappear at higher strain during relaxation, indicating an inelastic behavior.

In order to quantify the crimp pattern along a loading path, we measured the crimp period in the SHG images. Fig. 3G shows the variation of the crimp period at 0% strain (along the dotted line for 0% in Fig. 3F). The period decreases with the cycle number, which means that the crimps are increasingly marked in SHG images (see Fig. 3A, C and E) after every cycle. Note that complementary measurements of the crimp amplitude would require 3D reconstruction of the tendon fascicle by recording SHG image stacks instead of only one transverse section. This could result in confused data because of relaxation during the longer pauses, which would be needed for SHG imaging.

Fig. 3H displays the crimp period at 2% strain versus the cycles with ultimate strain above 4% (see the dotted line 2% in Fig. 3F). There are two points per cycle, the lowest one being always in the relaxation part. For cycles of a given series (same ultimate strain—same color in Fig. 3), we observe that the period increases between a relaxation and the next stretch.

We note that the crimp period, shown in Fig. 3H, evolves similarly to the lowest measurable strain, shown in Fig. 2E for the same tendon fascicle. Both of them indicate that there is an irreversible deformation of the tendon fascicle during preconditioning.

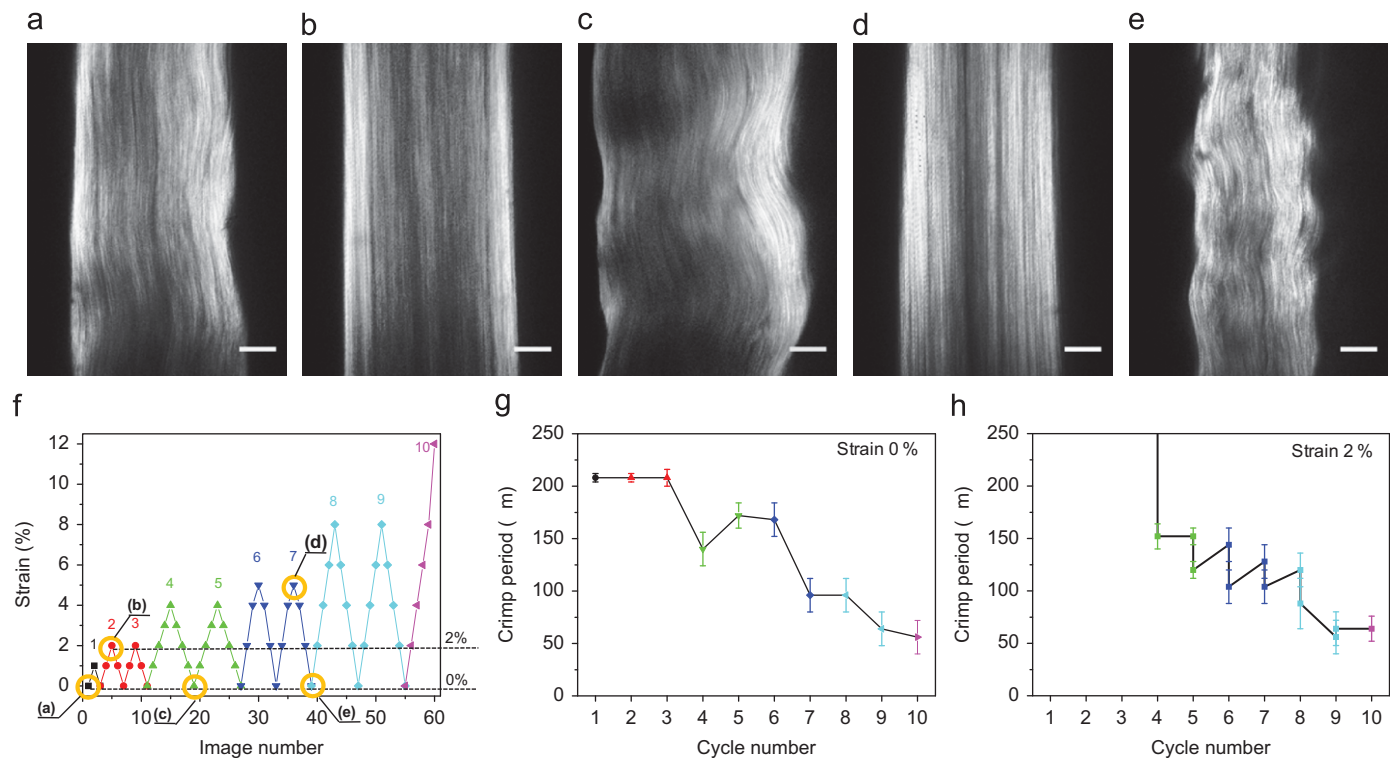


**Fig. 3.** SHG imaging of the tendon fascicle microstructure. (a)–(e) SHG images at the time points underlined in orange in (f); scale bars: 50  $\mu\text{m}$ . (f) Loading path. (g) Evolution of the crimp spatial period at 0% strain during the cycles. (h) Same at 2% strain. These imaging data were recorded simultaneously with the mechanical data displayed in Fig. 2, on the same tendon fascicle. (For interpretation of the references to color in this figure legend, the reader is referred to the web version of this article).

#### 4. Discussion

In this study, we successfully implemented continuous *in situ* SHG imaging of a tendon subjected to a mechanical assay. SHG microscopy advantageously provided optically sectioned images of the micrometer-scale fibrillar organization of the tendon. Our SHG images showed a better contrast than polarized-light microscopy images that integrate the tendon structure over its full thickness. Moreover, the high specificity of SHG microscopy for fibrillar collagen resulted in high-contrast images compared to other 3D techniques like confocal microscopy or optical coherence tomography.

SHG images and mechanical measurements show that preconditioning is associated with a change in the stress-free configuration. It is stronger during the first stretch for a given ultimate strain, although many more cycles are required to reach the limit curve (Abrahams, 1967). Preconditioning is associated both with a shift of the toe-region of the stress–strain curve to higher strains (Fig. 2F), and a decrease in the crimp period (Fig. 3G and H). We attribute this behavior to a sliding of the collagen fibrils with respect to each other, extending the relaxed length of the tendon fascicle. Since SHG observations are sensitive to the fibril scale, our results indicate that sliding occurs at a similar or smaller scale, but they cannot distinguish between fibrillar and intra-fibrillar sliding.

However, the preconditioning is not irreversible. During an extended pause at the initial length of the tendon fascicle, we observed a decrease of the resting length (see Fig. 2F). This recovery from previous preconditioning is usually attributed to a reconfiguration of the bonds between fibrils or lower-scale structures (Vesentini et al., 2005; Ciarletta and Ben Amar, 2009). On a shorter time scale, we observe that the crimp period at 2% strain increases significantly between a relaxation and the next stretching of the tendon fascicle. This was not observed at 0% strain, which indicates that relaxation involves different time scales, and therefore different length scales. We cannot access faster relaxation times than a few tenths of a second, which is the time needed to adjust imaging parameters (Gupta et al., 2010).

All these considerations indicate that preconditioning is mostly due to sliding of microstructures inside the fascicle. SHG imaging shows that a significant part of the sliding occurs between fibrils; previous works showed that sliding occurs between and inside the fibrils (Puxkandt et al., 2002; Screen et al., 2004; Cheng and Screen, 2007). We also observed that the preconditioned state is temporary and can recover, at least partially, on a longer time scale (Hansen et al., 2002).

#### 5. Conclusion

We developed a new multi-scale experiment to simultaneously monitor the fibrillar collagen architecture at microscopic scale and the strain–stress relationship at macroscopic scale in biological tissues. To that end, we combined a multiphoton microscope and a mechanical device, and we performed simultaneous SHG imaging and controlled mechanical loading of rat-tail tendon. This biomechanical setup has never been reported yet to the best of our knowledge. Our study provides a proof of concept that this device enables analysis of the connection between macroscopic response and microscopic structure of tissues. We showed that mechanical preconditioning mostly arises from sliding and is reversible on long time-scales. This supports the notion that the mechanical behavior of a tendon fascicle relies on its microstructure remodeling. Our experimental setup can be readily generalized to other mechanical assays and to any other bidimensional tissue, such as skin or cornea. SHG imaging can

also be combined with 2PEF imaging to visualize either elastin fibers or labeled cells. Our method should then permit continuous analysis of 3D remodeling of connective tissues in mechanical assays and bring new valuable information to biomechanics of microstructured tissues.

#### Conflict of interest statement

All authors have no conflict of interest and nothing to disclose.

#### Acknowledgments

We thank Daniel Caldemaïson and Viet Tran for their help in the design of the experimental setup.

#### References

- Abrahams, M., 1967. Mechanical behaviour of tendon *In Vitro*—a preliminary report. *Med. Biol. Eng.* 5, 433–443.
- Campagnola, P.J., Millard, A.C., Terasaki, M., Hoppe, P.E., Malone, C.J., Mohler, W.A., 2002. Three-dimensional high-resolution second-harmonic generation imaging of endogenous structural proteins in biological tissues. *Biophys. J.* 82, 493–508.
- Cheng, V.W.T., Screen, H.R.C., 2007. The micro-structural strain response of tendon. *J. Mater. Sci.* 42, 8957–8965.
- Ciarletta, P., Ben Amar, M., 2009. A finite dissipative theory of temporary interfibrillar bridges in the extracellular matrix of ligaments and tendons. *J. R. Soc. Interface* 6, 909–924.
- Cox, G., Kable, E., Jones, A., Fraser, I.K., Manconi, F., Gorrell, M.D., 2003. 3-dimensional imaging of collagen using second harmonic generation. *J. Struct. Biol.* 141, 53–62.
- Deniset-Besseau, A., Duboisset, J., Benichou, E., Hache, F., Brevet, P.F., Schanne-Klein, M.-C., 2009. Measurement of the Second-Order Hyperpolarizability of the Collagen Triple Helix and Determination of Its Physical Origin. *J. Phys. Chem. B* 113, 13437–13445.
- Erikson, A., Ortegren, J., Hompland, T., Davies, C.D., Lindgren, M., 2007. Quantification of the second-order nonlinear susceptibility of collagen I using a laser scanning microscope. *J. Biomed. Opt.* 12, 044002.
- Franchi, M., Fini, M., Quaranta, M., Pasquale, V.D., Raspanti, M., Giavaresi, G., Ottani, V., Ruggeri, A., 2007. Crimp morphology in relaxed and stretched rat Achilles tendon. *J. Anat.* 210, 1–7.
- Fratzl, P., 2003. Cellulose and collagen: from fibres to tissues. *Curr. Opin. Colloid Interface Sci* 8, 32–39.
- Fung, D.T., Sereysky, J.B., Basta-Pljakic, J., Laudier, D.M., Huq, R., Jepsen, K.J., Schaffler, M.B., Flatow, E.L., 2010. Second Harmonic Generation Imaging and Fourier Transform Spectral Analysis Reveal Damage in Fatigue-Loaded Tendons. *Ann Biomed. Eng.* 38, 1741–1751.
- Freund, I., Deutsch, M., Sprecher, A., 1986. Connective-tissue polarity—optical second-harmonic microscopy, crossed-beam summation, and small-angle scattering in rat-tail tendon. *Biophys. J.* 50, 693–712.
- Fung, D.T., Wang, V.M., Laudier, D.M., Shine, J.H., Basta-Pljakic, J., Jepsen, K.J., Schaffler, M.B., Flatow, E.L., 2009. Subrupture tendon fatigue damage. *J. Orthop. Res.* 27, 264–273.
- Gupta, H.S., Seto, J., Krauss, S., Boesecke, P., Screen, H.R.C., 2010. *In situ* multi-level analysis of viscoelastic deformation mechanisms in tendon collagen. *J. Struct. Biol.* 169, 183–191.
- Gusachenko, I., Latour, G., Schanne-Klein, M.-C., 2010. Polarization-resolved second harmonic microscopy in anisotropic thick tissues. *Opt. Express* 18, 19339–19352.
- Hansen, K.A., Weiss, J.A., Barton, J.K., 2002. Recruitment of tendon crimp with applied tensile strain. *J. Biomech. Eng.* 124, 72–77.
- Kastelic, J., Galeski, A., Baer, E., 1978. Multicomposite Structure of Tendon. *Connect. Tissue Res.* 6, 11–23.
- Ker, R.F., 2007. Mechanics of tendon, from an engineering perspective. *Int. J. Fatigue* 29, 1001–1009.
- LaComb, R., Nadiarnykh, O., Townsend, S.S., Campagnola, P.J., 2008. Phase matching considerations in second harmonic generation from tissues: effects on emission directionality, conversion efficiency and observed morphology. *Opt. Commun.* 281, 1823–1832.
- Legare, F., Pfeffer, C., Olsen, B.R., 2007. The role of backscattering in SHG tissue imaging. *Biophys. J.* 93, 1312–1320.
- Legerlotz, K., Riley, G.P., Screen, H.R.C., 2010. Specimens dimensions influence the measurement of material properties in tendon fascicles. *J. Biomech.* 43, 2274–2280.
- Pena, A.-M., Boulesteix, T., Dartigalongue, T., Schanne-Klein, M.-C., 2005. Chiroptical effects in the second harmonic signal of collagens I and IV. *J. Am. Chem. Soc.* 127, 10314–10322.

- Puxkandl, R., Zizak, I., Paris, O., Keckes, J., Tesch, W., Bernstorff, S., Purslow, P., Fratzl, P., 2002. Viscoelastic properties of collagen: synchrotron radiation investigations and structural model. *Philos. Trans. R. Soc. Lond. B Biol. Sci.* 357, 191–197.
- Redaelli, A., Vesentini, S., Soncini, M., Vena, P., Mantero, S., Montevecchi, F.M., 2003. Possible role of decorin glycosaminoglycans in fibril to fibril force transfer in relative mature tendons - a computational study from molecular to microstructural level. *J. Biomech.* 36, 1555–1569.
- Rigby, B.J., Hirai, N., Spikes, J.D., Eyring, H., 1959. The Mechanical Properties of Rat Tail Tendon. *J. Gen. Physiol.* 43, 265–283.
- Rivard, A., Laliberté, M., Bertrand-Grenier, A., Harnagea, C., Pfeffer, C.P., Vallières, M., St-Pierre, Y., Pignolet, A., Khakani, M.A.E., Légaré, F., 2011. The structural origin of second harmonic generation in fascia. *Biomed. Opt. Express* 2, 26.
- Screen, H.R.C., Bader, D.L., Lee, D.A., Shelton, J.C., 2004. Local strain measurement within tendon. *Strain* 40, 157–163.
- Screen, H.R.C., Shelton, J.C., Chhaya, V.H., Kayser, M.V., Bader, D.L., Lee, D.A., 2005. The influence of noncollagenous matrix components on the micromechanical environment of tendon fascicles. *Ann. Biomed. Eng.* 33, 1090–1099.
- Sionkowska, A., Wess, T., 2004. Mechanical properties of UV irradiated rat tail tendon (RTT) collagen. *Int. J. Biol. Macromol.* 34, 9–12.
- Stoller, P., Celliers, P.M., Reiser, K.M., Rubenchik, A.M., 2003. Quantitative second-harmonic generation microscopy in collagen. *Appl. Opt.* 42, 5209–5219.
- Stoller, P., Reiser, K.M., Celliers, P.M., Rubenchik, A.M., 2002. Polarization-modulated second harmonic generation in collagen. *Biophys. J.* 82, 3330–3342.
- Strupler, M., Pena, A.-M., Hernest, M., Tharoux, P.L., Martin, J.-L., Beaufort, E., Schanne-Klein, M.-C., 2007. Second harmonic imaging and scoring of collagen in fibrotic tissues. *Opt. Express* 15, 4054–4065.
- Strupler, M., Schanne-Klein, M.-C., 2010. Simulating second harmonic generation from tendon: do we see fibrils? *Biomedical Optics, OSA Technical Digest, paper BTuD83*.
- Vesentini, S., Redaelli, A., Montevecchi, F.M., 2005. Estimation of the binding force of the collagen molecule-decorin core protein complex in collagen fibril. *J. Biomech.* 38, 433–443.
- Viidik, A., Ekholm, R., 1968. Light and electron microscopic studies of collagen fibers under strain. *Anat. Embryol.* 127, 154–164.
- Williams, R.M., Zipfel, W.R., Webb, W.W., 2005. Interpreting second-harmonic generation images of collagen I fibrils. *Biophys. J.* 88, 1377–1386.
- Zipfel, W.R., Williams, R.M., Christie, R., Nikitin, A.Y., Hyman, B.T., Webb, W.W., 2003. Live tissue intrinsic emission microscopy using multiphoton-excited native fluorescence and second harmonic generation. *Proc. Natl. Acad. Sci. USA* 100, 7075–7080.
- Zoumi, A., Yeh, A., Tromberg, B.J., 2002. Imaging cells and extracellular matrix in vivo by using second-harmonic generation and two-photon excited fluorescence. *Proc. Natl. Acad. Sci. USA* 99, 11014–11019.

## 4.3 Varying fibril ordering in tendon

### 4.3.1 Introduction

In the previous section we demonstrated the feasibility of SHG imaging during mechanical assays. In particular, we showed that tissue undergoes morphological changes that are manifested by crimp disappearance upon stretching. Further stretching of the tendon above the limit of crimp disappearance resulted in higher measured stress and was accompanied by changes in internal structure which could not be directly observed in microscopic images. A tendon can roughly be represented as a bundle of more or less aligned collagen fibrils. One can assume that further stretching of such a bundle is accompanied by fibril alignment, and hence results in lateral order increase at the submicrometre scale. It was shown in 2.3.5 that P-SHG provides information on orientational disorder in fibrillar tissue by measuring changes in  $\rho$  parameter, which makes it a perfect tool for testing this assumption. Here we give a brief outline of the obtained results, which are detailed immediately after in the form of a journal article.

We performed P-SHG measurements in rat-tail tendon at increasing strain in the same ROI (region of interest). The minimal strain chosen for P-SHG measurements was just above the threshold of crimps disappearance, so all measurements were performed on morphologically straight tendon. We recorded polarization-resolved SHG-images at increasing depth according to the protocol described in section 3.2, and processed them using the phenomenological model introduced in the same section. At all strains, we thus extracted the linear and nonlinear optical parameters of tendon, that is, birefringence  $\Delta n$ , diattenuation  $1/\Delta I_a$ , polarization cross-talk  $\eta$  and SHG anisotropy parameter  $\rho$  (see Fig. 5 in the article in 4.3.2).

Measured birefringence monotonously increased and was slowly saturating with strain, as expected because the tissue became denser and more anisotropic. Attenuation decreased for polarizations both parallel and perpendicular to the tendon axis, as expected because aligned tissue became less scattering and more transparent. The tendon region near the water-tendon interface was shown to be the source of polarization cross-talk, presumably due to the presence of loose and highly disordered fibrils. This cross-talk decreased with strain, as all the fibrils became more aligned, and the surface was better defined. Finally, the SHG anisotropy parameter  $\rho$  was shown to vary in a non-monotonous way. At small strains,  $\rho$  decreased with strain, and hence with order, as predicted by our theoretical model introduced in section 2.3.5. For larger strains, however,  $\rho$  increased with strain. Possible explanation of this behavior in the framework of our model is that further stretching leads to rupture of individual fibrils within the tissue, which produces loose fibril ends contributing to  $\rho$  increase. Alternatively, there could be an additional

mechanism that was not accounted for in our approach. We assumed that the minimal measured  $\rho$  corresponded to the case of perfectly aligned fibrils and was equal to the anisotropy parameter at the fibrillar scale  $\rho_{\text{fib}}$ . Indeed, for the Eq. 2.26 the case of perfect fibril alignment  $\theta = 0$  gives  $\rho = \rho_{\text{fib}}$ . Our data thus provided a precise measurement of  $\rho_{\text{fib}}$ , which was in agreement with recently published calculations [112].

To conclude, we monitored linear and nonlinear optical parameters using P-SHG microscopy of tendon at different strains. To the best of our knowledge, this is the first experimental observation of  $\rho$  variation in the same ROI for a tendon fascicle upon mechanical traction. Additionally, the minimal observed  $\rho$  provided the best available estimation of the anisotropy parameter at the fibrillar scale  $\rho_{\text{fib}}$ .

### **4.3.2 Polarization-Resolved Second-Harmonic Generation in Tendon upon Mechanical Stretching**

## Polarization-Resolved Second-Harmonic Generation in Tendon upon Mechanical Stretching

Ivan Gusachenko,<sup>†‡</sup> Viet Tran,<sup>§</sup> Yannick Goulam Houssen,<sup>†</sup> Jean-Marc Allain,<sup>§</sup> and Marie-Claire Schanne-Klein<sup>†\*</sup>

<sup>†</sup>Laboratory for Optics and Biosciences, Ecole Polytechnique, Centre National de la Recherche Scientifique, Institut National de la Santé et de la Recherche Médicale U696, Palaiseau, France; <sup>‡</sup>Laboratory of Cellular Structure Morphology and Function, Siberian Branch of the Russian Academy of Sciences, Institute of Cytology and Genetics, Novosibirsk, Russia; and <sup>§</sup>Solids Mechanics Laboratory, Ecole Polytechnique, Centre National de la Recherche Scientifique, Palaiseau, France

**ABSTRACT** Collagen is a triple-helical protein that forms various macromolecular organizations in tissues and is responsible for the biomechanical and physical properties of most organs. Second-harmonic generation (SHG) microscopy is a valuable imaging technique to probe collagen fibrillar organization. In this article, we use a multiscale nonlinear optical formalism to bring theoretical evidence that anisotropy of polarization-resolved SHG mostly reflects the micrometer-scale disorder in the collagen fibril distribution. Our theoretical expectations are confirmed by experimental results in rat-tail tendon. To that end, we report what to our knowledge is the first experimental implementation of polarization-resolved SHG microscopy combined with mechanical assays, to simultaneously monitor the biomechanical response of rat-tail tendon at macroscopic scale and the rearrangement of collagen fibrils in this tissue at microscopic scale. These experiments bring direct evidence that tendon stretching corresponds to straightening and aligning of collagen fibrils within the fascicle. We observe a decrease in the SHG anisotropy parameter when the tendon is stretched in a physiological range, in agreement with our numerical simulations. Moreover, these experiments provide a unique measurement of the nonlinear optical response of aligned fibrils. Our data show an excellent agreement with recently published theoretical calculations of the collagen triple helix hyperpolarizability.

### INTRODUCTION

Polarization-resolved second-harmonic generation (P-SHG) microscopy has recently emerged as a new multiphoton modality that efficiently probes the three-dimensional architecture of collagenous tissues (1–13). This modality takes advantage of the high specificity of SHG signals for dense noncentrosymmetric macromolecular organizations (14–17) and of the sensitivity of polarimetric approaches to the molecular orientation distribution. It is of great interest for collagenous tissues because of the highly anisotropic organization of fibrillar collagens in tissues. Fibrillar collagens are characterized by a long triple-helical domain and self-assemble to form fibrils with various diameters and distributions depending on the tissue (18). The hierarchical organization of collagen is responsible for the biophysical and mechanical properties of most tissues. For instance, the transparency of cornea results from the almost crystalline order of 30-nm-diameter collagen fibrils within 2- $\mu\text{m}$ -thick stacked lamellas in the corneal stroma. In the same vein, the mechanical strength of tendons results from the many hierarchical levels of collagen organization within this tissue. Tendons are composed of collagen type I that forms  $\approx 200$ -nm-diameter fibrils, which further assemble to form a few  $\mu\text{m}$ -diameter fibers and finally around 100  $\mu\text{m}$ -diameter fascicles (19). The latter tissue has been extensively studied as a model system with

uniaxial symmetry because tendon fascicles are easily extracted from rat-tails (1,9,10,12,20).

Analysis of P-SHG images is a complex task in collagenous tissues because of the many parameters involved in the tissular response. Usually, the collagen SHG response is characterized by the SHG anisotropy parameter  $\rho$ , which is related to the ratio of the SHG responses when the excitation field is polarized parallel (respectively, perpendicular) to the tendon fascicle axis (1,3,5,6,8,9,11,12). However, the relationship of this parameter to the collagen molecular response and the fibril orientation distribution is not fully characterized yet. Moreover, tendon fascicles exhibit anisotropic linear optical properties, mainly birefringence and diattenuation, which may distort P-SHG data and impede measurements of  $\rho$  (1,7,9,10,21).

This article aims to determine the origin of the variations of the SHG anisotropy parameter  $\rho$  to serve as a possible probe of the collagen submicrometer-scale organization in various physiological conditions. To that end, we perform P-SHG measurements in rat-tail tendon fascicles subjected to varying mechanical loads. This method enables the characterization of the same tissue while varying the orientational distribution of collagen fibrils because mechanical load results in a rearrangement of the collagen fibrils within the tendon (22–24). In this way, we report what is, to our knowledge, the first experimental observation of  $\rho$ -variations in the same region of interest (ROI) of a tendon fascicle upon mechanical loading. We propose a theoretical analysis of these variations by considering collagen fibrils with identical tensorial SHG response but

Submitted December 14, 2011, and accepted for publication March 23, 2012.

\*Correspondence: marie-claire.schanne-klein@polytechnique.edu

Editor: Gijsje Koenderink.

© 2012 by the Biophysical Society  
0006-3495/12/05/2220/10 \$2.00

doi: 10.1016/j.bpj.2012.03.068

varying orientational distribution. We also carefully process our images to correct for artifacts related to linear optical anisotropy of tendon fascicles. We obtain a good agreement between experimental data and theoretical calculations, which indicates that variations of the SHG anisotropy parameter  $\rho$  are mainly due to a rearrangement of the fibril orientational distribution within the tissue.

In the following, we first present our experimental setup that combines a traction device with a P-SHG microscope. Then, we propose a theoretical approach to gain insight into the origin of the variation of the SHG anisotropy parameter  $\rho$ . Next, we present three-dimensional P-SHG images of tendon fascicles under mechanical loading and determine the variation of linear birefringence, diattenuation, and SHG anisotropy parameter  $\rho$  as a function of the fascicle strain. Finally, we discuss these results in our theoretical framework, before concluding.

## MATERIALS AND METHODS

### Tendon preparation

Tendons were extracted from Sprague-Dawley rat-tails (female,  $\approx 300$  g) that were kept frozen until dissection. The fascicles were rinsed in phosphate-buffered saline (PBS) and centrifuged at 4700 rpm to remove any other tissue components, as described previously (24). They were stored at  $4^\circ$  in PBS and used within a few days for the experiments. Tendon fascicles were first labeled with fluorescent latex beads ( $1\text{-}\mu\text{m}$  diameter, L1030; Sigma-Aldrich, St. Louis, MO) to enable precise localization of the tissue surface. They were then attached to the traction device by use of metallic plates with rod-shaped inserts. They were coiled on the rods in a symmetric manner and glued with cyanoacrylate on the metallic plates. Before mounting in the stretching device, they were suspended vertically and allowed to rotate freely so as to minimize initial torsion. The plates were then screwed to the testing device and immersed in a dish filled with PBS to prevent the tendon fascicle from drying. The bottom of the dish consisted of a glass coverslip to enable *trans*-detection of SHG signals (see Fig. 1).

### Polarization-resolved multiphoton microscopy

Multiphoton imaging was performed using a custom-built laser-scanning upright microscope as previously described (9,16). Briefly, excitation was provided by a femtosecond Titanium-sapphire laser tuned at 860 nm (Tsunami; Spectra-Physics, Tucson, AZ), which was focused using a water-immersion  $20\times$ , 0.95 NA objective with resolution typically  $0.4\ \mu\text{m}$  (lateral)  $\times$   $1.6\ \mu\text{m}$  (axial) near the sample surface. Multiphoton signals were collected with photon-counting photomultiplier tubes (P25PC; ET Enterprise, Uxbridge, United Kingdom) using appropriate dichroic mirrors and spectral filters as depicted in Fig. 1. 2PEF was detected in the backward direction and SHG either in the forward or backward directions. Multimodal images were usually recorded using 200 kHz pixel rate,  $0.8\ \mu\text{m}$  pixel size, and  $2\ \mu\text{m}$  z-step, with 15–20 mW excitation power at the focus. No degradation of the tendon fascicle was observed under these conditions.

Polarization-resolved imaging was achieved by tuning the polarization of the laser excitation and analyzing the forward SHG (F-SHG) signals (9). To that end, we inserted a linear infrared polarizer at the back pupil of the objective to correct the nonnegligible ellipticity of the excitation beam due to the optical components within the microscope. We thereby achieved a linear polarization with ellipticity  $<1\%$  at small scanning

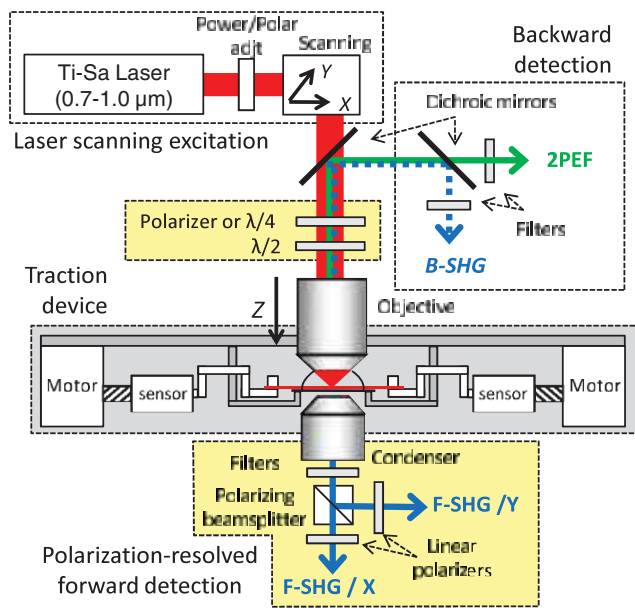


FIGURE 1 Laser-scanning multiphoton microscope with polarization-resolved detection of F-SHG signal and epi-detection of 2PEF signal and possibly of B-SHG signal. The symmetrical traction device is inserted between the objective and the condenser, with a glass window below the tendon fascicle.

angles. This linear polarization was tuned from  $-\pi/3$  to  $\pi/3$  (usually with  $\pi/12$  steps) by rotating an achromatic half-wave plate (MWPA2-22-700-1000; CVI-Melles Griot, Albuquerque, NM) placed just before the objective (see Fig. 1). F-SHG signals were analyzed using a polarizing beamsplitter cube (BBPC-550; CVI-Melles Griot). The extinction ratio of the  $x$ - and  $y$ -polarized detection channels was maximized by putting linear polarizers (03FPG021; CVI-Melles Griot) in front of the detectors. The relative transmission of these two channels was calibrated using a fluorescent slide before each experiment to enable quantitative comparison between  $x$ - and  $y$ -polarized F-SHG images (9). Image processing was performed using MATLAB (The MathWorks, Natick, MA) and ImageJ (W. Rasband, National Institutes of Health, Bethesda, MD) softwares with the MIJ plug-in (25).

### Traction device and loading path

The traction device was a custom-built uniaxial device designed to stretch the tendon fascicles in a symmetrical way to enable continuous imaging of the same region at the center of the fascicle. This device was composed of two motors (drl42pa2g-04; Oriental Motor, Tokyo, Japan) and two force sensors (k1563-100N; Annemasse, France) on both sides of the fascicle (see Fig. 1). Force and displacement were measured every 1 s. This device was inserted in place of the microscope stage, so that the tendon fascicle was imaged in an upright geometry, with F-SHG signals collected by a condenser lens just below the coverslip glass window of the PBS-filled dish. Multiphoton imaging was first performed continuously to adjust the position of the fascicle at the beam focus. The fascicles were then stretched until the crimps disappeared, and slightly relaxed to observe again the crimps. This position was referred as the zero strain, and the corresponding length of the fascicle as the reference length  $l_0$  (24). Strain was then obtained as the ratio of the total metallic plates displacement divided by this reference length (typically 40 mm). It could be slightly overestimated because of the uncertainty in the zero strain position, but the relative strain values were accurately determined.

Combined SHG imaging and mechanical assay were performed as follows. We increasingly stretched the fascicles at 10  $\mu\text{m/s}$  constant strain rate by steps of 1% strain. At each step, we stopped the motors and waited  $\sim 10$  min until the fascicle relaxed to a quasistatic state. We then recorded z-stacks of multiphoton images in immobilized fascicle. We verified that we always imaged the same region of the fascicle by looking at characteristic patterns from fluorescent beads on the fascicle. When necessary, we slightly adjusted the lateral and axial positions of the fascicle by moving the whole traction device by mean of micrometer stages. P-SHG imaging was then performed in a 20  $\mu\text{m} \times 28 \mu\text{m}$  ROI at the center of the fascicle.

We carried out measurements in seven stretched tendons; three of them were preconditioned by stretching directly to 6–8% and then relaxing until crimps were again observed (typically 2–4% strain instead of zero because of hysteresis). No significant behavior difference was observed between preconditioned and nonpreconditioned tendons.

## THEORETICAL BACKGROUND

### Second-harmonic generation in tendon

SHG is usually described using second-order nonlinear optical susceptibility tensor  $\chi^{(2)}$ . In this formalism, the nonlinear optical polarization at the harmonic frequency  $2\omega$ , induced by an incident electric field  $\mathbf{E}$  at frequency  $\omega$  in a uniform medium, is given by

$$P_i = \chi_{ijk}^{(2)} E_j E_k. \quad (1)$$

It is nonzero only in noncentrosymmetric media. Tendon fascicle are commonly assumed to have cylindrical symmetry (1,20), which reduces the number of independent nonvanishing tensorial components of  $\chi^{(2)}$ . Moreover, we assume that Kleinman symmetry applies because of the nonresonant character of the interaction (1,20). Within these assumptions,  $\chi^{(2)}$  has only two independent nonvanishing components:  $\chi_{xxx}$  and  $\chi_{xyy} = \chi_{yyx} = \chi_{yxx} = \chi_{zzz} = \chi_{zxx} = \chi_{zzx}$ , where  $x$  is the main axis of the tendon fascicle (1,20). P-SHG experiments give access to the ratio of these tensor components:  $\rho = \chi_{xxx}/\chi_{xyy}$ . This SHG anisotropy parameter measures the ratio of the SHG responses when the incident electric field is parallel (respectively, perpendicular) to the tendon axis.

### Collagen hierarchical structure and orientational disorder in tendon

The nonlinear susceptibility tensor  $\chi^{(2)}$  represents the macroscopic nonlinear response of the medium that is composed of elementary scatterers at a smaller scale. These elementary responses are described by a first hyperpolarizability tensor (26). The very elementary nonlinear scatterers in collagenous tissues are presumably the peptide bonds along the peptidic scaffold (3,27). These molecular entities present delocalized electrons in a noncentrosymmetric environment, which gives a nonvanishing second-harmonic response. Moreover, they are tightly aligned along the collagen triple helices and within the fibrils and fascicles, so that their small second-harmonic responses are coherently amplified and the resulting macroscopic response  $\chi^{(2)}$  is quite large (27).

Considering the hierarchical organization of collagen, one may define hyperpolarizability tensors at different scales: peptide bonds, triple helices, or fibrils (see Fig. 2 *a*). In this work, we assume that collagen triple helices and fibrils are quite rigid upon physiological mechanical loads, which means that physiological mechanical deformations are only accompanied with reorganization of fibrils within the fascicle. We therefore consider collagen fibrils as the relevant elementary nonlinear optical structure at submicrometer scale. Within this assumption, all the collagen fibrils exhibit the same first hyperpolarizability tensor  $\beta$  in their associated reference frames, but they show orientational dispersion around the fascicle main axis. Because the macroscopic SH polarization is obtained as the sum of elementary nonlinear dipole moments, the susceptibility tensor reads

$$\chi_{ijk}^{(2)} = N \langle \beta_{ijk}^{(2)} \rangle_{\Omega}, \quad (2)$$

where  $N$  is the fibril concentration and the average is taken over the angular distribution  $\Omega$  of fibrils. Local field factors have been neglected in this expression.

The fibrils are assumed to exhibit cylindrical symmetry like the fascicles, so that the nonzero hyperpolarizability

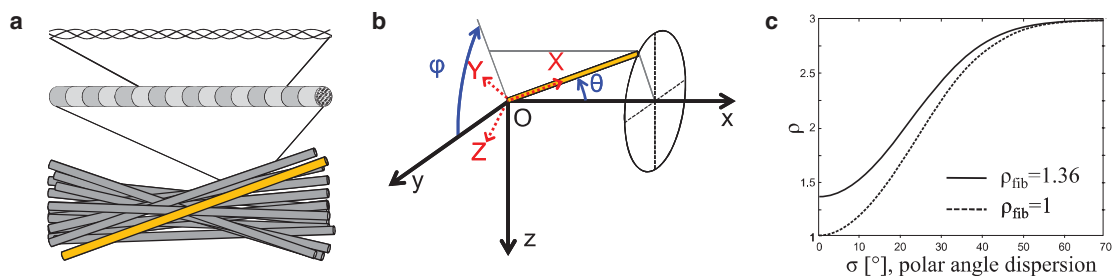


FIGURE 2 Orientational disorder in tendon. (*a*) Hierarchical structure of collagen, from molecule to fibril and fascicle. P-SHG probes the orientational distribution of fibrils within the fascicle. (*b*) Collagen fibril with  $(\theta, \phi)$  orientation.  $(x, y, z)$  and  $(X, Y, Z)$  denote laboratory frame and fibril frame, respectively. (*c*) Effective SHG anisotropy parameter  $\rho$  as a function of fibril orientation dispersion in the tendon fascicle for fibril parameter  $\rho_{\text{fib}} = 1$  and  $\rho_{\text{fib}} = 1.36$ .

components in the fibril frame are  $\beta_{XXX}$  and  $\beta_{XYY} = \beta_{YYX} = \beta_{YXX} = \beta_{XZZ} = \beta_{ZZX} = \beta_{ZZY} = \beta_{YYZ}$  for the same symmetry reasons as for  $\chi^{(2)}$ . The orientation of such a collagen fibril with cylindrical symmetry can be described by two angles  $(\theta, \varphi)$ , where  $\theta$  represents the polar angle between the fibril's main axis  $X$  and the  $x$  axis in the laboratory frame (Fig. 2 b) and  $\varphi$  is the azimuthal angle of the fibril with respect to the  $xy$  plane in the laboratory frame. For a single fibril at  $(\theta, \varphi)$ , the hyperpolarizability in the laboratory frame reads

$$\beta_{ijk} = \sum_{I,J,K} T_{iI} T_{jJ} T_{kK} \beta_{IJK}, \quad (3)$$

where  $(i,j,k)$  and  $(I,J,K)$  denote coordinates in the laboratory frame and in the fibril frame, respectively, and  $T$  is the Euler matrix (see the Supporting Material).

Moreover, at a smaller scale, the hyperpolarizability tensor of a collagen fibril can be related to the elementary hyperpolarizability tensor of a peptide bond  $\tilde{\beta}$  using an expression similar to Eq. 3,

$$\beta_{IJK} = \sum_{a,b,c} T_{Ia} T_{Jb} T_{Kc} \tilde{\beta}_{abc}, \quad (4)$$

where  $(a,b,c)$  and  $(I,J,K)$  denote coordinates in the peptide frame and in the fibril frame, respectively. It is usually assumed that the peptide bonds behave as rodlike nonlinear scatterers so that there is only one nonvanishing component  $\tilde{\beta}_{uuu}$  (3).

To summarize, we consider the nonlinear optical response of collagen at three different scales: the very elementary scale  $\tilde{\beta}$  that corresponds to the peptide bonds, the fibrils scale  $\beta$ , and the tissue scale  $\chi^{(2)}$  that is probed through imaging or spectroscopic experiments. As stated above, this three-scale approach aims to separate the scale of the fibrils that are considered as rigid entities from the scale of the tissue where the fibrils distribution may vary dramatically upon various perturbations.

### SHG anisotropy parameter at fibrillar and tissular scales

In the following, we further consider that fibrils are uniformly distributed around the  $x$  axis, with an orientational distribution

$$F(\theta, \varphi) = \frac{1}{2\pi} g(\theta),$$

where  $g(\theta)$  is an appropriate distribution density function of  $\theta$ . Using this distribution and Eqs. 2 and 3, the relationship between the macroscopic nonlinear response  $\chi^{(2)}$  and fibril first hyperpolarizability  $\beta$  reads

$$\chi_{xxx}^{(2)} = N\beta_{xxx} \langle \cos^3 \theta \rangle_g + 3N\beta_{xyy} \langle \cos \theta \sin^2 \theta \rangle_g, \quad (5)$$

$$\chi_{yyy}^{(2)} = \frac{1}{2} N \left( \beta_{xxx} \langle \cos \theta \sin^2 \theta \rangle_g + \beta_{xyy} \left( 3 \langle \cos^3 \theta \rangle_g - \langle \cos \theta \rangle_g \right) \right). \quad (6)$$

The SHG anisotropy parameter  $\rho$  is determined from

$$\rho = \frac{\chi_{xxx}^{(2)}}{\chi_{yyy}^{(2)}} = \frac{\rho_{\text{fib}} \langle \cos^3 \theta \rangle_g + 3 \langle \cos \theta \sin^2 \theta \rangle_g}{\frac{3}{2} \langle \cos^3 \theta \rangle_g - \frac{1}{2} \langle \cos \theta \rangle_g + \frac{1}{2} \rho_{\text{fib}} \langle \cos \theta \sin^2 \theta \rangle_g}, \quad (7)$$

where we have introduced an SHG anisotropy parameter at the scale of a single fibril  $\rho_{\text{fib}} = \beta_{xxx} / \beta_{xyy}$ .

At a smaller scale,  $\rho_{\text{fib}}$  may also be related to the angle  $\Theta$  of the elementary nonlinear scatterers to the fibril axis by deriving a relationship between  $\beta_{xxx}$  (respectively,  $\beta_{xyy}$ ) and  $\tilde{\beta}_{uuu}$  similarly to Eq. 5 (respectively, Eq. 6). In that case, because there is only one nonvanishing component  $\tilde{\beta}_{uuu}$ , these expressions simplify to (3,5,6)

$$\beta_{xxx} = N \tilde{\beta}_{uuu} \cos^3 \Theta, \quad (8)$$

$$\beta_{xyy} = \frac{1}{2} N \tilde{\beta}_{uuu} \cos \Theta \sin^2 \Theta, \quad (9)$$

and  $\rho_{\text{fib}}$  reads

$$\rho_{\text{fib}} = \frac{\beta_{xxx}}{\beta_{xyy}} = \frac{2}{\lg^2(\Theta)}. \quad (10)$$

This expression is strictly valid for a unique orientation  $\Theta$  of the elementary nonlinear scatterers to the fibril axis. It may be refined considering the accurate geometry of a triple-helix (27,28) and the structure of a fibril (29). It is noteworthy that we consider a rigid structure at this scale. Orientational disorder within the fascicle is only relevant at a larger scale that corresponds to the rearrangement of the fibrils upon stretching, as shown in Eq. 7.

We now focus on the fascicle scale and we examine Eq. 7. It shows that the parameter  $\rho$  that is measured using P-SHG experiments is related to the corresponding parameter  $\rho_{\text{fib}}$  at the fibril scale and to the angular dispersion of the fibrils within the focal volume

$$\sigma = \sqrt{\langle \theta^2 \rangle_g}.$$

Given the values of  $\rho$  reported in the literature, we expect that  $\rho_{\text{fib}} < 3$  for rat-tail tendon fascicle. In that case, the effective parameter  $\rho$  increases with  $\sigma$  that is with disorder (see the Supporting Material). The same trend has been reported in the particular case of a conical distribution at a fixed angle  $\theta$  when increasing  $\theta$  (12). Calculation of parameter  $\rho$  as a function of  $\sigma$  is displayed in Fig. 2 c in

the simplified case of a Gaussian distribution around the  $x$  axis,

$$g(\theta) \propto e^{-\frac{\theta^2}{2\sigma^2}}$$

(see the Supporting Material). The value  $\rho$  monotonically increases with angular dispersion up to 3. For example,  $\rho$  is calculated as 1.5 that is a typical value reported in the literature, using a fibril parameter  $\rho_{\text{fib}} = 1$  and orientation dispersion as small as  $15^\circ$ . As expected,  $\rho$  tends toward  $\rho_{\text{fib}}$  for  $\sigma$  tending toward zero. Our calculation thus demonstrates unambiguously that the measured SHG anisotropy parameter  $\rho$  reflects the orientational disorder of the fibrils within the fascicle.

### P-SHG in thick anisotropic tissues

The parameter  $\rho$  is measured using P-SHG imaging experiments. Advanced image processing is required to take into account possible polarization distortions due to propagation within the tendon fascicle, as reported in our recent article (9). Laser excitation is indeed affected by diattenuation and birefringence when propagating within this thick anisotropic tissue, while SHG radiation undergoes polarization scrambling. A complete description of our image processing is given as the Supporting Material. Briefly, we fit the SHG signal intensity along  $x$  polarization as

$$I^{2\omega}(\alpha) = A \cos 4\alpha + B \cos 2\alpha + C, \quad (11)$$

where  $\alpha$  is the polarization angle of the incident electric field in the  $xy$  plane. The parameter  $\rho$  then reads

$$\rho^2 e^{-\frac{2\eta}{\Delta n}} = \frac{A + B + C}{A - B + C}, \quad (12)$$

where  $\Delta I^{-1} = I_x^{-1} - I_y^{-1}$  is the diattenuation. Diattenuation corresponds to the difference of attenuation lengths for the two orthogonal polarizations of the incident beam: parallel ( $\alpha = 0$ ) and perpendicular ( $\alpha = \pi/2$ ) to the tendon fascicle axis. It can be extracted from experimental data by fitting  $I_{x,\alpha=0}^{2\omega}(z)$  and  $I_{x,\alpha=\pi/2}^{2\omega}(z)$   $z$ -profiles using exponential functions. Finally, we calculate a second parameter  $\Delta$  from  $A, B, C$  (see the Supporting Material) to extract the birefringence  $\Delta n$  and the amount of polarization scrambling  $\eta(z_0)$  near the tendon surface. This advanced data analysis method thus enables the determination of both linear and nonlinear optical properties in any ROI of the tendon fascicle.

## RESULTS

### Mechanical assays

We performed mechanical assays coupled with P-SHG measurements in tendon fascicles to characterize the variation of the collagen organization under mechanical

load. A typical loading path is displayed in Fig. 3, along with force measurements that show a relaxation while the strain is kept constant. We therefore always recorded SHG image stacks after  $\sim 10$ -min relaxation, to probe the fascicle in a quasi-steady state. The imaging recording time is quite long (typically 3 min; see boxes in Fig. 3 *a*) because many images (typically 850) are recorded to retrieve the polarization dependence at increasing depths within the fascicle.

The force-strain response of the tendon fascicle is displayed in Fig. 3 *b*. The force shows a slow continuous increase superimposed to steep variations related to fascicle relaxation while motors are immobile. The variation of the fascicle stiffness (slope of the force-strain curve) as measured between two successive steps with increasing strain is in good agreement with previously reported data (24,30). A toe region with increasing stiffness is observed below 3% strain. Then the fascicle exhibits a linear behavior with constant stiffness (3–6% strain). The tangent modulus is  $\sim 200$  MPa in this region, similarly to the values reported for fascicles in the literature (24,31,32). Finally, the stiffness decreases, indicating that force saturates at strains beyond 6%, which shows that the fascicle begins to break.

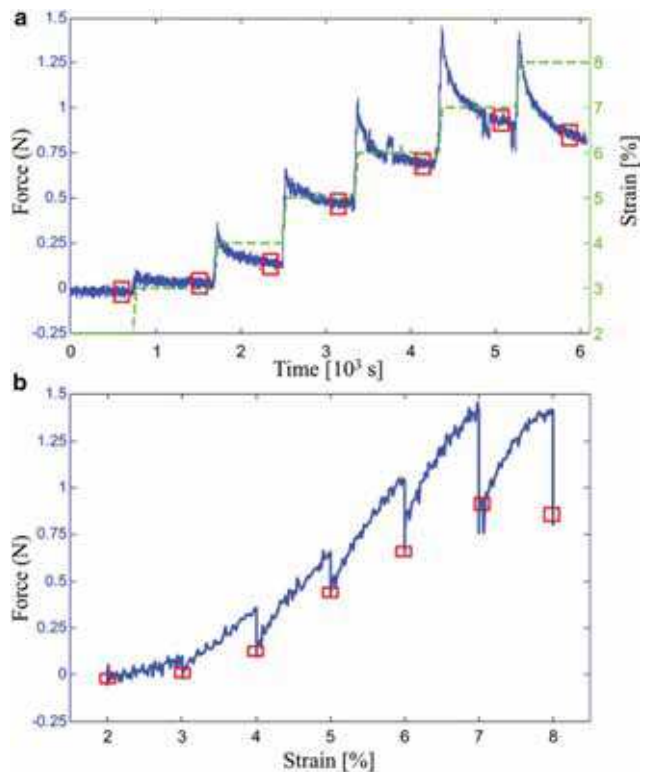


FIGURE 3 Mechanical behavior of a tendon fascicle. (*a*) Loading path of the mechanical assay (strain as a function of time, dotted line) and response of the tendon fascicle (force as a function of time, solid line). (Rectangles) Times when P-SHG imaging was performed. (*b*) Force variation as a function of strain along the loading path. Negative peaks at integer values correspond to tendon mechanical relaxation while motors are stopped.

### P-SHG images of tendon fascicle

Fig. 4 displays P-SHG imaging data from the same fascicle at 2% and 4% strains. SHG images exhibit a striated pattern that is characteristic for the collagen fibrillar organization in tendon fascicles (1,2,4,24) (see Fig. 4, *a* and *e*). It does not directly reproduce the fibril distribution within the fascicle, but corresponds to interference patterns resulting from the coherent summation of the SHG radiation from all the fibrils within the focal volume (33–35). We used simultaneous 2PEF imaging to visualize fluorescent beads that labeled the fascicle surface. We observed the same bead patterns at any strain, which indicates that we successfully imaged the same region of the fascicle thanks to symmetric stretching in our traction device. Slight displacements of this pattern between two successive strains were sometimes observed but remained much smaller than the microscope field of view. We then took advantage of these specific bead patterns to process P-SHG data exactly in the same ROI of the fascicle at any applied strain (see *yellow ROI* in Fig. 4, *a* and *e*). Fluorescent labeling of the fascicle also served as a depth reference  $z_0$  to locate the fascicle surface.

Fig. 4, *b* and *f*, displays the  $x$ -polarized SHG mean intensity in the highlighted ROI as a function of the depth within the fascicle and of the incident polarization angle  $\alpha$ . These polarimetric diagrams exhibit characteristic features that we attribute to polarization distortions (9):

First, the depth profiles at  $\pm \pi/4$  excitation angle display interference fringes with dark spots at  $\sim 40 \mu\text{m}$  depth from

tendon surface. These fringes are related to birefringence in the propagation of the laser excitation, which results in a phase delay between the  $x$ - and  $y$ -polarization components of the laser excitation. They appear near  $\pm \pi/4$  excitation angle because  $x$  and  $y$  components have similar amplitudes and destructive interferences are more effective.

Second, the depth profiles at 0 and  $\pm \pi/2$  angles are different, which indicates different attenuation lengths within the fascicle for  $x$ - and  $y$ -polarization components.

Note that the observed polarimetric diagrams are different at 2% and 4% strains: the dark spots are slightly sharper at 4% strain, whereas attenuation is stronger at 2% strain. We therefore expect quantitatively different parameters  $\rho$  after image processing.

### Determination of linear and nonlinear anisotropy parameters

These P-SHG data were fitted with a sum of  $\cos 2n\alpha$  functions ( $n = 0,1,2$ ) using Eq. 11. The obtained parameters  $A, B, C$  were then used to calculate the SHG anisotropy parameter  $\rho$  and the parameter  $\Delta$  as a function of depth within the tendon (see the Supporting Material). Fig. 4, *c* and *g*, displays raw and corrected values of  $\rho$ . The raw  $\rho$ -values decrease with increasing depth within the fascicle, whereas  $\rho$  is expected to be constant because the fascicle appears as a uniform medium. This artifactual decrease results from diattenuation that accumulates with depth. It is corrected accordingly using Eq. 12 and the diattenuation

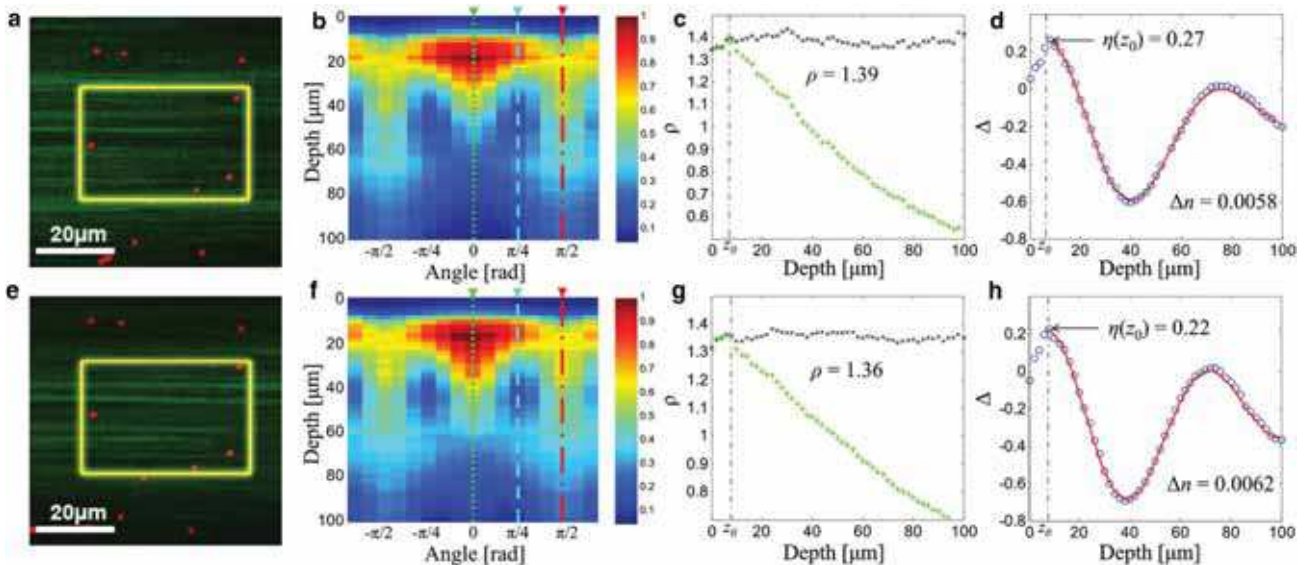


FIGURE 4 P-SHG imaging of the same fascicle at (*a–d*) 2% strain and (*e–h*) 4% strain. (*a* and *e*) Multiphoton images of the tendon fascicle labeled with fluorescent beads. SHG signal (*green color*) is specific for collagen and 2PEF signal (*red color*) reveals the beads. (*Yellow frames*) ROI used for data processing. Fluorescent bead pattern ensures that the same region of the fascicle is processed at any strain. Scale bar: 20  $\mu\text{m}$ . (*b* and *f*)  $x$ -polarized SHG mean intensity in the highlighted ROI as a function of the incident polarization angle  $\alpha$  and of the scanning depth in tendon. (*c* and *g*) Raw (*green*) and corrected (*black*)  $\rho$ -value as a function of depth. (*d* and *f*)  $\Delta$ -value as a function of depth (*blue points*), and fit (*red line*) using Eq. 11 and Eq. S10 in the Supporting Material.

lengths derived from the SHG depth profiles at 0 and  $\pi/2$  excitation angles. The corrected  $\rho$  then shows a nearly constant value as a function of depth, as expected.

Fig. 4, *d* and *h*, displays the depth profiles of  $\Delta$  (blue circles) as calculated from the P-SHG data. They exhibit oscillations that originate from the fascicle birefringence and reflect the phase shift between *x*- and *y*-polarization components that accumulates along propagation of the laser excitation within the tendon fascicle. The birefringence is then obtained from the position of the first maximum (see the Supporting Material). The decay of the oscillation amplitude is due to the diattenuation. Nonzero value of  $\Delta$  at  $z = z_0$  corresponds to polarization scrambling in the SHG propagation. This effect is nonnegligible at the surface of the fascicle, but vanishes within the tendon because  $\Delta$  is zero at the next maximum, where there is no contribution from birefringence. The theoretical expression of  $\Delta$  satisfactorily fits the measured  $\Delta$  depth profile (see red lines in Fig. 4, *d* and *h*). It provides the birefringence value  $\Delta n$  and the polarization scrambling at the fascicle surface  $\eta(z_0)$ . Here again, we obtain different parameters at 2% and 4% strains; a larger birefringence  $\Delta n$  and a smaller cross talk  $\eta(z_0)$  are observed at the largest strain.

### Variation of fibril orientation distribution with mechanical load

All the optical parameters obtained from P-SHG data are finally displayed as a function of strain in Fig. 5. They all exhibit nonnegligible variations with strain, whether they are linear or nonlinear optical parameters. We obtained similar results for all the tendon fascicles under study. The error bars in Fig. 5 are related to the fitting accuracy and not to the dispersion of different measurements, because this figure displays measurements in the same fascicle at increasing strain. The error bars were calculated using 95% confidence intervals for *A*, *B*, and *C* (data fit using Eq. 11), and taking into account the correlation of these parameters.

The SHG anisotropy parameter  $\rho$  decreases from 1.39 to 1.36 while stretching from 2% to 4% and then it increases up

to 1.42 (see Fig. 5 *a*). Its average value is in good agreement with our previous measurements (9). Note that  $\rho$  was determined at the fascicle surface, where the accumulated phase shift and the diattenuation are zero. The fascicle birefringence  $\Delta n$  monotonically increases with strain, going from 0.0058 to 0.0066 (see Fig. 5 *b*). The polarization scrambling at the fascicle surface  $\eta(z_0)$  decreases monotonically with strain (see Fig. 5 *c*). Finally, the attenuation lengths for *x*- and *y*-polarized fields also increase monotonically with strain (see Fig. 5 *d*). It means that the fascicle becomes more transparent both for *x*- and *y*-polarized fields when stretched. Diattenuation length is also increasing with strain. Note that the attenuation length for *y*-polarized field is the largest, which means that the tendon fascicle is more transparent for light polarized perpendicularly to the fibrils.

### DISCUSSION

Many articles have reported P-SHG comparative studies for different samples, with the aim to use variation of SHG anisotropy parameter  $\rho$  to identify different tissues or to find hallmarks of various pathologies (5–8). However, it is not well established yet how this parameter varies within the same tissue as a response to tissue perturbations. To the best of our knowledge, this article reports the first experimental observation of  $\rho$ -variations in the same ROI of a collagenous tissue. To that end, we implemented a unique experimental setup that combines P-SHG microscopy with mechanical assays, because mechanical loading is expected to induce a reorganization of the collagen distribution within the tissue. This setup was designed to always monitor the same ROI thanks to symmetric stretching. Accordingly, we successfully visualized the same region of a tendon fascicle that was increasingly stretched up to a few percents and we observed a significant variation of the SHG anisotropy parameter  $\rho$  with stretching. Our work then proves that  $\rho$  can vary as a function of mechanical load.

However, the SHG anisotropy parameter  $\rho$  is not the only optical parameter that is expected to vary upon tissue remodeling. Linear optical parameters may also vary when

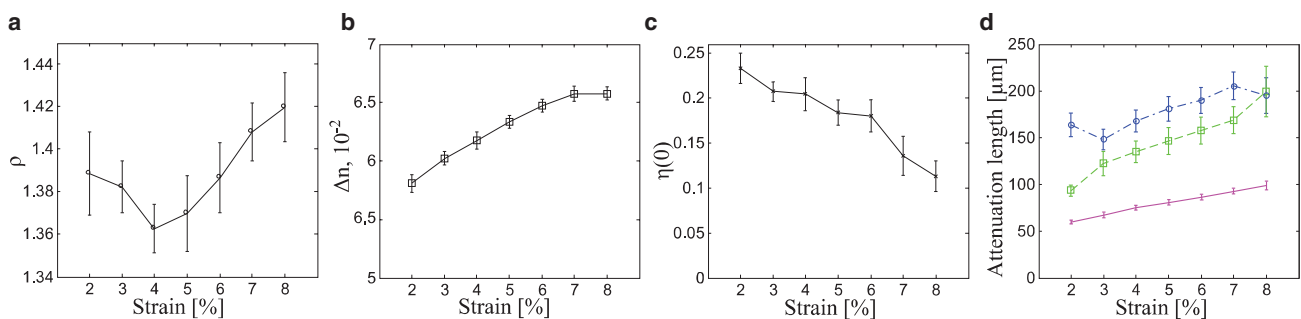


FIGURE 5 Tendon fascicle optical parameters obtained from P-SHG images as a function of strain. (a) SHG anisotropy parameter  $\rho$ . (b) Birefringence  $\Delta n$ . (c) Polarization scrambling at the fascicle surface  $\eta(z_0)$ . (d) Extraordinary attenuation length (*x* polarization, parallel to the fascicle main axis, solid line), ordinary attenuation length (*y* polarization, perpendicular to the fascicle main axis, dash-dotted line), and diattenuation length (dotted line).

the tendon fascicle is stretched, mainly the birefringence  $\Delta n$ , the diattenuation length  $\Delta l$ , and the polarization scrambling  $\eta(z_0)$  near the fascicle surface. Variations of all these parameters are mixed together in the P-SHG response because the polarization state of the excitation beam is modified by birefringence and diattenuation whereas polarization scrambling affects the polarization of the SHG signal. It is therefore mandatory to use an advanced image processing method to separate the variation of the nonlinear optical parameter  $\rho$  from the variations of the linear optical parameters  $\Delta n$ ,  $\Delta l$ , and  $\eta(z_0)$ . This approach advantageously enables monitoring of birefringence, diattenuation length, and polarization scrambling as a function of tendon stretching, which provides complementary information about the tissue reorganization at microscopic scale. Most importantly, we obtained reproducible experimental results with error bars small enough to observe significant variations of all the parameters of interest.

These variations with strain have to be related to the tendon microstructure and mechanics. The macroscopic mechanical properties of tendon fascicle have been extensively studied (22–24,30,36). A tendon in its relaxed state is usually considered as a bundle of packed fibrils with a crimped pattern. A mechanism explaining the evolution of the tangent modulus with strain in relationship with the fibril organization has been proposed (22). The initial toe region (see Fig. 3 *b*) is attributed to the straightening of the collagen fibrils. The linear region is then associated with a sliding of the fibrils in their proteoglycan matrix. These two regions correspond to physiological stretching of the tendon fascicle, while the next region showing force saturation at strain beyond 6% is characteristic for nonphysiological disruption of the tendon fascicle. In other words, stretching under physiological conditions is considered to result in a better alignment of the fibrils within the tendon fascicle and is associated with an increase of order and anisotropy of the tissue. Let us discuss in this framework the variations of the linear and nonlinear optical parameters we observed experimentally.

The measured birefringence increases with strain, as expected because the fibrils forming the fascicle become more aligned, increasing the anisotropy that translates into birefringence. It changes by 14% over the full loading path, and by ~7% over the maximal physiological strain range (2–4%).

The same explanation applies to the increase of the attenuation lengths  $l_x$  and  $l_y$ , but the variations are more dramatic. Thus,  $l_x$  exhibits 1.5-fold increase while stretched from 2% to 8%, and  $l_y$  exhibits 30% maximal increase. The stretched tendon fascicle with well-aligned fibrils appears to be more transparent for both parallel and perpendicular polarization of the infrared excitation field. The diattenuation length  $\Delta l$  changes even more drastically, displaying twofold increase with strain.

The polarization scrambling  $\eta(z_0)$  decreases with strain, as expected if we consider that the surface of an aligned

fascicle is smoother and better defined. Scrambling indeed occurs mainly near the surface, and better-aligned fibrils near the surface are expected to scramble the SHG polarization to a smaller extent.

The variation of  $\rho$  is not monotonic in contrast to the former parameters. It shows two different regions (see Fig. 5 *a*):  $\rho$  first decreases in the interval 2–4% and then rises up from 4% to 8%. This trend was observed for all studied tendons, whether preconditioned or not. The first decreasing part is in agreement with the model we introduced in the theoretical section. It reflects the decrease of  $\rho$  with increasing order in tissue, as obtained by the numerical simulation displayed in Fig. 2 *c*. This decreasing behavior corresponds to the heel region on the force-strain curve, which is associated with the physiological range of tendon stretching. It confirms that tendon stretching is associated with a rearrangement of collagen fibrils that results in a better alignment of these fibrils within the tendon fascicle (22–24).

In contrast, the second increasing region of  $\rho$  variation with strain indicates that the alignment of collagen fibrils is somewhat disrupted at higher strains. These strains do not correspond to physiological conditions according to the literature (23). This is confirmed by the saturation of the force observed in Fig. 3 *b*. We therefore expect that some fibrils begin to break, resulting in misaligned collagen subfibrils or molecules within the tendon fascicle. Alternatively, this increasing region of  $\rho$  at higher strains may be attributed to straightening of the collagen triple-helix itself (37). In this case, the increase of the measured parameter  $\rho$  results from variations of  $\rho_{\text{fib}}$  at the molecular scale, not from orientational changes at the fibrillar scale. We note that a behavior change is also observed to a lesser extent in the birefringence variation that appears to saturate at strains higher than 4%.

Let us now examine the quantitative values obtained for  $\rho$ . The range of the measured values for all strains is in good agreement with previous measurements, while the minimal value of  $\rho$  provides what to our knowledge is new information about the SHG response of collagen fibrils. This minimal value is obtained typically for 3–4% strains. It corresponds to well-ordered fibrils within the tendon fascicle, so that  $\rho \approx \rho_{\text{fib}}$  (see Eq. 7 with  $\theta$  uniformly equal to 0). Our measurements of stretched tendon fascicles thus quantify the SHG anisotropy parameter of collagen fibrils. This parameter is not accessible in relaxed tissues that exhibit a disordered distribution of collagen fibrils, except in the corneal stroma that is the only collagenous tissue with well-aligned fibrils as required for corneal transparency. However, measurements of  $\rho_{\text{fib}}$  in corneal stroma are less accurate than in stretched tendon fascicles because collagen fibrils are distributed in  $\approx 2\text{-}\mu\text{m}$ -thick lamellae. The  $\rho_{\text{fib}}$  measurements are then significantly disrupted at lamellar interfaces and somewhat along the whole lamellar thickness that approaches the axial optical resolution (13).

An interesting alternative method to measure the SHG anisotropy parameter of collagen fibrils would be to stretch individual collagen fibrils using micromechanical devices (38,39). However, we expect P-SHG signals of single fibrils to be quite small, which would probably deteriorate the accuracy of these measurements. P-SHG imaging in stretched tendon fascicles therefore appears to certainly provide the most accurate measurement of the SHG anisotropy at the fibrillar scale. We obtain  $\rho_{\text{fib}} = 1.36 \pm 0.01$  for the tendons under study.

This value is related to the orientational distribution of the elementary nonlinear scatterers within the fibrils (3,5,12,27). Considering that these elementary nonlinear scatterers are the peptide bonds and assuming that they all exhibit the same angle  $\Theta$  to the fibril axis,  $\rho_{\text{fib}} = 1.36$  gives  $\Theta = 50.5^\circ$  by use of Eq. 10. This value is close to the mean orientation of the peptide bonds to the helix axis ( $45.3^\circ$  pitch angle). This approach should, however, be refined as suggested recently (12,40,41). It indeed assumes that the elementary nonlinear dipoles are perfectly aligned along the peptide bonds, which has been questioned by quantum chemistry calculations (40). Moreover, side chains or other submolecular units in the amino acids may also contribute to the elementary nonlinear hyperpolarizability (11,12,41). Finally, the interactions between elementary effective nonlinear dipoles along the peptidic sequence may result in strong modifications of the total nonlinear response (12,40). Taking into account all these effects requires advanced theoretical calculations that need to be validated by accurate experimental measurements. In that regard, our measurements show a very good agreement with the value  $\beta_{\text{XXX}}/\beta_{\text{YYY}} = 1.4$  calculated by Tuer et al. (12) by use of ab initio modeling of the first hyperpolarizability of effective amino acids with corrections for pair interactions. Our results then confirm that the P-SHG response in single collagen fibrils is dominated by the orientation of the amino acids in the triple-helical structure.

## CONCLUSION

In this article, we showed that the P-SHG response of collagenous tissues mainly reflects the distribution of fibril orientation. For that purpose, we developed a three-scale theoretical approach of the collagen nonlinear optical response: the very elementary scale that corresponds to the nonlinear response of chemical moieties along the amino-acid sequence, the scale of the fibrils that are considered as rigid entities and the scale of the tissue where the fibrils show different orientations that may vary dramatically upon various perturbations. Our calculations indicate that more disordered distributions of fibril orientation in the tissue result in a larger SHG anisotropy parameter  $\rho$ . This was confirmed experimentally by stretching a rat-tail tendon fascicle while continuously monitoring  $\rho$  in the same ROI of the tissue. We observed unambiguously

a decrease of the SHG anisotropy parameter  $\rho$  to a minimum value that was attributed to the best alignment of the fibrils at a submicrometer scale. The SHG anisotropy parameter next increased for nonphysiological strains due to the disruption of the tissue. The minimum value of  $\rho$  measures the SHG anisotropy parameter at the fibril scale  $\rho_{\text{fib}}$ . Our measurements thus provide accurate information about the P-SHG response of single collagen fibrils that appear to confirm recent advanced theoretical calculations of the triple helix hyperpolarizability (12).

This approach may be generalized to other mechanical assays to gain insight into the relationship between mechanical loading of collagenous tissues at macroscopic scale and reorganization of collagen fibrils at the microscopic scale. It should also prove efficient to look at wound healing or any tissue remodeling in response to a variety of injuries. P-SHG microscopy coupled to our rigorous image processing and multiscale data analysis will enable measurements of local disorder in the collagen matrix that may reflect pathological processes and provide a quantitative tool for monitoring their progression.

## SUPPORTING MATERIAL

A complete description of  $\rho$ -calculation and of image processing are available at [http://www.biophysj.org/biophysj/supplemental/S0006-3495\(12\)00409-2](http://www.biophysj.org/biophysj/supplemental/S0006-3495(12)00409-2).

We gratefully acknowledge G. Liot from Institut Curie, Université Paris XI, for providing us with the rat-tails; V. de Greef, D. Caldemaison, X. Solinas, and J.-M. Sintès for technical implementation of the setup; and G. Latour, M. Zimmerley, F. Hache, and E. Beaurepaire for fruitful discussions.

## REFERENCES

1. Stoller, P., K. M. Reiser, ..., A. M. Rubenchik. 2002. Polarization-modulated second harmonic generation in collagen. *Biophys. J.* 82: 3330–3342.
2. Williams, R. M., W. R. Zipfel, and W. W. Webb. 2005. Interpreting second-harmonic generation images of collagen I fibrils. *Biophys. J.* 88:1377–1386.
3. Plotnikov, S. V., A. Millard, ..., W. Mohler. 2006. Characterization of the myosin-based source for second-harmonic generation from muscle sarcomeres. *Biophys. J.* 90:693–703.
4. Erikson, A., J. Örtengren, ..., M. Lindgren. 2007. Quantification of the second-order nonlinear susceptibility of collagen I using a laser scanning microscope. *J. Biomed. Optics.* 12:044002.
5. Tiaho, F., G. Recher, and D. Rouède. 2007. Estimation of helical angle of myosin and collagen by second harmonic generation imaging microscopy. *Opt. Express.* 15:12286–12295.
6. Han, X., R. M. Burke, ..., E. B. Brown. 2008. Second harmonic properties of tumor collagen: determining the structural relationship between reactive stroma and healthy stroma. *Opt. Express.* 16:1846–1859.
7. Mansfield, J. C., C. P. Winlove, ..., S. J. Matcher. 2008. Collagen fiber arrangement in normal and diseased cartilage studied by polarization sensitive nonlinear microscopy. *J. Biomed. Optics.* 13:044020.
8. Psilodimitrakopoulos, S., D. Artigas, ..., P. Loza-Alvarez. 2009. Quantitative discrimination between endogenous SHG sources in

- mammalian tissue, based on their polarization response. *Opt. Express*. 17:10168–10176.
9. Gusachenko, I., G. Latour, and M.-C. Schanne-Klein. 2010. Polarization-resolved second harmonic microscopy in anisotropic thick tissues. *Opt. Express*. 18:19339–19352.
  10. Ait-Belkacem, D., A. Gasecka, ..., S. Brasselet. 2010. Influence of birefringence on polarization resolved nonlinear microscopy and collagen SHG structural imaging. *Opt. Express*. 18:14859–14870.
  11. Su, P. J., W. L. Chen, ..., C. Y. Dong. 2011. Determination of collagen nanostructure from second-order susceptibility tensor analysis. *Biophys. J.* 100:2053–2062.
  12. Tuer, A. E., S. Krouglov, ..., V. Barzda. 2011. Nonlinear optical properties of type I collagen fibers studied by polarization dependent second harmonic generation microscopy. *J. Phys. Chem. B.* 115:12759–12769.
  13. Latour, G., I. Gusachenko, ..., M. C. Schanne-Klein. 2012. In vivo structural imaging of the cornea by polarization-resolved second harmonic microscopy. *Biomed. Opt. Express*. 3:1–15.
  14. Campagnola, P. J., A. C. Millard, ..., W. A. Mohler. 2002. Three-dimensional high-resolution second-harmonic generation imaging of endogenous structural proteins in biological tissues. *Biophys. J.* 82:493–508.
  15. Zipfel, W. R., R. M. Williams, ..., W. W. Webb. 2003. Live tissue intrinsic emission microscopy using multiphoton-excited native fluorescence and second harmonic generation. *Proc. Natl. Acad. Sci. USA*. 100:7075–7080.
  16. Strupler, M., A.-M. Pena, ..., M. C. Schanne-Klein. 2007. Second harmonic imaging and scoring of collagen in fibrotic tissues. *Opt. Express*. 15:4054–4065.
  17. Deniset-Besseau, A., P. De Sa Peixoto, ..., M. C. Schanne-Klein. 2010. Nonlinear optical imaging of lyotropic cholesteric liquid crystals. *Opt. Express*. 18:1113–1121.
  18. Hulmes, D. J. 2002. Building collagen molecules, fibrils, and supra-fibrillar structures. *J. Struct. Biol.* 137:2–10.
  19. Parry, D. A. D., and A. S. Craig. 1977. Quantitative electron microscope observations of the collagen fibrils in rat-tail tendon. *Biopolymers*. 16:1015–1031.
  20. Roth, S., and I. Freund. 1979. Second harmonic generation in collagen. *J. Chem. Phys.* 70:1637–1643.
  21. Nadiarnykh, O., and P. J. Campagnola. 2009. Retention of polarization signatures in SHG microscopy of scattering tissues through optical clearing. *Opt. Express*. 17:5794–5806.
  22. Puxkandl, R., I. Zizak, ..., P. Fratzl. 2002. Viscoelastic properties of collagen: synchrotron radiation investigations and structural model. *Philos. Trans. R. Soc. Lond. B Biol. Sci.* 357:191–197.
  23. Screen, H. R. C., D. L. Bader, ..., J. C. Shelton. 2004. Local strain measurement within tendon. *Strain*. 40:157–163.
  24. Houssen, Y. G., I. Gusachenko, ..., J. M. Allain. 2011. Monitoring micrometer-scale collagen organization in rat-tail tendon upon mechanical strain using second harmonic microscopy. *J. Biomech.* 44:2047–2052.
  25. Sage, D. 2011. MIJ: a JAVA package for bi-directional communication and data exchange from MATLAB to ImageJ/Fiji. <http://bigwww.epfl.ch/sage/soft/mij/>.
  26. Butcher, P. N., and D. Cotter. 1990. *The Elements of Nonlinear Optics*. Cambridge University Press, Cambridge, UK.
  27. Deniset-Besseau, A., J. Duboisset, ..., M.-C. Schanne-Klein. 2009. Measurement of the second order hyperpolarizability of the collagen triple helix and determination of its physical origin. *J. Phys. Chem. B.* 113:13437–13445.
  28. Beck, K., and B. Brodsky. 1998. Supercoiled protein motifs: the collagen triple-helix and the  $\alpha$ -helical coiled coil. *J. Struct. Biol.* 122:17–29.
  29. Orgel, J. P. R. O., T. C. Irving, ..., T. J. Wess. 2006. Microfibrillar structure of type I collagen in situ. *Proc. Natl. Acad. Sci. USA*. 103:9001–9005.
  30. Abrahams, M. 1967. Mechanical behavior of tendon in vitro. A preliminary report. *Med. Biol. Eng.* 5:433–443.
  31. Hansen, K. A., J. A. Weiss, and J. K. Barton. 2002. Recruitment of tendon crimp with applied tensile strain. *J. Biomech. Eng.* 124:72–77.
  32. Screen, H. R. C., J. C. Shelton, ..., D. A. Lee. 2005. The influence of noncollagenous matrix components on the micromechanical environment of tendon fascicles. *Ann. Biomed. Eng.* 33:1090–1099.
  33. Lacombe, R., O. Nadiarnykh, ..., P. J. Campagnola. 2008. Phase matching considerations in second harmonic generation from tissues: effects on emission directionality, conversion efficiency and observed morphology. *Opt. Commun.* 281:1823–1832.
  34. Strupler, M., and M.-C. Schanne-Klein. 2010. Simulating second harmonic generation from tendon—do we see fibrils? *Biomed. Optics*. Paper BTuD83.
  35. Rivard, M., M. Laliberté, ..., F. Légaré. 2010. The structural origin of second harmonic generation in fascia. *Biomed. Opt. Express*. 2:26–36.
  36. Fratzl, P. 2003. Cellulose and collagen: from fibers to tissues. *Curr. Opin. Colloid Interface Sci.* 8:32–39.
  37. Gautieri, A., S. Vesentini, ..., M. J. Buehler. 2011. Hierarchical structure and nanomechanics of collagen microfibrils from the atomistic scale up. *Nano Lett.* 11:757–766.
  38. van der Rijt, J. A. J., K. O. van der Werf, ..., J. Feijen. 2006. Micromechanical testing of individual collagen fibrils. *Macromol. Biosci.* 6:697–702.
  39. Shen, Z. L., M. R. Dodge, ..., S. J. Eppell. 2008. Stress-strain experiments on individual collagen fibrils. *Biophys. J.* 95:3956–3963.
  40. Loison, C., and D. Simon. 2010. Additive model for the second harmonic generation hyperpolarizability applied to a collagen-mimicking peptide (Pro-Pro-Gly)<sub>10</sub>. *J. Phys. Chem. A.* 114:7769–7779.
  41. Rocha-Mendoza, I., D. R. Yankelevich, ..., A. Knoesen. 2007. Sum frequency vibrational spectroscopy: the molecular origins of the optical second-order nonlinearity of collagen. *Biophys. J.* 93:4433–4444.

## 4.4 Discussion

In this work, we first observed and analyzed crimp behavior by SHG microscopy during series of load-relaxation cycles in rat-tail tendon. This cyclic loading represents a simple and comprehensive way to evidence the mechanical hysteresis of collagen tissue. Notably, we demonstrated that tissue preconditioning during first cycles in a series is related to changes in tendon stress-free state. In other words, the relaxed length of a tendon increases after preconditioning, and the heel region of the stress-strain curve is shifted towards higher strains.

On an improved experimental setup, we then performed P-SHG measurements of SHG anisotropy parameter  $\rho$  in a tendon undergoing mechanical loading. Mechanical loading is expected to induce a reorganization of the collagen fibril orientations within the tissue, which would result in a different SHG anisotropy parameter. Many groups have reported P-SHG comparative studies for different samples [15, 37, 38, 41], but  $\rho$  variations have never been reported within the same tissue as a response to tissue perturbations. In that respect, we present unique results on SHG anisotropy parameter  $\rho$  variations in tendon related to the change of orientational order of collagen fibrils. Other optical parameters such as tissue birefringence and attenuation length were shown to vary significantly upon loading, which provides complementary information about the tissue reorganization at microscopic scale. Most importantly, we obtained reproducible experimental results with error bars small enough to observe significant variations of all the parameters of interest.

In the time line of my thesis work, the numerical simulations of SHG in tendon described in chapter 3 were performed after the biomechanical studies of this chapter. However, these numerical simulations give a new insight on the interpretation of obtained P-SHG results we published in Biophysical Journal article [139], which should be discussed.

On one hand, in our P-SHG study we showed that a number of optical parameters varies upon mechanical load, notably the birefringence  $\Delta n$  and the SHG anisotropy parameter  $\rho$ . On the other hand, in the previous chapter we showed that the tissue birefringence can dramatically influence the apparent value of the anisotropy parameter  $\rho$ , though optical dispersion may partly alleviate this effect. Thus, the observed  $\rho$  variations with strain may be caused not only by fibril realignment in tendon (described in 2.3.5), but also by the artefactual changes in apparent  $\rho$  due to increasing birefringence (described in 3.3.3.6). The relative contributions of these two effects are not known *a priori*. In order to better understand the influence of the varying birefringence on  $\rho$  variations one may perform additional numerical simulations for different birefringence values  $\Delta n$ . However, we think that while the birefringence can influence the  $\rho$  measurements, its contribution is not dominant. Indeed, while the birefringence increases monotonously,

it is not the case for  $\rho$ , which first decreases and then increases with strain (see Fig. 5 in [139]). Additionally, while the birefringence saturates and varies slowly at large strains,  $\rho$  continues to vary significantly. These clues indicate that tendon stretching and hence, fibril reordering, has a significant effect on  $\rho$  change independently of the birefringence value in tissue.

To conclude, during this work we developed a new modality to study collagen tissues by combining controlled mechanical traction with SHG microscopy and advanced P-SHG measurements. This new modality required a verification of principle, which was performed as a first part of our biomechanical study. Afterwards, P-SHG measurements were performed in a stretched tendon, which revealed significant variation of SHG parameter of interest reflecting the change of disorder in tissue. These modality uniting mechanics and SHG can be readily generalized to more complex collagenous tissues such as skin, *dura mater* and cornea. We believe our findings have an important impact on the general understanding of SHG from tendons in particular, and collagenous tissues in general.



# Conclusions and Perspectives

In this work we developed a comprehensive theory for P-SHG microscopy, and tested this technique for probing collagen tissues organization at submicrometre scale. Our work involved three vast topics: the origin of SHG polarization distortion in thick anisotropic tissues, the coupling of SHG microscopy with mechanical studies in tendon, and the relationship between the internal tissue organization and tissue nonlinear susceptibility tensor probed by P-SHG. In this concluding section, we make a summary of the results we achieved in attempt to improve the present state of the art P-SHG microscopy, and briefly trace the main perspectives for further development of this technique.

We performed a systematic study to identify the effects influencing P-SHG measurements in collagen tissues. Our initial experimental study showed that polarization states of both excitation and SH waves in rat-tail tendon are influenced by three optical effects: birefringence, diattenuation, and polarization cross-talk. Their impact accumulates with propagation in tissue and eventually distorts the detected SHG polarization. Birefringence introduces a phase delay between two orthogonal polarizations of the excitation field, which drastically changes SHG intensity at certain depths. Diattenuation signifies that two orthogonal excitation polarizations undergo different attenuation in tissue, which directly impedes the measurements of nonlinear anisotropy of the sample. Finally, polarization cross-talk arises when radiated SHG waves change their polarization state by scattering on misaligned fibrils in tendon. We then developed a phenomenological theoretical model, which accounts for these effects, determines their magnitude based on P-SHG measurements, and eventually allows one to correct P-SHG data to access the actual SHG anisotropy in tissue.

After that, we numerically simulated the SHG microscopy in birefringent nonlinear media, such as tendon. In our simulations we explicitly accounted for tissue birefringence, but not for diattenuation and polarization cross-talk. The simulation results showed that tight vectorial focusing of the incident field has little effect on the polarization state. However, we identified an unexpectedly strong effect of local birefringence on SHG signal. Slightly different phase distributions within focal volume for incident ordinary and extraordinary waves resulted in drastically different SHG outcomes for these two waves. As a result, the measured tissue nonlinear anisotropy was directly affected by the dif-

ference in SHG efficiency, which was also shown to be influenced by index dispersion in the medium. This relative SHG efficiency cannot be measured independently, and thus cannot be easily corrected for.

We also coupled SHG imaging with mechanical assays in rat-tail tendon to monitor microscopic crimp morphology simultaneously with macroscopic stress-strain measurements. As this type of biomechanical setup has never been reported before, our work provides a proof of the concept that SHG microscopy is a promising complement for mechanical studies, which can elucidate the relationship between tissue microscopic structure and its macroscopic functional features.

Finally, we developed a theoretical model that links the submicrometre orientational organization of harmonophores within the tissue to its nonlinear anisotropy probed by P-SHG. Our calculations showed, that SHG anisotropy parameter  $\rho$  increases with orientational disorder, which makes  $\rho$  a promising indicator of internal tissue organization. We then tested this model by performing P-SHG measurements in an increasingly stretched rat-tail tendon, which is expected to undergo microscopic structural changes upon loading. Our experimental results showed that birefringence and diattenuation vary significantly as a function of strain. Most importantly, we unambiguously observed variations in SHG anisotropy  $\rho$ , which were attributed to the changes in the internal structure of the tissue.

In order to further improve the understanding of P-SHG in collagen tissues and increase precision on measured SHG anisotropy, additional studies may be contemplated. A logical way to upgrade polarization-resolved experiments is to implement full characterization of input and output polarization states according to Mueller matrix formalism. This requires generalization of this formalism to SHG analysis, and entails introducing polarization state generator and analyzer in the beam pathway, as in the recent paper of Mazumder et al. [144]. Additionally, an integral approach to study SHG efficiency dependence on birefringence, dispersion and beam phase may be undertaken. This approach should include elaborated theoretical considerations, numerical simulations, and independent measurements of tissue optical parameters. Finally, our experiments combining P-SHG imaging and biomechanical tissue testing may be generalized to other collagen tissues such as skin and cornea.

All results achieved in this work already provide a comprehensive study of P-SHG microscopy in collagen tissues. Our theoretical and numerical models, which have been tested experimentally on our unique biomechanical setup, make P-SHG a promising and confirmed tool to study variations in collagen tissues undergoing structural changes. We strongly believe that in the context of recently increasing interest to P-SHG modality, the results of this work makes a timely contribution to the area of advanced tissue microscopy.

# Appendix

## Implementation of numerical calculation

The form of the integral for the focal field  $\mathbf{E}$  (Eq. 3.2) suggests that Fourier Transform (FT) can be used to calculate the field distribution. In birefringent media, the calculation of fields  $\mathbf{E}^{o,e}$  from Hertz potentials  $\psi^{o,e}$  (Eq. 3.9) explicitly relies on FT. The most common way to implement FT numerically is via Discrete Fourier Transform (DFT). DFT and inverse DFT are defined as follows for an array of length  $N$ :

$$\begin{aligned} Y(k) &= \sum_{j=1}^N y(j) \omega_N^{(j-1)(k-1)} \\ y(j) &= \frac{1}{N} \sum_{k=1}^N Y(k) \omega_N^{-(j-1)(k-1)} \end{aligned} \quad (4.1)$$

where  $Y(k)$  is FT image ( $k$ -space) of  $y(j)$  ( $x$ -space) and  $\omega_N = e^{-i\frac{2\pi}{N}}$ . DFT is usually calculated via Fast Fourier Transform (FFT) algorithms. For example, Matlab uses FFTW library [145] with computational complexity of  $N \log N$  for any  $N$ . The drawback of this method is that the resolutions in  $k$ - and  $x$ -spaces are mutually dependent and coupled by the equation:

$$\Delta k = \frac{2\pi}{N \Delta x}. \quad (4.2)$$

For example, in the case of beam focusing, the resolution in the focal zone provided by DFT is determined by the diameter of the back pupil and is about  $\Delta x \sim 2\pi/k \sim \lambda$ , which is obviously insufficient for tight focusing. However, this property is purely a consequence of the method and doesn't have physical limitation beneath. Another drawback of DFT is that zero phase  $e^{i0}$  must correspond to the first element of  $y(j)$ , regardless of whether  $j$  corresponds to  $x = 0$  or not.

The problem of insufficient resolution in  $k$ -space is usually resolved by a technique named *zero padding*, which consists in enlarging  $y$  with additional zeros, bearing no additional information about the  $y$  itself. As it can be seen from 4.2, greater  $N$  with fixed  $\Delta x$  results in smaller  $\Delta k$ . The price to pay is evidently the calculation time. For example, for

1D-arrays a 10-fold increase in resolution, the calculation time will be  $\left(\frac{10N \log(10N)}{N \log(N)}\right) \geq 10$  times greater.

These two problems can be circumvented by using Chirp Z-Transform (CZT), which is defined in the following way:

$$Y(k) = \sum_{n=0}^{N-1} y(n)z^{nk}. \quad \text{for } k = 0..M-1. \quad (4.3)$$

Here,  $z$  is an arbitrary complex number, but here we will only consider the case of  $z = e^{i\phi}$ . While in DFT  $\phi$  is fixed to  $2\pi/N$ , in CZT it can be set manually, allowing for arbitrary  $x$ - and  $k$ -resolutions. CZT is efficiently calculated by two FFT and one inverse FFT, so it also has  $N \log N$  computational complexity. CZT has already been used for beam calculations [135]. In this work we give an alternative insight on the derivation of CZT as a form of FT with arbitrary discretization in  $x$ - and  $k$ -spaces.

We start from direct discretization of Fourier integral in order to obtain Fourier transform of the signal. For each point  $k_m$  one has

$$\tilde{f}(k_m) = \frac{1}{\sqrt{2\pi}} \int_{-\infty}^{\infty} f(x)e^{-ik_mx} dx \approx \frac{\Delta x}{\sqrt{2\pi}} \sum_{n=1}^N f(x_n)e^{-ik_mx_n}. \quad (4.4)$$

For a signal sampled between  $x_{min}$  and  $x_{max}$  with  $\Delta x = \frac{x_{max}-x_{min}}{N-1}$  and for the spectral region between  $k_{min}$  and  $k_{max}$  with  $\Delta k = \frac{k_{max}-k_{min}}{M-1}$ , the expression 4.4 reads:

$$\begin{aligned} & \frac{\Delta x}{\sqrt{2\pi}} \sum_{n=1}^N f(x_n)e^{-ik_mx_n} = \\ & = \frac{\Delta x}{\sqrt{2\pi}} \sum_{n=1}^N f(x_n)e^{-i[k_{min}+\Delta k(m-1)][x_{min}+\Delta x(n-1)]} \\ & = \frac{\Delta x}{\sqrt{2\pi}} e^{-ik_{min}x_{min}} \underbrace{\left[ e^{-ix_{min}\Delta k(m-1)} \left\{ \sum_{n=1}^N \overbrace{[f(x_n)e^{-ik_{min}\Delta x(n-1)}]}^* e^{-i\Delta k\Delta x(n-1)(m-1)} \right\} \right]}_{**} \end{aligned} \quad (4.5)$$

When  $k_{min}$  and  $x_{min}$  are zeros,  $M = N$  and  $\Delta x\Delta k = \frac{2\pi}{N}$ , the expression above simplifies to a standard DFT. Here, curly brackets signify  $N$ -to- $M$  CZT, while square brackets emphasize element-wise phase shift before CZT (\*, in  $x$ -space) and after CZT (\*\*, in  $k$ -space). The function we introduce uses  $(x_{min}, x_{max}, N)$  and  $(k_{min}, k_{max}, M)$  as parameters to calculate FT of the region of interest. In practice, we show 3 to 5-fold acceleration for one-dimensional FT, and even more for 2D- and 3D-FT as compared

to zero padding. However, it is necessary to ensure that sampled signal has enough information to reconstruct high frequencies, i.e. that  $\frac{2\pi}{\Delta x} \geq \max(|k_{max}|, |k_{min}|)$ , equality corresponding to a standard DFT.

## Calculation speed for focal field simulations

Field distribution is calculated independently for each  $z$ , so the task can be parallelized and accelerated using, for example, multicore general-purpose graphics processing units (GPGPU). We performed our simulations on an Intel Core2 6420 CPU with 4Gb RAM, equipped with NVIDIA GTX460 GPU. The code is written in Matlab using special plugin for GPU computing (Accelereyes Jacket, Accelereyes, trial version). Typical calculation time for 10 field components (2 ordinary and 3 extraordinary for both linear polarizations of the incident beam) with number of points  $64 \times 64 \times 256$  was about 0.5 s. We observed a 30-fold speed-up when using GPU for these calculations.



# Bibliography

- [1] S. Roth and I. Freund, “Coherent optical harmonic generation in rat-tail tendon,” *Optics Communications*, vol. 33, no. 3, pp. 292–296, 1980.
- [2] S. Roth and I. Freund, “Optical second-harmonic scattering in rat-tail tendon,” *Biopolymers*, vol. 20, pp. 1271–1290, June 1981.
- [3] S. Roth and I. Freund, “Second harmonic generation and orientational order in connective tissue: a mosaic model for fibril orientational ordering in rat-tail tendon,” *Journal of Applied Crystallography*, vol. 15, pp. 72–78, Feb. 1982.
- [4] I. Freund and M. Deutsch, “Second-harmonic microscopy of biological tissue,” *Optics letters*, vol. 11, pp. 94–98, Feb. 1986.
- [5] I. Freund, M. Deutsch, and A. Sprecher, “Connective tissue polarity. Optical second-harmonic microscopy, crossed-beam summation, and small-angle scattering in rat-tail tendon,” *Biophysical journal*, vol. 50, pp. 693–712, Oct. 1986.
- [6] P. Stoller, B.-M. Kim, A. M. Rubenchik, K. M. Reiser, and L. B. Da Silva, “Polarization-dependent optical second-harmonic imaging of a rat-tail tendon,” *Journal of biomedical optics*, vol. 7, pp. 205–214, Apr. 2002.
- [7] P. Stoller, K. M. Reiser, P. M. Celliers, and A. M. Rubenchik, “Polarization-modulated second harmonic generation in collagen,” *Biophysical journal*, vol. 82, pp. 3330–3342, June 2002.
- [8] P. J. Campagnola, A. C. Millard, M. Terasaki, P. E. Hoppe, C. J. Malone, and W. A. Mohler, “Three-Dimensional High-Resolution Second-Harmonic Generation Imaging of Endogenous Structural Proteins in Biological Tissues,” *Biophysical Journal*, vol. 81, no. 1, pp. 493–508, 2002.
- [9] W. R. Zipfel, R. M. Williams, and W. W. Webb, “Nonlinear magic: multiphoton microscopy in the biosciences,” *Nature biotechnology*, vol. 21, pp. 1369–1377, Nov. 2003.

- [10] W. R. Zipfel, R. M. Williams, R. Christie, A. Y. Nikitin, B. T. Hyman, and W. W. Webb, “Live tissue intrinsic emission microscopy using multiphoton-excited native fluorescence and second harmonic generation,” *Proceedings of the National Academy of Sciences of the United States of America*, vol. 100, pp. 7075–7080, June 2003.
- [11] P. Stoller, P. M. Celliers, K. M. Reiser, and A. M. Rubenchik, “Quantitative second-harmonic generation microscopy in collagen,” *Applied optics*, vol. 42, pp. 5209–5019, Sept. 2003.
- [12] C. Hsiao, Y. Sun, W. Lo, S.-J. Lin, S.-H. Jee, G. Jan, and C.-Y. Dong, “Imaging condition optimization in multiphoton microscopy of three-dimensional collagen fiber structures,” *Journal of the Chinese Chemical Society*, vol. 51, pp. 1115–1120, 2004.
- [13] R. M. Williams, W. R. Zipfel, and W. W. Webb, “Interpreting second-harmonic generation images of collagen I fibrils,” *Biophysical journal*, vol. 88, pp. 1377–1386, Feb. 2005.
- [14] F. Légaré, C. Pfeffer, and B. R. Olsen, “The role of backscattering in SHG tissue imaging,” *Biophysical journal*, vol. 93, pp. 1312–1320, Aug. 2007.
- [15] F. Tiaho, G. Recher, and D. Rouede, “Estimation of helical angles of myosin and collagen by second harmonic generation imaging microscopy,” *Optics express*, vol. 15, no. 19, pp. 12286–12295, 2007.
- [16] R. A. R. Rao, M. R. Mehta, and K. C. Toussaint, “Fourier transform-second-harmonic generation imaging of biological tissues,” *Optics express*, vol. 17, pp. 14534–42, Aug. 2009.
- [17] S.-P. Tai, T.-H. Tsai, W.-J. Lee, D.-B. Shieh, Y.-H. Liao, H.-Y. Huang, K. Zhang, H.-L. Liu, and C.-K. Sun, “Optical biopsy of fixed human skin with backward-collected optical harmonics signals,” *Optics express*, vol. 13, pp. 8231–42, Oct. 2005.
- [18] S. Zhuo, J. Chen, T. Luo, and D. Zou, “Multimode nonlinear optical imaging of the dermis in ex vivo human skin based on the combination of multichannel mode and Lambda mode,” *Optics express*, vol. 14, pp. 7810–20, Aug. 2006.
- [19] T. Luo, J. X. Chen, S. M. Zhuo, K. C. Lu, X. S. Jiang, and Q. G. Liu, “Visualization of collagen regeneration in mouse dorsal skin using second harmonic generation microscopy,” *Laser Physics*, vol. 19, pp. 478–482, Mar. 2009.
- [20] M. Han, G. Giese, and J. Bille, “Second harmonic generation imaging of collagen fibrils in cornea and sclera,” *Optics express*, vol. 13, pp. 5791–7, July 2005.

- [21] A. T. Yeh, N. Nassif, A. Zoumi, and B. J. Tromberg, “Selective corneal imaging using combined second-harmonic generation and two-photon excited fluorescence,” *Optics letters*, vol. 27, pp. 2082–4, Dec. 2002.
- [22] B. Vohnsen and P. Artal, “Second-harmonic microscopy of ex vivo porcine corneas,” *Journal of microscopy*, vol. 232, pp. 158–63, Oct. 2008.
- [23] P. Matteini, F. Ratto, F. Rossi, R. Cicchi, C. Stringari, D. Kapsokalyvas, F. S. Pavone, and R. Pini, “Photothermally-induced disordered patterns of corneal collagen revealed by SHG imaging,” *Optics express*, vol. 17, pp. 4868–78, Mar. 2009.
- [24] R. A. R. Rao, M. R. Mehta, S. Leithem, and K. C. Toussaint, “Quantitative analysis of forward and backward second-harmonic images of collagen fibers using Fourier transform second-harmonic-generation microscopy,” *Optics letters*, vol. 34, pp. 3779–81, Dec. 2009.
- [25] K. G. M. Brockbank, W. R. MacLellan, J. Xie, S. F. Hamm-Alvarez, Z. Z. Chen, and K. Schenke-Layland, “Quantitative second harmonic generation imaging of cartilage damage,” *Cell and tissue banking*, vol. 9, pp. 299–307, Dec. 2008.
- [26] M. Wang, K. Reiser, and A. Knoesen, “Spectral moment invariant analysis of disorder in polarization-modulated second-harmonic-generation images obtained from collagen assemblies,” *JOSA A*, vol. 24, no. 11, pp. 3573–3586, 2007.
- [27] A.-M. Pena, A. Fabre, D. Débarre, J. Marchal-Somme, B. Crestani, J.-L. Martin, E. Beaurepaire, and M.-C. Schanne-Klein, “Three-dimensional investigation and scoring of extracellular matrix remodeling during lung fibrosis using multiphoton microscopy,” *Microscopy research and technique*, vol. 70, pp. 1–9, 2007.
- [28] M. Strupler, A.-M. Pena, M. Hernest, P.-L. Tharaux, J.-L. Martin, E. Beaurepaire, and M.-C. Schanne-Klein, “Second harmonic imaging and scoring of collagen in fibrotic tissues,” *Optics express*, vol. 15, pp. 4054–65, Apr. 2007.
- [29] S.-W. Chu, T.-M. Liu, C.-K. Sun, C.-Y. Lin, and H.-J. Tsai, “Real-time second-harmonic microscopy based on a 2-GHz repetition rate Ti:sapphire laser,” *Optics express*, vol. 11, no. 8, pp. 933–938, 2003.
- [30] S. V. Plotnikov, A. C. Millard, P. Campagnola, and W. a. Mohler, “Characterization of the myosin-based source for second-harmonic generation from muscle sarcomeres,” *Biophysical journal*, vol. 90, pp. 693–703, Jan. 2006.
- [31] D. A. Dombeck, K. A. Kasischke, H. D. Vishwasrao, M. Ingelsson, B. T. Hyman, and W. W. Webb, “Uniform polarity microtubule assemblies imaged in native

- brain tissue by second-harmonic generation microscopy,” *Proceedings of the National Academy of Sciences of the United States of America*, vol. 100, pp. 7081–6, June 2003.
- [32] G. Mizutani, Y. Sonoda, H. Sano, M. Sakamoto, T. Takahashi, and S. Ushioda, “Detection of starch granules in a living plant by optical second harmonic microscopy,” *Journal of Luminescence*, vol. 87-89, pp. 824–826, May 2000.
- [33] G. Cox, N. Moreno, and J. Feijó, “Second-harmonic imaging of plant polysaccharides,” *Journal of biomedical optics*, vol. 10, no. 2, p. 024013, 2005.
- [34] R. M. Brown, A. C. Millard, and P. J. Campagnola, “Macromolecular structure of cellulose studied by second-harmonic generation imaging microscopy,” *Optics letters*, vol. 28, pp. 2207–9, Nov. 2003.
- [35] O. Nadiarynkh and P. Campagnola, “Retention of polarization signatures in SHG microscopy of scattering tissues through optical clearing,” *Optics express*, vol. 17, pp. 5794–806, Mar. 2009.
- [36] A. Erikson, J. Ortegren, T. Hompland, C. de Lange Davies, and M. Lindgren, “Quantification of the second-order nonlinear susceptibility of collagen I using a laser scanning microscope,” *Journal of biomedical optics*, vol. 12, no. 4, p. 044002, 2007.
- [37] X. Han, R. M. Burke, M. L. Zettel, P. Tang, and E. B. Brown, “Second harmonic properties of tumor collagen: determining the structural relationship between reactive stroma and healthy stroma,” *Optics express*, vol. 16, pp. 1846–59, Feb. 2008.
- [38] J. C. Mansfield, C. P. Winlove, J. Moger, and S. J. Matcher, “Collagen fiber arrangement in normal and diseased cartilage studied by polarization sensitive nonlinear microscopy,” *Journal of biomedical optics*, vol. 13, no. 4, p. 044020, 2008.
- [39] T. Yasui, K. Sasaki, Y. Tohno, and T. Araki, “Tomographic Imaging of Collagen Fiber Orientation in Human Tissue Using Depth-Resolved Polarimetry of Second-Harmonic-Generation Light,” *Optical and Quantum Electronics*, vol. 37, pp. 1397–1408, Jan. 2006.
- [40] C. Odin, Y. L. Grand, A. Renault, L. Gailhouse, and G. Baffet, “Orientation fields of nonlinear biological fibrils by second harmonic,” *Journal of Microscopy*, vol. 229, no. 1, pp. 32–38, 2008.
- [41] S. Psilodimitrakopoulos, S. I. C. O. Santos, I. Amat-Roldan, A. K. N. Thayil, D. Artigas, and P. Loza-Alvarez, “In vivo, pixel-resolution mapping of thick filaments’

- orientation in nonfibrillar muscle using polarization-sensitive second harmonic generation microscopy,” *Journal of biomedical optics*, vol. 14, no. 1, p. 014001, 2009.
- [42] J. Diamant, A. Keller, E. Baer, M. Litt, and R. G. C. Arridge, “Collagen; Ultrastructure and Its Relation to Mechanical Properties as a Function of Ageing,” *Proceedings of the Royal Society B: Biological Sciences*, vol. 180, pp. 293–315, Mar. 1972.
- [43] R. M. Alexander and H. C. Bennet-Clark, “Storage of elastic strain energy in muscle and other tissues,” *Nature*, vol. 265, pp. 114–117, 1977.
- [44] A. M. Cribb and J. E. Scott, “Tendon response to tensile stress: an ultrastructural investigation of collagen:proteoglycan interactions in stressed tendon,” *Journal of Anatomy*, vol. 187, pp. 423–428, 1995.
- [45] N. Sasaki and S. Odajima, “Elongation mechanism of collagen fibrils and force-strain relations of tendon at each level of structural hierarchy,” *Journal of Biomechanics*, vol. 29, no. 9, pp. 1131–1136, 1996.
- [46] J. Parkinson, A. Brass, G. Canova, and Y. Brechet, “The mechanical properties of simulated collagen fibrils,” *Journal of biomechanics*, vol. 30, no. 6, pp. 549–554, 1997.
- [47] K. Misof, G. Rapp, and P. Fratzl, “A new molecular model for collagen elasticity based on synchrotron X-ray scattering evidence.,” *Biophysical journal*, vol. 72, pp. 1376–81, Mar. 1997.
- [48] P. Fratzl, K. Misof, I. Zizak, G. Rapp, H. Amenitsch, and S. Bernstorff, “Fibrillar structure and mechanical properties of collagen,” *Journal of structural biology*, vol. 122, pp. 119–22, Jan. 1998.
- [49] R. Puxkandl, I. Zizak, O. Paris, J. Keckes, W. Tesch, S. Bernstorff, P. Purslow, and P. Fratzl, “Viscoelastic properties of collagen: synchrotron radiation investigations and structural model,” *Philosophical transactions of the Royal Society of London. Series B, Biological sciences*, vol. 357, pp. 191–7, Mar. 2002.
- [50] B. Alberts, A. Johnson, J. Lewis, M. Raff, K. Roberts, and P. Walter, *Molecular biology of the cell*. New York: Garland Science, 5th ed., 2008.
- [51] K. Beck and B. Brodsky, “Supercoiled protein motifs: the collagen triple-helix and the alpha-helical coiled coil,” *Journal of Structural Biology*, vol. 122, pp. 17–29, Jan. 1998.

- [52] Y. Komai and T. Ushiki, "The three-dimensional organization of collagen fibrils in the human cornea and sclera," *Investigative ophthalmology & visual science*, vol. 32, pp. 2244–58, July 1991.
- [53] Y. Ezura, S. Chakravarti, A. Oldberg, I. Chervoneva, and D. E. Birk, "Differential expression of lumican and fibromodulin regulate collagen fibrillogenesis in developing mouse tendons," *The Journal of cell biology*, vol. 151, pp. 779–88, Nov. 2000.
- [54] T. F. Linsenmayer, J. M. Fitch, and D. E. Birk, "Heterotypic collagen fibrils and stabilizing collagens," *Annals of the New York Academy of Sciences*, vol. 580, pp. 143–160, 1990.
- [55] J. E. Scott and C. R. Orford, "Dermatan sulphate-rich proteoglycan associates with rat tail-tendon collagen at the d band in the gap region," *The Biochemical journal*, vol. 197, no. 1, pp. 213–216, 1981.
- [56] J. E. Scott and D. A. D. Parry, "Control of collagen fibril diameters in tissues," *International journal of biological macromolecules*, vol. 14, pp. 292–3, Oct. 1992.
- [57] H. K. Graham, D. F. Holmes, R. B. Watson, and K. E. Kadler, "Identification of collagen fibril fusion during vertebrate tendon morphogenesis. The process relies on unipolar fibrils and is regulated by collagen-proteoglycan interaction," *Journal of molecular biology*, vol. 295, pp. 891–902, Jan. 2000.
- [58] D. J. S. Hulmes, D. F. Holmes, and C. Cummings, "Crystalline regions in collagen fibrils," *Journal of molecular biology*, vol. 184, pp. 473–7, Aug. 1985.
- [59] L. Jelinski, C. Sullivan, and D. A. Torchia, "<sup>2</sup>H NMR study of molecular motion in collagen fibrils," *Nature*, vol. 284, pp. 531–534, 1980.
- [60] D. J. S. Hulmes, T. J. Wess, D. J. Prockop, and P. Fratzl, "Radial packing, order, and disorder in collagen fibrils," *Biophysical journal*, vol. 68, pp. 1661–70, May 1995.
- [61] J. Woodhead-Galloway and P. Machin, "Modern theories of liquids and the diffuse equatorial X-ray scattering from collagen," *Acta Crystallographica Section A*, vol. 32, pp. 368–372, 1976.
- [62] M. Grynopas, "Three-dimensional packing of collagen in bone," *Nature*, vol. 265, pp. 381–382, 1977.
- [63] K. E. Kadler, D. F. Holmes, J. A. Trotter, and J. A. Chapman, "Collagen fibril formation," *The Biochemical journal*, vol. 316, pp. 1–11, May 1996.

- [64] D. J. S. Hulmes, “Building collagen molecules, fibrils, and suprafibrillar structures,” *Journal of structural biology*, vol. 137, no. 1-2, pp. 2–10, 2002.
- [65] V. L. C. Feitosa, B. D. C. Vidal, and E. R. Pimentel, “Optical anisotropy of a pig tendon under compression,” *Journal of anatomy*, vol. 200, pp. 105–11, Jan. 2002.
- [66] D. Z. Covizi, S. L. Felisbino, L. Gomes, E. R. Pimentel, and H. F. Carvalho, “Regional adaptations in three rat tendons,” *Tissue & cell*, vol. 33, pp. 483–90, Oct. 2001.
- [67] B. de Campos Vidal, “Image analysis of tendon helical superstructure using interference and polarized light microscopy,” *Micron*, vol. 34, pp. 423–32, Jan. 2003.
- [68] R. D. Young, “The ultrastructural organization of proteoglycans and collagen in human and rabbit scleral matrix,” *Journal of Cell Science*, vol. 74, pp. 95–104, 1985.
- [69] D. Maurice, “The structure and transparency of the cornea,” *The Journal of physiology*, vol. 136, pp. 263–286, 1957.
- [70] W. Radner, M. Zehetmayer, R. Aufreiter, and R. Mallinger, “Interlacing and Cross-Angle Distribution of Collagen Lamellae in the Human Cornea,” *Cornea*, vol. 17, no. 5, pp. 537–543, 1998.
- [71] G. B. Benedek, “Theory of transparency of the eye,” *Applied optics*, vol. 10, pp. 459–73, Mar. 1971.
- [72] R. M. Alexander, “Energy-saving mechanisms in walking and running,” *Journal of Experimental Biology*, vol. 160, pp. 55–69, 1991.
- [73] S. Vesentini, A. Redaelli, and F. M. Monteverchi, “Estimation of the binding force of the collagen molecule-decorin core protein complex in collagen fibril,” *Journal of biomechanics*, vol. 38, pp. 433–43, Mar. 2005.
- [74] P. Ciarletta and M. Ben Amar, “A finite dissipative theory of temporary interfibrillar bridges in the extracellular matrix of ligaments and tendons,” *Journal of the Royal Society, Interface*, vol. 6, pp. 909–24, Oct. 2009.
- [75] F. O. Schmitt, C. E. Hall, and M. A. Jakus, “Electron microscope investigations of the structure of collagen,” *Journal of Cellular and Comparative Physiology*, vol. 20, no. 1, pp. 11–33, 1942.

- [76] C. E. Hall, M. A. Jakus, and F. O. Schmitt, "Electron microscope observations of collagen," *Journal of the American Chemical Society*, vol. 64, no. 5, pp. 1234–1234, 1942.
- [77] E. A. G. Chernoff and D. A. Chernoff, "Atomic force microscope images of collagen fibers," vol. 10, pp. 596–599, AVS, 1992.
- [78] D. Baselt, J. Revel, and J. Baldeschwieler, "Subfibrillar Structure of Type I Collagen Observed by Atomic Force Microscopy," *Biophysical journal*, vol. 65, pp. 2644–2655, 1993.
- [79] I. Revenko, F. Sommer, D. T. Minh, R. Garrone, and J. M. Franc, "Atomic force microscopy study of the collagen fibre structure," *Biology of the cell*, vol. 80, pp. 67–9, Jan. 1994.
- [80] M. Gale, M. Pollanen, P. Markiewicz, and M. Goh, "Sequential Assembly of Collagen Revealed by Atomic Force Microscopy," *Biophysical journal*, vol. 68, pp. 2124–2128, 1995.
- [81] T. Gutschmann, G. E. Fantner, J. H. Kindt, M. Venturoni, S. Danielsen, and P. K. Hansma, "Force spectroscopy of collagen fibers to investigate their mechanical properties and structural organization," *Biophysical journal*, vol. 86, pp. 3186–93, May 2004.
- [82] S.-W. Chu, S.-P. Tai, M.-C. Chan, C.-K. Sun, I.-C. Hsiao, C.-H. Lin, Y.-C. Chen, and B.-L. Lin, "Thickness dependence of optical second harmonic generation in collagen fibrils," *Optics express*, vol. 15, pp. 12005–10, Oct. 2007.
- [83] A. Stylianou, M. Kyriazi, K. Politopoulos, and D. Yova, "Combined SHG signal information with AFM imaging to assess conformational changes in collagen," *Proc. 9th International Conference on Information Technology and Applications in Biomedicine*, no. November, pp. 5–7, 2009.
- [84] H. Maeda, "An Atomic Force Microscopy Study of Ordered Molecular Assemblies and Concentric Ring Patterns from Evaporating Droplets of Collagen Solutions," *Langmuir*, vol. 15, pp. 8505–8513, Nov. 1999.
- [85] G. Mosser, A. Anglo, C. Helary, Y. Bouligand, and M.-M. Giraud-Guille, "Dense tissue-like collagen matrices formed in cell-free conditions," *Matrix biology*, vol. 25, pp. 3–13, Jan. 2006.

- [86] F. Gobeaux, E. Belamie, G. Mosser, P. Davidson, P. Panine, and M.-M. Giraud-Guille, “Cooperative ordering of collagen triple helices in the dense state,” *Langmuir*, vol. 23, pp. 6411–7, May 2007.
- [87] L. J. Gathercole, A. Keller, and J. S. Shah, “The periodic wave pattern in native tendon collagen: correlation of polarizing with scanning electron microscopy,” *Journal of microscopy*, vol. 102, pp. 95–105, Sept. 1974.
- [88] Y. Feng and T. L. Simpson, “Comparison of Human Central Cornea and Limbus in Vivo Using Optical Coherence Tomography,” *Optometry and Vision Science*, vol. 82, no. 5, pp. 416–419, 2005.
- [89] C. Ustundag, H. Bahcecioglu, A. Ozdamar, C. Aras, R. Yildirim, and S. Ozkan, “Optical coherence tomography for evaluation of anatomical changes in the cornea after laser in situ keratomileusis,” *Journal of cataract and refractive surgery*, vol. 26, pp. 1458–62, Oct. 2000.
- [90] I. Grulkowski, M. Gora, M. Szkulmowski, I. Gorczynska, D. Szlag, S. Marcos, A. Kowalczyk, and M. Wojtkowski, “Anterior segment imaging with Spectral OCT system using a high-speed CMOS camera,” *Optics express*, vol. 17, pp. 4842–58, Mar. 2009.
- [91] M. Pircher, E. Götzinger, R. A. Leitgeb, A. Fercher, and C. Hitzenberger, “Measurement and imaging of water concentration in human cornea with differential absorption optical coherence tomography,” *Optics express*, vol. 11, pp. 2190–7, Sept. 2003.
- [92] G. Latour, G. Georges, L. S. Lamoine, C. Deumié, J. Conrath, and L. Hoffart, “Light scattering from human corneal grafts: Bulk and surface contribution,” *Journal of Applied Physics*, vol. 108, no. 5, p. 053104, 2010.
- [93] G. Latour, G. Georges, L. S. Lamoine, C. Deumié, J. Conrath, and L. Hoffart, “Human graft cornea and laser incisions imaging with micrometer scale resolution full-field optical coherence tomography,” *Journal of biomedical optics*, vol. 15, no. 5, p. 056006, 2010.
- [94] K. Hansen, J. Barton, and J. A. Weiss, “Optical coherence tomography imaging of collagenous tissue microstructure,” *Proc. SPIE BIOS 2000*, vol. 3914, no. January, 2000.
- [95] K. A. Hansen, J. A. Weiss, and J. K. Barton, “Recruitment of Tendon Crimp With Applied Tensile Strain,” *Transactions of the ASME*, vol. 124, pp. 72–77, 2002.

- [96] A. Podoleanu, J. Rogers, and D. Jackson, “OCT en-face images from the retina with adjustable depth resolution in real time,” *IEEE Journal of Selected Topics in Quantum Electronics*, vol. 5, no. 4, pp. 1176–1184, 1999.
- [97] N. A. Nassif, B. Cense, B. H. Park, M. C. Pierce, S. H. Yun, B. E. Bouma, G. J. Tearney, T. C. Chen, and J. F. de Boer, “In vivo high-resolution video-rate spectral-domain optical coherence tomography of the human retina and optic nerve,” *Optics express*, vol. 12, no. 3, pp. 367–376, 2004.
- [98] W. Denk, J. H. Strickler, and W. W. Webb, “Two-photon laser scanning fluorescence microscopy,” *Science*, vol. 248, pp. 73–76, Oct. 1990.
- [99] W. Boyd, *Nonlinear Optics*. San Diego: Academic Press, 2nd ed., 2003.
- [100] M. Gu and C. J. R. Sheppard, “Comparison of three-dimensional imaging properties between two-photon and single-photon fluorescence microscopy,” *Journal of Microscopy*, vol. 177, no. 2, pp. 128–137, 1995.
- [101] P. Franken, A. Hill, C. Peters, and G. Weinreich, “Generation of Optical Harmonics,” *Physical Review Letters*, vol. 7, no. 4, pp. 118–120, 1961.
- [102] D. Débarre, *Microscopie par génération de troisième harmonique appliquée à la biologie*. PhD thesis, Ecole Polytechnique, 2006.
- [103] N. Olivier, *Contrast Mechanisms & Wavefront Control in Coherent Nonlinear Microscopy*. PhD thesis, Ecole Polytechnique, 2009.
- [104] D. Débarre, W. Supatto, A.-M. Pena, A. Fabre, T. Tordjmann, L. Combettes, M.-C. Schanne-Klein, and E. Beaurepaire, “Imaging lipid bodies in cells and tissues using third-harmonic generation microscopy,” *Nature Methods*, vol. 3, no. 1, pp. 47–53, 2006.
- [105] D. Débarre, N. Olivier, and E. Beaurepaire, “Signal epidetection in third-harmonic generation microscopy of turbid media,” *Optics express*, vol. 15, pp. 8913–24, July 2007.
- [106] N. Olivier, F. Aptel, K. Plamann, M.-C. Schanne-Klein, and E. Beaurepaire, “Harmonic microscopy of isotropic and anisotropic microstructure of the human cornea,” *Optics express*, vol. 18, pp. 5028–40, Mar. 2010.
- [107] M. D. Duncan, J. Reintjes, and T. J. Manuccia, “Scanning coherent anti-Stokes Raman microscope,” *Optics letters*, vol. 7, pp. 350–2, Aug. 1982.

- [108] L. Moreaux, O. Sandre, and J. Mertz, “Membrane imaging by second-harmonic generation microscopy,” *JOSA B*, vol. 17, no. 10, pp. 1685–1694, 2000.
- [109] M. Strupler, *Imagerie du collagène par microscopie multiphotonique. Application aux fibroses rénales*. PhD thesis, Ecole Polytechnique, 2008.
- [110] Y. Barad, H. Eisenberg, M. Horowitz, and Y. Silberberg, “Nonlinear scanning laser microscopy by third harmonic generation,” *Applied Physics Letters*, vol. 70, no. 8, pp. 922–924, 1997.
- [111] A. Deniset-Besseau, J. Duboisset, E. Benichou, F. Hache, P.-F. Brevet, and M.-C. Schanne-Klein, “Measurement of the second-order hyperpolarizability of the collagen triple helix and determination of its physical origin,” *The journal of physical chemistry. B*, vol. 113, pp. 13437–45, Oct. 2009.
- [112] A. E. Tuer, S. Krouglov, N. Prent, R. Cisek, D. Sandkuijl, K. Yasufuku, B. C. Wilson, and V. Barzda, “Nonlinear optical properties of type I collagen fibers studied by polarization dependent second harmonic generation microscopy,” *The journal of physical chemistry. B*, vol. 115, pp. 12759–69, Nov. 2011.
- [113] C. Loison and D. Simon, “Additive model for the second harmonic generation hyperpolarizability applied to a collagen-mimicking peptide (Pro-Pro-Gly)<sub>10</sub>,” *The journal of physical chemistry. A*, vol. 114, pp. 7769–79, July 2010.
- [114] A.-M. Pena, T. Boulesteix, T. Dartigalongue, and M.-C. Schanne-Klein, “Chiroptical effects in the second harmonic signal of collagens I and IV,” *Journal of the American Chemical Society*, vol. 127, pp. 10314–22, July 2005.
- [115] D. A. D. Parry and A. S. Craig, “Quantitative Electron Microscope Observations of the Collagen Fibrils in Rat-Tail Tendon,” *Biopolymers*, vol. 16, pp. 1015–1031, 1977.
- [116] T. Hompland, A. Erikson, M. Lindgren, T. Lindmo, and C. de Lange Davies, “Second-harmonic generation in collagen as a potential cancer diagnostic parameter,” *Journal of biomedical optics*, vol. 13, no. 5, p. 054050, 2008.
- [117] P. Réfrégier, M. Roche, and S. Brasselet, “Precision analysis in polarization-resolved second harmonic generation microscopy,” *Optics letters*, vol. 36, pp. 2149–51, June 2011.
- [118] I. Amat-Roldan, S. Psilodimitrakopoulos, P. Loza-Alvarez, and D. Artigas, “Fast image analysis in polarization SHG microscopy,” *Optics express*, vol. 18, pp. 17209–19, Aug. 2010.

- [119] J. Duboisset, D. Aït-Belkacem, M. Roche, H. Rigneault, and S. Brasselet, “Generic model of the molecular orientational distribution probed by polarization-resolved second-harmonic generation,” *Physical Review A*, vol. 85, pp. 1–9, Apr. 2012.
- [120] A. Lembares, X. H. Hu, and G. W. Kalmus, “Absorption spectra of corneas in the far ultraviolet region,” *Investigative ophthalmology & visual science*, vol. 38, pp. 1283–7, May 1997.
- [121] C. A. Dailey, B. J. Burke, and G. J. Simpson, “The general failure of Kleinman symmetry in practical nonlinear optical applications,” *Chemical Physics Letters*, vol. 390, pp. 8–13, May 2004.
- [122] A. E. Tuer, S. Krouglov, R. Cisek, D. Tokarz, and V. Barzda, “Three-Dimensional Visualization of the First Hyperpolarizability Tensor,” *Journal of Computational Chemistry*, vol. 32, pp. 1128–1134, 2011.
- [123] L. Bozec, G. van der Heijden, and M. Horton, “Collagen fibrils: nanoscale ropes,” *Biophysical journal*, vol. 92, pp. 70–5, Jan. 2007.
- [124] P. Fratzl, “Cellulose and collagen: from fibres to tissues,” *Current opinion in colloid and interface science*, vol. 8, pp. 32–39, 2003.
- [125] P.-J. Su, W.-L. Chen, Y.-F. Chen, and C.-Y. Dong, “Determination of collagen nanostructure from second-order susceptibility tensor analysis,” *Biophysical journal*, vol. 100, pp. 2053–62, Apr. 2011.
- [126] D. Aït-Belkacem, A. Gasecka, F. Munhoz, S. Brustlein, and S. Brasselet, “Influence of birefringence on polarization resolved nonlinear microscopy and collagen SHG structural imaging,” *Optics express*, vol. 18, pp. 14859–70, July 2010.
- [127] X. Wang and L. V. Wang, “Propagation of polarized light in birefringent turbid media: a Monte Carlo study,” *Journal of biomedical optics*, vol. 7, pp. 279–90, July 2002.
- [128] M. Xu, “Electric field Monte Carlo simulation of polarized light propagation in turbid media,” *Optics express*, vol. 12, pp. 6530–9, Dec. 2004.
- [129] J. C. Ramella-Roman, S. A. Prahl, and S. L. Jacques, “Three Monte Carlo programs of polarized light transport into scattering media: part I,” *Optics express*, vol. 13, pp. 4420–4438, Dec. 2005.
- [130] D. Arifler, I. Pavlova, A. Gillenwater, and R. Richards-Kortum, “Light scattering from collagen fiber networks: micro-optical properties of normal and neoplastic stroma,” *Biophysical journal*, vol. 92, pp. 3260–74, May 2007.

- [131] L. Novotny and B. Hecht, *Principles of nano-optics*. Cambridge: Cambridge University Press, 2006.
- [132] S. Hacyan and R. Jáuregui, “Evolution of optical phase and polarization vortices in birefringent media,” *Journal of Optics A: Pure and Applied Optics*, vol. 11, p. 085204, Aug. 2009.
- [133] P. C. Clemmow, “The theory of electromagnetic waves in a simple anisotropic medium,” *Proceedings IEE*, vol. 110, no. 1, pp. 101–106, 1963.
- [134] P. C. Clemmow, “The resolution of a dipole field into transverse electric and transverse magnetic waves,” *Proceedings IEE*, vol. 110, no. 1, pp. 107–111, 1963.
- [135] M. Leutenegger, R. A. R. Rao, R. A. Leitgeb, and T. Lasser, “Fast focus field calculations,” *Optics express*, vol. 14, pp. 11277–91, Nov. 2006.
- [136] N. J. Kemp, H. Zaatari, J. Park, H. G. Rylander, and T. Milner, “Form-biattenuance in fibrous tissues measured with polarization-sensitive optical coherence tomography (PS-OCT),” *Optics express*, vol. 13, pp. 4611–28, June 2005.
- [137] J. Park, N. J. Kemp, H. G. Rylander, and T. Milner, “Complex polarization ratio to determine polarization properties of anisotropic tissue using polarization-sensitive optical coherence tomography,” *Optics express*, vol. 17, pp. 13402–17, Aug. 2009.
- [138] I. Gusachenko, G. Latour, and M.-C. Schanne-Klein, “Polarization-resolved Second Harmonic microscopy in anisotropic thick tissues,” *Optics express*, vol. 18, pp. 19339–52, Aug. 2010.
- [139] I. Gusachenko, V. Tran, Y. G. Houssen, J.-M. Allain, and M.-C. Schanne-Klein, “Polarization-Resolved Second-Harmonic Generation in Tendon upon Mechanical Stretching,” *Biophysical Journal*, vol. 102, pp. 2220–2229, May 2012.
- [140] A. N. Bashkatov, E. A. Genina, V. I. Kochubey, and V. V. Tuchin, “Estimation of wavelength dependence of refractive index of collagen fibers of scleral tissue,” in *Controlling Tissue Optical Properties: Application in Clinical Study. Proceedings of SPIE*, vol. 4162, pp. 265–268, 2000.
- [141] G. Latour, I. Gusachenko, L. Kowalczyk, I. Lamarre, and M.-C. Schanne-Klein, “In vivo structural imaging of the cornea by polarization-resolved second harmonic microscopy,” *Biomedical optics express*, vol. 3, pp. 1–15, Jan. 2012.
- [142] H. R. C. Screen, D. L. Bader, D. a. Lee, and J. C. Shelton, “Local Strain Measurement within Tendon,” *Strain*, vol. 40, pp. 157–163, Nov. 2004.

- [143] Y. Goulam Houssen, I. Gusachenko, M.-C. Schanne-Klein, and J.-M. Allain, “Monitoring micrometer-scale collagen organization in rat-tail tendon upon mechanical strain using second harmonic microscopy,” *Journal of biomechanics*, vol. 44, pp. 2047–52, July 2011.
- [144] N. Mazumder, J. Qiu, M. R. Foreman, C. M. Romero, C.-W. Hu, H.-R. Tsai, P. Torok, and F.-J. Kao, “Polarization-resolved second harmonic generation microscopy with a four-channel Stokes-polarimeter,” *Optics Express*, vol. 20, no. 13, pp. 14090–14099, 2012.
- [145] M. Frigo and S. G. Johnson, “FFTW : an adaptative software architecture for the FFT,” in *Proceedings of the 1998 IEEE International Conference on Acoustics, Speech and Signal Processing*, pp. 1381–1384, 1998.



## Summary

Collagen is a major structural protein that forms various macromolecular organizations in tissues and is responsible for the biomechanical properties of most organs. Second harmonic generation (SHG) microscopy is a valuable imaging technique to probe collagen fibrillar organization. This work is aimed at implementing and characterizing polarization-resolved SHG (P-SHG) and coupling this technique to biomechanical assays to provide multiscale structural information on collagen tissues.

We first studied the linear propagation effects that affect P-SHG imaging of thick anisotropic tissues such as collagen tissues. We developed a theoretical model that accounts for birefringence, diattenuation, and polarization scrambling, and obtained an excellent agreement with our P-SHG measurements in rat-tail tendon. Moreover we performed numerical simulations of light propagation and harmonic generation in tendon and cornea, which confirmed the crucial role of birefringence for P-SHG signal formation.

We then implemented a new experimental device that combined mechanical testing with SHG imaging. It enabled visualization of the tendon crimp morphology at the micrometer scale during macroscopic strain–stress measurements. Our results proved that continuous SHG imaging allows for elucidating the link between macroscopic response and microscopic structure of tissues.

Finally, we developed a theoretical model, which relates the P-SHG signal anisotropy to the orientational order of its SHG-capable constituents at submicrometer scale. We tested our model by performing P-SHG measurements in increasingly stretched tendon, and successfully characterized variations of fibril disorder within fascicle with strain.

**Key words:** second harmonic microscopy, optical polarization, collagen, biomechanics, numerical simulations, biological tissues.

## Résumé

Le collagène est une protéine de structure majeure qui forme diverses organisations macromoléculaires dans les tissus, et est responsable des propriétés biomécaniques de la plupart des organes. La génération de seconde harmonique (SHG) est une technique d'imagerie adaptée pour sonder l'organisation fibrillaire du collagène. Ce travail vise à implémenter et à caractériser la SHG résolue en polarisation (P-SHG), et à coupler cette technique à des essais biomécaniques pour obtenir des informations structurales multiéchelles sur les tissus collagéniques.

Nous avons d'abord étudié les effets optiques linéaires qui influencent l'imagerie P-SHG dans les tissus anisotropes denses tels que les tissus collagéniques. Nous avons développé un modèle théorique qui prend en compte la biréfringence, la diatténuation et le mélange de polarisation, et nous avons obtenu un excellent accord avec nos mesures P-SHG dans le tendon de queue de rat. De plus, nous avons effectué des simulations numériques de la propagation du faisceau d'excitation et de la formation du signal SHG dans le tendon et la cornée. Ces simulations ont confirmé le rôle crucial de la biréfringence en P-SHG.

Nous avons ensuite mis en place un dispositif expérimental combinant des essais mécaniques avec l'imagerie SHG. Cela a permis de visualiser la morphologie du tendon à l'échelle micrométrique pendant les essais mécaniques macroscopiques. Nos résultats ont montré que l'imagerie SHG sous traction permet d'élucider le lien entre la réponse macroscopique des tissus et leur structure microscopique.

Enfin, nous avons développé un modèle théorique pour relier l'anisotropie du signal P-SHG à l'ordre orientationnel submicrométrique des harmonophores dans le tissu. Nous avons testé ce modèle par des mesures P-SHG sur un tendon soumis à une élongation croissante. Nous avons alors caractérisé avec succès les variations d'organisation des fibrilles dans le tendon en fonction de l'élongation.

**Mots-clés :** microscopie de seconde harmonique, polarisation optique, collagène, biomécanique, simulations numériques, tissus biologiques.